Defect Structure & Catalytic Activity of Yttria-Stabilised Zirconia

Thesis submitted for the degree of Doctor of Philosophy

Dominic Chaopradith

Department of Chemistry

University College London

2017

Declaration

I, Dominic Chaopradith confirm that the work presented in this thesis is my own. Where information has been derived from other sources, I confirm that this has been indicated in the thesis.

……

Abstract

Yttria-stabilised zirconia (YSZ) is an important technological material for a number of wide-ranging applications. Of interest to this thesis is the experimental finding that YSZ is an active catalyst for methane partial oxidation. Within this thesis computer simulations are performed in order to investigate the reaction pathway for this catalytic partial oxidation of methane (CPOM), as well as to understand better the defect arrangements and ordering present in YSZ.

In the first instance water adsorption on YSZ is investigated. Here the surface models used throughout this thesis are developed and the study of surface hydration is not only important when considering CPOM but also of fundamental importance and interest to solid oxide fuel cell applications. It is found that a very strong dissociative chemisorption of water with one hydroxyl occupying a stoichiometric oxygen vacancy can occur due to local structure rearrangement in YSZ.

Surface reduction and re-oxidation calculations reveal that oxygen ion mobility within YSZ lowers the reduction energy, giving rise to a plausible mechanism for generating partially reduced molecular oxygen species on the YSZ surface presenting an active surface for oxidation catalysis. CPOM calculations on this activated and oxidised surface reveal the Mars-van Krevelen nature of catalysis on YSZ and demonstrate that methane oxidation occurs via a formaldehyde intermediate, which in agreement with experiment will further oxidise to a stable surface formate species.

Finally a solid-solution investigation for yttria doping into zirconia over a range of dopant concentrations provides not only a method for effectively sampling the extremely large configuration space of YSZ, reproducing a number of macroscopic experimental observables about the system, but also yields local structure information about the yttrium and vacancy distribution of YSZ. In particular the energetic favourability of the yttrium-vacancy second nearest neighbour separation is established and its effect on vacancy separation revealed.

Table of Contents

Chapter 1

Methane and Synthesis Gas

This chapter discusses the importance of methane as a chemical feedstock, and in particular the indirect upgrading of methane via synthesis gas. The three major synthesis gas production processes; methane steam reforming, methane dry reforming and methane partial oxidation are discussed. Catalytic partial oxidation is viewed as a favourable process due to the mild thermodynamic exothermicity of the reaction and desirable hydrogen to carbon monoxide ratio of the synthesis gas produced for downstream upgrading applications. Yttria stabilised zirconia has been shown to be active for methane partial oxidation and the experimental evidence is reviewed, providing the basis for the majority of the computational study contained in this thesis.

1.1 Introduction

Methane, the principle component of natural gas, is currently used for heating, power generation, and as a feedstock for chemical production. There is globally a large abundance of natural gas reserves which are forecast to outlast oil reserves and, whilst fossil fuels are finite and diminishing, the proven reserves of natural gas continue to increase due in part to both more sophisticated exploration techniques and for example the development of fracking technology and the subsequent boom in shale gas production[1]. However, despite this relative abundance of natural gas, there are a number of issues to consider concerning its efficient and effective use. In the first instance whilst, more and more natural gas reserves are being discovered these are increasingly located in 'difficult zones', such as offshore or Arctic/Siberian regions[2,3], far away from consumption sites. Transportation of natural gas from production to consumption sites can occur either via gas pipelines or through pressurisation to liquid natural gas. However, both of these transportation methods are expensive or hazardous. Furthermore, the direct usage of natural gas for heating and power generation purposes suffers due to its low energy density[4]. As a result processes for the indirect usage of methane via synthesis gas (syngas), in which methane is 'upgraded' to more valuable or useful products, have been well studied and are well established industrially. There are also direct methane upgrading technologies; however, they are usually limited by selectivity and activity. Some of the direct and indirect uses of methane are depicted in figure 1.1.

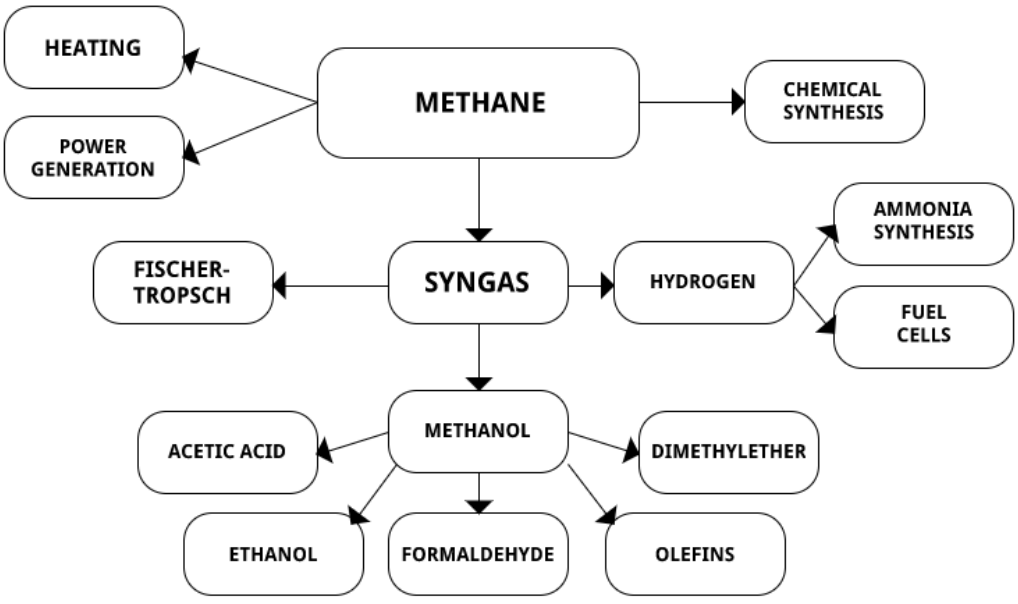

Figure 1.1 Some important direct and indirect uses of methane adapted from works by Holmen[5] and Wender[6].

1.2 Direct Methane Upgrading

The direct conversion of methane to a wide variety of higher value products has been demonstrated[5,7], of which the oxidative coupling of methane to C_2 hydrocarbons and the selective oxidation of methane to methanol and formaldehyde are of particular interest, although this process is not scalable commercially.

1.2.1 Oxidative Coupling of Methane

Oxidative coupling of methane (OCM) involves reacting CH_4 with O_2 over solid catalysts in order to form higher hydrocarbons (1.1) and (1.2), predominantly ethane as a primary product and subsequently ethylene as a secondary product following dehydrogenation. An early work by Keller and Bhasin[8] showed that two methane molecules were coupled oxidatively in a cyclic process over a PbO/Al_2O_3 catalyst producing both ethane and ethylene.

$$2CH_4 + \tfrac{1}{2}O_2 \rightarrow C_2H_6 + H_2O \qquad \Delta H^{\circ}_{298} = -88\ kJmol^{-1} \qquad (1.1)$$

$$2CH_4 + O_2 \rightarrow C_2H_4 + 2H_2O \qquad \Delta H^{\circ}_{298} = -141\ kJmol^{-1} \qquad (1.2)$$

The generally accepted mechanism for OCM involves the heterogeneous generation of methyl radicals on the solid catalyst followed by homogenous gas-phase recombination of the radicals in order to form ethane[9], and whilst C_2 selectivities of up to 80% can be achieved the per pass yield is limited to 25%, with the predicted upper theoretical limit of C_2 yield to be roughly 30% at 1 atm[5]. In addition to the low C_2 yields and CH_4 conversions, OCM also suffers from being a high temperature process (> 1000 K), as well as most OCM catalysts also being active for further C-H bond activation in the C_2 hydrocarbons leading to combustion and the formation of CO_2 and H_2O.

1.2.2 Selective Oxidation of Methane

The direct partial oxidation of methane to methanol (1.3) can occur both catalytically and non-catalytically. The non-catalytic routes, operated at high pressure (30-60 bar) and at temperatures of 723-773 K, can achieve methanol selectivities of up to 80%[10]. However, methane conversion per pass is typically < 10% requiring large recycle ratios; the resulting low yields of methanol also present problems for product separation due to low partial pressures. Furthermore, increasing methane conversion leads to lower methanol selectivity.

$$CH_4 + \tfrac{1}{2}O_2 \rightarrow CH_3OH \qquad \Delta H^{\circ}_{298} = -27\ kJmol^{-1} \qquad (1.3)$$

The catalytic routes mainly focus on metal oxide materials and similar to the non-catalytic routes selectivities of ~ 70% can be achieved (in this instance formaldehyde is produced, not methanol) but with very low methane conversions.

1.3 Indirect Methane Upgrading

The indirect usage of methane occurs via methane oxyforming, producing a mixture of carbon monoxide and hydrogen known as syngas. Whilst the focus of this work is primarily concerned with syngas production from natural gas sources it is worth noting that syngas can also be derived from coal, petroleum, biomass, and organic waste.

1.3.1 Applications of Synthesis Gas

The syngas produced from methane oxyforming can be used for (but is not limited to) Fischer-Tropsch synthesis in order to produce higher hydrocarbons, Methanol synthesis and subsequent fuel or fine-chemical production, and Hydrogen production. The required properties of the syngas mixture, in particular the H_2/CO ratio, depend on the desired synthesis. For example methanol and Fischer-Tropsch syntheses require a H_2/CO ratio of 2, whilst higher ratios are desirable for hydrogen production and subsequent reactions such as ammonia synthesis.

Methanol synthesis (1.4) is carried out over copper-zinc-alumina catalysts at pressures of 50-100 bar and temperatures of 500-550 K[11]. Methanol can be used as a fuel itself, for the production of octane extender fuel additives (methyl t-butyl ether), the synthesis of other fuels (DME), and formaldehyde synthesis. For comparison with direct synthesis methods, methanol synthesis from syngas has a selectivity of greater than 99% and conversion per pass is typically 50%.

$$CO + 2H_2 \rightarrow CH_3OH \qquad \Delta H^{\circ}_{298} = -91\ kJmol^{-1} \qquad (1.4)$$

Fischer-Tropsch synthesis (1.5) converts synthesis gas into higher hydrocarbons, which are predominantly used as liquid fuels[12]. Current commercial F-T synthesis is carried out in two separate regimes; high temperature F-T operates using iron catalysts at temperatures of ~600 K for the production of olefins and gasoline, whilst low temperature F-T occurs at a temperature of ~500 K using cobalt or iron catalysts in order to produce higher molecular weight hydrocarbon waxes or diesel.

$$nCO + (2n+1)H_2 \rightarrow C_nH_{(2n+2)} + nH_2O \qquad \Delta H^{\circ}_{298} = -205\ kJmol^{-1} \qquad (1.5)$$

Ammonia synthesis[13] (1.6) carried out via the Haber-Bosch process uses hydrogen, predominantly produced from syngas, in nitrogen fixation. The synthesis of ammonia from syngas is arguably its most important use as the majority of the ammonia produced is used for the fertilisation of agricultural crops. Industrially the reaction is carried out at pressures of 150-250 bar and temperatures of 673-773 K using iron-based catalysts.

$$N_2 + 3H_2 \rightarrow NH_3 \qquad \Delta H^{\circ}_{298} = -92\ kJmol^{-1} \qquad (1.6)$$

Where hydrogen production is the intended application water can be added to syngas, oxidising carbon monoxide to carbon dioxide and liberating hydrogen. This process is known as the water gas shift reaction (1.7) and control over the equilibrium allows the H_2/CO ratio of syngas to be tuned[14].

$$CO + H_2O \rightarrow CO_2 + H_2 \qquad \Delta H^{\circ}_{298} = -41\ kJmol^{-1} \qquad (1.7)$$

1.3.2 Methane Oxyforming

Methane oxyforming is the collective term for the reforming and partial oxidation reactions by which methane is converted into synthesis gas. The three main methane oxyforming pathways, which produce syngas with differing H_2/CO ratios are as follows; (1.8) methane steam reforming, (1.10) methane dry reforming, and (1.11) methane partial oxidation.

1.3.2.1 Methane Steam Reforming

Methane steam reforming is the principle industrial process used for syngas production. The reaction was first studied in the mid 1920's and has been a commercial industrial process since the mid 1930's[15].

$$CH_4 + H_2O \rightarrow CO + 3H_2 \qquad \Delta H^{\circ}_{298} = +206\ kJmol^{-1} \qquad (1.8)$$

Nickel, iron, cobalt, and platinum-group metals have been shown to catalyse methane steam reforming to thermodynamic equilibrium although most industrial catalysts are nickel-based due to low cost and fast turnover rates. However, nickel catalysts are prone to coking with the carbon deposition causing deactivation. As well as being active for methane steam reforming, nickel will decompose methane to carbon and hydrogen, and it also catalyses the Boudard reaction (1.9) in which carbon monoxide is converted in to carbon and carbon dioxide.

$$2CO \rightarrow CO_2 + C \qquad \Delta H^{\circ}_{298} = +86\ kJmol^{-1} \qquad (1.9)$$

Catalyst coking through CO decomposition can be suppressed by adding steam well in excess of the stoichiometric requirement of the methane steam reforming reaction. Excess steam favours the production of CO_2 over CO via the water-gas shift reaction, thus reducing the amount of carbon formation from the Boudard reaction. In addition to the issues of catalyst deactivation, methane steam reforming suffers from being a highly endothermic reaction requiring high reaction temperatures, typically greater than 1073 K. The addition of excess super-heated steam also creates extra expense and the CO/H_2 ratio is not ideal for the downstream processes of methanol and Fischer-Tropsch synthesis. Furthermore, in practice steam reforming is often coupled with direct oxidation in the process known as auto-thermal reforming, in which a composition of heated steam and methane gases is fed into a reactor and mixed with oxygen allowing partial combustion to occur before the hot reaction gas reaches the catalyst bed. However, this also requires a source of external oxygen and results in an extremely high temperature combustion zone in the reactor.

1.3.2.2 Methane Dry Reforming

Methane dry reforming was first studied in 1928 by Fischer and Tropsch and involves using CO_2 as an oxidant for methane reforming in order to produce a stoichiometric composition of syngas[15]. This process can be beneficial when carried out alongside steam reforming in order to compensate for the high H_2/CO ratio and provide a more desirable syngas composition for downstream Fischer-Tropsch and methanol synthesis. Additionally dry reforming can take advantage of some natural gas reserves that already contain high levels of CO_2. Strikingly similar metals to those that are active for steam reforming (Iron, cobalt, nickel, and the noble metals) are also catalysts for dry reforming[16]. However, dry reforming of methane is an even more endothermic process than steam reforming, requiring larger heat and therefore energy inputs.

$$CH_4 + CO_2 \rightarrow 2CO + 2H_2 \qquad \Delta H^{\circ}_{298} = +247\ kJmol^{-1} \qquad (1.10)$$

This reaction can also be considered to have positive environmental implications, with the notion that dry reforming converts two greenhouse gasses into a valuable feedstock. However, the large heat requirements for this endothermic process are usually coupled with the production of CO_2.

1.3.2.3 Methane Partial Oxidation

Methane partial oxidation offers an attractive route for the production of synthesis gas with a H_2/CO ratio of 2, ideal for downstream methanol or Fischer-Tropsch synthesis. In contrast to both dry and steam reforming, methane partial oxidation is mildly exothermic. The favourable

H_2/CO ratio means that less tuning of the syngas mixture via the water gas shift reaction is required, in particular the removal of valuable hydrogen following steam reforming, whilst the exothermicity could mean that savings can be made with regards to heating when compared to the endothermic reforming reactions.

$$CH_4 + \frac{1}{2}O_2 \rightarrow CO + 2H_2 \qquad \Delta H^{\circ}_{298} = -38\ kJmol^{-1} \qquad (1.11)$$

The non-catalytic homogenous partial oxidation of methane is a well-established process for syngas production. It is used industrially as part of the Shell middle distillate synthesis[17] plant in which syngas is produced with high selectivity at high temperature (>1400 K) and pressures of 50-70 bar. Whilst these reaction conditions are not advantageous over the catalysed reforming reactions, the use of catalysts for the catalytic partial oxidation of methane (CPOM) can greatly reduce the operating temperatures and pressures.

1.4 Catalytic Partial Oxidation of Methane

Initial studies into the catalytic partial oxidation of methane to synthesis gas began in the first half of the 20th century and as with both steam reforming and dry reforming the focus was largely on supported nickel catalysts. However, high selectivities to syngas were only achieved at temperatures in excess of 1123 K, and with the observation of carbon formation and the resulting catalyst deactivation investigation into CPOM was largely ignored until the late 1980's[18]. A resurgence in CPOM studies occurred after Green *et al.* observed high yields of syngas whilst investigating the oxidative coupling of methane on pyrochlores containing noble and rare-earth metals[19,20]. In particular good methane partial oxidation activity was observed when ruthenium reduction occurred in the lanthanum pyrochlore $Ln_2Ru_2O_7$, which resulted in a lanthanum-oxide supported ruthenium metal catalyst. Furthermore almost no carbon deposition was observed on this ruthenium catalyst. The types of catalysts used for CPOM can broadly be separated into two categories; (i) supported nickel, iron, and cobalt catalysts, and (ii) supported noble metal catalysts.

1.4.1 Nickel, Iron, and Cobalt Catalysts

Synthesis gas production with a H_2/CO ratio of 2 was observed at temperatures of 1000-1200 K at a pressure of 1 bar on supported nickel catalysts, although a major drawback is that nickel is also very active for carbon formation. Lunsford *et al.*[21] studied methane partial oxidation on an alumina supported nickel system and found that complete conversion of methane and a selectivity to CO of roughly 95% could be achieved at temperatures above 973 K. However, an excess of oxygen, with regards to the partial oxidation stoichiometry (O_2/CH4 > 0.5), was

required in order to do so. Furthermore, it was discovered that there were three separate regions within the catalyst bed; (i) $NiAl_2O_4$, (ii) NiO/Al_2O_3 which is active for methane combustion to water and carbon dioxide, and (iii) supported nickel metal which catalyses the dry and steam reforming reactions. Extensive research has also been carried out in order to reduce the amount of carbon deposition and to increase the stability of nickel catalysts. Choudhary *et al.*[22,23,24,25] in particular have examined in detail supporting nickel and nickel-oxide on a wide variety of metal oxide support materials. They have also found that addition of cobalt to NiO/Yb_2O_3, NiO/ZrO_2 and NiO/ThO_2 catalysts reduces the rate of carbon formation and decreases the temperature at which methane partial oxidation begins, which is due to the presence of cobalt promoting the reduction of nickel and therefore enhancing the catalytic activity.

1.4.2 Noble Metal Catalysts

Green *et al.*[18,19,26] investigated CPOM over noble metal catalysts and rare-earth ruthenium pyrochlores. They found that high yields of synthesis gas with high methane conversion, total oxygen conversion, and selectivities to CO and H_2 of 97 and 99 % respectively were obtained at a temperature of 1050 K and a pressure of 1 bar. Furthermore the reactions were catalysed to thermodynamic equilibrium with very low levels of carbon deposition.

1.4.3. Reaction Mechanism

Two general mechanisms for CPOM have been proposed; (i) an indirect method in which the total combustion of methane occurs before subsequent reforming reactions, and (ii) a direct partial oxidation mechanism in which surface carbon and oxygen species combine directly to form partial oxidation products. The indirect method is also known as the combustion reforming reaction (CRR), as in the first instance methane is combusted in order to produce carbon dioxide and water, which then go on to be used in dry and steam reforming reactions respectively. In this case syngas is a secondary product of methane oxidation. The CRR mechanism was first alluded to when Vermeiren *et al.*[27] repeated the experiments of Prettre *et al.*[28] and found a non-uniform temperature profile across the catalyst bed. The temperature at the front of the catalyst bed was significantly higher than that in regions further along the bed, as well as the temperature of the furnace itself. These reactor hotspots indicate an exothermic reaction taking place. The total oxidation of methane to water and carbon dioxide (1.12) is an extremely exothermic process and accounts well for the temperature variation observed.

$$CH_4 + 2O_2 \rightarrow CO_2 + 2H_2O \qquad \Delta H^{\circ}_{298} = -806\ kJmol^{-1} \qquad (1.12)$$

A direct partial oxidation mechanism was proposed by Hickman and Schmidt[29,30,31] in order to explain the results of their work examining methane oxidation on rhodium and platinum coated

monolith catalysts. They constructed a model that incorporates the elementary adsorption, desorption and surface reaction steps of methane and oxygen decomposing into surface adatoms before recombining to form syngas as a primary product. The model and their experimental results fitted to within a few percent.

1.5 Yttria-stabilised Zirconia as a CPOM Catalyst

Whilst zirconia materials are more commonly used as supports in catalysis, for metal nano-particle catalysts, yttria-stabilised zirconia (YSZ) has been demonstrated to catalyse methane oxidation in the absence of a metal catalyst. Methane oxidation was investigated over a range of metal-oxides with YSZ being the most active[32,33], and it was found that whilst activity and selectivity is greater for metal catalysts, metal-oxide catalysts offer greater stability. On the back of these findings a substantial set of experiments was carried out by Zhu *et al.* investigating all facets of methane oxidation catalysis on YSZ. Initial work[34] noted that methane oxidation on YSZ began at ~823 K, with full oxygen- and 42% methane conversion occurring at 1223 K. The primary products of methane oxidation on YSZ were found to be; CO, CO_2, H_2, and H_2O. From these findings the authors propose a dual-bed reactor system in which methane and oxygen are reacted over YSZ until oxygen is fully converted in the first bed, with the product effluent and unreacted methane subsequently transferred to a second catalyst bed containing a cobalt metal catalyst in which steam and dry reforming reactions take place. In this case direct partial oxidation of methane occurs on YSZ before the indirect reforming reactions occur in the second catalyst bed. This provides a neat solution to the problems associated with large temperature gradients occurring in the traditional combustion reforming mechanism of syngas production as ideally only the mildly exothermic partial oxidation reaction is occurring; nevertheless and deep oxidation would only occur in the first reactor bed containing the stable metal-oxide catalyst, and the cobalt metal catalyst is prevented from exposure to high-temperature oxygen so metal catalyst deactivation through volatile oxide loss is avoided.

The conversion/yield of reactants and products of CPOM on YSZ, reproduced from reference [34], is given in figure 1.2. Interestingly, as well as the primary CPOM products, trace amounts of C_2 hydrocarbons are detected in the product stream. As well as methane oxidation occurring it appears that methane coupling is also carried out to some extent, particularly at higher temperatures.

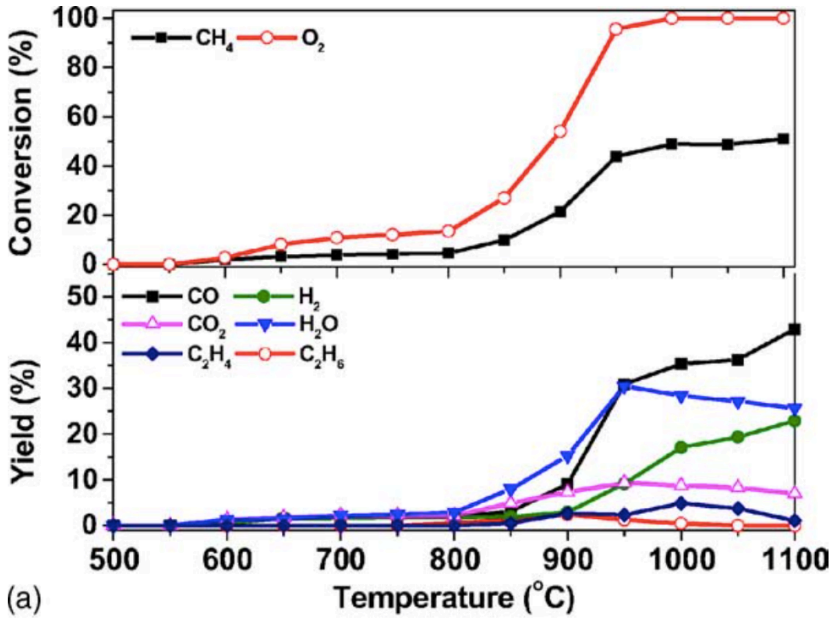

Figure 1.2. Conversion/yield of CPOM over YSZ as a function of reaction temperature. Reproduced from reference [34].

1.5.1 CPOM Reaction Scheme

After these discoveries the authors carried out a series of in depth investigations in order to elucidate the reaction scheme. In the first instance catalytic measurements of methane oxidation were carried out with increasing temperature[35], as with the experiment displayed in figure 1.2 reactant gases were flowed over the catalyst and the temperature varied with the system reaching steady state before measurement. Trace amounts of formaldehyde and formic acid were also detected in the product stream, alongside the previously observed primary products and trace amounts of C_2 hydrocarbons. The detection of formaldehyde and formic acid led to the hypothesis that formaldehyde and surface formate could be reaction intermediates in the oxidation of methane, which was tested with further transient catalytic experiments as well as FTIR and temperature programmed desorption and decomposition experiments.

In situ IR experiments studying methane oxidation were carried out over a range of temperatures from 303-748 K. In each case the catalyst was 'activated *in situ*' at 873 K with 20% O_2 in helium, before cooling to the reaction temperature. Formate bands appear in the IR spectra for reactions at temperatures above 673 K, with no other surface intermediates detected and no primary reaction products in the effluent stream. It is interesting to note that methane can be oxidised to surface formate species, on an activated catalyst sample, at these reaction temperatures whilst further decompositions of the surface formate does not occur. Temperature

programmed desorption and decomposition of the surface formate was then carried out with the major decomposition products detected being; CO, CO_2, H_2, and H_2O, with desorption peaks for all products occurring between 850-878 K.

Despite no formaldehyde being detected in the in situ IR experiments, oxidative conversion of formaldehyde on YSZ was also investigated because of its presence in the product streams of earlier experiments. As with formate decomposition and CPOM experiments the primary products observed are CO, CO_2, H_2, and H_2O. However, methane and methanol signals were also detected at low temperatures (< 623 K), which, however, disappeared rapidly upon increasing the temperature. Furthermore, cofeeding formaldehyde into the methane and oxygen streams in CPOM experiments showed that when oxygen was fully converted at a temperature of 1073 K the yields of CO, CO_2, and H_2 increased with increasing formaldehyde partial pressure and the yield of H_2O and conversion of CH_4 decreased. Whilst at lower reaction temperatures when oxygen was not completely consumed, the conversion of methane remained constant and the yields of all primary products increased with increasing formaldehyde partial pressure. The observation of formaldehyde and formic acid in the CPOM product stream and the subsequent experiments finding the same primary products with extremely similar product distributions confirm both formaldehyde and formate as reaction intermediates. From these studies Zhu *et al.* proposed the reaction scheme presented in figure 1.3 as that of CPOM on YSZ.

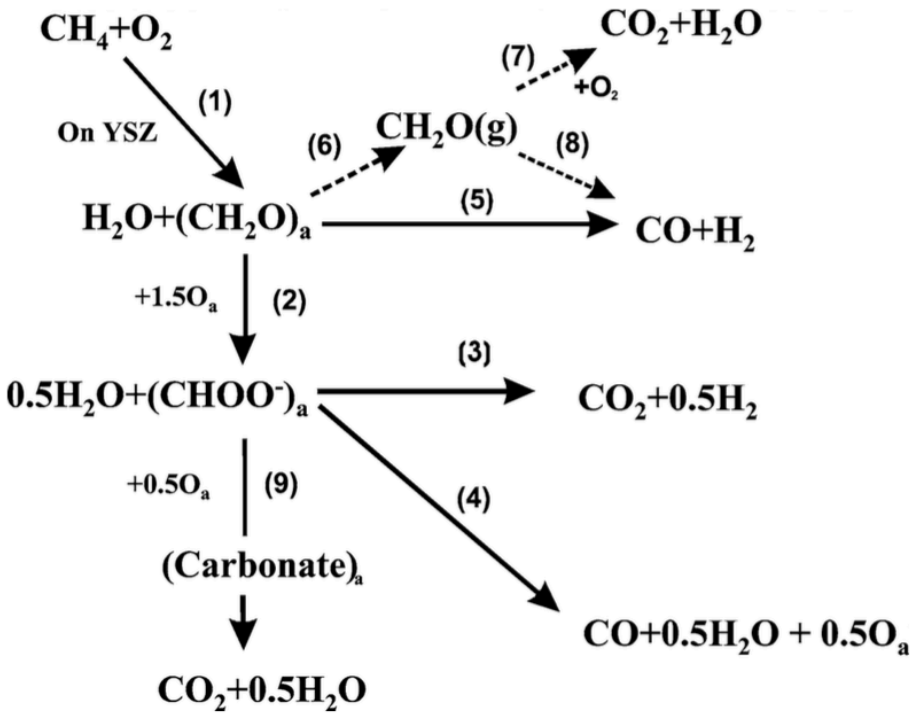

Figure 1.3. Reaction scheme for CPOM on YSZ. Reproduced from reference [35].

1.5.2. Effect of Surface Composition

In the experiments described above only one type of YSZ catalyst was used which contained 12 wt.% yttria in zirconia. As part of their investigations Zhu *et al.* also considered how changing the yttrium content would affect the catalytic behaviour[36]. Four YSZ catalyst concentrations were used; 5, 9, 12, and 14 wt.%. The catalysts also undergo different pre-treatment conditions with samples calcined at 1173, 1273 or 1373 K. Furthermore; the 5, 9, and 14 wt.% samples are from one company and the 12 wt.% sample from another. Transient catalytic tests are run under similar conditions to those that have been described previously, namely that the catalysts are activated with O_2/He at 1073K before cooling to reaction temperature and having CH_4/O_2 flow over the fixed bed catalyst system. In addition to the catalytic measurements, detailed catalyst characterisation was undertaken with chemical composition of the material measured by X-ray fluorescence (XRF) and the surface composition measured by low-energy ion scattering (LEIS).

Catalyst (wt.%)	Calcination Temperature (K)	Surface Area (m^2/g)	Composition (mol %)				Surface Y_2O_3 concentration (mol %)
			ZrO_2	Y_2O_3	TiO_2	HfO_2	
YSZ (5)	1173	14.9	95.63	3.19	0.005	1.17	14
YSZ (9)	1173	13.1	93.74	5.13	0.005	1.13	-
YSZ (14)	1173	13.1	90.46	8.46	0.005	1.08	11
YSZ (14)	1273	10.2	-	-	-	-	14
YSZ (14)	1373	7.0	-	-	-	-	12
YSZ (12)	1173	22.0	90.98	7.82	0.279	0.92	19
YSZ (12)	1273	13.0	-	-	-	-	-
YSZ (12)	1373	4.5	-	-	-	-	29

Table 1.1. Compositions, surface areas, and calcination temperatures of YSZ catalysts.

The composition and surface areas of the catalysts are given in table 1.1 and discussed below. Hafnia and titania were the major contaminants detected in the catalysts sourced from both companies, although significantly more titania was found in the 12 wt.% samples when compared to the other catalysts. However, it appears that these contaminants are confined to the bulk of the materials as neither hafnia nor titania could be detected on the surface of any of the catalysts with LEIS. The surface concentration of yttria in the 5, 9, and 14 wt.% samples appears independent of the bulk concentration with a surface yttria concentration of 12±2 mol%. Additionally for the 14 wt.% sample different surface areas are reported for different calcination temperatures; these are 13.1, 10.2, and 7.0 m^2/g for 1173, 1273, and 1373 K respectively. The

surface yttria concentration remains unaffected by calcination temperature. However, in the 12 wt.% sample the surface yttria concentration ranges from 19 to 29 mol%, and the surface areas are 22.0, 13.0, and 4.5 m^2/g for calcination at 1173, 1273, and 1373 K respectively. Furthermore LEIS measurement and sputtering with high and low $^4He^+$ ion intensity showed that more than half of the outermost surface of the 12 wt.% samples were covered by impurities, whereas hardly any impurities were detected on the 5, 9, and 14 wt.% samples.

In catalytic tests, the YSZ samples from both companies, as well as a pure zirconia sample, were measured for CPOM activity. All samples were active for CPOM with oxygen and methane conversion occurring, and the primary CPOM products; CO, CO_2, H_2, and H_2O detected. The methane and oxygen conversions for each sample at 873 K are presented in table 1.2. The conversions observed on the 5, 9, and 14 wt.% samples are identical, which could be related to the seemingly independent surface yttria concentration. Furthermore, they are much more active than pure zirconia, which is in turn much more active than the 12 wt.% YSZ sample containing a large degree of surface contamination. This observation suggests that doping zirconia with yttria increases its CPOM activity, and that surface contamination severely decreases the activity of YSZ. However, the authors note that the decrease in activity in the 12 wt.% sample could also be due to the high surface yttria concentration as oxygen vacancy clustering could occur, which is known to decrease the mobility of vacancies in the bulk.

Catalyst (wt.% yttria)	**Conversion* (%)**	
	O_2	**CH_4**
ZrO_2	28	11
YSZ (5)	58	21
YSZ (9)	58	21
YSZ (14)	58	21
YSZ (12)	13	5

Table 1.2. Catalytic performance of ZrO_2 and YSZ catalysts. *The conversion is an estimate from Fig. 6 in reference [36].

1.5.3 The Role of Oxygen

Transient methane pulse experiments and isotopic oxygen exchange reactions were carried out in order to investigate the role of oxygen in CPOM and the interaction of gas-phase oxygen with the catalyst surface. These results found that CPOM on YSZ and ZrO_2 occurs via a Mars-van Krevelen type mechanism, in which methane is selectively oxidised by lattice oxygen[37]. In the first instance isotopic oxygen exchange on YSZ and ZrO_2 was carried out in the absence of

methane. The catalyst samples were 'pre-oxidised' in flowing oxygen/helium at 1073 K for one hour and cooled or heated to the required reaction temperature (303 ≤ T ≤ 1173 K) before isotopically labeled $^{18}O_2$ was pulsed onto the materials. Similar oxygen exchange behavior was observed on both materials with the oxygen exchange reaction occurring more slowly on ZrO_2 at temperatures below 973 K. The onset of oxygen exchange began at 573 K, with both $^{16}O_2$ and $^{16}O^{18}O$ detected, until the amount of $^{16}O^{18}O$ liberated peaked at ~873 K, before levels of $^{16}O_2$ rose at the expense of $^{16}O^{18}O$. The initial $^{18}O_2$ was completely converted to $^{16}O_2$ at temperatures above 1073 K. The isotopic product distribution for oxygen exchange as a function of temperature over YSZ is given in figure 1.4.

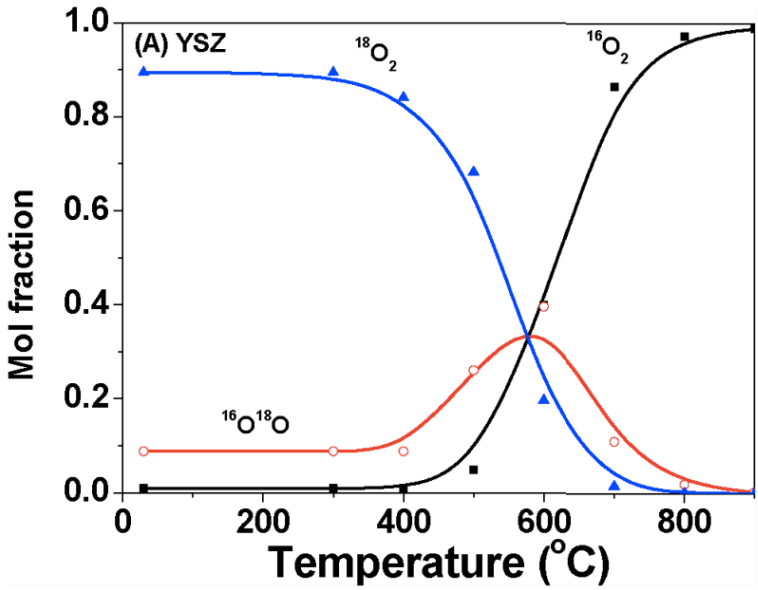

Figure 1.4. Isotopic oxygen exchange on YSZ. Reproduced from reference [37].

Isotopic oxygen exchange was then carried out in the presence of methane. As with the first experiment the catalysts are 'pre-oxidised' and these reactions were carried out at 873 K, except in this case methane and isotopically labelled $^{18}O_2$ are pulsed over the catalysts simultaneously. All the primary CPOM products were detected on both ZrO_2 and YSZ. In the case of YSZ only products containing $^{16}O_2$ were detected, showing that CPOM on YSZ at 873 K occurs via a Mars-van Krevelen type mechanism as methane is exclusively oxidised by lattice oxygen. Furthermore the rate of oxygen conversion was enhanced by the presence of methane, suggesting that methane and oxygen do not compete for the same adsorption sites in accordance with a redox type mechanism. The situation on pure ZrO_2 is slightly different in that a detectable amount of $C^{16}O^{18}O$ was observed, although ^{16}O-containing products were still dominant.

Methane activation was studied by preforming methane pulse experiments over both ZrO_2 and YSZ in the absence of oxygen at 1173 K. When the samples were again subject to the 'pre-oxidation' treatment (in oxygen/helium at 1073 K for one hour, before heating to the reaction temperature) and methane pulsed over the catalysts; all primary CPOM products were produced. However, when the samples were 'pre-reduced' H_2 was formed from the decomposition of CH_4 but no oxygen containing products were produced. In repeated methane pulsing experiments over the 'pre-oxidised' YSZ, a total of 22 methane pulses were carried out, by the end of which lattice oxygen had been 'exhausted' and only H_2 was produced, with accompanying carbon deposition on the catalyst, from the decomposition of methane. It was estimated that 5.5±0.5 x 10^{17} oxygen atoms per meter squared (O/m_2) were extracted by methane from pre-oxidised YSZ. Oxygen was then pulsed over the oxygen-exhausted YSZ and first CO, then CO_2 were liberated from the surface with subsequent oxygen pulses until only molecular O_2 was detected. In this case 6.1±0.5 x 10^{17} O/m_2 were 'stored' or replenished into the YSZ catalyst. The authors continue by discussing the role of lattice oxygen in CPOM over YSZ and ZrO_2 and hypothesise over the relative rates of reaction (YSZ is more active for CPOM than ZrO_2). They argue that surface lattice oxygen is extracted during CPOM, and that in ZrO_2 re-oxidation of the vacant sites occurs by direct activation of molecular oxygen at the site from which oxygen has been removed. However, the extrinsic oxygen vacancies present in YSZ as a result of yttrium doping both facilitate surface oxygen exchange and allow for rapid oxygen diffusion with the lattice, so that oxygen replenishment does not have to occur solely at oxygen consumption sites. This idea is depicted in figure 1.5.

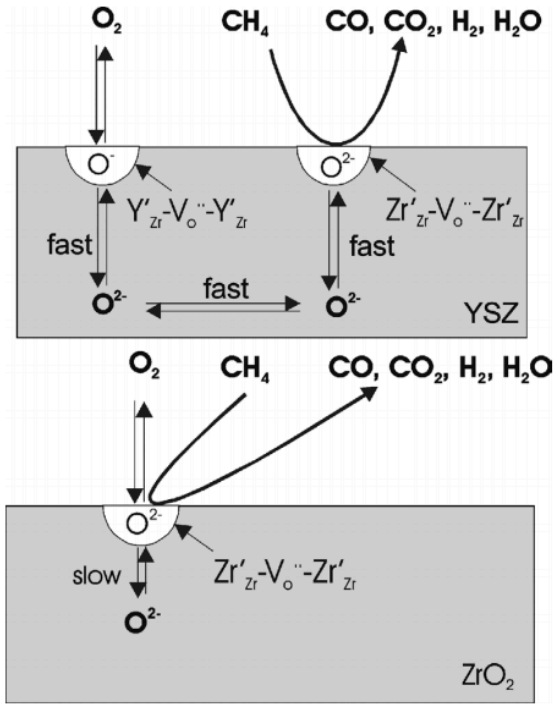

Figure 1.5. Cartoon of CPOM on YSZ and ZrO_2. Reproduced from reference [37].

1.5.4 Effect of Surface Structure

The effect of the structure and morphology of ZrO_2 and YSZ on CPOM was then investigated by studying the activation of O_2 and N_2O as probe oxidants[38]. It was found that N_2O dissociation on YSZ and ZrO_2 gave rise to two different types of oxygen species, identified by two separate peaks in the temperature programmed desorption (TPD) spectra. The first oxygen species 'α-O' is found in higher quantities on ZrO_2 than on YSZ, and the amount of 'α-O' is also found to decrease with increasing calcination temperature on YSZ; it occurs only as a result of N_2O decomposition. The authors assign this 'α-O' as associated with zirconium cations at structural defects, such as steps, kinks, and corners, which are less abundant in YSZ and also become increasingly sparse with increasing crystallite regularity as a result of higher calcination temperatures. The higher calcination temperatures also resulted in the formation of more low-index planes. The second species, 'β-O', can be formed from both N_2O and O_2 activation, although it is worth noting that molecular oxygen activation results only in the formation of 'β-O'. This 'β-O' species is attributed to surface vacancies formed by partial reduction, or removal of surface lattice oxygen ions. It was found that the more active CPOM catalysts could desorb more 'β-O' and desorb it more easily. The authors then speculate that YSZ surface reducibility increases with increasing zirconium cation coordination number, as surface lattice oxygen would be more easily removed when the original coordination number is high. This hypothesis is in line with catalysts calcined at higher temperature being more active as the exposure of lower index planes and increased crystallite regularity would give rise to more higher coordinate Zr-cations on the surface.

1.5.5 Effect of Surface Water and Hydroxyl Groups

The effect of surface water and hydroxyl groups on CPOM over YSZ was investigated, in particular the question of how water affects the oxidation of formaldehyde to formate was paid close attention[39]. First, water was co-fed with oxygen and methane in the reactant stream for CPOM over YSZ, carried out at 873 K. The yields of primary CPOM products were measured as a function of the partial pressure of water and the results showed that the selectivity to both CO and H_2 increased with increasing water partial pressure, at the expense of H_2O and CO_2. The increase in both CO and H_2 selectivity excludes the possibility that this change is brought about by the water-gas shift reaction $(CO + H_2O \leftrightharpoons CO_2 + H_2)$. Furthermore the conversion of methane is unaffected by the addition of water, excluding the possibility of steam reforming of methane contributing to this increase, which would not be expected to occur at this low a temperature. Secondly, FT-IR spectra of formaldehyde adsorption was carried out on both hydrated and dehydrated YSZ samples pre-activated at 773 K. These spectra are displayed in figure 1.6. Formate is observed as a major surface species on both the dehydrated and hydrated samples, and signals assigned to methoxy and dioxymethylene species are also

observed on both samples to varying degrees. However, notably peaks in the IR spectra corresponding to coordinated formaldehyde species are only present for the hydrated sample. The intensities of the formate band in the IR spectra are shown in figure 1.7, and show that dehydrated YSZ is more active for the conversion of formaldehyde to formate than hydrated YSZ. In accordance with the reaction scheme proposed earlier (figure 1.3) it would appear that water prevents the oxidation of formaldehyde to formate, stabilising formaldehyde on the surface, and thus promotes the decomposition of formaldehyde to CO and H_2.

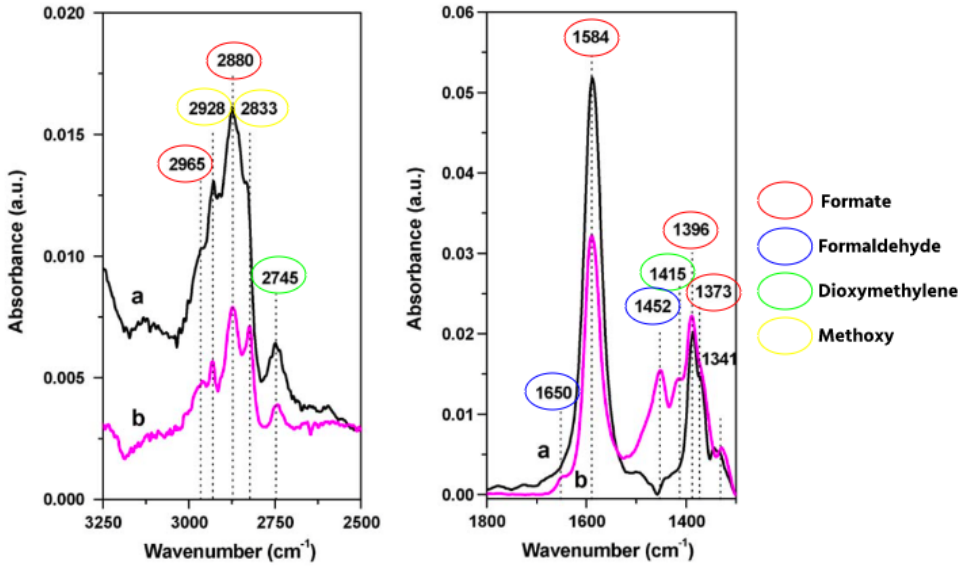

Figure 1.6. FT-IR spectra of formaldehyde adsorbed on (a) dehydrated (black) and (b) hydrated (pink) YSZ samples. Reproduced from reference [39].

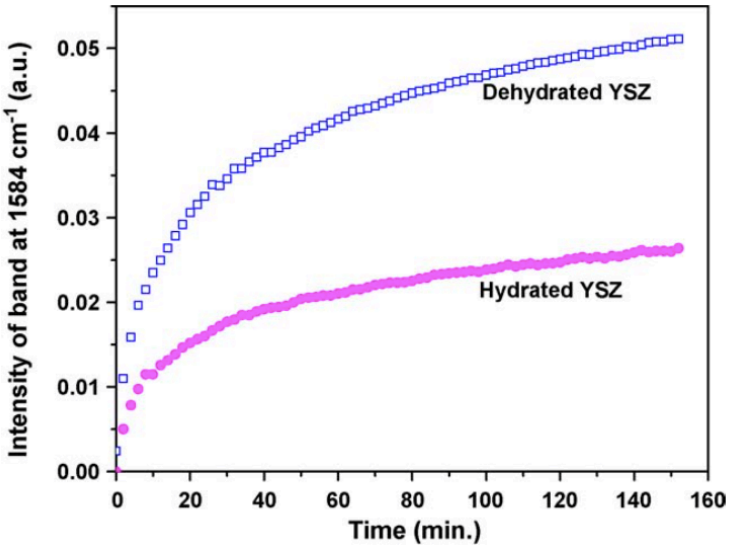

Figure 1.7. Intensity of formate band with adsorption time. Reproduced from reference [39].

1.6 Summary

Catalytic partial oxidation of methane to synthesis gas is an important industrial reaction for methane upgrading, which has been demonstrated to take place on yttria-stabilised zirconia. The primary products for CPOM on YSZ are CO, CO_2, H_2, and H_2O, and the reaction mechanism is thought to proceed via both formaldehyde and formate intermediates. Furthermore, isotopic experiments show that the products contain only lattice oxygen, the reaction therefore occurs via a Mars-van Krevelen type mechanism. Pre-oxidation of YSZ gives rise to active surfaces on which CPOM can occur, and oxygen exchange occurs with lattice oxygen at high temperature; although the role of oxygen within CPOM on YSZ is unclear. Additionally the presence of water increases selectivity to syngas. Whilst there is good evidence for the reaction scheme for CPOM on YSZ, details of the reaction pathway are unknown. This thesis aims to use computer simulations in order to identify some of these details, and in particular establish the role of oxygen in catalytic reactions on YSZ.

References:

1. BP, BP Statistical Review of World Energy. 2016.
2. Leprince, P.; Valais, M., More natural-gas - A multidisciplinary challenge. *Energy Sources* **1993,** *15* (1), 95-104.
3. Lunsford, J. H., Catalytic conversion of methane to more useful chemicals and fuels: a challenge for the 21st century. *Catalysis Today* **2000,** *63* (2-4), 165-174.
4. Hutchings, G. J.; Joyner, R. W., Prospects for the partial oxidation of natural-gas. *Chemistry & Industry* **1991,** (16), 575-578.
5. Holmen, A., Direct conversion of methane to fuels and chemicals. *Catalysis Today* **2009,** *142* (1-2), 2-8.
6. Wender, I., Reactions of synthesis gas. *Fuel Processing Technology* **1996,** *48* (3), 189-297.
7. Alvarez-Galvan, M. C.; Mota, N.; Ojeda, M.; Rojas, S.; Navarro, R. M.; Fierro, J. L. G., Direct methane conversion routes to chemicals and fuels. *Catalysis Today* **2011,** *171* (1), 15-23.
8. Keller, G. E.; Bhasin, M. M., Synthesis of ethylene via oxidative coupling of methane. 1. Determination of active catalysts. *Journal of Catalysis* **1982,** *73* (1), 9-19.
9. Campbell, K. D.; Lunsford, J. H., Contribution of gas-phase radical coupling in the catalytic-oxidation of methane. *Journal of Physical Chemistry* **1988,** *92* (20), 5792-5796.
10. Tabata, K.; Teng, Y.; Takemoto, T.; Suzuki, E.; Banares, M. A.; Pena, M. A.; Fierro, J. L. G., Activation of methane by oxygen and nitrogen oxides. *Catalysis Reviews-Science and Engineering* **2002,** *44* (1), 1-58.
11. Chinchen, G. C.; Denny, P. J.; Jennings, J. R.; Spencer, M. S.; Waugh, K. C., Synthesis of methanol. 1. Catalysts and kinetics. *Applied Catalysis* **1988,** *36* (1-2), 1-65.
12. Christensen, T. S.; Primdahl, II, Improve syngas production using autothermal reforming. *Hydrocarbon Processing* **1994,** *73* (3), 39-&.
13. Erisman, J. W.; Sutton, M. A.; Galloway, J.; Klimont, Z.; Winiwarter, W., How a century of ammonia synthesis changed the world. *Nature Geoscience* **2008,** *1* (10), 636-639.
14. Ratnasamy, C.; Wagner, J. P., Water Gas Shift Catalysis. *Catalysis Reviews-Science and Engineering* **2009,** *51* (3), 325-440.
15. York, A. P. E.; Xiao, T. C.; Green, M. L. H.; Claridge, J. B., Methane oxyforming for synthesis gas production. *Catalysis Reviews-Science and Engineering* **2007,** *49* (4), 511-560.
16. Lavoie, J. M., Review on dry reforming of methane, a potentially more environmentally-friendly approach to the increasing natural gas exploitation. *Frontiers in Chemistry* **2014,** *2*.
17. Eilers, J.; Posthuma, S. A.; Sie, S. T., The shell middle distillate synthesis process (SMDS). *Catalysis Letters* **1991,** *7* (1-4), 253-269.
18. York, A. P. E.; Xiao, T. C.; Green, M. L. H., Brief overview of the partial oxidation of methane to synthesis gas. *Topics in Catalysis* **2003,** *22* (3-4), 345-358.
19. Ashcroft, A. T.; Cheetham, A. K.; Foord, J. S.; Green, M. L. H.; Grey, C. P.; Murrell, A. J.; Vernon, P. D. F., Selective oxidation of methane to synthesis gas - using transition-metal catalysts. *Nature* **1990,** *344* (6264), 319-321.
20. Vernon, P. D. F.; Green, M. L. H.; Cheetham, A. K.; Ashcroft, A. T., Partial oxidation of methane to synthesis gas. *Catalysis Letters* **1990,** *6* (2), 181-186.
21. Dissanayake, D.; Rosynek, M. P.; Kharas, K. C. C.; Lunsford, J. H., Partial oxidation of methane to carbon-monoxide and hydrogen over a Ni/Al2O3 catalyst. *Journal of Catalysis* **1991,** *132* (1), 117-127.
22. Choudhary, V. R.; Rajput, A. M.; Rane, V. H., Low-temperature catalytic selective partial oxidation of methane to CO and H-2 over Ni/Yb2O3. *Journal of Physical Chemistry* **1992,** *96* (22), 8686-8688.
23. Choudhary, V. R.; Rajput, A. M.; Rane, V. H., Low-temperature oxidative conversion of methane to synthesis gas over Co rare-earth-oxide catalysts. *Catalysis Letters* **1992,** *16* (3), 269-272.
24. Choudhary, V. R.; Rane, V. H.; Rajput, A. M., Selective oxidation of methane to CO and H2 over unreduced NiO-rare earth oxide catalysts. *Catalysis Letters* **1993,** *22* (4), 289-297.
25. Choudhary, V. R.; Rajput, A. M.; Prabhakar, B., Nonequilibrium oxidative conversion of methane to CO and H-2 with high selectivity and productivity over Ni/Al2O3 at low-temperatures. *Journal of Catalysis* **1993,** *139* (1), 326-328.

26. Ashcroft, A. T.; Cheetham, A. K.; Green, M. L. H.; Grey, C. P.; Vernon, P. D. F., Oxidative coupling of methane over tin-containing rare-earth pyrochlores. *Journal of the Chemical Society-Chemical Communications* **1989,** (21), 1667-1669.
27. Vermeiren, W. J. M.; Blomsma, E.; Jacobs, P. A., Catalytic and thermodynamic approach of the oxyreforming reaction of methane. *Catalysis Today* **1992,** *13* (2-3), 427-436.
28. Prettre, M.; Eichner, C.; Perrin, M., The catalytic oxidation of methane to carbon monoxide and hydrogen. *Transactions of the Faraday Society* **1946,** *42* (3-4), 335-340.
29. Hickman, D. A.; Schmidt, L. D., Synthesis gas-formation by direct oxidation of methane over Pt monoliths. *Journal of Catalysis* **1992,** *138* (1), 267-282.
30. Hickman, D. A.; Schmidt, L. D., Production of syngas by direct catalytic-oxidation of methane. *Science* **1993,** *259* (5093), 343-346.
31. Hickman, D. A.; Haupfear, E. A.; Schmidt, L. D., Synthesis gas-formation by direct oxidation of methane over Rh monoliths. *Catalysis Letters* **1993,** *17* (3-4), 223-237.
32. Steghuis, A. G.; vanOmmen, J. G.; Seshan, K.; Lercher, J. A., New highly active catalysts in direct partial oxidation of methane to synthesis gas. *Natural Gas Conversion Iv* **1997,** *107*, 403-408.
33. Steghuis, A. G.; van Ommen, J. G.; Lercher, J. A., On the reaction mechanism for methane partial oxidation over yttria/zirconia. *Catalysis Today* **1998,** *46* (2-3), 91-97.
34. Zhu, J.; Rahuman, M.; van Ommen, J. G.; Lefferts, L., Dual catalyst bed concept for catalytic partial oxidation of methane to synthesis gas. *Applied Catalysis a-General* **2004,** *259* (1), 95-100.
35. Zhu, J. J.; van Ommen, J. G.; Lefferts, L., Reaction scheme of partial oxidation of methane to synthesis gas over yttrium-stabilized zirconia. *Journal of Catalysis* **2004,** *225* (2), 388-397.
36. Zhu, J. J.; van Ommen, J. G.; Knoester, A.; Lefferts, L., Effect of surface composition of yttrium-stabilized zirconia on partial oxidation of methane to synthesis gas. *Journal of Catalysis* **2005,** *230* (2), 291-300.
37. Zhu, J. J.; van Ommen, J. G.; Bouwmeester, H. J. M.; Lefferts, L., Activation of O-2 and CH4 on yttrium-stabilized zircoma for the partial oxidation of methane to synthesis gas. *Journal of Catalysis* **2005,** *233* (2), 434-441.
38. Zhu, J. J.; Albertsma, S.; van Ommen, J. G.; Lefferts, L., Role of surface defects in activation of O-2 and N2O on ZrO2 and yttrium-stabilized ZrO2. *Journal of Physical Chemistry B* **2005,** *109* (19), 9550-9555.
39. Zhu, J.; van Ommen, J. G.; Lefferts, L., Effect of surface OH groups on catalytic performance of yittrium-stabilized ZrO2 in partial oxidation of CH4 to syngas. *Catalysis Today* **2006,** *117* (1-3), 163-167.

Chapter 2

Yttria Stabilised Zirconia

Chapter 2 gives an introduction and overview into zirconia-based materials. The temperature dependence of the phases of pure zirconia is presented before discussing doped materials. Yttria stabilised zirconia is given particular attention and the experimental and theoretical literature investigating the microscopic defect structure of both the bulk and surfaces of the material is considered in depth. The defect chemistry of this material influences its behaviour and properties, and unresolved questions surrounding the local atomic structure present a significant challenge when modelling this system.

2.1 Introduction

Zirconia-based materials are an important class of technologically relevant metal-oxides, and as such have received significant interest in a variety of research fields. Pure zirconia is most commonly used as a support material for metal nanoparticle catalysts whilst also, as noted in the previous chapter, being able to catalyse directly certain reactions, although with significantly less activity than metal catalysts. Yttria-doping results in a more stable support material, a zirconia-yttria solid solution, alleviating some of the problems associated with the temperature-dependent phase transitions of zirconia, whilst also enhancing the catalytic activity of the material. Furthermore, the introduction of charge compensating oxygen vacancies upon yttria-doping results in yttria-stabilised zirconia (YSZ) becoming a fast oxygen anion conductor, leading to its use as an electrolyte in solid oxide fuel cells as well as in gas sensor applications.

2.2 Zirconia Structure and Phase Transitions

Pure zirconia (ZrO_2) has three zero-pressure temperature dependent polymorphs. At lower temperatures ZrO_2 adopts a monoclinic baddelyite structure ($P2_1/C$), which is stable upon heating to a temperature of roughly 1400K[1] at which point the monoclinic to tetragonal phase transition occurs. The tetragonal phase ($P4_2/nmc$) is observed between approximately 1400-2600K[2], at temperatures above which ZrO_2 will assume the cubic fluorite structure ($Fm3m$)[3]. These three ambient pressure polymorphs are shown in figure 2.1, reproduced from early work carried out by Catlow *et al.*[4]

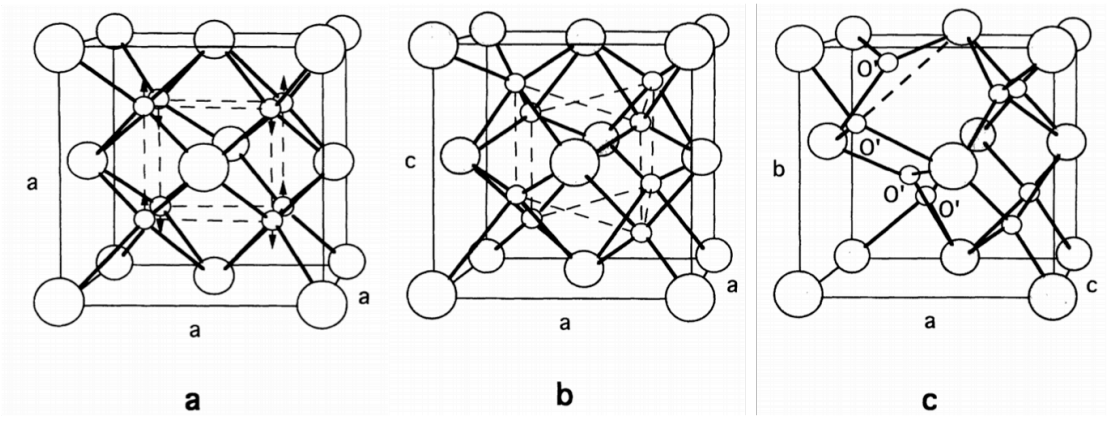

Figure 2.1. Schematic representations of the three ZrO_2 polymorphs; (a) cubic, (b) tetragonal and (c) monoclinic, reproduced from reference [4]. Large spheres represent Zr^{4+} cations and small spheres represent O^{2-} anions, a, b and c represent the crystalline axes.

The cubic form of pure zirconia (c-ZrO_2) is shown in fig 2.1. (a). The Zr^{4+} cations occupy a face-centred cubic (fcc) lattice arrangement and are eightfold coordinated by O^{2-} anions, which occupy the tetrahedral hole sites. Each oxygen ion is fourfold coordinated by surrounding

zirconia ions. The oxygen ions form a primitive cubic sub-lattice as shown by the dashed lines between them. The tetragonal polymorph (t-ZrO_2), fig 2.1. (b), can be considered as a distorted form of the cubic structure, in which the anion sub-lattice is displaced along the <001> crystallographic direction (c-axis). The origin of the cubic-tetragonal phase transition is in the displacement of oxygen ions in c-ZrO_2 owing to an X_2^- phonon vibration[5] as represented by the arrows in fig 2.1. (a). The anions and cations in the tetragonal phase are four- and eightfold coordinated respectively, as they are in c-ZrO_2, but with two different Zr-O distances. In contrast with the t-ZrO_2 and c-ZrO_2 phases, the low-temperature monoclinic phase (m-ZrO_2), depicted in fig 2.1. (c), has distorted sevenfold coordinated zirconia cations and oxygen ions are both three- and fourfold coordinated. The threefold coordinated oxygen ions are denoted by $O^{'}$ in fig 2.1. (c). The monoclinic-tetragonal transition is a first order displacive martensitic phase transition, in which the crystal undergoes shearing due to the substantial difference of the crystal structures of the two phases[6].

A simplistic view of the cation coordination observed in the three zirconia polymorphs can be obtained by considering Pauling's model[7], which treats crystal anions and cations as tightly packed hard spheres. This approach views cations as having a coordinated polyhedron of surrounding anions and determines the cation coordination number by the radius ratio, R^+/R^-, of the cation and anion. The minimum radius ratio for eightfold cation coordination as seen in the fluorite structure is 0.732, and that of the sixfold coordination environment in rutile structures is 0.414[7]. Zirconia has a radius ratio (Zr^{4+}/O^{2-}) of 0.62, which suggests that the zirconium cation is too small to adopt the eightfold coordinated fluorite structure and too large to be that of a sixfold coordinated rutile structure[8], as demonstrated by the room-temperature instability of the cubic phase of zirconia and relaxation to the sevenfold coordinated monoclinic polymorph. Whilst this simple model gives some insight into the observed phases of zirconia it does not provide a comprehensive understanding of the cationic coordination seen, due in part to the partial covalent nature of the Zr-O bond[9].

2.3 Phase Stabilisation of Zirconia

The temperature dependence of the structure of pure ZrO_2, as displayed by the three temperature dependent polymorphs, is undesirable for the high temperature industrial applications of zirconia-based materials such as supports for heterogeneous catalysis and as electrolytes in SOFCs. The volume expansion caused by the phase transitions, in particular the martensitic shear that accompanies the monoclinic-tetragonal transition, induces large stresses that cause pure zirconia to crack when cooled. In order to overcome this problem and produce a ceramic material with high mechanical and thermal stability, phase stabilisation of zirconia can be achieved by doping with a wide range of cations from other metal oxide materials. The cubic

form of zirconia can be stabilised down to room temperature by both aliovalent and isovalent cation doping of the pure ZrO_2 system.

2.3.1 Divalent Cation Doping

Divalent alkaline earth cations; Mg^{2+} and Ca^{2+}, have been used as dopants for the phase stabilisation of zirconia[10]. The dopant metal cations occupy Zr^{4+} lattice sites and charge compensating oxygen vacancies are created. This doping process is expressed below in Kröger-Vink notation, with M representing the divalent metal cation:

$$MO + Zr_{Zr} + O_O \rightarrow M''_{Zr} + V_O^{\cdot\cdot} + ZrO_2 \quad (2.1)$$

The substitution of the divalent cation on the Zr^{4+} site gives an effective charge of 2-, whilst the removal of an O^{2-} anion leaves a vacancy with an effective charge of 2+, so the overall defect cluster of one substituted cation and one oxygen vacancy is charge neutral. The creation of an oxygen vacancy serves to reduce the average coordination number of the zirconia cations whilst also allowing the oxygen anion sub-lattice to relax, which inhibits certain phonon modes that drive phase transition. Reducing the average coordination number of the zirconia cations helps stabilise the material due to the tendency of Zr^{4+} cations to adopt lower coordination numbers, as predicted from cation size considerations and witnessed in the low-temperature m-ZrO_2, than the eightfold coordination of the pure c-ZrO_2. However, the M^{2+}/Zr^{4+} dopant charge mismatch induces structural instability at high temperatures that leads to phase segregation[11].

2.3.2 Trivalent Cation Doping

The cubic fluorite phase of zirconia can also be stabilised through doping with trivalent cations. Substitution of Zr^{4+} cations with trivalent metal cations stabilises c-ZrO_2 in much the same way as doping with divalent cations, by both serving to reduce the average coordination number of zirconia cations and by the introduction of oxygen vacancies; which allow the oxygen anion sub-lattice to relax. The trivalent defect cluster requires the substitution of two M^{3+} cations onto Zr^{4+} lattice sites for each oxygen vacancy created; the overall doping is expressed in Kröger-Vink notation as follows:

$$M_2O_3 + 2\,Zr_{Zr} + O_O \rightarrow 2\,M'_{Zr} + V_O^{\cdot\cdot} + 2\,ZrO_2 \quad (2.2)$$

Trivalent cations from rare-earth sesquioxides have been shown to stabilise c-ZrO_2 to varying degrees depending on the solubility of the oxide in ZrO_2, which is governed by the size match of cationic radii and the similarity of the cation and anion sub-lattices of the sesquioxides to those of ZrO_2[12]. The rare-earth cubic C-type sesquioxides, R_2O_3 where R = Tb-Lu, Y and Sc[13], have the highest solubility in c-ZrO_2 due to the structural similarities of the oxide lattices. The C-type sesquioxides, structure displayed in figure 2.2[12], can be viewed as the cubic fluorite phase where ¼ of the oxygen anions have been removed, with the remaining anions undergoing a small displacement away from the ideal fluorite lattice sites.

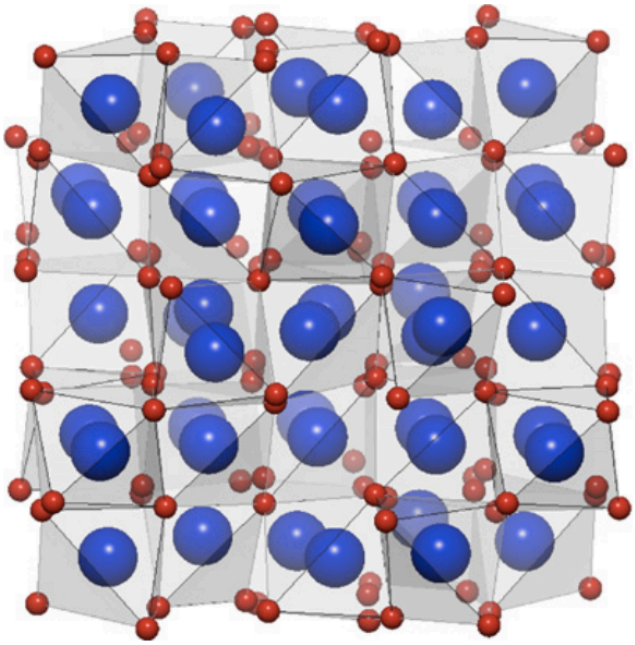

Figure 2.2. Polyhedral representation of the cubic C-type R_2O_3 structure reproduced from reference [12]. Large blue spheres represent cation sites with small red spheres depicting anion sites.

Due to economic considerations only yttria is widely used to stabilise c-ZrO_2 for high temperature industrial applications. However, Yb- and Sc-doped zirconia both show higher conductivity than yttria stabilised zirconia[14], and Scandia stabilised zirconia in particular has received considerable interest as a potential electrolyte for SOFCs[15,16,17].

2.3.3 Tetravalent Cation Doping

Isovalent doping with tetravalent cations that have a larger ionic radius than Zr^{4+} can also be used to stabilise the cubic phase of zirconia, due to the lattice expansion that occurs upon doping with the larger cation, which in practice is most commonly achieved by doping with ceria. Ce^{4+} has an ionic radius of 0.097nm, compared to 0.079nm of the Zr^{4+} cation[18]. However,

cerium will readily reduce from Ce^{4+} to Ce^{3+}, which can have two effects on the stabilisation process: firstly Ce^{3+} has yet a larger ionic radius of 0.114nm, and secondly the reduction to trivalent cerium will result in the formation of charge compensating oxygen vacancies[19]. It has been shown that cerium is required at a concentration of ~70% to stabilise fully the cubic phase of zirconia at high temperature[20], effectively resulting in zirconium doped ceria.

2.4 Yttria Stabilised Zirconia

As noted, yttria doping is the most common method used for the stabilisation of cubic zirconia and as a form of trivalent cation doping, substitution of the Zr^{4+} cations with Y^{3+} along with the formation of an oxygen vacancy will occur during stabilisation. Various different phases are generated from the yttria-zirconia solid-solution, depending on the system composition, as shown in figure 2.3[21].

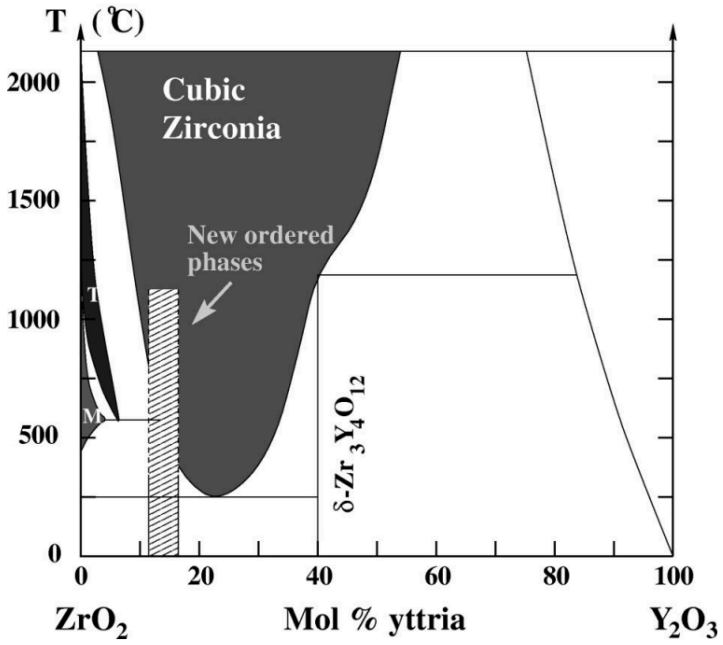

Figure 2.3. Yttria-zirconia solid solution phase diagram, reproduced from reference [21].

The cubic phase can be stabilised by yttria down to room temperature, although the oxygen anions are displaced away from the ideal lattice sites so the phase is often best described as a metastable tetragonal phase without tetragonal distortion of the lattice parameters, i.e. c/a = 1. Full stabilisation of this cubic-like phase occurs at ~10 mol% yttria (Y_2O_3) doping. Above 40 mol% yttria doping the system crystallises as $Y_4Zr_3O_{12}$, a rhomboherdral δ-phase. The introduction of oxygen vacancies allows oxygen ions to migrate rapidly within the material, which is an important feature for its use in SOFCs. This ionic conductivity has been shown to be at a maximum in 8-10 mol% (Y_2O_3) YSZ[22]. Whilst the macroscopic properties of YSZ are relatively easy to obtain, understanding the microscopic defect structure is more challenging

and has received considerable interest. Determining the defect structures present in YSZ is of great interest for understanding the properties displayed in the material, in particular the ionic conductivity, the stability experienced upon doping, and the active sites used for catalysis.

2.4.1 Experimental Defect Structure

There have been a whole host of different experimental techniques used in studies to identify the defect structure present in YSZ. Whilst they are not all in complete agreement, direct comparison between studies is made difficult due to the different compositions of YSZ used and the different treatments of the materials in their preparations.

An early study from Steele *et al.*[23] studied 18, 22 and 26% YSZ (mol % $YO_{1.5}$) using Bragg neutron diffraction and diffuse scattering of long wavelength neutrons. They determined the lattice parameters to be 5.1429, 5.1487, and 5.1562 Å. The authors note that there is a continuous transition between the tetragonal and cubic structure, explained by the intergrowth of the two phases. However, the Bragg experiments also showed that for 22 and 26% YSZ, only the cubic fluorite reflections were detected, and that oxygen anions are displaced in the <100> direction towards the vacancy. From their results the authors obtain good agreement with previously calculated theoretical values for diffuse scattering, when they consider yttrium ions to be in nearest neighbour (NN) positions to the oxygen vacancy. However, they also proposed that the relaxation can be viewed as that of Zr^{4+} reducing the average Zr-O bond length by having 7-coordinate zirconia NN to the vacancy, with Y^{3+} in second nearest neighbour (2NN) sites, which results in an average Zr-O bond length of 2.15 Å, comparable to the 2.16 Å distance found in monoclinic ZrO_2.

Various successive neutron and x-ray diffraction studies produce the following results for anionic and cationic displacement in c-ZrO_2. The transition between cubic and tetragonal phases is also noted by Faber *et al.*[24] and Osborn *et al.*[25]. The majority of studies find anion displacements along the <100> direction[26,27,28,29] and cation displacements along the <110> direction[29,30], although anion and cation displacements were also reported along the <110>[24] and <111>[26] directions respectively. Horiuchi *et al.*[27] also noticed small thermal displacements of anions in the <111> direction.

Catlow *et al.*[31] used extended x-ray adsorption fine structure (EXAFS) techniques in order to establish the local structure environments observed in 18% (wt.%) YSZ. They noticed that the local structure environment of the Zr^{4+} cation is much more disordered than that of the Y^{3+} cation, and that the average Zr-O distance (2.16 Å) is considerably shorter than the mean Y-O distance (2.28 Å). This difference in the local disorder is best described by having a vacancy situated NN to the Zr^{4+} cations, allowing zirconia to adopt the preferred 7-coordinate

environment of the low temperature polymorph of m-ZrO_2, and by having the larger Y^{3+} cations occupying eightfold coordinated 2NN sites to the vacancy. Furthermore the observed Zr-O bond distance is comparable to the average Zr-O distance of 2.15 Å present in monoclinic zirconia. It was also found that increasing the temperature resulted in the local structures of yttria and zirconia becoming more similar, as increased anion mobility leads to the occurrence of yttrium ions being situated in NN sites to anion vacancies.

Subsequent EXAFS studies over a large concentration range of both yttria- and ytterbia-stabilised zirconia yielded similar results[32,33]. They both found that at low concentrations, oxygen vacancies were preferentially located next to Zr^{4+} cations, with zirconia having a lower average coordination number than the dopant cation. However, as dopant concentration, and therefore the number of vacancies, increased, the coordination of both the dopant cation and zirconia decreased, with vacancies in NN sites to dopant cations.

Most recently Kawata *et al.*[34] probed the local structure of 6-43 mol% (Y_2O_3) YSZ through the use of ^{89}Y MAS-NMR. In their study they took x-ray diffraction patterns of samples of 5.9, 9.8 and 42.9% YSZ, which all displayed a single phased cubic fluorite form. The results from the MAS-NMR spectra showed three different coordination environments for yttria; sixfold, sevenfold and eightfold. The low concentration samples contained exclusively eightfold yttria up to a concentration of 10%, whereafter the presence of sevenfold coordinated yttria can be detected. At concentrations above 19% there is a significant amount of sevenfold coordinated yttria present and at 42% the yttria is mostly sevenfold coordinated, with both sixfold and eightfold coordinated yttria also present.

2.4.2 Computational Defect Structure

Many studies have used computational modelling in an attempt to clarify and further understand the experimentally presented defect structure in YSZ. In particular much of the initial modelling focussed on investigating the experimental findings of Goff *et al.*[35], who reported that there were locally ordered phases in YSZ up to a dopant concentration of 15% Y_2O_3, which contained isolated oxygen vacancies and vacancy pairs on nearest neighbour anion sites along the <111> direction. They found that oxygen vacancies cause tetragonal distortions at a dopant concentration of 9%, and that with increasing dopant concentration vacancy pairs pack together like in the rhombohedral δ-phase to form aggregates.

Bogicevic *et al.*[21] conducted an electronic structure computational study to try and identify the defect ordering in doped cubic zirconia systems. The calculated energetic ordering of the zero-pressure polymorphs of zirconia is in good qualitative agreement with other theoretical studies as well as experiment. To investigate different doping concentrations of YSZ, a lattice algebra

technique is used to enumerate the positions of the fcc lattice and all configurations are generated and tested. From their methods, the δ-phase of YSZ is successfully predicted; they find that oxygen vacancies are preferentially situated as NN to the smallest cation in the system (Zr^{4+} in the case of YSZ), and that oxygen vacancies repel each other at short distances, but will align along the <111> direction as third nearest neighbours (3NN) to each other. However, all of their calculations are carried out using only primitive cells with a maximum of 23 atoms in. As a consequence of the small cell size used, 3NN is the maximum distance apart the oxygen vacancies can be, and the authors do not address the periodicity inherent in the calculations. In a later paper, they further probe defect interactions in YSZ[36]. From these calculations they find that vacancy separation at 3NN distances occur as a result of balancing repulsive electrostatic interactions with attractive elastic interactions. Through the use of the larger 40 atom system, they report that separating vacancies further than 3NN results in a less stable system, although again interactions of the unit cells across periodic boundaries are not considered.

Ostanin *et al.*[37] used first principles modelling to investigate the band structure of YSZ in comparison with experimentally obtained values through energy-loss near-edge structure (ELNES) techniques. Their method was 'benchmarked' by correctly predicting the low-pressure phase ordering of the 3 ambient-pressure zirconia polymorphs. They then simulated 33 mol% (Y_2O_3) YSZ by examining the 11-atom $Zr_2Y_2O_7$ system shown in figure 2.4 (presumably the same unit cell used by Bogicevic above). They find that anions are shifted away from ideal lattice sites in the <100> direction and cations along the <110> direction. The results obtained agree with previous work[38] but the authors admit that this is a simplistic model which contains artificial cation layering.

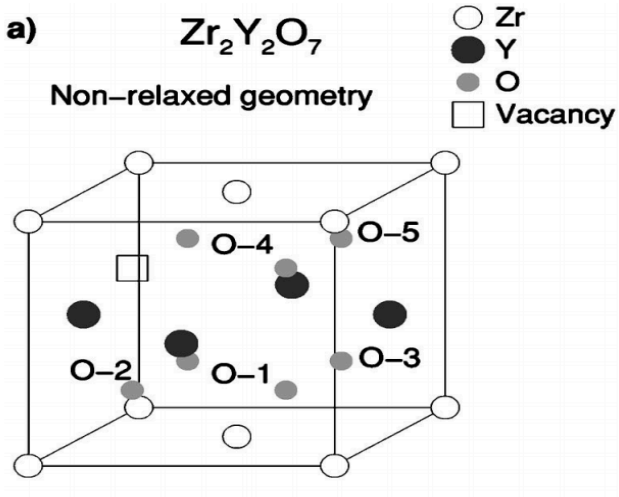

Figure 2.4. $Zr_2Y_2O_7$ unit cell used to simulate 33 mol% YSZ, reproduced from reference [37].

In an attempt to use a more sophisticated model two studies were carried out using 96-atom supercell models, which introduced 1,2 and 3 defect clusters, representing dopant concentrations of 3.2, 6.7 and 10.4 mol% Y_2O_3 respectively. The first study[39] examined the local atomic displacement of a single defect cluster before investigating the interactions of defect clusters with each other. With one defect cluster in a 96-atom supercell, they found that anions around the dopant Y^{3+} cations relax away from the ion along the <111> direction to accommodate the longer Y-O bond, whilst Zr^{4+} cations NN to the vacancy relax away along the <111> direction, and NN anions relax towards the vacancy along the <100> direction. When investigating a dopant concentration of 6.7% by having two defect clusters in the 96-atom supercell, vacancy-vacancy pairs were studied in four pairing directions; <100>, <110>, <111> and <112>, with the <111> direction showing the most stability. Furthermore, having the vacancies either side of one Zr^{4+} cation was found to be the most stable configuration in the tetragonal system, whilst the cubic system showed two arrangements of vacancies and cations roughly equal in energy, as shown in figure 2.5. However, having the vacancies either side of a Zr^{4+} cation was found to not be energetically favourable in 10.3% YSZ. A higher dopant concentration of 14.3% was also studied through the introduction of four defect clusters into the 96-atom supercell, although by keeping all the Y^{3+} cations in 2NN positions to vacancies it was possible to have 4 Y^{3+} ions in the 2NN shell, which may not be the lowest energy structure.

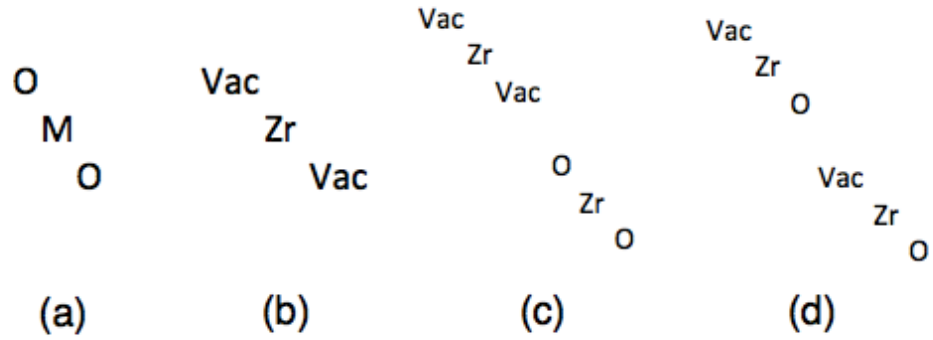

Figure 2.5. (a) the general oxygen-metal-oxygen tri-layer form present in c-ZrO_2. (b) vacancy pairing either side of a Zr^{4+} cation. (c) and (d) vacancy pair chains stable in c-ZrO_2.

The second study[40] showed that with one defect cluster present, the most stable configuration is with the oxygen vacancy at the 2NN position to yttrium. When simulating 2 and 3 defect clusters, the yttrium ions were kept at 2NN positions to the vacancies, and the vacancies were positioned in NN anion sites along the <111> direction. The results of these simulations showed that, in good agreement with experiment[41], the mono- and di-vacancy were more stable in a tetragonal configuration, while the tri-vacancy system was more stable in a cubic configuration. Cousland *et al.*[42] also achieve good correlation with experimental photoemission data through

modelling higher dopant concentrations by aligning vacancies in the <111> direction and positioning Y ions 2NN to vacancy sites.

There have been numerous other studies that investigate bulk ZrO_2 and vacancy ordering in bulk YSZ through the use of computational modelling at both the semi-empirical and first-principles levels of theory. Many investigations successfully model the phase transitions of the pure zirconia polymorphs[43,44], but the system becomes more difficult to represent when having to consider doping effects. The majority of the studies that investigate the positions of vacancies with respect to cations find the most stable structures to have vacancies situated in NN sites to zirconium and 2NN sites to yttrium[45,46,47,48], or more generally for doping zirconia with other metals that vacancies are preferentially situated in NN sites to the smaller cation in the system[4,49]. Figure 2.6 represents NN and 2NN sites to the vacancy in YSZ.

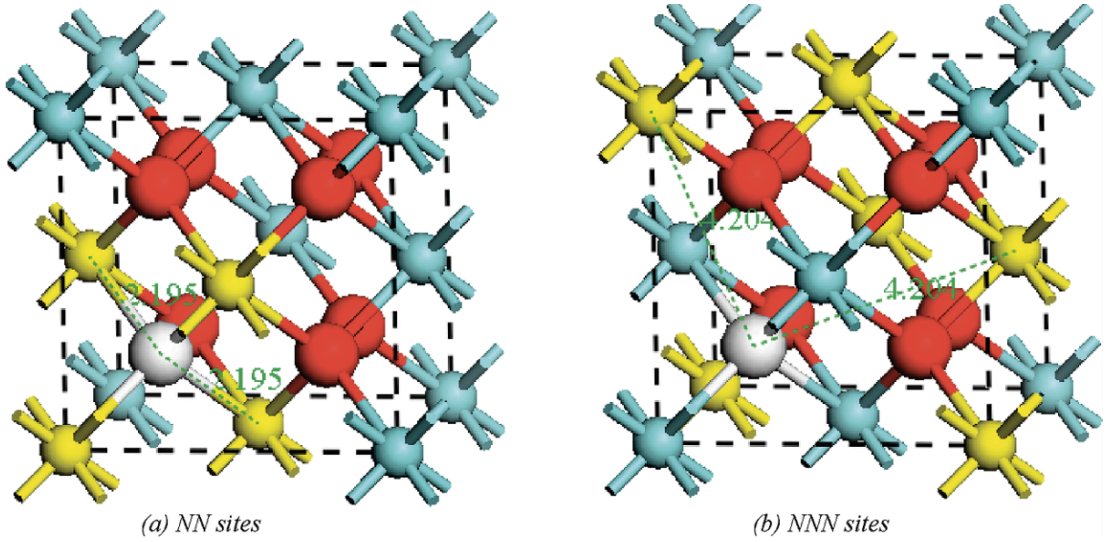

Figure 2.6. Yttrium in (a) NN sites and (b) 2NN sites to the vacancy. Blue, yellow, red and white spheres represent zirconium, yttrium, oxygen and the vacancy respectively. Reproduced from reference [47].

A recent work from Liu *et al.*[48] also tries to take into account cation-cation interaction unlike many previous studies. They suggest that it is energetically favourable to have the yttrium ions as far apart as possible. However, they report different results for the tetragonal supercell, and at the low level of doping present in their study full cubic stabilisation is not achieved so it is hard to take the cation spacing as a true representation. Although the model used is not an exact representation at low concentrations, the energies they obtain do correctly predict the concentration at which the tetragonal-cubic phase stabilisation occurs.

Both experimental and computational studies of the defect structure in YSZ agree that oxygen vacancies are more stable when situated in NN sites to zirconium cations and 2NN sites to

yttrium, and that oxygen ions are displaced along the <100> direction towards the vacancy. The oxygen anion displacement is indicative of the cubic-tetragonal phase transition and confirms the metastable tetragonal nature of the YSZ system. However, whilst experimental results are obtained from YSZ samples with yttria doping concentrations relevant for industrial applications, the majority of the modelling studies only consider the introduction of a single defect cluster. The simulation of YSZ systems with more realistic percentage yttria content has been limited to studying unit cell systems or approximating dopant positions by extrapolating the defect configuration found for an isolated vacancy cluster.

2.5 Zirconia and Yttria Stabilised Zirconia Surfaces

Determining the surface characteristics and behaviour of zirconia and YSZ is crucial for understanding catalytic applications and the chemistry of SOFC interphases. Morterra *et al.*[50] have shown experimentally that the cubic c-(111) surface dominates the YSZ morphology. Many computational studies have also investigated the low-index surfaces of pure zirconia, also showing the c-(111) surface to be the lowest energy one. (N.B. these studies report their findings as either the tetragonal t-(101) surface or c-(111); these two surfaces are structurally equivalent.) The surface energies calculated for the c-(111) surface from these studies are presented below in table 2.1.

Reference	Number of Layers	Surface Energy (J/m^2)	Level of theory
[51]	6	1.485	Hartree-Fock
	6	1.226	Interatomic Potentials
[52]	4	1.239	DFT – LDA
[53]	5	1.045	DFT – GGA
[54]	4	1.316	DFT – LDA
	4	1.088	DFT – GGA
[55]	6	1.102	DFT – GGA
[47]	3	1.210	Interatomic Potentials
[56]	1	0.76	Hybrid DFT
	2	0.97	Hybrid DFT

Table 2.1. Calculated surface energies for the c-(111) surface of pure ZrO_2.

The wide range of surface energies in table 2.1 show that when modelling surface systems, for even the simple case of pure zirconia, it is not straightforward to obtain a fundamental property such as the surface energy. This is in part due to the surface energy being very small when compared to the total energy of the system, Hofmann[55] reports that the surface energy is eight

orders of magnitude smaller than the total energy. Whilst it has already been shown that simulating industrially relevant dopant concentrations for bulk YSZ is non-trivial, additional complexity is introduced when modelling the YSZ surface due to the possibility of surface segregation effects. Furthermore, two experimental studies have investigated the surface energies of YSZ, results given in table 2.2. The surface energy varies with both dopant concentration and the state of the surface, highlighting the complexity of the surface system.

Reference	System Studied	Surface Energy (J/m^2)
[57]	10-YSZ	1.57
[58]	Hydrated 8-YSZ	0.85
	Hydrated 12-YSZ	1.27
	Anhydrous 8-YSZ	1.16
	Anhydrous 12-YSZ	1.80

Table 2.2. Surface energies of YSZ from microcalorimetry experiments. The number in system studied; i.e. 10-YSZ, refers to the mol% dopant concentration of Y_2O_3 in ZrO_2.

Eichler *et al.*[59] undertook an electronic structure investigation into the surface termination of ZrO_2 and were the first to consider introducing yttrium into the surface. Their previous work from bulk YSZ showed that yttrium is more stable in 2NN sites to oxygen vacancies, and that the most stable configuration they found had an yttrium-yttrium distance of 3.65 Å. To examine the behaviour of yttrium at the surface they introduced one of these yttrium-vacancy-yttrium (Y-V-Y) defect 'triangles' into their pure ZrO_2 surface model. By calculating the energies of moving the defect cluster from the bulk like region towards the surface they conclude that the surface system is more stable with yttrium close to the surface. Xia *et al.*[47] first undertook a semi-empirical study of the pure ZrO_2 low index surfaces, which found the c-(111) surface to be the most stable, before introducing a Y-V-Y defect cluster into the ZrO_2 surface system through the use of a 2D slab model. The yttria concentration was varied by extending the surface repeat unit. They report that yttrium saturation of the outermost layer occurs at 12.5 mol% Y_2O_3 and that segregation is favourable up to a depth of 4 layers. A similar study by Stanek[60] also shows similar results. However, Lahiri *et al.*[61] conducted a combined XPS, STM and ReaxFF study of the YSZ surface, which computationally predicts an yttrium surface saturation of 49 mol% ($YO_{1.5}$), which is in fairly good agreement with the XPS data obtained in their work, which showed a surface concentration between 30-45%.

Xia *et al.*[62,63] then reinvestigated the ZrO_2 surface as well as topological surface features with DFT. They had a 3 tri-layer model with a 15 Å vacuum gap and kept the bottom four layers fixed. Yttrium doping was then considered by introducing Y-V-Y clusters into both terrace and step models. However, in order to minimise the difficulty in the system set-up, only defect clusters with yttrium in NN positions to the vacancy were considered, which results in similar surface segregation effects found previously from the semi-empirical results. The most stable site for yttrium doping on the terrace surface was found to have the two yttrium ions aligned in the z-direction and the vacancy in-between in the first oxygen sub-surface layer, as shown in figure 2.7.

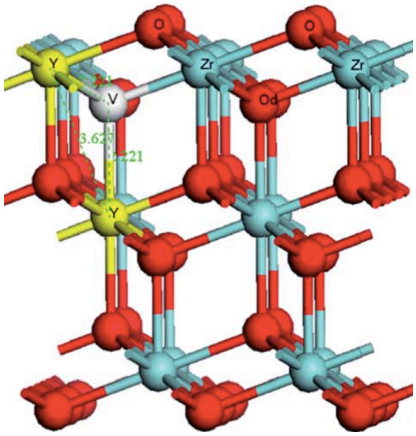

Figure 2.7. YSZ surface model with the vacancy in the first oxygen sub-surface layer. Reproduced from reference [63].

2.6 Summary

Yttria doping of zirconia results in a stabilisation of the cubic fluorite phase whilst introducing fast anion conductivity to the material and enhancing the catalytic activity. These material properties are dependent on the defect structure of the material and although it is generally accepted that the charge compensating vacancies introduced upon doping are preferentially situated at 2NN sites to dopant yttrium cations, and despite great experimental and theoretical effort in identifying this, precise details of the atomic structure still remain elusive. The work carried out within this thesis aims to build upon the current literature by using larger and more realistic surface models for YSZ, as well as providing greater detail about the local atomic structure present in the bulk material. The use of larger, more realistic surface models allows for a better representation of catalytic processes, as more molecules can be co-adsorbed on the surface, which as is seen in chapters 5 and 6 leads to the evaluation of a previously un-explored catalytic mechanism on YSZ. The local atomic structure work of chapter 7 aims to provide more detail of this long-disputed aspect of YSZ in the hope of providing good foundations for guiding the creation of future YSZ models.

2.7 Note on YSZ Dopant Concentrations

There are a number of different ways in which the dopant concentration of YSZ is reported in the literature, which can be the source of some confusion. Hopefully the following notes will bring some clarity to the different formats that dopant concentration is reported in and their relation to one another.

2.7.1 Mol% Y_2O_3

Yttria-stabilised zirconia is a solid solution of the parent oxides yttria (Y_2O_3) and zirconia (ZrO_2). The most commonly used description of the dopant concentration is the mole percentage of Y_2O_3. We will use the example of 9 mol% YSZ as this is an industrially relevant dopant concentration and one which is the primary focus of this thesis. 9 mol% YSZ represents the solid solution of yttria and zirconia comprising $(ZrO_2)_{0.91}(Y_2O_3)_{0.09}$. The following details how ~9 mol% YSZ is calculated and represented in the models used in this thesis. The unit cell of cubic ZrO_2 contains 4 Zr atoms and 8 O atoms. The 3x3x3 supercell (used in chapter 7) has the formula $Zr_{108}O_{216}$. A dopant concentration of ~9 mol% YSZ is achieved by the introduction of 18 substitutional yttrium cations and 9 oxygen vacancies; giving the supercell formula $Y_{18}Zr_{90}O_{207}$. This supercell contains 9 Y_2O_3 formula units and 90 ZrO_2 formula units, therefore yttria accounts for 9 out of a total of 99 formula units. The dopant percentage calculation is given as:

$$\begin{aligned} mol\%\ Y_2O_3 &= Y_{18}Zr_{90}O_{207} \\ &= 9\ Y_2O_3 + 90\ ZrO_2 \\ &= 9/99 = 9.09\ mol\% \end{aligned}$$

2.7.2 Mol% $YO_{1.5}$

A second way in which the YSZ dopant concentration is reported is mol% $YO_{1.5}$, which is equivalent to cation % – the percentage of total cation sites. Taking the same supercell from above the mol% $YO_{1.5}$ is calculated as:

$$\begin{aligned} mol\%\ YO_{1.5} &= Y_{18}Zr_{90}O_{207} \\ &= 18\ YO_{1.5} + 90\ ZrO_2 \\ &= 18/108 = 16.67\ mol\% \end{aligned}$$

2.7.3 Wt.% Y_2O_3

Finally the dopant concentration can also be expressed as the weight percentage (wt.%) of yttria in the sample. The atomic masses of yttrium, zirconium, and oxygen are 88.9, 91.2, and 16 respectively. This gives the molecular weight of zirconia (ZrO_2) as 123.2 (91.2 + 2x16), and the molecular weight of yttria (Y_2O_3) as 285.8 (2x88.9 + 3x16). Sticking with the example of 9 mol% Y_2O_3 – for 1 mole of 9 mol% YSZ there are 0.91 moles ZrO_2 and 0.09 moles Y_2O_3, the wt.% is then calculated as:

$$\begin{aligned} mass\ of\ 0.91\ moles\ ZrO_2 &= 0.91\ mols \times 123.2\ \ g/mol \\ &= 112.1\ g \end{aligned}$$

$$\begin{aligned} mass\ of\ 0.09\ moles\ Y_2O_3 &= 0.09\ mols \times 285.8\ \ g/mol \\ &= 20.3\ g \end{aligned}$$

$$wt.\%\ Y_2O_3 = \frac{20.3}{20.3 + 112.1} = 15.33\%$$

It can be seen from the three above examples that the same physical case of 9 mol% Y_2O_3 can be represented and reported by rather different dopant concentrations. One must therefore take care and exercise caution when both utilising the reported literature and reporting dopant concentration values. For the majority of this study the dopant concentration is given as mol% Y_2O_3, although we have tried to be as thorough as possible to explicitly state the dopant concentration being used throughout and should this differ. Overall the values for 9 mol% Y_2O_3 in these three different dopant concentrations are given as:

$$9\ mol\%\ Y_2O_3\ \approx 16.67\ mol\%\ YO_{1.5}\ \approx 15.33\ wt.\%\ Y_2O_3$$

References:

1. Teufer, G., Crystal structure of tetragonal ZrO2. *Acta Crystallographica* **1962,** *15* (NOV), 1187-&.
2. Patil, R. N.; Subbarao, E. C., Axial thermal expansion of ZrO2 and HfO2 in range room temperature to 1400 degrees C. *Journal of Applied Crystallography* **1969,** *2*, 281-&.
3. Yoshimura, M., Phase-stability of Zirconia. *American Ceramic Society Bulletin* **1988,** *67* (12), 1950-1955.
4. Stefanovich, E. V.; Shluger, A. L.; Catlow, C. R. A., Theoretical-study of the stabilization of cubic-phase ZrO2 by impurities. *Physical Review B* **1994,** *49* (17), 11560-11571.
5. Cormack, A. N.; Parker, S. C., Some observations on the role of dopants in phase-transitions in zirconia from atomistic simulations. *Journal of the American Ceramic Society* **1990,** *73* (11), 3220-3224.
6. Heuer; A.H, Science and Technology of Zirconia. Hobbs; L.W, Eds. The American Ceramics Society: Advances in Ceramics, 1981; Vol. 3.
7. Pauling, L., The principles determining the structure of complex ionic crystals. *Journal of the American Chemical Society* **1929,** *51*, 1010-1026.
8. Etsell, T. H.; Flengas, S. N., Electrical properties of solid oxide electrolytes. *Chemical Reviews* **1970,** *70* (3), 339-&.
9. Ho, S. M., On the structural chemistry of zirconium-oxide. *Materials Science and Engineering* **1982,** *54* (1), 23-29.
10. Duwez, P.; Odell, F.; Brown, F. H., Stabilization of zirconia with calcia and magnesia. *Journal of the American Ceramic Society* **1952,** *35* (5), 107-113.
11. Dhas, N. A.; Patil, K. C., Properties of magnesia-stabilized zirconia powders prepared by a combustion route. *Journal of Materials Science Letters* **1993,** *12* (23), 1844-1847.
12. Zinkevich, M., Thermodynamics of rare earth sesquioxides. *Progress in Materials Science* **2007,** *52* (4), 597-647.
13. Wu, B.; Zinkevich, M.; Aldinger, F.; Wen, D.; Chen, L., Ab initio study on structure and phase transition of A- and B-type rare-earth sesquioxides Ln(2)O(3) (Ln = La-Lu, Y, and Sc) based on density function theory. *Journal of Solid State Chemistry* **2007,** *180* (11), 3280-3287.
14. Yashima, M.; Kakihana, M.; Yoshimura, M., Metastable-stable phase diagrams in the zirconia-containing systems utilized in solid-oxide fuel cell application. *Solid State Ionics* **1996,** *86-8*, 1131-1149.
15. Cai, Z.; Lan, T. N.; Wang, S.; Dokiya, M., Supported Zr(Sc)O-2 SOFCs for reduced temperature prepared by slurry coating and co-firing. *Solid State Ionics* **2002,** *152*, 583-590.
16. Kobayashi, K.; Takahashi, I.; Shiono, M.; Dokiya, M., Supported Zr(Sc)O-2 SOFCs for reduced temperature prepared by electrophoretic deposition. *Solid State Ionics* **2002,** *152*, 591-596.
17. Raming, T.; Winnubst, L.; Verweij, H., The synthesis and characterisation of mixed Y2O3-doped ZrO2 and alpha-Fe2O3 nanosized powders. *Journal of Materials Chemistry* **2002,** *12* (12), 3705-3711.
18. Yashima, M.; Morimoto, K.; Ishizawa, N.; Yoshimura, M., Difusionless tetragonal cubic transformation temperature in zirconia ceria solid-solutions. *Journal of the American Ceramic Society* **1993,** *76* (11), 2865-2868.
19. Balducci, G.; Kaspar, J.; Fornasiero, P.; Graziani, M.; Islam, M. S.; Gale, J. D., Computer simulation studies of bulk reduction and oxygen migration in CeO2-ZrO2 solid solutions. *Journal of Physical Chemistry B* **1997,** *101* (10), 1750-1753.
20. Yashima, M.; Morimoto, K.; Ishizawa, N.; Yoshimura, M., Zirconia ceria solid-solution synthesis and the temperature time transformation diagram for the 1/1 composition. *Journal of the American Ceramic Society* **1993,** *76* (7), 1745-1750.
21. Bogicevic, A.; Wolverton, C.; Crosbie, G. M.; Stechel, E. B., Defect ordering in aliovalently doped cubic zirconia from first principles. *Physical Review B* **2001,** *64* (1).
22. Krishnamurthy, R.; Yoon, Y. G.; Srolovitz, D. J.; Car, R., Oxygen diffusion in yttria-stabilized zirconia: A new simulation model. *Journal of the American Ceramic Society* **2004,** *87* (10), 1821-1830.
23. Steele, D.; Fender, B. E. F., Structure of cubic ZrO2-YO1.5 solid-solutions by neutron-scattering. *Journal of Physics C-Solid State Physics* **1974,** *7* (1), 1-11.

24. Faber, J.; Mueller, M. H.; Cooper, B. R., Neutron-diffraction study of Zr(Ca,Y)O2-X - Evidence of differing mechanisms for internal and external distortions. *Physical Review B* **1978,** *17* (12), 4884-4888.
25. Hull, S.; Farley, T. W. D.; Hackett, M. A.; Hayes, W.; Osborn, R.; Andersen, N. H.; Clausen, K.; Hutchings, M. T.; Stirling, W. G., Quasielastic diffuse neutron-scattering from yttria-stabilized zirconia at elevated-temperatures. *Solid State Ionics* **1988,** *28*, 488-492.
26. Morinaga, M.; Cohen, J. B.; Faber, J., X-ray-diffraction study of Zr(Ca,Y)O2-X .1. average structure. *Acta Crystallographica Section A* **1979,** *35* (SEP), 789-795.
27. Horiuchi, H.; Schultz, A. J.; Leung, P. C. W.; Williams, J. M., Time-of-flight neutron-diffraction study of a single-crystal of yttria-stabilized zirconia, Zr(Y)O1.862, at high-temperature and in an applied electrical-field. *Acta Crystallographica Section B-Structural Science* **1984,** *40* (AUG), 367-372.
28. Howard, C. J.; Hill, R. J.; Reichert, B. E., Structures of the ZrO2 polymorphs at room-temperature by high-resolution neutron powder diffraction. *Acta Crystallographica Section B-Structural Science* **1988,** *44*, 116-120.
29. Argyriou, D. N., Measurement of the static disorder contribution to the temperature factor in cubic stabilized ZrO2. *Journal of Applied Crystallography* **1994,** *27*, 155-158.
30. Welberry, T. R.; Withers, R. L.; Thompson, J. G.; Butler, B. D., Diffuse-scattering in yttria-stabilized cubic zirconia. *Journal of Solid State Chemistry* **1992,** *100* (1), 71-89.
31. Catlow, C. R. A.; Chadwick, A. V.; Greaves, G. N.; Moroney, L. M., EXAFS study of yttria-stabilized zirconia. *Journal of the American Ceramic Society* **1986,** *69* (3), 272-277.
32. Veal, B. W.; McKale, A. G.; Paulikas, A. P.; Rothman, S. J.; Nowicki, L. J., EXAFS study of yttria stabilized cubic zirconia. *Physica B & C* **1988,** *150* (1-2), 234-240.
33. Komyoji, D.; Yoshiasa, A.; Moriga, T.; Emura, S.; Kanamaru, F.; Koto, K., EXAFS study of the fluorite-type compounds in the systems (1-X)ZrO2-XYbO1.5 (X = 0.18-less-than-or-equal-to-X-less-than-or-equal-to-0.5) and Zr2Ln2O7 (Ln = Tb, Dy, Ho, Er, AND Yb). *Solid State Ionics* **1992,** *50* (3-4), 291-301.
34. Kawata, K.; Maekawa, H.; Nemoto, T.; Yamamura, T., Local structure analysis of YSZ by Y-89 MAS-NMR. *Solid State Ionics* **2006,** *177* (19-25), 1687-1690.
35. Goff, J. P.; Hayes, W.; Hull, S.; Hutchings, M. T.; Clausen, K. N., Defect structure of yttria-stabilized zirconia and its influence on the ionic conductivity at elevated temperatures. *Physical Review B* **1999,** *59* (22), 14202-14219.
36. Bogicevic, A.; Wolverton, C., Nature and strength of defect interactions in cubic stabilized zirconia. *Physical Review B* **2003,** *67* (2).
37. Ostanin, S.; Craven, A. J.; McComb, D. W.; Vlachos, D.; Alavi, A.; Finnis, M. W.; Paxton, A. T., Effect of relaxation on the oxygen K-edge electron energy-loss near-edge structure in yttria-stabilized zirconia. *Physical Review B* **2000,** *62* (22), 14728-14735.
38. French, R. H.; Glass, S. J.; Ohuchi, F. S.; Xu, Y. N.; Ching, W. Y., Experimental and theoretical determination of the electronic-structure and optical-properties of 3 phases of ZrO2. *Physical Review B* **1994,** *49* (8), 5133-5141.
39. Ostanin, S.; Craven, A. J.; McComb, D. W.; Vlachos, D.; Alavi, A.; Paxton, A. T.; Finnis, M. W., Electron energy-loss near-edge shape as a probe to investigate the stabilization of yttria-stabilized zirconia. *Physical Review B* **2002,** *65* (22).
40. Ostanin, S.; Salamatov, E.; Craven, A. J.; McComb, D. W.; Vlachos, D., Theory of the phases and atomistic structure of yttria-doped zirconia. *Physical Review B* **2002,** *66* (13).
41. Vlachos, D.; Craven, A. J.; McComb, D. W., The influence of dopant concentration on the oxygen K-edge ELNES and XANES in yttria-stabilized zirconia. *Journal of Physics-Condensed Matter* **2001,** *13* (48), 10799-10809.
42. Cousland, G. P.; Cui, X. Y.; Smith, A. E.; Stampfl, C. M.; Wong, L.; Tayebjee, M.; Yu, D.; Triani, G.; Evans, P. J.; Ruppender, H. J.; Jang, L. Y.; Stampfl, A. P. J., A medium-energy photoemission and ab-initio investigation of cubic yttria-stabilised zirconia. *Journal of Applied Physics* **2014,** *115* (14).
43. Kralik, B.; Chang, E. K.; Louie, S. G., Structural properties and quasiparticle band structure of zirconia. *Physical Review B* **1998,** *57* (12), 7027-7036.
44. Jomard, G.; Petit, T.; Pasturel, A.; Magaud, L.; Kresse, G.; Hafner, J., First-principles calculations to describe zirconia pseudopolymorphs. *Physical Review B* **1999,** *59* (6), 4044-4052.

45. Eichler, A., Tetragonal Y-doped zirconia: Structure and ion conductivity. *Physical Review B* **2001,** *64* (17).
46. Stapper, G.; Bernasconi, M.; Nicoloso, N.; Parrinello, M., Ab initio study of structural and electronic properties of yttria-stabilized cubic zirconia. *Physical Review B* **1999,** *59* (2), 797-810.
47. Xia, X.; Oldman, R.; Catlow, R., Computational Modeling Study of Bulk and Surface of Yttria-Stabilized Cubic Zirconia. *Chemistry of Materials* **2009,** *21* (15), 3576-3585.
48. Ding, H. P.; Virkar, A. V.; Liu, F., Defect configuration and phase stability of cubic versus tetragonal yttria-stabilized zirconia. *Solid State Ionics* **2012,** *215*, 16-23.
49. Khan, M. S.; Islam, M. S.; Bates, D. R., Cation doping and oxygen diffusion in zirconia: a combined atomistic simulation and molecular dynamics study. *Journal of Materials Chemistry* **1998,** *8* (10), 2299-2307.
50. Morterra, C.; Cerrato, G.; Ferroni, L.; Montanaro, L., Surface characterization of yttria-stabilized tetragonal ZrO2 .1. structural, morphological, and surface hydration features. *Materials Chemistry and Physics* **1994,** *37* (3), 243-257.
51. Gennard, S.; Cora, F.; Catlow, C. R. A., Comparison of the bulk and surface properties of ceria and zirconia by ab initio investigations. *Journal of Physical Chemistry B* **1999,** *103* (46), 10158-10170.
52. Christensen, A.; Carter, E. A., First-principles study of the surfaces of zirconia. *Physical Review B* **1998,** *58* (12), 8050-8064.
53. Haase, F.; Sauer, J., The surface structure of sulfated zirconia: Periodic ab initio study of sulfuric acid adsorbed on ZrO2(101) and ZrO2(001). *Journal of the American Chemical Society* **1998,** *120* (51), 13503-13512.
54. Iskandarova, I. M.; Knizhnik, A. A.; Rykova, E. A.; Bagatur'yants, A. A.; Potapkin, B. V.; Korkin, A. A., First-principle investigation of the hydroxylation of zirconia and hafnia surfaces. *Microelectronic Engineering* **2003,** *69* (2-4), 587-593.
55. Hofmann, A.; Clark, S. J.; Oppel, M.; Hahndorf, I., Hydrogen adsorption on the tetragonal ZrO2(101) surface: a theoretical study of an important catalytic reactant. *Physical Chemistry Chemical Physics* **2002,** *4* (14), 3500-3508.
56. Bandura, A. V.; Evarestov, R. A., Ab initio structure modeling of ZrO2 nanosheets and single-wall nanotubes. *Computational Materials Science* **2012,** *65*, 395-405.
57. Drazin, J. W.; Castro, R. H. R., Water Adsorption Microcalorimetry Model: Deciphering Surface Energies and Water Chemical Potentials of Nanocrystalline Oxides. *Journal of Physical Chemistry C* **2014,** *118* (19), 10131-10142.
58. Costa, G. C. C.; Ushakov, S. V.; Castro, R. H. R.; Navrotsky, A.; Muccillo, R., Calorimetric Measurement of Surface and Interface Enthalpies of Yttria-Stabilized Zirconia (YSZ). *Chemistry of Materials* **2010,** *22* (9), 2937-2945.
59. Eichler, A.; Kresse, G., First-principles calculations for the surface termination of pure and yttria-doped zirconia surfaces. *Physical Review B* **2004,** *69* (4).
60. Stanek, C. R.; Grimes, R. W.; Rushton, M. J. D.; McClellan, K. J.; Rawlings, R. D., Surface dependent segregation of Y2O3 in t-ZrO2. *Philosophical Magazine Letters* **2005,** *85* (9), 445-453.
61. Lahiri, J.; Mayernick, A.; Morrow, S. L.; Koel, B. E.; van Duin, A. C. T.; Janik, M. J.; Batzill, M., Modification of Active Sites on YSZ(111) by Yttria Segregation. *Journal of Physical Chemistry C* **2010,** *114* (13), 5990-5996.
62. Xia, X.; Oldman, R. J.; Catlow, C. R. A., Zirconium dioxide topological surfaces with low coordination sites. *Journal of Materials Chemistry* **2011,** *21* (38), 14549-14558.
63. Xia, X.; Oldman, R. J.; Catlow, C. R. A., Oxygen adsorption and dissociation on yttria stabilized zirconia surfaces. *Journal of Materials Chemistry* **2012,** *22* (17), 8594-8612.

Chapter 3

Computational Details

The background theory behind the computational simulation methods used throughout this thesis is introduced in chapter 3. The mathematical formalisms of the classical interatomic potentials methods and the quantum mechanical electronic structure methods are given in brief and we present the various techniques to make them practicable for the calculations performed in this thesis.

3.1 Introduction

Theoretical chemistry is the combination of mathematical methods and the fundamental laws of physics in order to study processes of chemical relevance. In general, chemistry is concerned with the interactions of atoms or molecules, which can be considered as collections of positive nuclei and negative electrons. The most important physical force for chemical phenomena is the Coulomb interaction between charged particles. Therefore to study chemistry computationally we must be able to describe the interactions between the components of our system, which is to have the mathematical form of the force between charged particles. Broadly speaking atomic and molecular modelling techniques are separated into two categories; (i) force-field methods in which parameterised interatomic potentials describe atomic interactions in terms of classical particle forces between different atomic species but do not treat electrons explicitly, and (ii) electronic structure methods which are based in quantum mechanics and aim to solve the Schrödinger equation in order to directly describe collections of atoms and molecules in terms of the interactions of electrons and nuclei.

3.2 Force-field Methods

Atomistic simulations with force-field methods avoid explicitly solving the Schrödinger equation by using inter-atomic potentials to describe the interactions of atoms and to express the potential energy of a system. The potential energy function, $U(r_1, r_2, \dots, r_N)$, of an N-atom system expresses the energy of the system as a function of the nuclear coordinates and is expanded to include all of the many-body interaction terms[1,2]:

$$U = \sum_{i}^{N} \varphi_i(r_i) + \frac{1}{2} \sum_{i}^{N} \sum_{j}^{N} \varphi_{ij}(r_i, r_j) + \frac{1}{6} \sum_{i}^{N} \sum_{j}^{N} \sum_{k}^{N} \varphi_{ijk}(r_i, r_j, r_k) + \dots \quad (3.1)$$

where φ_{ij} and φ_{ijk} are the two-body and three-body functions dependent on the positions of pairs of atoms i and j, and the positions of atoms i, j, and k respectively. However, in practice approximating the potential energy to include only the two-body terms provides a good description of the system. These two-body functions can be separated into long-range Coulombic, and short-range non-Coulombic terms (V_{ij}):

$$\varphi_{ij}(r_i, r_j) = \frac{q_i q_j}{r_{ij}} + V_{ij}(r_{ij}) \quad (3.2)$$

3.2.1 Long-range Coulombic Interaction

The electrostatic Coulomb term is a function of the charges (q_i) on atoms and their interatomic distances:

$$U_{el} = \frac{1}{2}\sum_{i}^{N}\sum_{j}^{N}\frac{q_i q_j}{r_{ij}} \tag{3.3}$$

According to this equation the potential energy between ions decreases as a function of $1/r$; although the number of interacting ions increases with the surface area of a sphere, $4\pi r^2$. Therefore the interaction energy due to the increasing number of interacting ions increases faster than the energy decreases with increasing distance, making the Coulomb energy difficult to evaluate. However, the Ewald summation provides an elegant solution to this problem in which the Coulombic interaction is split into short-range and long-range contributions, which are evaluated, and whose sum converges quickly, in real space and reciprocal space respectively[3]. This approach can be viewed as the addition and subtraction of atom centred Gaussian distributions in order to screen point charges and maintain charge neutrality[2].

$$U^{real} = \frac{1}{2}\sum_{i}^{N}\sum_{j}^{N}\frac{q_i q_j}{r_{ij}}\, erfc\left(\eta^{1/2} r_{ij}\right) \tag{3.4}$$

$$U^{recip.} = \frac{1}{2}\sum_{i}^{N}\sum_{j}^{N}\sum_{G}\frac{4\pi}{V} q_i q_j \exp\left(iG \cdot r_{ij}\right)\frac{exp(-G^2/4\eta)}{G^2} \tag{3.5}$$

$$U^{self} = -\sum_{i}^{N} q_i^2 \left(\frac{\eta}{\pi}\right)^{1/2} \tag{3.6}$$

Here G is a reciprocal lattice vector, V is the volume of the unit cell, and η is a parameter that controls the division between real and reciprocal space and is chosen minimise the number of terms evaluated within each space for a given accuracy. The spurious interaction of each Gaussian with itself is corrected for in the self-energy term and the total electrostatic energy can then be given by:

$$U_{el} = U^{real} + U^{recip.} + U^{self} \tag{3.7}$$

3.2.2 Short-range Non-Coulombic Interaction

The non-Coulombic interactions are usually approximated as analytical functions containing both attractive and repulsive terms[1]. The repulsive term describes the Pauli repulsion due to overlap of closed shell electron configurations, whilst the attractive term represents van der Waals and covalence effects. A schematic representation of this short-range potential energy between two ions is given in figure 3.1.

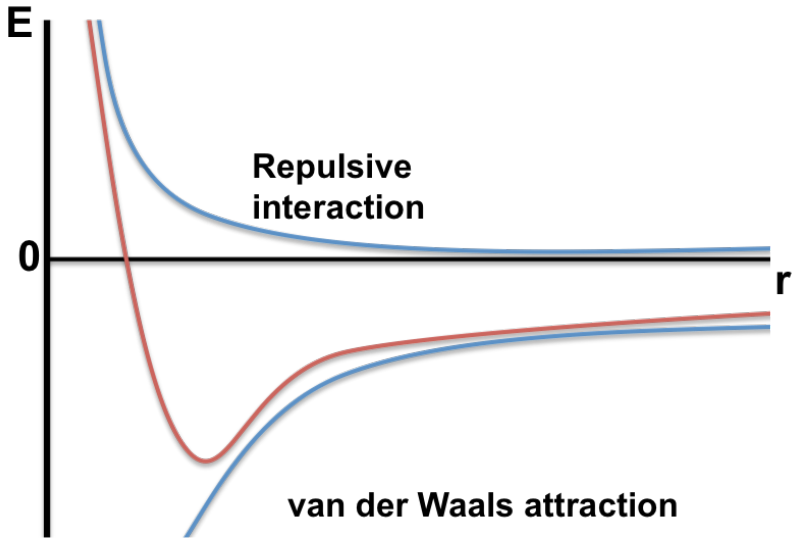

Figure 3.1. Cartoon representation of the short-range non-Coulombic interaction between ions as a function of interatomic distance; comprising repulsive and attractive components.

At short distances the repulsive force dominates as electron clouds overlap and repel each other, whilst at larger distances the attractive dispersion force plays a larger role. Many different functions can be used to represent the non-Coulombic interaction between atoms. The Buckingham potential, widely used for modelling ionic solids, is employed in this thesis and can be written as:

$$V(r) = A\,exp\left(\frac{-r}{\rho}\right) - \frac{C}{r^6} \tag{3.8}$$

where A, C, and ρ are constants which are derived either from fitting to experimental data or ab-initio calculations. In practice the short-range non-Coulombic interactions require a finite cut-off distance to be specified, although the potential should not be terminated abruptly at the cut-off but should tent smoothly towards zero.

3.2.3 Ionic Polarisation: The Shell Model

Polarisation is the displacement largely of the valence electrons due to the presence of an electric field and is an important effect to consider when studying ionic materials. Whilst the force-fields method described above treats ions as point charges, this model can be refined to include polarisation effects by treating each ion as having a core and shell region[4,5]. The core represents the nucleus and the core electrons, whilst the shell represents the valence electrons. The core and shell are coupled via a harmonic spring as illustrated in figure 3.2.

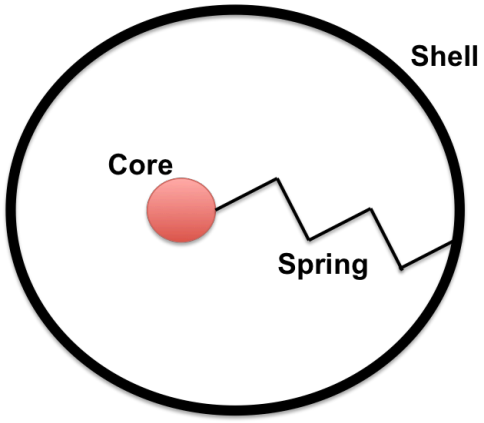

Figure 3.2. Polarisable ion model with the ionic core connected to the valence electron shell via a harmonic spring.

Within the shell model the free ion polarisability (α) is related to the shell charge (Y) and the spring constant (k) according to the following equation[6]:

$$\alpha = \frac{Y^2}{k} \tag{3.9}$$

3.3 Electronic Structure Methods

In order to study the electronic structure and interactions present in a chemical system one must turn to quantum mechanics as electrons are quantum particles, the behaviour of which cannot be described by classical mechanics. Analytical quantum mechanical descriptions are only feasible for one-electron systems, so a number of approximations are introduced in order to allow for computation of interesting and relevant chemical systems. In quantum mechanics the state of a system is completely specified by the wavefunction; a function of time and the three position coordinates for each particle in the system, which contains all the information that can be known about the system. Consideration of the time-independent wavefunction (Ψ) is the first

approximation introduced into most electronic structure methods, which aim to solve the non-relativistic time-independent many-body Schrödinger equation.

$$\hat{\mathrm{H}}\Psi(\{R_A\},\{r_i,\sigma_i\}) = E\Psi(\{R_A\},\{r_i,\sigma_i\}) \tag{3.10}$$

The wavefunction in this case, for a system containing M nuclei and N electrons, is dependent on the all spatial coordinates of the nuclei $(R_A, A = 1,\dots,M)$ and the spatial and spin coordinates of the electrons $(r_i,\sigma_i, i = 1,\dots,N)$. The total energy operator (the Hamiltonian, $\hat{\mathrm{H}}$) contains all possible interactions between electrons and nuclei, and can be expanded as[7]:

$$\hat{\mathrm{H}} = -\sum_{i=1}^{N}\frac{\nabla_i^2}{2} - \sum_{A=1}^{M}\frac{\nabla_A^2}{2M_A} + \sum_{i=1}^{N}\sum_{j>i}^{N}\frac{1}{|r_i - r_j|} + \sum_{A=1}^{M}\sum_{B>A}^{M}\frac{Z_A Z_B}{|R_A - R_B|} - \sum_{i=1}^{N}\sum_{A=1}^{M}\frac{Z_A}{|r_i - R_A|} \tag{3.11}$$

The above equation is given in atomic units; M_A is the mass ratio of nucleus A to the mass of an electron, Z_A is the atomic number of nucleus A, and ∇_i^2 and ∇_A^2 are the Laplacian operators. The kinetic energies of the electrons and nuclei are given by the first two terms respectively, and the electron-electron and nuclear-nuclear Coulomb repulsions are given by the third and fourth terms respectively. The fifth term is the Coulomb attraction between electrons and nuclei.

3.3.1 The Born-Oppenheimer Approximation

The second approximation made is with regards to the mass difference between nuclei and electrons. Electrons are much lighter than nuclei and hence move a lot faster than nuclei, the electrons are considered to adjust instantaneously to the nuclear geometry so that effectively electronic motion occurs around stationary nuclei. This is known as the adiabatic or Born-Oppenheimer approximation[8], and it allows for the separation of nuclear and electronic motion. With fixed nuclear positions the nuclei kinetic energy term can be neglected and the nuclei-nuclei repulsion can be applied as a constant for a given configuration of nuclei. The remaining terms are collected together in the electronic Hamiltonian ($\hat{\mathrm{H}}_e$):

$$\hat{\mathrm{H}}_e = -\sum_{i=1}^{N}\frac{\nabla_i^2}{2} + \sum_{i=1}^{N}\sum_{j>i}^{N}\frac{1}{|r_i - r_j|} - \sum_{i=1}^{N}\sum_{A=1}^{M}\frac{Z_A}{|r_i - R_A|} \tag{3.12}$$

The solution to the Schrödinger equation involving the electronic Hamiltonian can then be re-written with an electronic wavefunction (Ψ_e) which only depends on the electronic spatial and spin coordinates as the nuclear coordinates remain fixed. For further simplicity the electron spatial and spin coordinates can be contained within one variable (x_i), so the electronic Schrödinger equation becomes;

$$\hat{\mathrm{H}}_e \Psi_e(\{x_i\}) = E_e \Psi_e(\{x_i\}) \tag{3.13}$$

The total energy for a system with some fixed configuration of nuclei can then be described to consist of the electronic Hamiltonian and the constant nuclear-nuclear repulsion term.

$$E_{total} = E_e + \sum_{A=1}^{M} \sum_{B>A}^{M} \frac{Z_A Z_B}{|R_A - R_B|} \tag{3.14}$$

Even with the above approximations in place, of using the time-independent Schrödinger equation under the Born-Oppenheimer regime, an exact analytical solution is available only for systems containing one electron. The nature of the problem is greatly simplified by introducing an independent particle model, in which the motion of one electron is considered in isolation, independent of the motion of all the other electrons in the system.

3.3.2 Hartree-Fock Theory

The origin of a quantum chemical independent particle model is the Hartree-Fock (HF) theory, a wavefunction based method. Initially Hartree[9] developed a model to express the total N-electron wavefunction of interacting electrons ($\Psi(x_i)$) as the product of N single electron wavefunctions ($\phi(x_i)$).

$$\Psi(x_i, x_j, \ldots, x_N) \approx \phi_i(x_i)\phi_j(x_j) \ldots \phi_N(x_N) \tag{3.15}$$

However, this original Hartree wavefunction does not satisfy the antisymmetry property of the wavefunction. The total electronic wavefunction must be antisymmetric with respect to the exchange of any two electrons as they are spin ½ particles, and the Pauli exclusion principle is a direct consequence of this antisymmetry. Fock[10] then introduced a description of the total wavefunction that captures the antisymmetry of fermions. This Hartree-Fock wavefunction ($\Psi^{HF}(\{x_i\})$) takes the form of a single Slater determinant[11], which is a linear combination of the product of independent electron wavefunctions with all combinations of the permutations of their coordinates.

$$\Psi(x_i, x_j, \ldots, x_N) \approx \Psi^{HF}(\{x_i\}) = \frac{1}{\sqrt{N!}} \begin{vmatrix} \phi_i(x_i) & \phi_j(x_i) & \cdots & \phi_N(x_i) \\ \phi_i(x_j) & \phi_j(x_j) & \cdots & \phi_N(x_j) \\ \vdots & \vdots & \ddots & \vdots \\ \phi_i(x_N) & \phi_j(x_N) & \cdots & \phi_N(x_N) \end{vmatrix} \tag{3.16}$$

The result of this Slater determinant wavefunction means that exchange of any two electrons coordinates results in exchanging the two columns inside the determinant, therefore the electron antisymmetry is described correctly. For example in a two-electron system:

$$\Psi(x_1, x_2) = \frac{1}{\sqrt{2!}} [\phi_1(x_1)\phi_2(x_2) - \phi_2(x_1)\phi_1(x_2)] = -\Psi(x_2, x_1) \tag{3.17}$$

Using the HF wavefunction the electronic energy can be re-written as;

$$E^{HF} = \langle \Psi^{HF} | \hat{\mathrm{H}}_e | \Psi^{HF} \rangle \tag{3.18}$$

The energy can be minimised variationally by solving one-electron Schrödinger equations subject to the independent electron wavefunctions being orthonormal:

$$\hat{F}_i \phi_i(x_i) = \in_i \phi_i(x_i), \quad \hat{F}_i = -\frac{\nabla^2}{2} + V^{ext}(x_i) + V^{Hartree}(x_i) + V_i^{Exchange}(x_i) \tag{3.19}$$

$\hat{F}_i$ is the Fock operator, a one-electron Hamiltonian, and $\in_i$ is the one electron energy. The first two terms of the Fock operator are the electron kinetic energy and external potential (nuclei-electron) attraction terms respectively. The third and fourth terms concern electron-electron interactions; the third term (Hartree potential) is the Coulomb repulsion between the i^{th} electron and the electron density produced by all electrons. The fourth term (exchange potential) is a result of the antisymmetry of the wavefunction. The HF energy is calculated within a self-consistent loop; an initial guess for the occupied orbitals is used to generate the Hartree potential, which is then used within the Fock operator to determine a new set of orbitals, these new orbitals then provide a new Hartree potential and the process is repeated until convergence occurs.

Although Hartree-Fock theory treats exchange of electrons with the same spin exactly, the mean-field treatment of electron-electron Coulomb repulsion of one electron with the electron density of all electrons is a major drawback of this method, as this provides an inaccurate spatial description of electrons compared to the real many-electron interacting system. The Hartree-Fock limit is the energy obtained from the HF method when using a complete basis set, which will always be higher in energy than the exact solution to the non-relativistic time-independent Schrödinger equation. The difference between the HF limit and the exact solution is known as the electron correlation energy. Despite the correlation energy being only a small fraction of the total energy it can be very important for systems of chemical and physical interest. To this end many methods, described as post-Hartree-Fock methods, have been developed to calculate electron correlation within wavefunction-based theory. These methods

include; Møller-Plesset perturbation theory, configuration interaction, and coupled cluster methods, which usually involve relaxing the condition that the wavefunction is given by a single Slater determinant and the correlation energy is calculated by the way of electronic excitations from occupied to virtual orbitals. However, these higher-level techniques become increasingly computationally expensive and remain impractical for studying large system sizes. HF theory[12] scales computationally as N^4 whereas for post-HF methods[13,14] scaling can be between N^5-N^7.

3.3.3 Density Functional Theory

In contrast to the Hartree-Fock method, Density Functional Theory (DFT) does not attempt to solve the many electron wavefunction but instead uses the electron density ($\rho(r)$) as the fundamental parameter from which to obtain the ground-state properties of a system. Unlike the wavefunction, which is not a physical observable, the electron density is a physical characteristic of atoms and molecules. This is in theory a profound simplification to the size of the problem. The wave function for an N electron system will contain 3^N variables, whereas the density only depends on three spatial coordinates, regardless of the size of the system. The electron density determines the probability of finding an electron in a given volume (r), and for an N electron system is defined as:

$$\rho(r) = N \int \dots \int |\Psi(x_1, x_2, \dots, x_N)|^2 dx_1 dx_2 \dots dx_N \tag{3.20}$$

The electron density is real and non-negative, dependent on three spatial position variables, which integrates to give the total number of electrons.

$$N = \int \rho(r)\, dr \tag{3.21}$$

3.3.3.1 The Thomas-Fermi Model

The Thomas-Fermi (TF) model[15,16] was the first attempt to describe systems in terms of functionals of the electron density. In the TF model the energy functional is separated into three terms; kinetic energy, electron-nuclei, and electron-electron interactions. The kinetic energy is approximated as that of the uniform electron gas and is given by;

$$T[\rho(r)] = C_F \int \rho^{5/3}(r)\, dr \ , \ where\ C_F = \frac{3}{10}(2\pi^2)^{2/3} = 2.871 \tag{3.22}$$

The electron-nuclei attraction and electron-electron repulsion are given by their classical expressions, so that the total energy of a system in terms of the electron density is given by;

$$E[\rho(r)] = C_F \int \rho^{5/3}(r)\, dr - Z \int \frac{\rho(r)}{r}\, dr + \frac{1}{2} \iint \frac{\rho(r_1)\rho(r_2)}{|r_1 - r_2|} dr_1 dr_2 \tag{3.23}$$

The inexact approximation of the kinetic energy functional is the largest source of error in TF theory. The total and kinetic energies are of the same order of magnitude resulting in TF theory being very sensitive to the choice of kinetic energy functional. Additionally, whilst the uniform electron gas assumption in the TF model holds well for describing the valence electrons in a periodic metallic system it completely fails to predict bonding and all atoms repel each other.

3.3.3.2 Hohenberg-Kohn Theorems

The Hohenberg-Kohn proofs give DFT its firm mathematical grounding[17]. These two theorems are: (i) the external potential to within an additive constant (and therefore the total energy) is a unique functional of the electron density, and (ii) the ground-state electron density can be found variationally. The external potential of the electronic Hamiltonian only depends on the configuration of the nuclei and is shown to be uniquely determined by the electron density as follows. First suppose there is a collection of atoms subject to an external potential ($\upsilon(r)$), for which the electron density is known and determines the potential and all of the system properties. Secondly suppose there is a second potential ($\upsilon'(r)$) that can also give the same electron density. This gives two different Hamiltonians ($\hat{\mathrm{H}}$) and ($\hat{\mathrm{H}}'$) which have different normalised wavefunctions (Ψ) and (Ψ') but have the same ground state electron density, which gives:

$$\begin{aligned} E_0 < \langle \Psi' | \hat{\mathrm{H}} | \Psi' \rangle &= \langle \Psi' | \hat{\mathrm{H}}' | \Psi' \rangle + \langle \Psi' | \hat{\mathrm{H}} - \hat{\mathrm{H}}' | \Psi' \rangle \\ &= E_0' + \int \rho(r)[\upsilon(r) - \upsilon'(r)]\, dr \end{aligned} \tag{3.24}$$

where E_0 and E_0' are the ground-state energies for $\hat{\mathrm{H}}$ and $\hat{\mathrm{H}}'$ respectively. We can also get:

$$\begin{aligned} E_0' < \langle \Psi | \hat{\mathrm{H}}' | \Psi \rangle &= \langle \Psi | \hat{\mathrm{H}}' | \Psi \rangle + \langle \Psi | \hat{\mathrm{H}}' - \hat{\mathrm{H}} | \Psi \rangle \\ &= E_0 + \int \rho(r)[\upsilon(r) - \upsilon'(r)]\, dr \end{aligned} \tag{3.25}$$

Adding these two equations gives $E_0 + E_0' < E_0' + E_0$. This obvious contradiction means that there are no two different external potentials that can give the same electron density. The energy can then be written as contributions of the electron kinetic energy, electron-nuclei attraction and electron-electron repulsion as a function of the density, as seen before in the Thomas-Fermi model.

$$\begin{aligned} E[\rho(r)] &= T[\rho(r)] + V_{ne}[\rho(r)] + V_{ee}[\rho(r)] \\ &= \int \rho(r)v(r)\,dr + F_{HK}[\rho(r)] \end{aligned} \tag{3.26}$$

As explained above the external potential solely depends on the configuration of the nuclei, and exhibits a one to one correspondence with the electron density, the electron kinetic energy and electron-electron repulsion can then be separated from the external potential and contained within a universal functional $F_{HK}[\rho(r)]$, which only depends on the electron density. However, the functional form of this universal functional is unknown and it still contains the complex electron-electron interactions.

3.3.3.3 Kohn-Sham DFT

The commonly used form in the practical application of DFT comes from the re-introduction of orbitals as an independent particle DFT as suggested by Kohn and Sham[18]. The system is represented as a set of non-interacting electrons in moving within an effective external potential so that the density of the non-interacting system is the same for the interacting real system. The energy of the system can now be written as:

$$E[\rho(r)] = \int \rho(r)v(r)\,dr + T_s[\rho(r)] + E^{Hartree}[\rho(r)] + E_{xc}[\rho(r)] \tag{3.27}$$

The Kohn-Sham formalism represents the energy of the system as that of; the external potential, the kinetic energy of non-interacting electrons (T_s), the classical electron-electron Coulomb repulsion (Hartree energy), and the many-body quantum effects, which are contained within the exchange-correlation energy (E_{xc}). Whilst this increases the complexity of the problem from a 3- to 3^N-variable one, it is advantageous to do so as the majority of the kinetic energy can now be calculated exactly. The effective potential can then be defined as:

$$V^{eff} = \frac{\delta\{\int \rho(r)v(r)\,dr + E^{Hartree}[\rho(r)] + E_{xc}[\rho(r)]\}}{\delta\rho(r)} = v(r) + \int \frac{\rho(r')}{|r-r'|}\,dr' + v_{xc}(r) \quad (3.28)$$

where $v_{xc}(r)$ is the exchange-correlation potential;

$$v_{xc}(r) = \frac{\delta E_{xc}[\rho(r)]}{\delta\rho(r)} \quad (3.29)$$

This gives the following one-electron Schrödinger-like equations:

$$\left[-\frac{1}{2}\nabla^2 + V^{eff}\right]\emptyset_i = \epsilon_i\emptyset_i \quad (3.30)$$

where $\{\emptyset_i\}$ are the Kohn-Sham one-electron orbitals and ϵ_i the respective energies of these orbitals, which gives rise to an independent particle model, like in the Hartree-Fock approach, which needs to be solved iteratively. Whilst this Kohn-Sham DFT approach very closely resembles the Hartree-Fock wavefunction approach, a significant difference is introduced with the inclusion of the exchange-correlation potential, which contains all the non-classical many-body electron-electron effects and not only the exact exchange energy of HF theory.

3.3.3.4 Exchange-Correlation Functionals

Up to this point Kohn-Sham DFT remains an exact theorem; however, the exact form of the exchange-correlation energy functional is unknown and in practice requires approximating. The success of Kohn-Sham DFT is that relatively simple approximations for the exchange-correlation functional yield good results. Expressions for the E_{xc} functional are usually separated into exchange and correlation terms, where ε is the energy density:

$$E_{xc} = E_x[\rho(r)] + E_c[\rho(r)] = \int \varepsilon_x[\rho(r)]\rho(r)dr + \int \varepsilon_c[\rho(r)]\rho(r)dr \quad (3.31)$$

In order to consider exchange and correlation the spin-density must be taken into account. The correlation of electrons of parallel spin will be different from that of electrons with opposite spin, whereas exchange only occurs between electrons of the same spin. The spin polarisation can be given in terms of the spin density (ζ);

$$\zeta = \frac{\rho_\alpha(r) - \rho_\beta(r)}{\rho_\alpha(r) + \rho_\beta(r)} \tag{3.32}$$

Exchange-correlation energy functionals are categorised according to their complexity; three commonly used types of E_{xc} functional will be discussed further: (i) the local density approximation (LDA), (ii) generalised-gradient approximations (GGA), and (iii) hybrid functionals.

(i) The local density approximation (LDA)

Under the local density approximation a real inhomogeneous system is divided into infinitesimal volumes, in which the electron density is regarded to be constant. The exchange-correlation energy for each volume is then given by the exchange-correlation energy of the uniform electron gas (UEG) for that density[19]. The total LDA exchange-correlation energy is given by:

$$E_{xc}^{LDA}[\rho] = \int \rho(r)\, \varepsilon_{xc}^{UEG}\big(\rho(r)\big)\, dr \tag{3.33}$$

The exchange energy of the UEG is known exactly and is described as:

$$E_x^{LDA}[\rho] = -\frac{3}{4}\left(\frac{3}{\pi}\right)^{1/3} \int \rho^{4/3}(r)\, dr \tag{3.34}$$

However, there is no known expression for the correlation energy. The correlation energy is usually obtained by fitting to the quantum Monte Carlo data for the correlation energy density calculated in the work of Alder and Ceperley[20]. The LDA is strictly only valid for systems with slowly varying densities and works well for describing metals. Part of the success of the LDA in this regard is due to a systematic error cancellation, as the LDA underestimates correlation but overestimates exchange for inhomogeneous systems. Whilst the LDA performs well for metals it overestimates binding energies of molecules and cohesive energies of solids as well as underestimating lattice constants. Furthermore, weakly bonded van der Waals and hydrogen-bonded systems are not well described.

(ii) The Generalised Gradient Approximation (GGA)

The LDA is the simplest possible approximation to the exchange-correlation energy and it is understood that the local uniform density at each point is not sufficient for describing the rapidly varying electron density of inhomogeneous systems; as such the gradient of the density ($\nabla\rho(r)$) is included into exchange-correlation functionals. The first attempt to include the density

gradient was in the gradient expansion approximation (GEA), in which the exchange-correlation energy at a given point is expressed as a Taylor expansion including the density and higher derivatives of the density:

$$E_{xc} = \int (\rho(r), \nabla\rho(r), \nabla^2\rho(r), \dots)\varepsilon_{xc}(r)\ dr \tag{3.35}$$

However, it was found that a direct implementation of the GEA actually worsened performance compared to the LDA[21]. Methods were then developed to include the gradient of the density in a more general way, giving rise to generalised gradient approximation (GGA) functionals in which terms involving the gradient are introduced as a correction term to the LDA[22]. For example the general form of GGA exchange-correlation energy functionals is:

$$E_{xc}^{GGA}[\rho] = \int f^{GGA}(\rho(r), \nabla\rho(r))\ dr \tag{3.36}$$

in which, f^{GGA} is the GGA-functional dependent on both the density and the density gradient. Within the GGA the exchange energy is given by:

$$E_x^{GGA}[\rho] = \int \rho(r)\varepsilon_x^{UEG}\big(\rho(r)\big)\, F_x^{GGA}(s)\ dr \tag{3.37}$$

The GGA exchange energy comprises the original LDA exchange energy multiplied by an exchange 'enhancement' factor, determined by the choice of GGA functional, which depends on the dimensionless reduced gradient (s):

$$s = \frac{|\nabla\rho(r)|}{2(3\pi^2)^{1/3}\rho(r)^{4/3}} \tag{3.38}$$

Furthermore, the Perdew-Burke-Ernzerhof (PBE)[23] functional used in this thesis has the following functional form for the exchange energy:

$$F_x^{PBE}(s) = 1 + a - \frac{a}{(1 + bs^2/a)} \tag{3.39}$$

where (a) and (b) are physically derived parameters. The functional form for the gradient corrected correlation energy is given by the LDA correlation energy with the addition of an enhancement factor, which similarly is a complex function of the dimensionless gradient (s).

(iii) Hybrid Functionals

Hybrid functionals represent a further advancement to the exchange-correlation energy functional form in which a portion of 'exact' exchange energy from the Hartree-Fock functional is added to a typical DFT exchange-correlation functional. The hybrid exchange-correlation energy functional is given by[24]:

$$E_{xc} = \int_0^1 U_{xc}^{\lambda}\, d\lambda \tag{3.40}$$

where λ is an interelectronic coupling strength parameter, which turns on the electron-electron Coulomb repulsion, and U_{xc}^{λ} is the potential energy of exchange and correlation at λ. This expression connects the non-interacting reference system with the fully interacting system with density $\rho(r)$. The full Hartree-Fock exchange is given at $\lambda = 0$ (the non-interacting limit); therefore it is expected that incorporating a fraction of exact exchange will improve LDA and GGA exchange-correlation functionals. The quantum chemistry hybrid functional B3LYP has three parameters that control the mixing of HF exchange and DFT exchange and correlation, which are determined by fitting to experiment, and has the following form:

$$E_{xc} = E_{xc}^{LDA} + a_1(E_x^{HF} - E_x^{LDA}) + a_2\Delta E_x^{GGA} + a_3\Delta E_c^{GGA} \tag{3.41}$$

A popular reformulation of this gives the basis of many hybrid GGA functionals of the form:

$$E_{xc} = E_x^{GGA} + a(E_x^{HF} - E_x^{GGA}) \tag{3.42}$$

in which $a = 0.25$, so that the functional contains 25% HF exchange, based on perturbation theory. For example when using this in conjunction with the PBE–GGA functional we get the hybrid PBE0 functional.

Although DFT is in principle an exact theory there are a number of problems encountered in its application, the biggest of which is the excessive delocalisation of electrons as a result of the self-interaction error that arises from the approximate exchange-correlation functionals used. This self-interaction error leads to the underestimation of material band-gaps, barriers to chemical reactions, and charge transfer excitation energies. The origin of this error is due to the electron-electron Coulomb repulsion term, in the Kohn-Sham Hamiltonian this term is a functional of the electron density, but since each individual electron contributes to the electron density an electron interacts with, and 'repels', itself giving a non-zero Coulomb term for a one-electron system. An exact exchange-correlation functional would cancel this self-interaction but

this does not occur in LDA or GGA functionals. Hybrid functionals contain some degree of self-interaction cancellation as a portion of the exact HF exchange is added in.

3.3.4 Electronic Structure of Periodic Solids

Periodic solids can be thought of as extended systems with an infinite number of electrons and nuclei. They are considered to consist of a unit cell, the smallest motif that describes the entire symmetry of the system, repeated periodically in all directions. This inherent periodicity of solids is vital to both the concept and practice of solid-state electronic structure theory and calculations.

3.3.4.1 Plane Waves

The foundation of solid-state DFT is based upon Bloch's Theorem[3], which states that in a periodic potential ($U(r)$), where $U(r+R) = U(r)$ and R is the Bravais lattice vector, the eigenfunctions of a single-electron Hamiltonian $\hat{\mathrm{H}} = -\frac{1}{2}\nabla^2 + U(r)$ can be written as the product of a plane wave and a function that has the same periodicity of the potential:

$$\phi_{n,k}(r) = e^{ik\cdot r}\mu_{n,k}(r) \tag{3.43}$$

Here $e^{ik\cdot r}$ is the plane wave, and $\mu_{n,k}(r)$ is a function where $\mu_{n,k}(r+R) = \mu_{n,k}(r)$. The index *n* is a second quantum number and *k* represents the set of plane waves within each unit cell.

3.3.4.2 K-points

Whilst Bloch's Theorem allows the electronic wavefunction to be expanded as a discrete set of plane waves, for an infinite system an infinite number of k wave-vectors are required to represent the infinite number of electrons. However, in an infinite periodic system the k-point spacing goes to zero and k becomes a continuous variable. Furthermore, it is the occupied states at each k-point that contribute to physical properties such as the electronic potential, electron density, and total energy. The small spacing between electronic wavefunctions at k-points that are very close together means that these wavefunctions will be very similar, it is therefore possible to represent a region of k-space by evaluation of a single k-point. This allows for calculating only a finite number of k-points in the regime of k-point sampling. Integration over the 1st Brillouin zone (the reciprocal space unit cell) provides a way to calculate the electron density in computational DFT. To increase computational efficiency the integral is approximated as a sum over selected k-points. An accurate representation is achieved by sampling select points as the wavefunction varies smoothly in reciprocal space. A regular mesh of k-points in

reciprocal space can be used for the sum and an efficient method for generating k-point meshes was provided by Monkhorst and Pack[25,26]. Errors obtained in the total energy due to inadequate k-point sampling can be reduced to zero by using a denser k-point mesh, it is therefore important to test the convergence of results with k-point sampling.

3.3.4.3 Cutoff Energy

The periodic function $\mu_{n,k}(r)$ can be expanded with plane waves whose wave vectors are reciprocal lattice vectors (G) of the periodic lattice:

$$\mu_{n,k}(r) = \sum_{G} C_{n,G}\, e^{iG\cdot r} \tag{3.44}$$

allowing the electronic wavefunction to be written as:

$$\phi_{n,k}(r) = \sum_{G} C_{n,k+G}\, e^{i(k+G)\cdot r} \tag{3.45}$$

Similarly when solving the one-electron Kohn-Sham equations within a periodic effective potential the Kohn-Sham wavefunction can be expanded with plane wave basis sets and these Kohn-Sham equations can be rewritten as:

$$\sum_{G} \left[\frac{1}{2}|k+G'|^2\delta_{G,G'} + V^{eff}(G-G')\right] C_{n,k+G'} = \epsilon_n C_{n,k+G} \tag{3.46}$$

where $\delta_{G,G'}$ is the Kronecker δ and reflects that the kinetic energy is diagonal. The sum over G' requires an infinite number of G wave vectors but the coefficient $C_{n,k+G}$ is typically more important for plane waves with small kinetic energy than those with large kinetic energy. The set of planes waves can then be truncated to only include those with a lower kinetic energy than some cutoff (E_{cut}).

$$\frac{1}{2}|k+G|^2 \leq E_{cut} \tag{3.47}$$

These G vectors are chosen as a set of points on a regular grid in reciprocal space and summing over a finite number of G vectors yields a sufficiently accurate answer. However, like k-points the kinetic energy cutoff must be converged with respect to the properties of the system, i.e. the total energy.

3.3.5 Pseudopotentials

When studying chemistry and condensed matter physics the most important interactions are those of valence electrons. Whilst plane waves provide a good representation for the valence states, core electrons do not have a free-electron-like wavefunction. The strong Coulomb potential of the nuclei on core electrons and the orthogonality requirement cause rapid oscillations of the wavefunction in the core region. An accurate description of this varying core wavefunction would require huge numbers of plane waves. A practical solution to this is the introduction of pseudopotentials, by replacing the nuclei and core electrons by an effective potential felt by the valence electrons, pseudopotentials serve to increase the computational efficiency of a calculation by both reducing the number of electrons in the calculation and requiring fewer plane waves to describe the core region. A schematic representation of the pseudopotential method is given in figure 3.3.

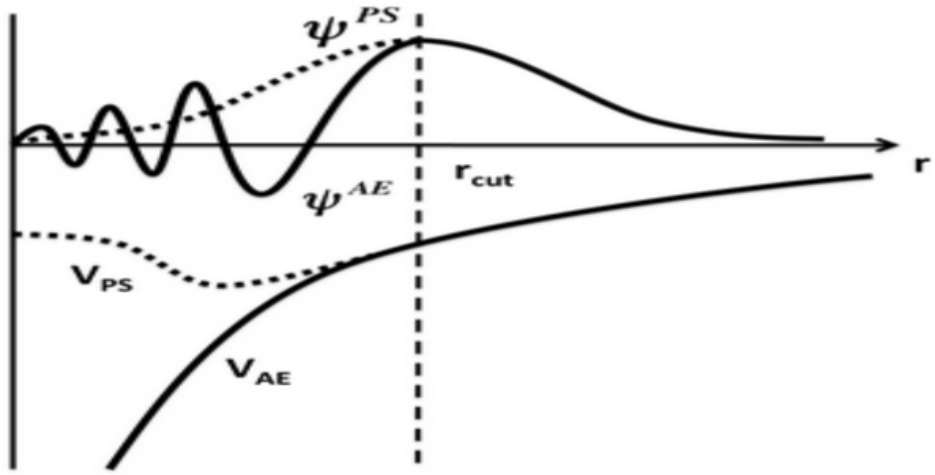

Figure 3.3. Schematic representation of the pseudo-potential and pseudo-wavefunction (dashed lines) and their all-electron counterparts (solid lines). Both the pseudo and all-electron parts display the same behavior after r_{cut} the 'core' cutoff radius. Reproduced from reference [27].

3.3.5.1 Projector Augmented Wave Pseudopotentials

The projector augmented wave (PAW) scheme developed by Blöchl[28,29] is an all-electron approach to treating the core and valence wavefunction, and is the pseudopotential form used in calculations carried out within this thesis. In the PAW method space is divided into atom-centred augmentation spheres and a bonding valence region outside the spheres. It works by mapping a smooth auxiliary wavefunction onto the true all electron wavefunction through the use of a linear transformation within the augmentation sphere and projecting the smooth pseudo

valence wavefunction into the core region. This method operates under a frozen-core principle in which the core electrons are unaffected by bonding.

3.4 Energy Minimisation Methods

The Global potential energy surface (GPES) is a representation of all possible ways of arranging the species of a given system and their corresponding potential energy. This can be considered as forming a multidimensional hyper-surface, with as many dimensions as there are degrees of freedom in the system. Different features of this hyper-surface determine important features of the system; any minima represent stable or meta-stable states, the global minimum corresponds to the most stable configuration of atoms possible, and saddle-points represent transition-states between two minima. Energy minimisation takes a given input structure and attempts to find minima on the energy hyper-surface, which will typically be a local minimum on the (GPES) that is closest to starting coordinates. The location of the global minimum requires exploring the entire hyper-surface, which is practically impossible. However various global optimisation techniques are used in order to sample the GPES, although these cannot guarantee finding the global minimum and still present a considerable challenge.

Energy minimisation will typically involve the calculation of the energy of the system with initial atomic coordinates before using the derivative of a small move in coordination space or the net forces on the ions to determine the search direction to generate a new set of coordinates and re-evaluate the energy. For any given atomic coordinate positions the internal energy can be considered as the following Taylor expansion[2]:

$$U(x + \delta x) = U(x) + \frac{\partial U}{\partial x}\,\delta x + \frac{1}{2!}\frac{\partial^2 U}{\partial x^2}\,(\delta x)^2 + \ldots \tag{3.48}$$

where the first derivative is the gradient (g) and the second derivative describes the curvature (rate of change of the gradient) of the GPES referred to as the Hessian matrix (H).

3.4.1 Steepest Descent

The steepest descent algorithm is a first order minimisation technique[2], which involves calculating the energy and the gradient, and using the gradient to determine the direction of movement. A line search is then used to determine the magnitude of the step length by considering points in a line from the initial coordinates, all of the energies along the direction of the line are determined and the gradient is recalculated from the new minimum. This process is repeated until convergence, although it is known to be inefficient as all previous information gained about the hyper-surface is ignored and whilst this is a good method for minimising

systems which are far away from the minimum, convergence for systems close to the minimum is slow as the line searches oscillate about the minimum.

3.4.2 Conjugate Gradients

The conjugate gradient algorithm[2] is similar to that of the steepest descent method, and actually will use the same 'steepest' gradient as the initial step, although instead of performing subsequent line searches along the next steepest gradient to the previous search direction the 'history' of the searches are 'remembered' and the new search direction is taken as orthogonal to the previous search vectors. This allows for much more efficient convergence than the steepest descent method. Furthermore, for a quadratic energy surface with N variables the conjugate gradient method will converge to the minimum in N steps.

3.4.2 Newton-Raphson

The Newton-Raphson method[2] expands the energy minimisation step to include both the gradient and the curvature of the hyper-surface, with the displacement vector (Δx) from the current position to the minimum given by:

$$\Delta x = -\alpha H^{-1} g \tag{3.49}$$

where α is a scalar used to ensure that a minimum is found instead of a maximum. The gradient, g, identifies the direction of the search and the curvature is used to determine where the function passes through a minimum along that direction. Here the calculation of the Hessian matrix of second derivatives, H, is the most computationally expensive step, so 'Quasi-Newton-Raphson' methods are employed whereby full calculation of the Hessian matrix is not required at each step but only when triggered by the following criteria: (i) a maximum number of cycles for updating has been exceeded, (ii) the angle between the gradient vector and the search vector exceeds a given threshold, (iii) the energy has dropped by more than a certain threshold in one cycle, meaning the curvature is likely to have changed, or (iv) the energy cannot be lowered by line minimisation along the current search vector.

3.5 Transition State Finding

Catalysis is very much dependent on identifying rates of reactions, which in turn require elucidating transition states and reaction pathways of molecules. In this study the nudged-elastic band (NEB) method[30] is adopted in an attempt to find the transition states and activation barriers to processes of interest. The NEB method is an efficient way for finding the minimum energy pathway (MEP) between the initial and final state of a transition. It takes starting and end

points of a process and creates a series of images in-between the two via a linear interpolation of the input geometries. A spring-like force is added to join neighbouring images in order to maintain the spacing between images, preventing them from relaxing to the same minimum. The perpendicular component of the spring and the parallel component of the true force are projected out during the minimisation of the elastic band. This forces the images to follow the minimum energy path by minimizing in all directions except that of the principle reaction path. This also ensures that band follows a continuous path even when more than one MEP is present. The NEB concept is represented pictographically in figure 3.4.

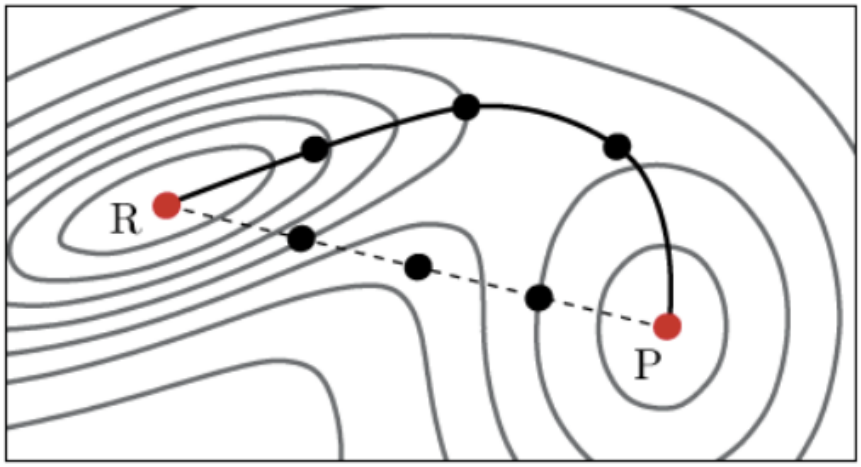

Figure 3.4. NEB pathway schematic, showing the linear interpolation between starting and final states (dashed line) and the MEP the band relaxes to (solid line) reproduced from [31].

The climbing-image NEB[32] method is a refinement of the NEB and coupled with an improved tangent definition[33], the transition state can be more accurately calculated. In this approach after a few iterations of the normal NEB the force on the highest energy image is inverted. The remaining images converge to MEP whilst the image with the highest energy is forced upwards in energy to the saddle-point.

3.6 Symmetric Vacuum Slabs

Symmetric vacuum slab models are employed for the surface calculations in this thesis in order to cancel out any cross-slab dipoles introduced by the surface adsorption of molecules. When performing surface calculations using periodic DFT codes the situation that arises is one of having infinite ‘layers’ of an infinitely wide two dimensional slab with a vacuum spacing separating the slab layers, with each slab having two surfaces exposed to the vacuum. The adsorption of a molecule on one surface of the slab will introduce a cross-slab dipole. Due to the periodicity of the surface supercell the effect of the dipole becomes exacerbated and manifests in the electrostatic potential of the vacuum layer not being flat and not having a characteristic

'potential jump' in the vacuum layer[34]. Symmetrically adsorbing molecules on either surface of a slab will cancel out the effects of the dipoles introduced, however dipole correction schemes[35,36] are also provided by many DFT codes for the case of adsorbing molecules on just one side of the slab. These dipole corrections enforce the flat nature of the vacuum electrostatic potential. Whilst the symmetric adsorption of molecules will cancel out the introduced dipole without requiring any enforcement of the behaviour of the electrostatic potential, it is worth noting that additional complexities will be introduced when considering nudged elastic band calculations due to the presence of two unstable modes within the simulation cell.

3.7 DFT and YSZ

The choice of DFT functional and level of theory used is something that must be carefully considered when undertaking computational studies. The well-known self-interaction error of GGA DFT can present a number of problems depending on the system being studied. In the mean-field treatment of electrons in the independent particle formalism of Kohn-Sham DFT an electron will un-physically repel itself to some extent. This self-interaction causes electrons to delocalise excessively, which will therefore impact upon the study of any systems in which electron localisation is important. Two approaches that can be undertaken in order to mitigate the effects of electron self-interaction are: (i) the use of hybrid functionals, and (ii) the DFT+U approach. Hybrid functionals, as discussed in section 3.3.3.4, include a portion of the Hartree-Fock exchange, resulting in self-interaction error cancelation, and as such allow for electrons to remain localised. In the DFT+U approach[37,38] electron localisation is made possible by the addition of a Hubbard-like U term to the standard GGA functional, which in effect penalises partial orbital occupancy thus serving to reduce excessive electronic delocalisation.

Furthermore, there are additional considerations that require careful treatment when studying catalysis on oxides. Due to the Mars-van Krevelen nature of catalysis on oxides, whereby lattice oxygen is incorporated into reaction products and replaced by the dissociation and incorporation of molecular oxygen, the oxygen vacancy formation energy (and the nature of the oxygen vacancy) of the oxide material as well as the description of the diatomic oxygen bond will be important when evaluating the energies of catalytic pathways. Firstly, standard GGA-DFT overestimates the oxygen-oxygen bond strength[39], which is important to keep in mind considering reaction enthalpies. Secondly, the nature of the oxygen vacancy created by oxygen atom removal can have a profound impact on the system if the incorrect DFT method is used. For example in the reducible oxides TiO_2 and CeO_2, oxygen vacancy formation via oxygen atom removal gives rise to a change in oxidation state of the metals. Two Ti^{4+} and Ce^{4+} cations become Ti^{3+} and Ce^{3+} ions, the two electrons left over from oxygen atom removal are each localised on one metal centre. However, within standard GGA-DFT these electrons are delocalised over more than one metal centre and are hence unrepresentative of the real

situation. In the cases of TiO_2 and CeO_2 reduction, hybrid functionals and the DFT+U regime respectively have been used in order to preserve the correct electron localisation[39]. Unlike the case for reducible oxides, oxygen vacancy formation in irreducible oxides, such as MgO, leads to the excess electrons from oxygen atom removal remaining 'trapped' in the lattice site from where the oxygen has been removed. The correct qualitative electronic picture of this system is given by standard GGA-functionals[39]. As seen previously[39] and discussed in chapter 5 of this thesis, ZrO_2 and YSZ have similar oxygen vacancy formation behaviour as the MgO case discussed here and as such standard GGA-DFT will adequately describe the correct qualitative electronic structure of these systems.

3.8 Computer Codes

Density functional theory calculations of bulk materials and catalytic surface studies of chapters 3-6 are carried out using the VASP code (Vienna Ab-initio Simulation Package)[40,41]. The majority of the calculations are carried out using the PBE exchange-correlation functional[23]. The PBE_{sol}[42], PBE_{sol}-0, and HSE06[43] functionals are also used although their use is explicitly stated when this is the case.

Interatomic potentials calculations of bulk zirconia, yttria, and YSZ solid-solutions are carried out using the GULP code (General Utility Lattice Program)[2]. The potentials used to describe the atomic interactions are presented in full in chapter 7.

The solid-solution structure generation and 'basin-hopping' solid-solution mixing operations detailed in chapter 7 are carried out using the KLMC code (Knowledge Led Master Code).

3.9 Calculation Information

Bulk calculations carried out using both the GULP and VASP codes employ periodic boundary conditions in which the unit cell of the calculation input is tessellated in three dimensions and extended to infinity providing the environment for the simulation, which means that any change to the unit cell is replicated in all of the repeating periodic images of the unit cell. Surface calculations carried out in VASP also employ periodic boundary conditions under the vacuum slab model of surfaces. Here the surface can be thought of as an infinite repeating layer of atoms in the unit cell extended in the x- and y-directions, and this layer repeated above and below the surface separated by a vacuum. The vacuum-gap must be large enough so that the top of one slab and bottom of another do not interact with each other. Specific details about the calculation inputs are given in subsequent chapters.

3.10 Computers

Initial DFT surface and bulk calculations, including the vacuum slab system set up, were carried out on the University College London computing clusters ‘Legion’ and ‘Grace’, which typically have 16 CPUs and 64GB RAM per node. The majority of the subsequent surface adsorption calculations were performed on the UK national supercomputing facility ‘ARCHER’, which has 24 CPUs and 64GB RAM per node. A typical surface adsorption calculation would run on 10 nodes for up to 24 hours. Furthermore, whilst interatomic potentials calculations using GULP can be run on single computer cores calculations of the ~10,000 structure ensembles in chapter 7 were performed as sets of independent parallel jobs on ARCHER, and the global optimisation runs performed on Legion.

References:

1. Catlow, C. R. A.; Kotomin, E., *Computational Materials Science*. IOS Press: 2001.
2. Gale, J. D.; Rohl, A. L., The General Utility Lattice Program (GULP). *Molecular Simulation* **2003,** 29, (5), 291-341.
3. Kittel, C., *Introduction to Solid State Physics*. Wiley: 1996; Vol. Seventh Edition.
4. Khan, M. S.; Islam, M. S.; Bates, D. R., Cation doping and oxygen diffusion in zirconia: a combined atomistic simulation and molecular dynamics study. *Journal of Materials Chemistry* **1998,** 8, (10), 2299-2307.
5. Dick, B. G.; Overhauser, A. W., Theory of the dielectric constants of alkali halide crystals. *Physical Review* **1958,** 112, (1), 90-103.
6. Catlow, C. R. A.; Cheetham, A. K.; Day, P., *Solid State Chemistry: Techniques*. Oxford University Press: 1986.
7. Thakkar, A. J., *Quantum Chemistry*. Morgan & Claypool: 2014.
8. Born, M.; Oppenheimer, R., Quantum theory of molecules. *Annalen Der Physik* **1927,** 84, (20), 0457-0484.
9. Hartree, D. R., The wave mechanics of an atom with a non-Coulomb central field Part I theory and methods. *Proceedings of the Cambridge Philosophical Society* **1928,** 24, 89-110.
10. Fock, V., Approximation method for the solution of the quantum mechanical multibody problems. *Zeitschrift Fur Physik* **1930,** 61, (1-2), 126-148.
11. Slater, J. C., Note on Hartree's method. *Physical Review* **1930,** 35, (2), 0210-0211.
12. Scuseria, G. E.; Lee, T. J., Comparison of coupled-cluster methods which include the effects of connected triple excitations. *Journal of Chemical Physics* **1990,** 93, (8), 5851-5855.
13. Strout, D. L.; Scuseria, G. E., A quantitative study of the scaling properties of the Hartree-Fock method. *Journal of Chemical Physics* **1995,** 102, (21), 8448-8452.
14. Tang, K. C.; Edmiston, C., More efficient method for basis transformation of electron interaction integrals. *Journal of Chemical Physics* **1970,** 52, (2), 997-&.
15. Thomas, L. H., The calculation of atomic fields. *Proceedings of the Cambridge Philosophical Society* **1927,** 23, 542-548.
16. Fermi, E., A statistical Method for Determining some Properties of the Atoms and its Application to the Theory of the periodic Table of Elements. *Zeitschrift Fur Physik* **1928,** 48, (1-2), 73-79.
17. Hohenberg, P.; Kohn, W., Inhomogeneous electron gas. *Physical Review B* **1964,** 136, (3B), B864-+.
18. Kohn, W.; Sham, L. J., Self-consistent equations including exchange and correlation effects. *Physical Review* **1965,** 140, (4A), 1133-&.
19. Perdew, J. P.; Zunger, A., Self-interaction correction to density-functional approximations for many-electron systems. *Physical Review B* **1981,** 23, (10), 5048-5079.
20. Ceperley, D. M.; Alder, B. J., Ground-state of the electron-gas by a stochastic method. *Physical Review Letters* **1980,** 45, (7), 566-569.
21. Capelle, K., A bird's-eye view of density-functional theory. *Brazilian Journal of Physics* **2006,** 36, (4A), 1318-1343.
22. Perdew, J. P.; Chevary, J. A.; Vosko, S. H.; Jackson, K. A.; Pederson, M. R.; Singh, D. J.; Fiolhais, C., Atoms, molecules, solids, and surfaces - applications of the generalized gradient approximation for exchange and correlation. *Physical Review B* **1992,** 46, (11), 6671-6687.
23. Perdew, J. P.; Burke, K.; Ernzerhof, M., Generalized gradient approximation made simple. *Physical Review Letters* **1996,** 77, (18), 3865-3868.
24. Becke, A. D., A new mixing of Hartree-Fock and local density-functional theories. *Journal of Chemical Physics* **1993,** 98, (2), 1372-1377.
25. Chadi, D. J.; Cohen, M. L., Special points in brillouin zone. *Physical Review B* **1973,** 8, (12), 5747-5753.
26. Monkhorst, H. J.; Pack, J. D., Special points for brillouin-zone integrations. *Physical Review B* **1976,** 13, (12), 5188-5192.
27. http://cmt.dur.ac.uk/sjc/thesis_dlg/node21.html
28. Blochl, P. E., Projector augmented-wave method. *Physical Review B* **1994,** 50, (24), 17953-17979.

29. Kresse, G.; Joubert, D., From ultrasoft pseudopotentials to the projector augmented-wave method. *Physical Review B* **1999,** 59, (3), 1758-1775.
30. Jonsson; H, Nudged elastic band method for finding minimum energy paths of transitions. In *Classical and Quantum Dynamics in Condensed Phase Simulations*, Mills; G, Eds. World Scientific, 1998; p 385.
31. http://quantumwise.com/documents/manuals/ATK-2008.10/chap.relax.html
32. Henkelman, G.; Uberuaga, B. P.; Jonsson, H., A climbing image nudged elastic band method for finding saddle points and minimum energy paths. *Journal of Chemical Physics* **2000,** 113, (22), 9901-9904.
33. Henkelman, G.; Jonsson, H., Improved tangent estimate in the nudged elastic band method for finding minimum energy paths and saddle points. *Journal of Chemical Physics* **2000,** 113, (22), 9978-9985.
34. Bengtsson, L., Dipole correction for surface supercell calculations. *Physical Review B* **1999,** 59, (19), 12301-12304.
35. Makov, G.; Payne, M. C., Periodic boundary-conditions in ab-initio calculations. *Physical Review B* **1995,** 51, (7), 4014-4022.
36. Neugebauer, J.; Scheffler, M., Adsorbate-substrate and adsorbate-adsorbate interactions of Na and K adlayers on Al(111). *Physical Review B* **1992,** 46, (24), 16067-16080.
37. Liechtenstein, A. I.; Anisimov, V. I.; Zaanen, J., Density-functional theory and strong-interactions - orbital ordering in Mott-Hubbard insulators. *Physical Review B* **1995,** 52, (8), R5467-R5470.
38. Dudarev, S. L.; Botton, G. A.; Savrasov, S. Y.; Szotek, Z.; Temmerman, W. M.; Sutton, A. P., Electronic structure and elastic properties of strongly correlated metal oxides from first principles: LSDA+U, SIC-LSDA and EELS study of UO2 and NiO. *Physica Status Solidi a-Applications and Materials Science* **1998,** 166, (1), 429-443.
39. Pacchioni, G., Modeling doped and defective oxides in catalysis with density functional theory methods: Room for improvements. *Journal of Chemical Physics* **2008,** 128, (18).
40. Kresse, G.; Furthmuller, J., Efficiency of ab-initio total energy calculations for metals and semiconductors using a plane-wave basis set. *Computational Materials Science* **1996,** 6, (1), 15-50.
41. Kresse, G.; Furthmuller, J., Efficient iterative schemes for ab initio total-energy calculations using a plane-wave basis set. *Physical Review B* **1996,** 54, (16), 11169-11186.
42. Perdew, J. P.; Ruzsinszky, A.; Csonka, G. I.; Vydrov, O. A.; Scuseria, G. E.; Constantin, L. A.; Zhou, X. L.; Burke, K., Restoring the density-gradient expansion for exchange in solids and surfaces. *Physical Review Letters* **2008,** 100, (13).
43. Krukau, A. V.; Vydrov, O. A.; Izmaylov, A. F.; Scuseria, G. E., Influence of the exchange screening parameter on the performance of screened hybrid functionals. *Journal of Chemical Physics* **2006,** 125, (22).

Chapter 4

Water Adsorption on YSZ

Chapter 4 presents the first computational results obtained in this thesis. The bulk system is discussed briefly in relation to initial parameter screening before the additional complexity of surface systems are discussed. The development of the surface model used throughout the next three chapters is presented – a novel approach for YSZ surface study that attempts to address some of the limitations of previous models. Finally water adsorption on the YSZ surface is investigated; the presence of vacancy-vacancy interactions in this new surface model reveals a very strong dissociative adsorption of water.

4.1 Introduction

The results section of this thesis begins by investigating the adsorption of water at the surface of YSZ. Water adsorption on YSZ is of interest for a number of reasons; chiefly in relation to the theme of the thesis, as discussed in chapter 1, water is a primary product of methane partial oxidation and also displays interesting behaviour in stabilising surface formaldehyde species and increasing product selectivity towards syngas[1]. Furthermore, water is produced at the anode of solid oxide fuel cells, so understanding the interaction of water with YSZ is both of direct relevance to the catalytic chemistry evaluated in this thesis as well as of fundamental importance in SOFC processes. Studying water adsorption on the YSZ surface also provides some degree of benchmarking for the surface models used, as there is existing literature for the adsorption of water onto pure zirconia surfaces. Prior to the investigation of water adsorption, details about the development of the model will be given.

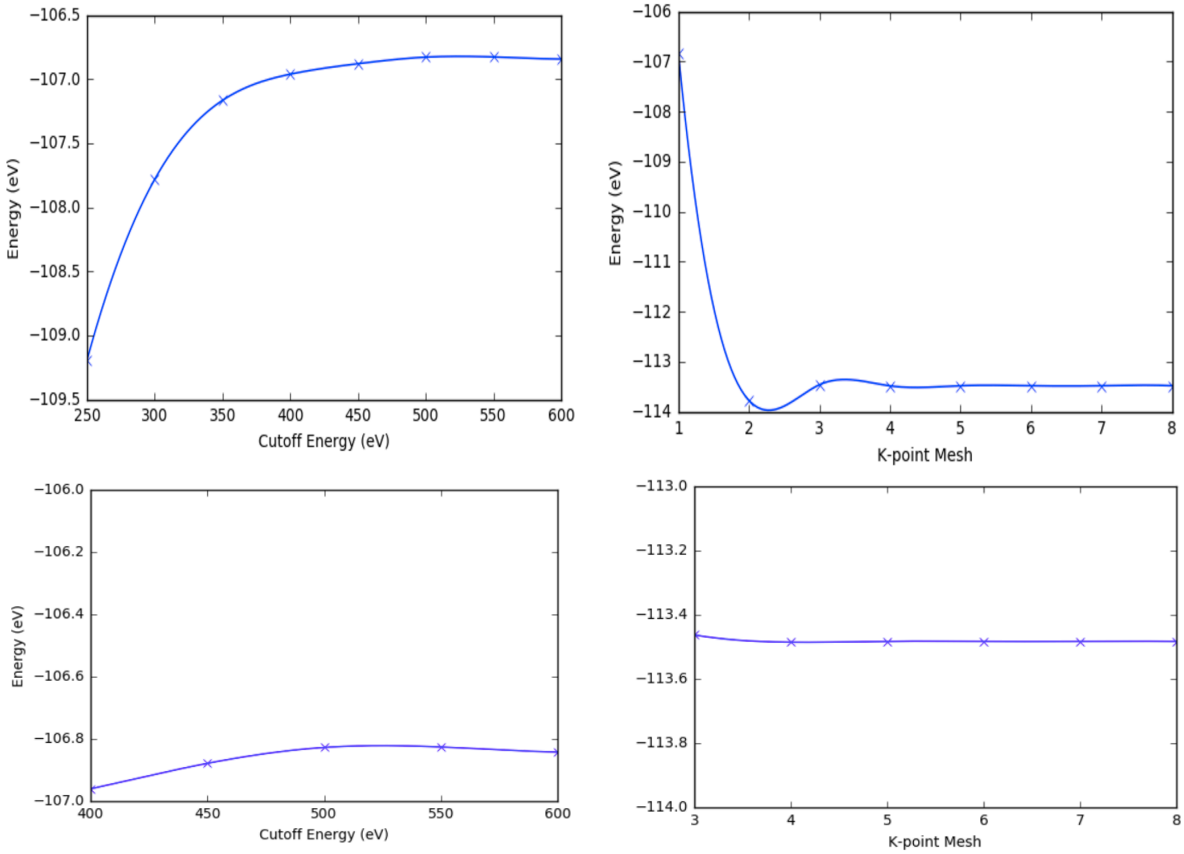

Figure 4.1. Unit cell energy as a function of; plane-wave cutoff energy (left) and k-point mesh density (right), with magnifications of the 'convergence regions' given below. A value of '2' for the k-point mesh represents a 2x2x2 Monkhorst-Pack k-point grid.

4.2 Convergent Parameters

When performing plane-wave DFT calculations there are a number of parameters that must be optimised to ensure that the system is being described properly. It is important to check the convergence of these adjustable parameters; for example one must find the minimum settings to be used in order that increasing the basis-set size or the density of the k-point mesh used does not change the properties obtained from the calculations. The convergence of both increasing plane-wave cutoff energy and k-point mesh for the pure ZrO_2 cubic unit cell is presented in figure 4.1. Unless otherwise stated, all DFT calculations are carried out using the PBE exchange-correlation functional within the VASP code.

4.3 Bulk ZrO_2 Properties

On the basis of the parameter convergence calculations a 4x4x4 k-point mesh and a plane wave cutoff energy of 500 eV were selected as the minimum parameters for subsequent calculations. The unit cell lattice parameter of pure cubic zirconia was optimised under these conditions and the results are compared with experimental and previous computational values in table 4.1. The structural properties obtained with interatomic potentials match closest with the experimental values, and although the GGA-DFT functionals overestimate the lattice parameter slightly, the agreement between the DFT studies is very good.

Property	Experiment[2]	Interatomic Potentials[2]	DFT (GGA-PW91)[3]	DFT – This study (GGA-PBE)
Lattice parameter (Å)	5.070	5.076	5.123	5.123
Zr-Zr distance (Å)	3.589	3.589	3.622	3.627
Zr-O distance (Å)	2.204	2.189	2.218	2.221
O-O distance (Å)	2.563	2.538	2.561	2.565

Table 4.1. Comparison of unit cell lattice parameter and atomic geometry properties obtained from this study with previous experimental and computational results.

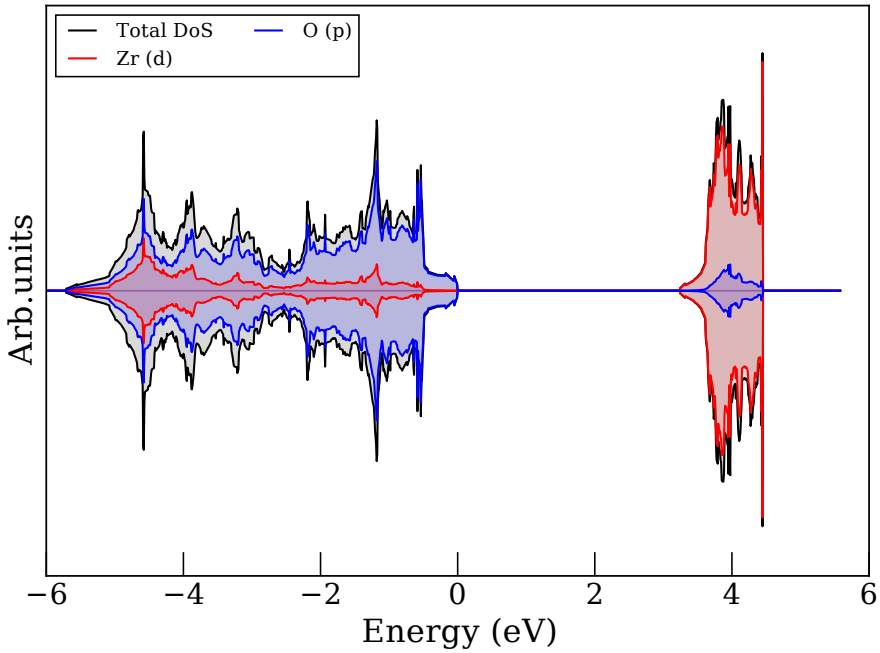

Figure 4.2. Cubic ZrO_2 unit cell valence electron density of states.

The density of states for the valence electrons of the pure cubic ZrO_2 unit cell is given in figure 4.2. The valence band is comprised mostly of oxygen 2p states whilst the conduction band consists mainly of zirconium 3d states. The Fermi-level of the material is set to zero in figure 4.2 showing that the conduction band contains only unoccupied states. The calculated band gap of 3.24 eV is lower than that of the experimentally determined values of ~ 4-6 eV dependent on the experimental method used in order to determine the band gap[4,5]. However, the value calculated here is in good agreement with other calculated results using similar techniques; Xia *et al.*[6] obtain a band gap value of 3.22 eV using plane wave DFT and the PW91-GGA functional, whilst Ricca *et al.*[7] calculate a value of 3.81 eV using the PBE-GGA functional with an all-electron Gaussian function basis-set as implemented in the CRYSTAL code. The under-estimation of band gaps is a well-known issue with using GGA-DFT, and although the calculated band gap is smaller than the experimental band gap the wide-gap insulating nature of the zirconia material is preserved.

4.4 Surface Models

The primary focus of the research carried out within this thesis concerns the surface reaction mechanism of the catalytic partial oxidation of methane on YSZ. In order to conduct this research, the interaction, oxidation, and decomposition of a range of molecules, involved in the CPOM mechanism, with the surface will need to be calculated, requiring a YSZ surface model

representative of the behaviour of real surfaces, and that is large enough to accommodate these adsorption and oxidation processes whilst negating any spurious interactions between periodic images of these molecules. A number of computational studies have investigated the adsorption of molecules on the YSZ surface[8,9,10]. In these studies, the oxygen-terminated cubic-(111) surface is investigated, which has been shown experimentally to dominate the surface morphology of YSZ, as it is the most stable surface plane[11]. Similar models are used in all of these studies; they consist of a (2x2) surface supercell containing 12-ZrO_2 formula units (36 atoms) arranged over three oxygen-zirconium-oxygen tri-layers (9-atomic layers), with the bottom three or four atomic layers fixed to bulk positions and a vacuum gap of ~10Å. These fixed slab-systems are ~7.25Å wide in the a- and b- crystallographic directions and have a slab thickness of ~7.5Å, a dopant concentration of 9.09 mol% Y_2O_3 is achieved through the introduction of one Y-V-Y dopant cluster. Whilst these models have been used to good effect there are a number of drawbacks due to the small system size; (i) the small surface area of the slab prevents the adsorption of multiple molecules on the surface without the possibility of interactions between periodic images occurring, (ii) the adsorption of a molecule on one side of a fixed-slab model introduces a dipole across the cell which can lead to artefacts being introduced into the calculations as a result of the periodic boundary conditions, (iii) fixing the bottom atomic layers can introduce strain into the system by preventing long-range relaxation effects, and (iv) although an industrially relevant dopant concentration is achieved by the introduction of one dopant cluster, this forms a highly ordered system in which vacancies and dopant yttrium atoms are repeated periodically, which is unlikely to represent real YSZ surfaces.

4.4.1 Fixed Slab Models

Despite the above mentioned limitations of small fixed-slab models for representing the YSZ system, pure zirconia fixed-slab models of the cubic-(111) surface were investigated in relation to a number of key quantities which much be considered when performing surface calculations. In all of the fixed slab calculations performed here, the lowest atomic tri-layer was kept fixed with all other atoms allowed to relax. The size of the vacuum gap, the surface energy and the surface adsorption of a water molecule were investigated in a (2x2) surface expansion model. The total energy of a 3 tri-layer system was found to converge with a vacuum gap distance of 15Å, whilst the surface energy of the system and the adsorption energy as a function of the number of tri-layers in the slab are displayed in figure 4.3. The surface energy is calculated as:

$$E_{surface} = \frac{E_{slab} - nE_{bulk}}{2A} \tag{4.1}$$

whereby nE_{bulk} gives the corresponding energy for the same number of formula units contained within the surface slab model when compared to the bulk unit cell, and A is the surface area of the slab. The adsorption energy is calculated as:

$$E_{ads} = E_{surface+adsorbate} - (E_{surface} + E_{adsorbate}) \quad (4.2)$$

We see from figure 4.3 that there is only a very small variation in the surface energy with increasing numbers of surface layers. The surface energy is calculated to be ~0.855 J/m^2, which is lower than previously calculated values of 1.119[12], 1.488[13] or 1.450[7] J/m^2 for the cubic-(111) surface. However, it is worth noting that these previous studies all use different DFT functionals at different levels of theory, and that these functionals are different from the PBE functional used in this study. Details of these systems are provided in table 4.2, additionally it is worth noting that in this work the surface energies were calculated for a 2x2 surface expansion whereas the other studies in question used unit cell surface systems. Furthermore, the work of Ricca *et al.* shows the difference in the surface energy calculated for tetragonal-(101) surface using the PBE or hybrid PBE0 functional can be ~0.5 J/m^2. The surface energy obtained in this work using the PBE0 functional for the 3 tri-layer surface is 1.13 J/m^2, giving a difference to the PBE surface energy of ~0.3 J/m^2 which is in line with what has been observed previously.

Reference:	Surface	Surface Energy (J/m^2)	Functional and potential type
This work	6L – c(111)	0.855	PBE/PAW
	6L – c(111)	1.13	PBE-0/LCAO
[6]	6L – t(101)	1.512	PBE-0/LCAO
	6L – t(101)	1.090	PBE/PAW
	5L – c(111)	1.450	PBE-0/LCAO
[11]	5L – c(111)	1.119	LDA/PAW
[12]	5L – c(111)	1.488	HF/LCAO

Table 4.2. Surface energies of different ZrO_2 surface systems, and the functional and pseudopotential type for each calculation. 6L refers to 6 surface tri-layers, c(111) is the cubic(111) surface and t(101) the tetragonal(101) surface. LCAO and PAW are linear combination of atomic orbitals and projector augmented wave respectively.

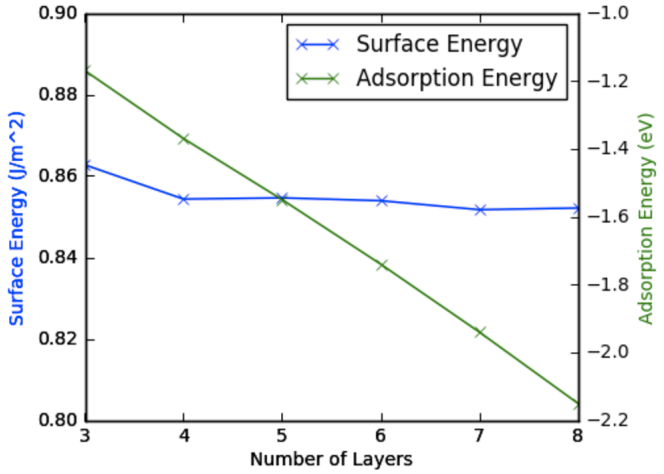

Figure 4.3. Surface energy and water adsorption energy as a function of the number of tri-layers in the surface model for the cubic-(111) surface of pure ZrO_2.

In contrast to the surface energy, the adsorption energy of one molecule of water onto the surface diverges with increasing slab thickness. This divergence of adsorption energy with number of layers appears counter-intuitive. However, upon examination of the resultant geometries after water adsorption one can see that there is a large degree of oxygen anion sub-lattice distortion as oxygen ions move off the ideal cubic lattice sites. As discussed in chapter 2, at low temperature ZrO_2 adopts a monoclinic structure whilst the high-temperature cubic phase is not stable under ambient conditions. The relaxation of the oxygen sub-lattice observed here, induced by water adsorption, allows the system to adopt the more thermodynamically favourable monoclinic/tetragonal forms in opposition to the cubic form, which is artificially enforced in the simulation. Increasing the slab thickness allows for more oxygen relaxation towards a more stable form, which explains the divergence of the adsorption energies. From these initial calculations, it is apparent that obtaining reliable molecular adsorption energies on pure cubic ZrO_2 is non-trivial due to the nature of zirconia, and whilst doping with yttria stabilises the cubic phase the exact method of this stabilisation is not clear, and further complexity is added into the surface systems when introducing dopant yttrium atoms and oxygen vacancies.

4.4.2 Symmetric Slab Models

The surface models used in this thesis are a new approach for YSZ, which aim to negate the limitations of small fixed-slab models mentioned above. We have developed symmetric slabs which are a (4x4) surface supercell expansion containing 96 ZrO_2 formula units (288 atoms, 6 tri-layers) with a slab thickness of 16.36 Å and a vacuum separation of 15 Å between the periodically repeated slabs. The slab width is ~14.6Å and all of the atoms in the model are relaxed. Calculations on the large symmetric YSZ slab models were carried out with a 1x1x1 k-

point mesh, geometric updates were performed when the electronic energy difference subsequent electronic optimisation steps was $<1x10^{-5}$ eV, and calculations were deemed converged when the forces on each ion were <0.02 eV/Å. Large symmetric slabs can allow for the adsorption of multiple molecules without periodic images interacting, whilst cancelling out cross-slab dipoles induced by molecular adsorption. Allowing all atoms to relax also prevents strain being introduced from artificially fixing atom positions. However, in order to maintain the same 9.09 mol% Y_2O_3 dopant concentration, 8 Y-V-Y defect clusters are required. Vacancy-vacancy interactions in YSZ are not well understood in the bulk material let alone in surface systems and the system size is too large to explore comprehensively; the vacancy distribution is therefore, at this stage, guided by an extrapolation of the experimental evidence that vacancies reside in the NNN position to yttrium ions, as discussed in sections 2.4.1 and 2.4.2. The issue of vacancy-vacancy interactions in realistic systems of YSZ is discussed in depth in chapter 7. In the first instance, a number of different symmetric slab surface models are created with unordered dopant cation and vacancy arrangements. The energies of these systems, after structural optimisation, span a range of ~2.2 eV. A model was then created in which the vacancy and dopant yttrium ions are placed in periodically repeating locations, as would be the case if the smaller slabs used previously and described above were periodically repeated as they are in calculations under periodic boundary conditions. Interestingly this highly-ordered system is found to be the lowest energy one, a further 3 eV more stable than the lowest energy unordered structure. However, as previously mentioned this highly-ordered system is unlikely to represent realistic YSZ sample, and furthermore, as is discussed in chapter 7, it has been argued that in reality the energetic ground-state of YSZ is unlikely to ever be attained.

The highly-ordered model and one of the unordered systems were then selected for further study, these surface models are described in detail below. The surface models used are shown in figure 4.4. The multi-region slab model, unordered system, allows for a variety of surface topologies to be described as it contains; (i) an isolated sub-surface vacancy, (ii) surface regions free from vacancies and (iii) a vacancy 'cluster' region to probe the effect of vacancy-vacancy interactions. Whereas the periodic vacancy model, highly-ordered system, maintains the same dopant concentration as the multi-region model, but only contains one type of defect topology. In this case four isolated sub-surface vacancies, with oxygen vacancies in NNN to yttrium ions, are repeated periodically across the surface. It is important to note that for both slab systems described here, only stoichiometric oxygen vacancies, resulting from charge compensation due to the aliovalent doping of Y^{3+} onto Zr^{4+} sites, are considered. Vacancies formed as a result of surface reduction are investigated in chapter 5.

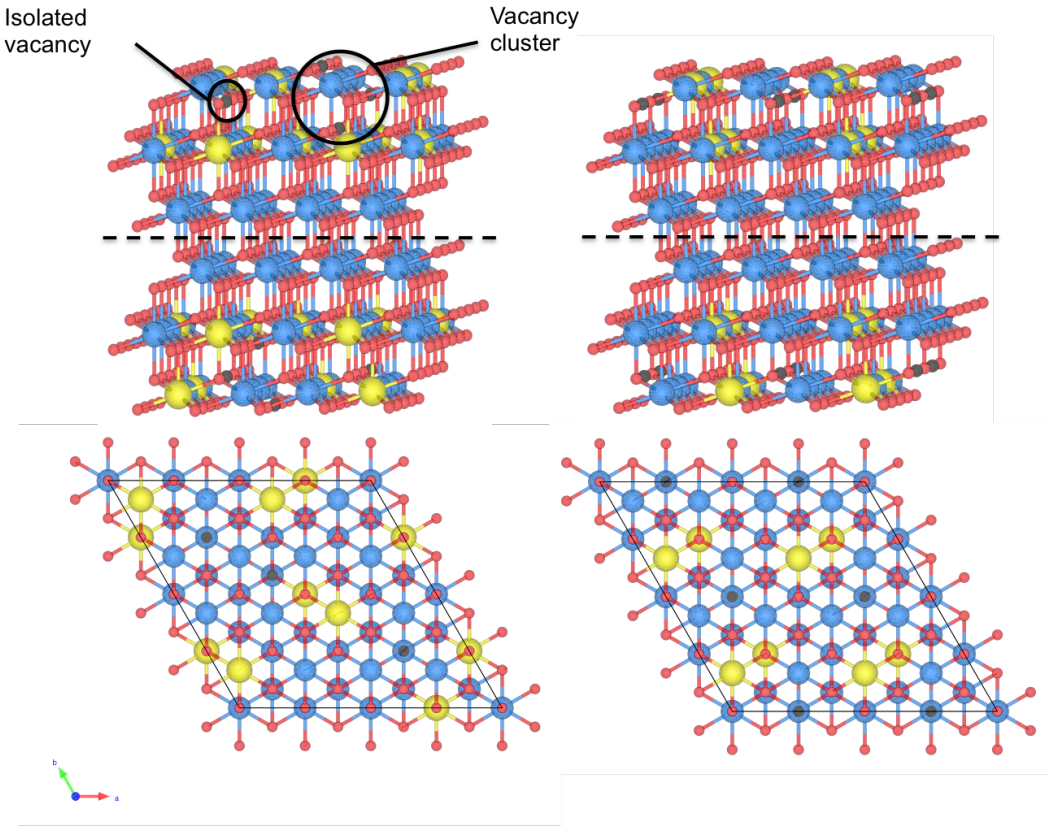

Figure 4.4. Un-relaxed six layer symmetric slab systems; side view (top) and top view (bottom), multi-region slab (left) and periodic vacancy slab (right). Zirconium, yttrium and oxygen ions are blue, yellow and red respectively; with vacancy positions displayed as black spheres. The slab has inversion symmetry about the mid point of the system; the dotted line separates the two symmetric halves.

The yttria concentration of the slab is 9 mol% Y_2O_3, and in order to account for yttrium surface segregation, four Y-V-Y defect clusters were introduced into the top two tri-layers of the surface only, resulting in a surface dopant concentration of 14.3 mol% Y_2O_3. In accordance with previous findings on the nature of the Y-V-Y defect cluster (sections 2.4.1 and 2.4.2), the oxygen vacancies are situated in NNN positions to yttrium cations, with the exception of the lower-most vacancy in the 'vacancy cluster' region of the multi-region slab, which is NN to one yttrium and NNN to another.

In order to create the starting surfaces used for adsorption calculations, three optimization runs were performed to obtain 'pre-relaxed' slabs. This procedure was used to generate both multi-region and periodic vacancy pre-relaxed slabs. The pre-relaxation process is described in detail below for the multi-region slab; similar findings are calculated for the periodic vacancy slab. Firstly, yttrium cations and oxygen vacancies were introduced symmetrically on either side of the slab model of the ideal c-ZrO_2 (111) surface. The surface with the vacancies introduced was

geometry optimised, keeping the supercell size and shape constrained whilst allowing the ionic positions to move. A large relaxation of the ions, particularly the oxygen anion sub-lattice, was observed, as shown in table 4.3. This phenomenon has been previously reported when introducing vacancies into c-ZrO_2 models[14].

	Atomic Coordinate Displacement (Å)								
	Run 1			Run 2			Run 3		
Species	**x**	**y**	**z**	**x**	**y**	**z**	**x**	**y**	**z**
Zr	0.174	0.166	0.109	0.072	0.095	0.044	0.014	0.012	0.006
Y	0.118	0.184	0.098	0.091	0.097	0.071	0.055	0.030	0.015
O	0.305	0.311	0.132	0.176	0.160	0.083	0.024	0.021	0.010

Table 4.3. Average displacement in atomic coordinate upon subsequent geometry optimization runs. Run 1; relaxation away from ideal cubic positions upon vacancy introduction. Run 2; relaxation after water adsorption. Run 3; relaxation after removal of adsorbate.

Secondly, a water molecule was then adsorbed symmetrically on either surface of the slab model; there is very little relaxation of the cationic positions (<0.1Å for all atomic coordinates) yet a further large relaxation of the oxygen ion sub-lattice was observed (0.17 and 0.16Å in the x and y directions). Finally, the water molecules were removed and the slab geometry re-optimised. The resulting structure had very little relaxation of the atomic positions (<0.055Å for all atomic coordinates) and so this 'pre-relaxed' surface was then used for adsorption calculations from which the adsorption energies and geometries reported in the next section were derived. These three geometry optimization steps show that on introduction of oxygen vacancies local relaxation of atomic positions around the oxygen vacancy occurs, whilst atomic positions far from the vacancies remain on the ideal lattice sites. Water adsorption induces further relaxation of the oxygen sub-lattice, and as the sub-lattice remains distorted upon removal of water this result suggests that the slab generated after the first run is slightly metastable and that the adsorption of water pushes the atomic positions towards the energy minimum. This pre-relaxation process highlights the complexity of the energy landscape of YSZ, as the stabilised system is best described as a metastable tetragonal state in which the oxygen ions are displaced away from the ideal lattice sites of the cubic-fluorite phase[15]. The changes in ionic positions upon subsequent geometry optimizations can be seen in figure 4.5.

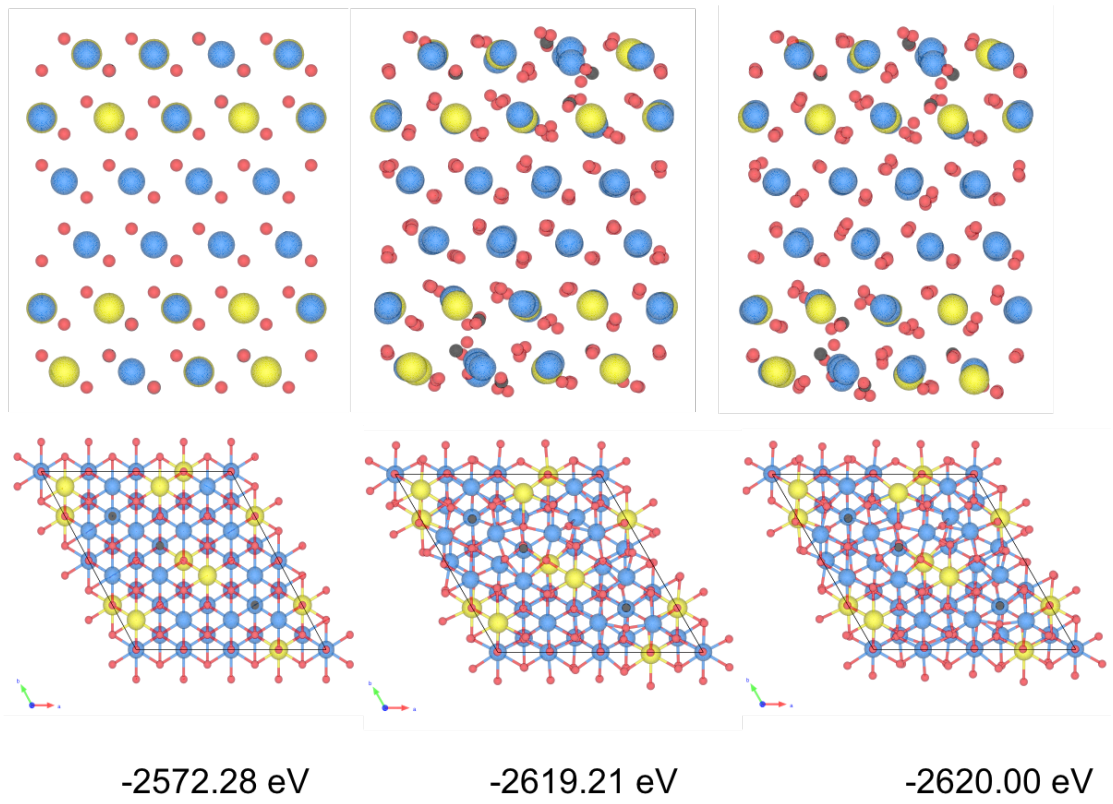

Figure 4.5. Multi-region symmetric slab side and top views; (Left) initial atomic positions, (centre) after structural relaxation and (right) after water adsorption and removal of water. The final structure on the right gives the starting 'pre-relaxed' slab for adsorption calculations. Black spheres are included to indicate initial vacancy positions. The numbers indicate the absolute DFT energy calculated for each structure.

A single electronic SCF calculation for the starting atomic positions is initially performed and a large stabilization occurs after geometry optimization of the introduced vacancies. The 'pre-relaxation' process of adsorbing and then removing water further stabilises the surface slab, by 0.79 eV, due to further relaxation of the oxygen ion sub-lattice. It is worth noting that whilst this stabilization is much smaller than that of the initial geometry optimization, and relatively small when compared to the absolute total energy of the system, it is of the same order of magnitude calculated for molecular adsorptions on the surface.

As discussed earlier, the current models employed for molecular adsorption calculations on the YSZ system use three-layer vacuum slabs with the bottom most layer held fixed in bulk lattice positions. A dopant concentration of 9 mol% is built into these 36 atom slabs through the introduction of a single Y-V-Y defect cluster repeated under periodic boundary conditions. However, this structure contains only the specific case of periodic vacancy-vacancy interactions, without addressing the possibility of short-range concerted vacancy interactions. An early

experimental paper by Goff et al.[16] studied the defect structure of YSZ with x-ray and neutron diffraction techniques. They found vacancies to align along the <111> direction at yttrium concentrations below 15 mol %, and that these vacancy pairs pack together at higher yttrium concentrations to resemble the $Zr_3Y_4O_{12}$ δ-YSZ phase. Bogicevic et al.[17] investigated the nature and strength of defect interactions in YSZ computationally and in agreement with Goff's experimental work conclude that vacancies will order as third nearest neighbors (3NN) along the <111> direction, in both dilute solid solutions and the ordered 40 mol% Y_2O_3 δ-YSZ phase, as a result of balancing electrostatic and elastic effects. Furthermore, Pietrucci et al.[18] investigated the effect of vacancy-vacancy interactions on vacancy diffusion (oxygen migration) starting with vacancies as 3NN. They found that both single vacancy and concerted multiple vacancy jumps can occur in YSZ, and that whilst this many-body problem is not well understood, existing models can be improved by considering vacancy-vacancy interactions. In this work, the periodic vacancy-vacancy interaction case used in earlier computational YSZ adsorption studies is modelled in the periodic vacancy slab, whilst the vacancy cluster region included in the multi-region surface model contains the experimentally observed 3NN oxygen vacancy separation and serves to probe the vacancy-vacancy interactions computationally as suggested in the previous studies. Although the periodic vacancy slab is the lower energy system, indicating that the thermodynamic ground state could be an ordered system, the vacancies are not expected to remain in this perfect periodic arrangement under catalytic operation at high temperature and it is debatable whether such a system could ever be achieved. The multi-region slab, with its extended oxygen anion relaxation, therefore serves to provide insight into the nature of the surface under operating conditions.

4.5 Water Adsorption

The adsorption of water both as a molecule and in a dissociative mode is now explored in detail. Molecular water adsorption is observed on both the periodic vacancy slab and the multi-region model, whereas full dissociative adsorption into separated surface hydroxyls was only found to be possible in the vacancy cluster region of the multi-region slab. Adsorbates were placed symmetrically on either surface of the slab, as shown in figure 4.6, and all atoms in the simulation were relaxed. The adsorption energy, E_{ads}, was calculated as:

$$E_{ads} = \frac{E_{s+a} - (E_s + 2E_a)}{2} \tag{4.3}$$

where E_{s+a} is the energy of the surface-adsorbate system, E_s is the energy of the bare surface and E_a is the energy of the gas-phase adsorbate molecule. The factor of two for E_a accounts for two adsorbate molecules in the simulation cell and the resulting value of E_{ads} is the adsorption energy per molecule. Activation barriers were calculated via transition state searches using nudged elastic band (NEB) calculations[19], and Bader charge analysis was performed to evaluate atomic charges[20].

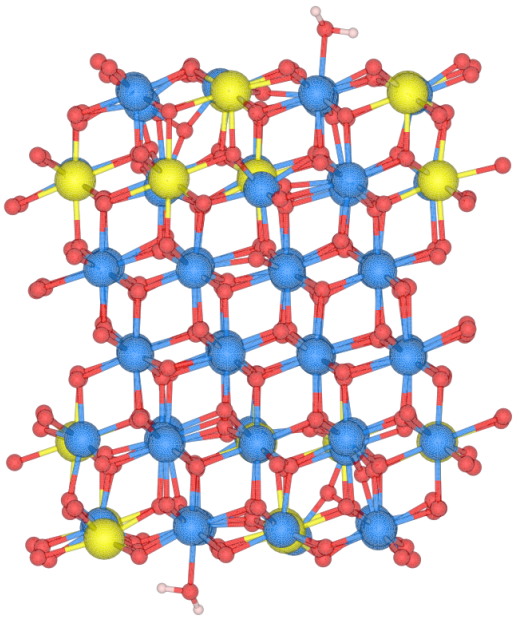

Figure 4.6. Symmetrically adsorbed molecular water on either side of the surface slab model. The surface slab contains a centre of inversion, symmetrically equivalent positions of (x,y,z) are given by (-x,-y,-z).

4.5.1 Molecular Adsorption

Water adsorption has been probed for a variety of different surface sites on the 'pre-relaxed' 9 mol% YSZ vacuum slab system. Geometry optimization simulations were performed placing a water molecule initially ~1.5 Å above the surface. Water was found to adsorb by molecular chemisorption; a typical structure is shown in figure 4.7, in which the water oxygen coordinates to a surface cation and a slight elongation of one water O-H bond occurs as water hydrogen-bonds to a surface oxygen ion. This adsorption mode is the same as molecular water adsorption found on pure ZrO_2, which has been well described previously[21]. The adsorption energies and structural properties of the molecularly adsorbed water states on the multi-region slab are given in table 4.4 and are discussed in detail below.

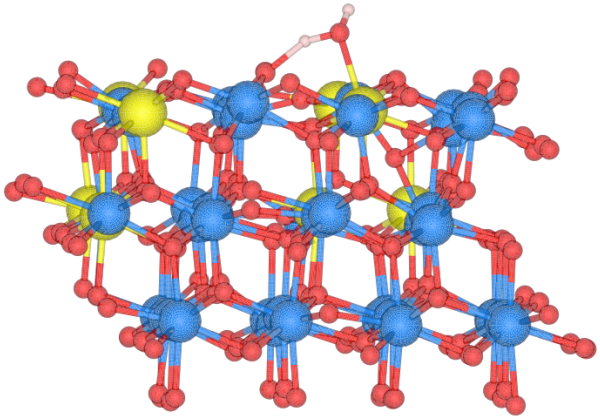

Figure 4.7. Hydrogen-bonded molecular water adsorption on YSZ, only one half of the symmetric slab is shown.

The water molecules in configurations 1, 5 and 6 were started near the isolated sub-surface vacancy; in configurations 2 and 3 they were above the cluster region and in system 4 began above a surface region with no defects. The water adsorption energies have a range of 0.5 eV and there appears to be no single parameter on which the strength of the interaction depends. The site of initial adsorption does not provide a clear picture of the energy as 1 and 6 are the second weakest and strongest adsorptions, yet both start near the isolated vacancy, whilst 3 and 4 have very similar adsorption energies and are in very differing surface regions, while 2 is the weakest adsorption although starting near the vacancy cluster. Hydrogen bonding character can be identified by examining the structural properties of the water molecule. A reduction of the $H_{(water)}$-$O_{(surface)}$ bond length increases the length of one of the water O-H bonds and the bond angle, indicative of H-bonding. Surprisingly there is no clear link between H-bonding character and interaction strength, although the largest degree of H-bonding is observed when the water oxygen is coordinated to a surface yttrium cation. Configurations 1 and 5 are those with the most H-bonding character, but differ in energy by 0.33 eV. The extent of anionic sub-lattice relaxation also does not fully explain the variations in the adsorption energy. The largest stabilization on adsorption occurs for system 6, in which the largest sub-lattice relaxation occurs. However, the second largest degree of relaxation is seen in the configuration with the lowest adsorption energy. The lack of a single parameter controlling the adsorption energy indicates that the factors controlling the strength of the interaction are complex and depend on the local structure of the adsorption site, although the relative similarities in energies indicates a flat potential energy surface on which a variety of molecularly adsorbed water species will be found.

		Bond Lengths (Å)				Bond Angle (°)	Slab Oxygen Relaxation (Å)		
Config. number	Eads (eV)	$O_{(w)}$-$M^{+}_{(s)}$	$O_{(w)}$-$H1_{(w)}$	$O_{(w)}$-$H2_{(w)}$	$H_{(w)}$-$O_{(s)}$	H-O-H	x	y	z
1	-0.76	2.39 (Y)	0.97	1.05	1.49	111.48	0.080	0.087	0.033
2	-0.69	2.45 (Zr)	0.97	0.99	1.88	106.15	0.031	0.026	0.015
3	-0.83	2.36 (Zr)	0.98	1.02	1.66	109.31	0.050	0.049	0.023
4	-0.85	2.35(Zr)	0.98	1.01	1.77	106.13	0.031	0.034	0.017
5	-1.09	2.32 (Y)	0.97	1.08	1.43	110.87	0.069	0.078	0.028
6	-1.19	2.34 (Zr)	0.98	1.04	1.50	105.08	0.127	0.129	0.055
Water	-	-	0.97	0.97	-	104.49	-	-	-

Table 4.4. Adsorption energies (E_{ads}) and structural properties of adsorbed water systems. The average relaxation oxygen ions in the anionic sub-lattice is given for each atomic coordinate. The subscripts (w) and (s) represent whether the atom originates from the water molecule or surface respectively.

The water adsorption modes on the periodic vacancy slab observed after structural relaxation were all molecular chemisorption configurations similar to those described above for the multi-region slab. Very little relaxation of the anionic sub-lattice is observed and the water adsorption energies are -0.48 and -0.81 eV when the water oxygen is coordinated to surface zirconium or yttrium respectively. The lack of extended relaxation in the oxygen sub-lattice upon water adsorption, and the lower adsorption energies observed on the periodic vacancy slab suggest that the energy of the interaction is dependent on the specific state of the surface due to extended oxygen sub-lattice relaxation, but as seen before this relationship is not straightforward.

4.5.2 Dissociative Adsorption

Dissociative chemisorption of water to two surface hydroxyls, in the defect cluster region, was found to occur with a much larger adsorption energy of -2.20 eV. The starting and final structures for the dissociative adsorption mode are shown in figure 4.8. A concerted movement of oxygen ions (or vacancies) is observed on structural relaxation in which the water hydroxyl fills a surface vacancy and an inter-layer oxygen ion relaxes into a sub-surface vacancy site. A nudged elastic band calculation of this water dissociation shows the process to be barrierless.

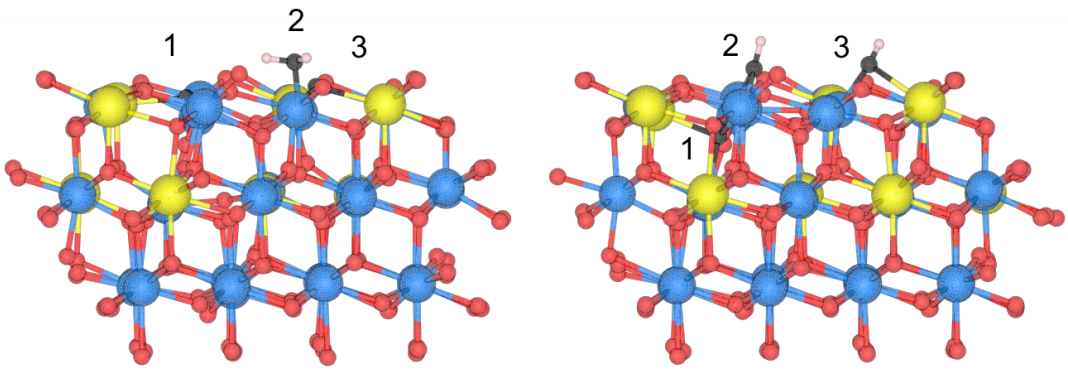

Figure 4.8. Molecularly adsorbed water (left) and dissociated surface hydroxyls (right). Black spheres and numbers are used to indicate specific oxygen atoms.

Bader analysis has been performed to evaluate the charges on the ions in the water adsorption systems. For reference the average values for ionic charges of the bare surface, gas-phase water and the respective bulk systems are given alongside the Bader charges of the adsorbed water systems in table 4.5. The average ionic charges of the atoms in the slab adsorption systems are indicated by (a) in the table, whilst specific individual atomic charges for oxygen ions originating from the water molecule or the YSZ surface are denoted (m*) and (s*) respectively. The positive charge for zirconium ions in the surface slab models decreases slightly compared with bulk ZrO_2, particularly in the case of under-coordinated surface ions, and the lower values compared to ideal formal charges indicates appreciable covalent bonding character. Molecular adsorption of water leads to increased negative and positive charge on the water oxygen and hydrogen species respectively, as electron density moves from hydrogen towards the oxygen coordinated to a surface cation. The negative charge on the surface oxygen ion H-bonded to the molecular water also increases. On dissociation to hydroxyl species, the negative charge on the water oxygen decreases whilst the negative charge on the surface oxygen species, which accepts a proton from molecular water, increases. The incorporation of water oxygen into a surface vacancy as a surface hydroxyl is indicated by this reduction in negative charge. Whilst the negative charges on the water (m*) and surface (s*) oxygen species in the dissociated water system are larger than the average oxygen ion charge of -1.19 e^- in the bare surface system, they are both representative of surface oxygen species as oxygen Bader charges of up to -1.28 e^- are observed in both the bulk and top layer of the bare surface system.

	Bader Charge (e^-)					
Species	Bulk ZrO_2	Bulk Y_2O_3	Gas-phase water	Bare Surface	Molecular water	Dissociated water
Zr	+2.34	-	-	$+2.29_{(a)}$	$+2.29_{(a)}$	$+2.30_{(a)}$
Y	-	+2.16	-	$+2.20_{(a)}$	$+2.20_{(a)}$	$+2.19_{(a)}$
O	-1.17	-1.43	-1.17	$-1.19_{(a)}$ $-1.22_{(s*)}$	$-1.31_{(m*)}$ $-1.26_{(s*)}$	$-1.26_{(m*)}$ $-1.29_{(s*)}$
H	-	-	+0.57	-	+0.64	+0.60

Table 4.5. Bader charge analysis of molecular and dissociated water, bulk systems, gas-phase water and the bare surface values are given for reference.

This mode of dissociative water adsorption could not be replicated on the periodic vacancy model as no surface vacancy is available for the water hydroxyl; our model contains the most stable defect cluster arrangement of a sub-surface oxygen vacancy NNN to two Y cations. When attempting to create a surface vacancy periodic defect cluster model, the surface vacancies become filled with sub-surface oxygen ions during the pre-relaxation process. We propose the defect cluster region of the multi-region surface, with concerted vacancy-vacancy movement, is therefore necessary for this dissociative water interaction to occur.

To date, the water-YSZ surface interaction has only been studied via investigations of hydrogen dissociation to surface hydroxyls, on a YSZ+O model, and subsequent desorption of water from the surface to the gas phase. In the YSZ+O systems, the fixed slab model does not contain a charge compensating oxygen vacancy, as it is proposed that under SOFC operation oxide ions would have diffused from the bulk to fill vacancy sites at the surface. Gorski[22] and Shishkin[9] both calculate exothermic hydrogen dissociation to surface hydroxyl species on the YSZ+O surface, and find that systems of two surface hydroxyls and molecularly adsorbed water are energetically favorable compared to desorption of water to the gas phase, leaving behind a stoichiometric YSZ surface. However, the activation barriers to these processes are very different. The adsorption energies and activation energies from both these studies are given in table 4.6. The adsorption energies for molecular water adsorption and dissociative chemisorption in this study are larger than have been found previously, owing to the thicker vacuum slab allowing for the modelling of extended lattice relaxation effects. However, the barrierless dissociation of adsorbed water to two surface hydroxyl species is in agreement with the work carried out by Shiskin et al. The much larger energy of the chemisorbed hydroxyls is due to the concerted oxygen movement possible in the defect cluster region of the slab, resulting from vacancy-vacancy interactions, which have not beforehand been incorporated into models of the YSZ surface system.

	Eads (ev)		Forward barrier (ev)		Backwards barrier (ev)		
Author	2 $OH_{(ads)}$	$H_2O_{(ads)}$	$OH_{(ads)}$ to $H_2O_{(ads)}$	$H_2O_{(ads)}$ to $H_2O_{(g)}$	$H_2O_{(g)}$ to $H_2O_{(ads)}$	$H_2O_{(ads)}$ to $OH_{(ads)}$	$H_2O_{(g)}$ to $OH_{(ads)}$
Shishkin et al.[9]	-0.91	-0.52	0.43	0.52	-	0.04	-
Gorski et al.[22]	-0.54	-0.43	1.82	-	-	-	1.26
This Work	-2.20	-0.50 to -1.19	-	-	0.00	0.00	0.00

Table 4.6. Surface water configuration adsorption energies and reaction barriers from previous studies.

4.6 Summary and Conclusions

The bulk properties of cubic ZrO_2 are easily obtainable with DFT; however zirconia and YSZ surfaces present a number of challenges due to the nature of the material. Cubic ZrO_2 surfaces undergo significant atomic displacement, particularly of the anionic sub-lattice, upon molecular adsorption, which is a result of cubic zirconia only being stable at high temperatures, and in the low temperature monoclinic and tetragonal polymorphs zirconium atoms have an energetic tendency to adopt lower coordination numbers or have oxygen atoms displaced away from the ideal fluorite lattice sites of the cubic structure. Yttria doping stabilises the cubic phase, but the lack of detailed knowledge of the local structure of YSZ, with regards to vacancy-vacancy interactions in particular, introduces added complexity into YSZ surface models.

We have developed a new slab model for YSZ surface adsorption calculations, which contains distinct surface regions enabling the simulation of different surface environments within the same model. The isolated vacancy and defect-absent regions probe the common, previously studied, surface regions of YSZ, whilst the inclusion of a defect cluster region attempts to include experimentally and computationally observed vacancy-vacancy interactions. The much larger slab allows the inclusion of extended anionic sub-lattice relaxation, previously unattainable in the models used to study the YSZ surface, whilst the symmetric adsorption of molecules either side of the slab negates any cross-slab dipoles introduced on adsorption. The large oxygen displacement observed in the YSZ model, as well as the artificial example of the fixed slab cubic-ZrO_2 model, is considered to be a real effect, which leads to a more realistic description of the YSZ system. It is well known that YSZ is a locally disordered structure, with cubic symmetry only manifesting over long range. Molecular water adsorption on the surface

has been well characterised and the dissociation of surface water to surface hydroxyl species is demonstrated to be a barrierless process. The strong adsorption energies observed in our calculations for both molecular and dissociated water explain the experimentally observed strong adsorption of water on YSZ catalysts, characterised by a delayed product signal for water compared to other methane partial oxidation products, during CPOM reactions[23]. The defect cluster region of the surface model has allowed concerted oxygen (vacancy) movements, on surface adsorption, to be identified for the first time on this system.

The very strong binding of a water hydroxyl into a stoichiometric surface vacancy in the defect cluster region is important when considering the catalytic activity of YSZ for CPOM and methane steam reforming. Formaldehyde has been proposed as a major intermediate for CPOM[24]. Lattice oxygen on the YSZ surface, replaced by activated molecular oxygen in a Mars-van Krevelen scheme, is considered to abstract hydrogen from methane to form formaldehyde as the major intermediate. This surface formaldehyde species can then either be further oxidised to surface formate and subsequently total oxidation products, or it can be converted directly to the partial oxidation products forming syngas. As surface vacancies are proposed as active sites for the activation of molecular oxygen[23], strong binding of water derived hydroxyls at these sites could compete with molecular oxygen adsorption. Blocking oxygen activation could then inhibit further oxidation of formaldehyde to formate, which could possibly explain the increased selectivity to syngas observed when water is added to the CPOM reactant mixture[1]. The vacancy cluster region, where water dissociation occurs, also introduces coordinatively unsaturated zirconium ions into the surface. A related effect has been seen whereby water will compete with N_2O for under coordinated zirconium surface sites[25]. More detailed study of surface redox processes and the methane partial oxidation mechanism is presented in chapters 5 and 6.

References

1. Zhu, J.; van Ommen, J. G.; Lefferts, L., Effect of surface OH groups on catalytic performance of yittrium-stabilized ZrO2 in partial oxidation of CH4 to syngas. *Catalysis Today* **2006,** 117, (1-3), 163-167.
2. Xia, X.; Oldman, R.; Catlow, R., Computational Modeling Study of Bulk and Surface of Yttria-Stabilized Cubic Zirconia. *Chemistry of Materials* **2009,** 21, (15), 3576-3585.
3. Cooper, C., Computational Modelling of Yttrium Stabilised Zirconia in Catalysis. In Dept. Chemistry, UCL, 2013; Vol. EngD Thesis.
4. McComb, D. W., Bonding and electronic structure in zirconia pseudopolymorphs investigated by electron energy-loss spectroscopy. *Physical Review B* **1996,** 54, (10), 7094-7102.
5. French, R. H.; Glass, S. J.; Ohuchi, F. S.; Xu, Y. N.; Ching, W. Y., Experimental and theoretical determination of the electronic-structure and optical-properties of 3 phases of ZrO2. *Physical Review B* **1994,** 49, (8), 5133-5141.
6. Xia, X.; Oldman, R. J.; Catlow, C. R. A., Zirconium dioxide topological surfaces with low coordination sites. *Journal of Materials Chemistry* **2011,** 21, (38), 14549-14558.
7. Ricca, C.; Ringuede, A.; Cassir, M.; Adamo, C.; Labat, F., A Comprehensive DFT Investigation of Bulk and Low-Index Surfaces of ZrO2 Polymorphs. *Journal of Computational Chemistry* **2015,** 36, (1), 9-21.
8. Xia, X.; Oldman, R. J.; Catlow, C. R. A., Oxygen adsorption and dissociation on yttria stabilized zirconia surfaces. *Journal of Materials Chemistry* **2012,** 22, (17), 8594-8612.
9. Shishkin, M.; Ziegler, T., The Oxidation of H(2) and CH(4) on an Oxygen-Enriched Yttria-Stabilized Zirconia Surface: A Theoretical Study Based on Density Functional Theory. *Journal of Physical Chemistry C* **2008,** 112, (49), 19662-19669.
10. Cooper, C. S.; Oldman, R. J.; Catlow, C. R. A., Oxidative methane activation over yttrium stabilised zirconia. *Chemical Communications* **2015,** 51, (27), 5856-5859.
11. Morterra, C.; Cerrato, G.; Ferroni, L.; Montanaro, L., Surface Characterization of yttria-stabilized tetragonal ZrO2 .1. structural, morphological, and surface hydration features. *Materials Chemistry and Physics* **1994,** 37, (3), 243-257.
12. Gennard, S.; Cora, F.; Catlow, C. R. A., Comparison of the bulk and surface properties of ceria and zirconia by ab initio investigations. *Journal of Physical Chemistry B* **1999,** 103, (46), 10158-10170.
13. Christensen, A.; Carter, E. A., First-principles study of the surfaces of zirconia. *Physical Review B* **1998,** 58, (12), 8050-8064.
14. Ricca, C.; Ringuede, A.; Cassir, M.; Adamo, C.; Labat, F., Revealing the properties of the cubic ZrO2 (111) surface by periodic DFT calculations: reducibility and stabilization through doping with aliovalent Y2O3. *Rsc Advances* **2015,** 5, (18), 13941-13951.
15. Yashima, M.; Morimoto, K.; Ishizawa, N.; Yoshimura, M., Zirconia ceria solid-solution synthesis and the temperature time transformation diagram for the 1/1 composition. *Journal of the American Ceramic Society* **1993,** 76, (7), 1745-1750.
16. Goff, J. P.; Hayes, W.; Hull, S.; Hutchings, M. T.; Clausen, K. N., Defect structure of yttria-stabilized zirconia and its influence on the ionic conductivity at elevated temperatures. *Physical Review B* **1999,** 59, (22), 14202-14219.
17. Bogicevic, A.; Wolverton, C., Nature and strength of defect interactions in cubic stabilized zirconia. *Physical Review B* **2003,** 67, (2).
18. Pietrucci, F.; Bernasconi, M.; Laio, A.; Parrinello, M., Vacancy-vacancy interaction and oxygen diffusion in stabilized cubic ZrO(2) from first principles. *Physical Review B* **2008,** 78, (9), 7.
19. Henkelman, G.; Jonsson, H., Improved tangent estimate in the nudged elastic band method for finding minimum energy paths and saddle points. *Journal of Chemical Physics* **2000,** 113, (22), 9978-9985.
20. Tang, W.; Sanville, E.; Henkelman, G., A grid-based Bader analysis algorithm without lattice bias. *Journal of Physics-Condensed Matter* **2009,** 21, (8).
21. Haase, F.; Sauer, J., The surface structure of sulfated zirconia: Periodic ab initio study of sulfuric acid adsorbed on ZrO2(101) and ZrO2(001). *Journal of the American Chemical Society* **1998,** 120, (51), 13503-13512.

22. Gorski, A.; Yurkiv, V.; Starukhin, D.; Volpp, H.-R., H2O chemisorption and H-2 oxidation on yttria-stabilized zirconia: Density functional theory and temperature-programmed desorption studies. *Journal of Power Sources* **2011,** 196, (17), 7188-7194.
23. Zhu, J. J.; van Ommen, J. G.; Bouwmeester, H. J. M.; Lefferts, L., Activation of O-2 and CH4 on yttrium-stabilized zircoma for the partial oxidation of methane to synthesis gas. *Journal of Catalysis* **2005,** 233, (2), 434-441.
24. Zhu, J. J.; van Ommen, J. G.; Lefferts, L., Reaction scheme of partial oxidation of methane to synthesis gas over yttrium-stabilized zirconia. *Journal of Catalysis* **2004,** 225, (2), 388-397.
25. Zhu, J. J.; Albertsma, S.; van Ommen, J. G.; Lefferts, L., Role of surface defects in activation of O-2 and N2O on ZrO2 and yttrium-stabilized ZrO2. *Journal of Physical Chemistry B* **2005,** 109, (19), 9550-9555.

Chapter 5

Redox Properties of YSZ

Chapter 5 investigates the reduction of bulk zirconia and YSZ surface systems. The nature of non-stoichiometric defects in YSZ are discussed and compared with the available literature. Subsequent re-oxidation of the reduced surface systems is performed, leading to the creation of an 'active YSZ+O' surface. The validity of a surface reduction/oxidation mechanism on this typically non-redox active oxide is then considered. The presence of charge compensating vacancies and the resultant oxygen anion mobility induced is suggested as important in promoting redox activity in YSZ.

5.1 Introduction

Yttria-stabilised zirconia is not traditionally considered a redox active oxide. However, there are a number of indications in the literature that surface redox chemistry may be important in YSZ. First, YSZ was displayed to be an active catalyst in its own right for catalytic methane partial oxidation and isotopically labelled oxygen experiments determined that this catalysis was of a Mars-van Krevelen nature as the oxidation products exclusively contained lattice oxygen[1]. Further isotopic oxygen experiments showed thermally activated exchange directly with YSZ lattice oxygen, with both CPOM and oxygen exchange reactions beginning at ~773K and complete oxygen conversion attained at ~1173K[1]. These findings of oxygen dissociation, exchange, and liberation strongly suggest that YSZ exhibits some redox behaviour.

5.1.1 F-Centres

This chapter is concerned with both the bulk reduction of zirconia and YSZ surfaces and the subsequent re-oxidation of these reduced surfaces. Reduction in this case occurs as a result of oxygen atom removal, as is discussed throughout the following sections, which creates F-centres within the material. F-centres are the, perhaps slightly strange, phenomenon of having trapped localised electrons in solids[2]. They get their name from the German *Farbzentrum* (colour-centre) as the presence of these trapped electrons results in the introduction of mid-gap states, which typically absorb visible light and cause transparent materials to become coloured. Whilst early work on these types of lattice defects was concerned with the alkali halides[2], oxygen atom removal and the subsequent F-centres created in oxide materials are considered to produce important properties for a wide variety of technologically relevant applications[2,3,4].

5.2 Bulk ZrO_2 Reduction

The reduction of bulk zirconia was studied first in order to obtain reference values for the vacancy formation energy. Reduction of the ZrO_2 system is achieved by removing an oxygen ion from the bulk material and allowing the internal coordinates of the system to relax. The vacancy formation energies for removing one oxygen atom from 2x2x2, 3x3x3, and 4x4x4 ZrO_2 supercells, given in table 5.1, are calculated as follows;

$$E_{vf} = E_r - E_{nr} + \tfrac{1}{2}EO_2 \qquad (5.1)$$

where E_{vf} is the vacancy formation energy, E_r is the energy of the reduced system, and E_{nr} is the energy of the starting non-reduced system.

Supercell Size (No. atoms)	Vacancy Formation Energy (eV)
2x2x2 (96)	5.60
3x3x3 (324)	5.51
4x4x4 (728)	5.54

Table 5.1. Vacancy formation energy in ZrO_2 for increasing size supercell systems.

On structural relaxation after the removal of an oxygen ion, only very small relaxations, of oxygen ions surrounding the vacancy, towards the vacancy are detected. A maximum oxygen movement of 0.08Å occurs in the 2x2x2 supercell, whilst the average for all oxygen atoms in the cell is <0.02Å. However, whilst the absolute value of the atomic displacement is not large it does appear to be a relatively long-range effect. Small oxygen displacements away from the ideal cubic lattice sites can be detected at a distance of >7.5Å from the vacancy in the 4x4x4 supercell; a similar effect has also been seen up to 9Å away from the vacancy site in an embedded cluster study by Ramo *et al.*[5]. Furthermore, inspection of the electronic states following vacancy formation shows the appearance of a doubly occupied defect energy level within the band gap. This density of states for the reduced system and the partial charge density of the vacancy are depicted in figures 5.1 and 5.2 respectively.

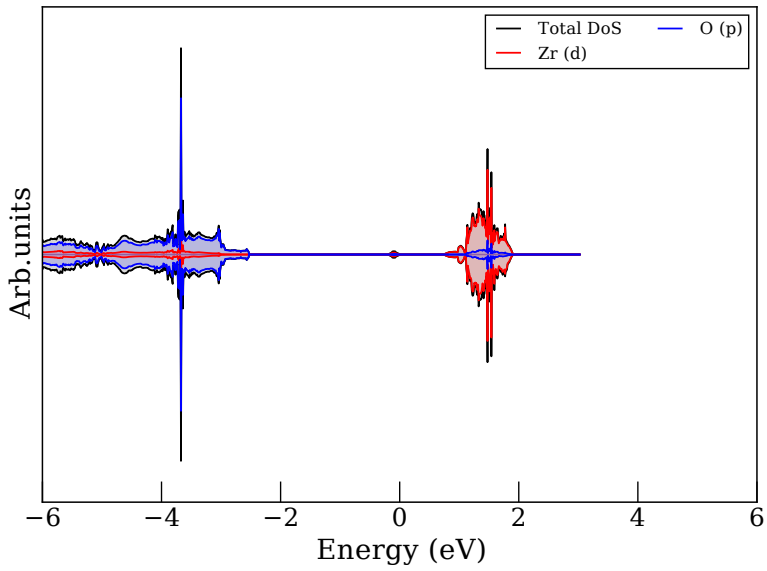

Figure 5.1. Density of states for the reduced 2x2x2 ZrO_2 supercell.

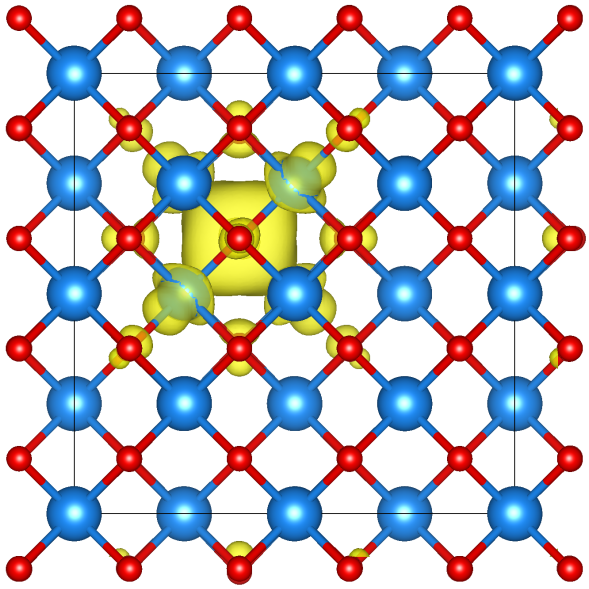

Figure 5.2. Partial charge density of the vacancy in the 2x2x2 ZrO_2 supercell after reduction. Blue and red spheres represent zirconium and oxygen ions respectively, yellow regions represent charge density isosurfaces.

The Fermi-energy in the DOS plot in figure 5.1 is set to zero, showing that the gap-state is occupied. The position of the gap-state is also in the upper half of the band-gap, closer to the conduction band than the valence band. The vacancy charge density manifests as a rounded tetrahedron with the charge density mostly localised in the site of the missing oxygen atom, although some of this charge density is delocalised into the dz^2 orbitals of the four nearest neighbour zirconium cations. The presence and location of the gap-state as well as the shape of the resultant vacancy is in good agreement with previous bulk ZrO_2 studies[5,6,3,7]. Whilst the vacancy formation energy calculated for bulk ZrO_2 of ~5.5 eV is lower than the value of 7.2 eV calculated by Gionco *et al.*[7] using the B3LYP DFT functional, in a linear combination of atomic orbitals approach adopted in the CRYSTAL code, the vacancy in the Gionco study only appears to be delocalised over two nearest neighbour zirconium cations and not all four as in this study and elsewhere[5,6,3].

5.3 YSZ Surface Reduction

We now explore reduction of YSZ on both terrace and step models of the cubic-(111) surface. The terrace model is the same surface model developed in chapter 4, whilst the creation of the step model is detailed in section 5.3.2. As discussed in greater detail below, surface reduction is achieved by removal of an oxygen atom from the uppermost surface oxygen layer on terraces or the step-edge positions on steps. Whereas YSZ naturally contains charge compensating

stoichiometric oxygen vacancies, surface reduction leads to the formation of non-stoichiometric oxygen vacancies. In all cases removal of an oxygen atom is accompanied by the formation of a doubly occupied defect state situated within the band gap of the material, as is observed for bulk ZrO_2. The density of states for both the stoichiometric YSZ surface and a reduced YSZ surface are given in figure 5.3; in each case the Fermi-level is set to zero. The valence and conduction bands of both surfaces consist mainly of oxygen 2p, and zirconium 4d states respectively. The stoichiometric surface displays the wide band-gap insulating nature of YSZ, whereas the reduced surface contains a doubly occupied mid-gap state. This result highlights the fact that although charge compensating oxygen vacancies are present in stoichiometric YSZ, these vacancies are of a fundamentally different character compared to the F-centre vacancies created upon surface reduction.

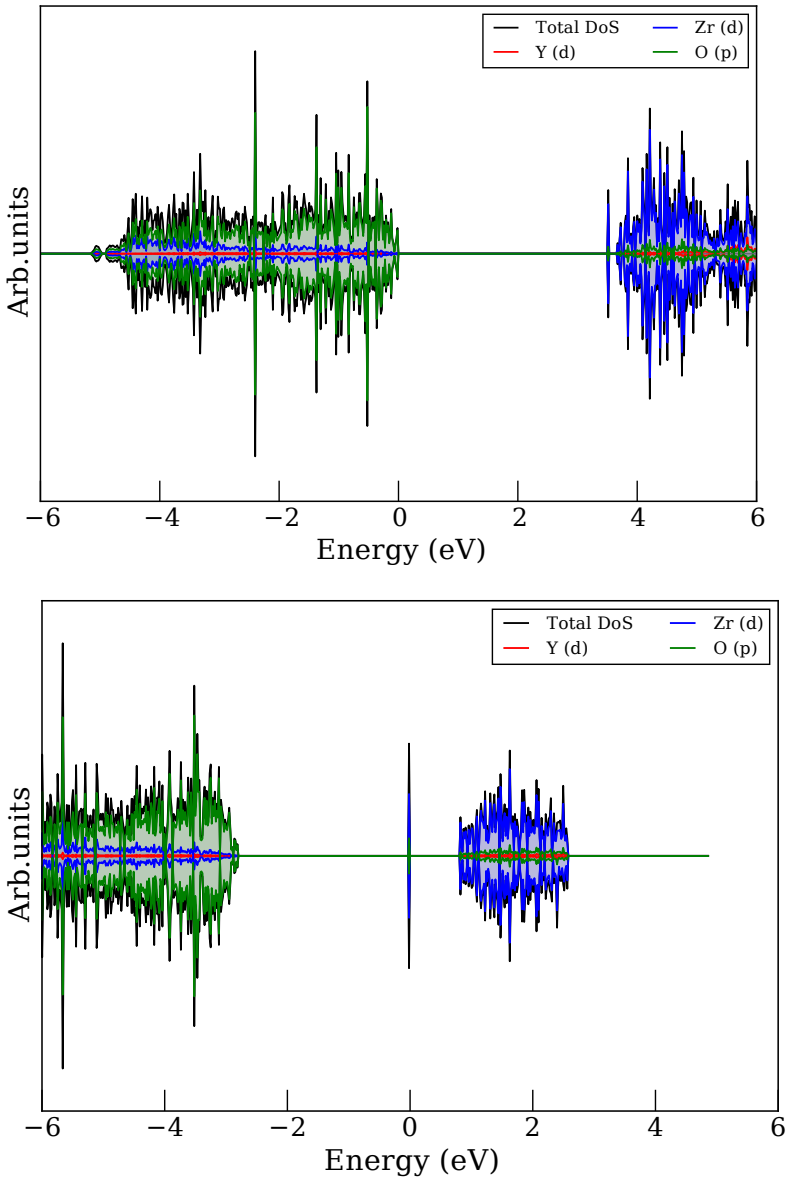

Figure 5.3. Density of states for the stoichiometric terrace surface (top) and reduced terrace surface (bottom).

5.3.1 Terrace Surface

Surface reduction has been calculated by removal of each of the 16 inequivalent oxygen atoms in the top-most surface oxygen layer. Oxygen vacancy formation energies along with details of the mid-gap state, oxygen ion relaxation and the location and delocalisation of the vacancies created for each of these 16 configurations is presented in table 5.2. The vacancy formation energies are similar in energy to the value of +5.83 eV calculated by Grau-Crespo *et al.* for the pure ZrO_2 cubic-(111) surface[8].

System	E_{vf} (eV)	Band gap (eV)	ΔE VBM-V_O (eV)	ΔE CBM-V_O (eV)	Average oxygen relaxation (Å)			Maximum oxygen relaxation (Å)			Vacancy position	Vacancy delocalisation
					x	y	z	x	y	z		
1	4.50	3.56	2.62	-0.94	0.10	0.10	0.09	1.44	0.85	1.41	Sub-surface	4 Zr, 1 Y
2	4.66	3.60	2.75	-0.86	0.12	0.13	0.13	0.63	0.94	1.25	Sub-surface	3 Zr, 1 Y
3	4.83	3.49	2.53	-0.96	0.09	0.08	0.10	0.83	0.48	1.23	Surface	3 Zr
4	4.89	3.60	2.71	-0.88	0.11	012	0.12	0.76	0.81	1.17	Surface	3 Zr
5	5.26	3.46	2.07	-1.39	0.08	0.09	0.09	0.68	1.04	0.90	Sub-surface	3 Zr, 1 Y
6	5.35	3.49	2.80	-0.69	0.09	0.10	0.12	0.59	0.56	0.70	Surface	3 Zr
7	5.47	3.51	2.74	-0.78	0.10	0.09	0.12	0.60	0.57	0.69	Surface	3 Zr
8	5.68	3.50	2.66	-0.83	0.09	0.09	0.12	0.60	0.57	0.68	Surface	2 Zr, 1 Y
9	5.69	3.48	3.04	-0.44	0.10	0.10	0.11	0.61	0.63	0.68	Surface	3 Zr
10	5.78	3.51	2.71	-0.79	0.10	0.10	0.12	0.60	0.56	0.70	Surface & sub-surface	4 Zr, 1 Y
11	5.82	3.49	2.82	-0.67	0.12	0.11	0.12	0.68	0.59	0.70	Surface	2 Zr, 1 Y
12	5.92	3.34	2.35	-0.99	0.12	0.11	0.11	0.63	0.99	0.68	Surface	3 Zr
13	6.00	3.54	3.07	-0.47	0.10	0.10	0.11	0.60	0.54	0.68	Surface	3 Zr, 1 Y
14	6.11	3.20	2.40	-0.79	0.03	0.03	0.03	0.22	0.32	0.13	Surface & sub-surface	4 Zr, 1 Y
15	6.36	3.46	2.84	-0.63	0.02	0.02	0.02	0.16	0.10	0.09	Surface	3 Zr, 1 Y
16	6.95	3.46	3.09	-0.43	0.01	0.01	0.01	0.07	0.06	0.06	Surface	2 Zr, 1 Y

Table 5.2. Oxygen vacancy formation energies (E_{vf}) and position of the defect state (V_O) relative to the valence band maximum (VBM) and conduction band minimum (CBM) for the reduction of terrace surfaces. The average ionic relaxation for all oxygen atoms as well as the maximum relaxation for single oxygen atoms is given, and the spatial position of the vacancy charge density and the extent of delocalisation towards surrounding cations is also presented.

As can be seen, there is a large range of vacancy formation energies (+4.50 to +6.95 eV). The different configurations have been ranked by vacancy formation energy. Systems 1 and 3 are explored below in greater detail as examples of systems having low vacancy formation energies. One can immediately notice the similarities of the defect states for systems 1 and 3: they both lie in the middle of the band gap ~2.5 eV above the VBM and ~1 eV below the CBM. Visualisation of the vacancy electron density isosurface is provided in figure 5.4, along with the initial and final atomic positions for the vacancy formation process and highlighted oxygen atom movement. It is interesting to note that the most stable vacancy (system 1, + 4.50 eV) relocates to the sub-surface upon geometry optimisation, despite being created by removal of a surface oxygen atom. The approximately spherical charge densities and detailed electronic structure observed at the surface (system 3) and sub-surface (system 1) vacancies, are in good agreement both with the bulk ZrO_2 results above and previous computational studies of neutral oxygen vacancy F-centres (V^0) in both cubic[6,5] and tetragonal[7] ZrO_2. These vacancies are formed from a combination of the Zr 4*d* orbitals nearest-neighbour to the vacancy with electron density delocalised into the cation dz^2 orbitals. Bader charge analysis of system 3 confirms this reduction of neighbouring zirconium cations, with ~1.2 e^- distributed between the three cations. The ionic charges of three surface Zr ions changing from ~ + 2.30 e^- in the stoichiometric surface to + 2.02, + 1.95 and + 1.75 e^- in the reduced surface. Whilst some of the charge density is delocalised over surrounding cations a large portion of it remains in the vacancy site, the surface cations are therefore only partially reduced at variance with what is observed on reducible oxides such as ceria.

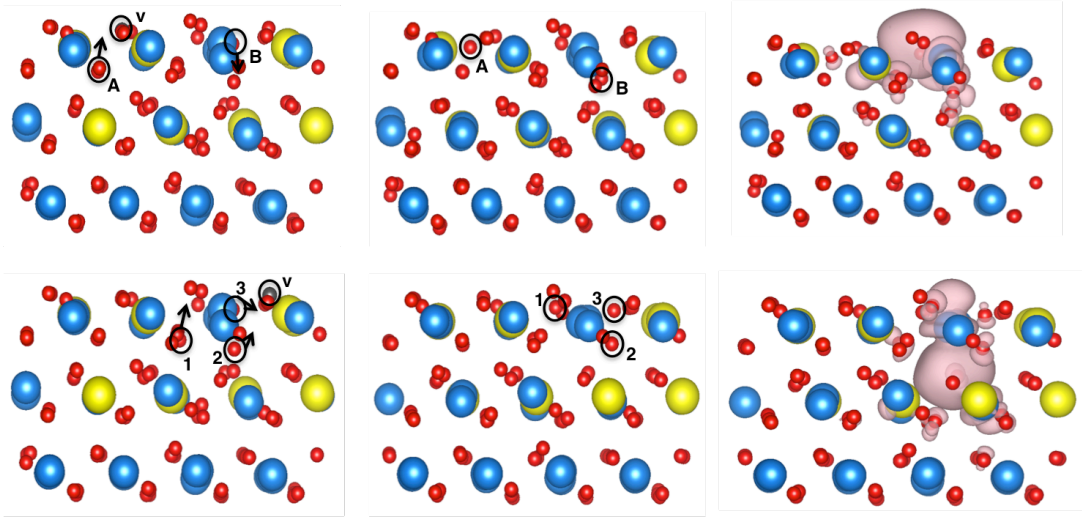

Figure 5.4. Initial and final atomic positions, and vacancy electron density isosurfaces for systems 3 (top) and 1 (bottom). Specific oxygen atoms are highlighted and the arrows indicate the displacement direction, 'v' denotes the oxygen removed in order to create the vacancy. For brevity only one half of the symmetric slab is shown.

The two highest energy reduced terrace surfaces (systems 15 and 16) are now presented in further detail. Both systems have defect levels at higher energies within the band-gap, closer to the conduction band. Visualisation of the vacancy isosurfaces is provided in figure 5.5. Unlike the lower energy reduced surfaces, the vacancies in systems 15 and 16 both have an yttrium ion nearest neighbour to the vacancy. The higher level of the defect states in the band-gap for these systems may be due to the contribution of yttrium 4*d* orbitals to the vacancy. It has been shown previously that on doping ZrO_2 with yttrium, although Y-4*d* states contribute to the bottom of the conduction band, they lie at higher energies than the corresponding Zr-4*d* states[9]. In comparison with the low energy vacancies, the charge density of systems 2 and 3 does not delocalise onto the yttrium cations and instead extends towards other nearby zirconium ions. Whilst, this finding suggests that zirconium is more readily reduced than yttrium, it is worth noting that the size of this effect will be exaggerated by the well-known tendency of GGA-DFT to delocalise excessively charge density.

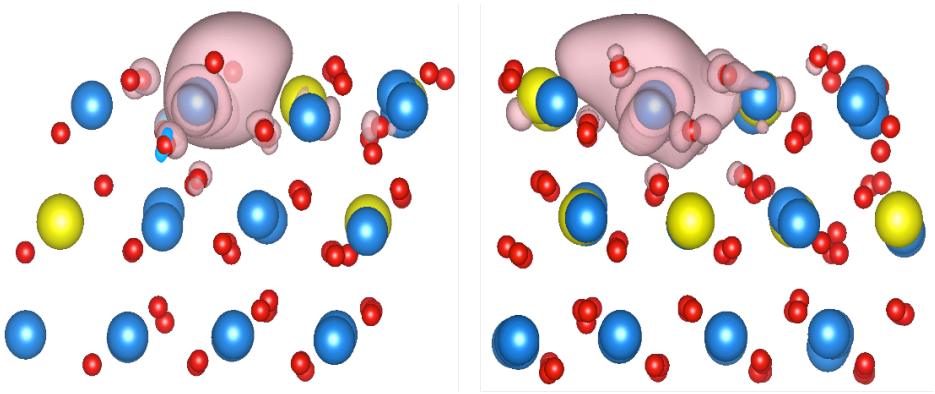

Figure 5.5. Visualised vacancy partial charge density on reduced YSZ, systems 16 (left) and 15 (right).

Whilst the position in the band-gap and nature of the F-centre defect state created by oxygen atom removal show clear differences between the systems with the very lowest and the highest vacancy formation energies, this trend does not strictly hold for the full range of reduced systems with intermediate vacancy formation energies. The extent of oxygen ion relaxation after surface reduction is perhaps more relevant when evaluating the ease of vacancy formation. The average relaxation of all oxygen atoms in the surface slab, as well as the maximum displacements in each crystallographic direction for an individual atom are given in table 5.2 for each of the different vacancy systems. We note that the maximum relaxation refers to that of any oxygen atom in the system in a particular direction and that the x, y and z displacements do not necessarily belong to the same oxygen atom. The higher energy reduced surfaces show only a very small degree of oxygen ion sub-lattice relaxation, both for the average relaxation over the entire system and the movement of individual atoms in any one direction. For example

the three highest energy structures have average oxygen relaxations of less than 0.05Å, and a maximum oxygen displacement of 0.32Å. On the other hand, whilst the remaining 13 structures all have very similar average oxygen ion relaxations (~0.1Å), the 5 lowest energy structures all have at least one oxygen atom move more than 1Å in any direction after structural relaxation. For example systems 1 and 3 there are large displacements of a small number of oxygen ions upon geometry optimisation (shown in figure 5.4).

5.3.2 Step Surface

Step surfaces of the c-(111) YSZ terrace were created by removing 4 ZrO_2 formula units from the top surface row on either side of the symmetric surface slab model of pure ZrO_2. Removal of 4 ZrO_2 formula units per half of the symmetric slab is the equivalent of removing 1⁄4 of surface cation sites and results in the creation of 8 under-coordinated cation step sites per half of the slab (16 in total in the simulation cell). Four yttrium-vacancy-yttrium (Y-V-Y) defect clusters were then introduced symmetrically on either side of the slab giving the stoichiometric YSZ step surface model with a dopant concentration of 10 mol%. Figure 5.6 shows one of the symmetric step models used. Black spheres indicate vacancy positions; some of these vacancies are 'hidden' by lattice oxygen atoms. In order to clarify, the four vacancies are circled and labelled (V1-4) and their corresponding symmetric vacancies also highlighted (V1`-4`). X and X' are symmetric vacancies which correspond to the periodic images of V1 and V1`.

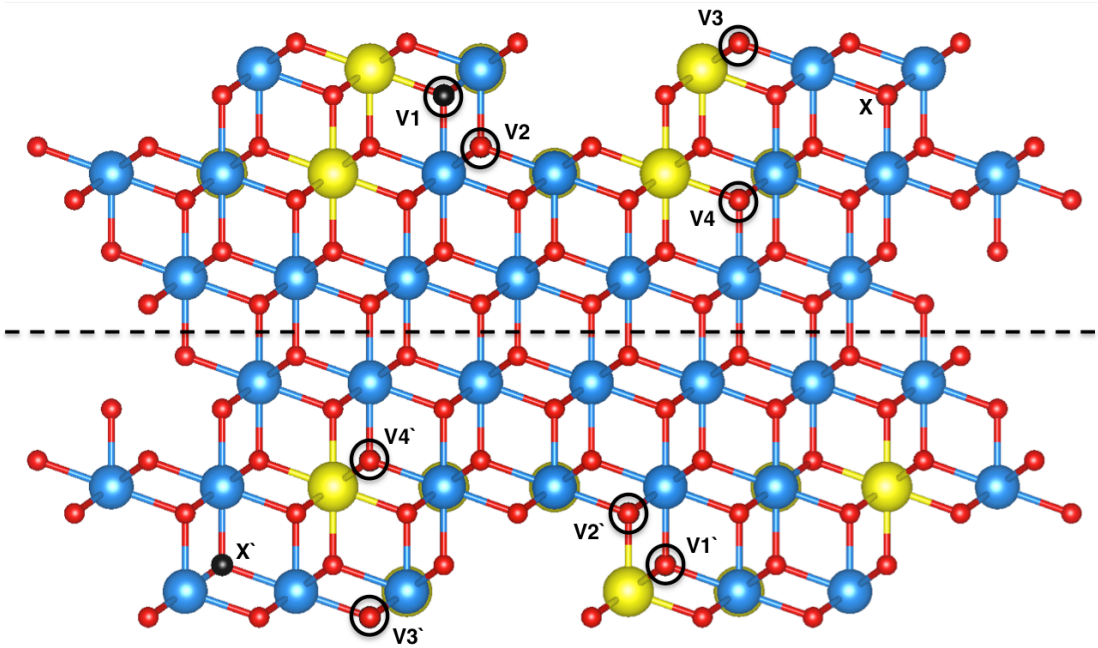

Figure 5.6. Symmetric step surface model.

As with the terrace surfaces, oxygen vacancy formation on step surfaces occurs with a large range of formation energies as evident in table 5.3. However, quite unlike the situation on terraces there appears to be no correlation between the position of the defect level within the band gap and the vacancy formation energy on step surfaces. The higher energy reduced step systems (3 and 4) have vacancy formation energies of similar magnitude to those of the terrace surfaces, whilst systems 1 and 2 have significantly lower formation energies (~ +3.8 eV). The starting and final positions of the introduced vacancies, which is determined by the site from which the oxygen atom is removed and the subsequent location of the defect-state charge density isosurface, explains better the differences in vacancy formation energies. The highest energy neutral vacancy F-centre remains localised on the surface step-edge in the region from which oxygen is removed in system 4, whereas in systems 1, 2 and 3 the vacancy relocates to the sub-surface. Furthermore, the system 1 vacancy remains adjacent to a cation neighbouring the site of the removed oxygen, whilst the vacancies in the lower energy systems 2 and 3 move away from the step edge and relocate to a sub-surface site where the vacancy density is not delocalised over any of the cations initially neighbouring the removed oxygen. This vacancy relocation is shown for system 2 in figure 5.7.

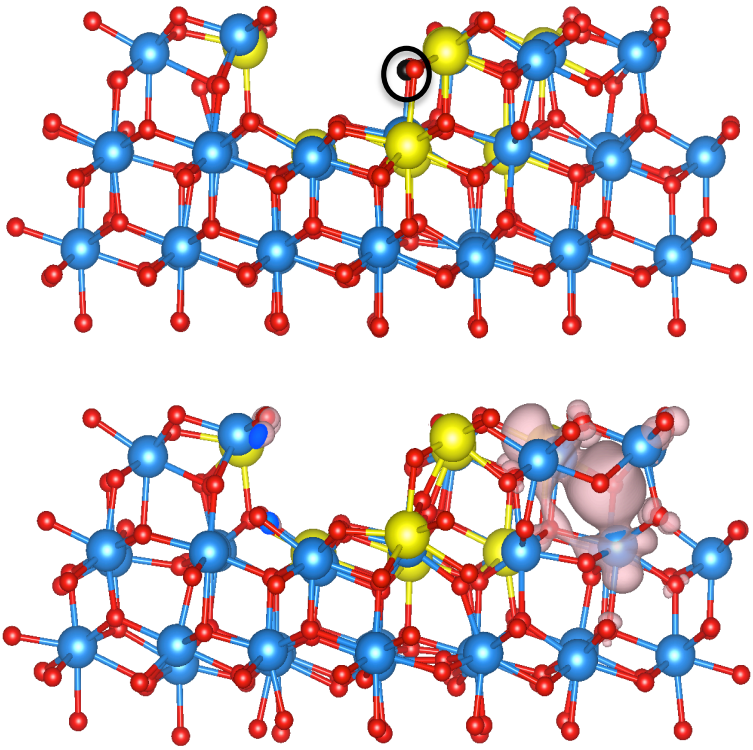

Figure 5.7. Step surface system 2; initial configuration (top) with oxygen to be removed circled, and final configuration (bottom) showing defect state isosurface.

System	E_{vf} (eV)	Band gap (eV)	ΔE VBM-V_O (eV)	ΔE CBM-V_O (eV)	Average oxygen relaxation (Å)			Maximum oxygen relaxation (Å)		
					x	y	z	x	y	z
1	3.82	2.80	1.82	-0.98	0.10	0.13	0.14	0.50	1.10	1.20
2	3.86	3.43	2.04	-1.39	0.13	0.13	0.13	1.13	1.83	0.71
3	4.68	3.31	1.74	-1.57	0.05	0.07	0.06	0.30	0.55	0.43
4	5.24	2.90	1.96	-0.94	0.05	0.05	0.04	0.31	0.56	0.42

Table 5.3. Step surface reduction information.

System	E_{vf} (eV)	E_{ads} (eV)	ΔE E_{vf} – E_{ads} (eV)	O-O bond length (Å)	Average oxygen relaxation (Å)			Maximum oxygen relaxation (Å)			Ads mode	Molecular oxygen coordination
					x	y	z	x	y	z		
1	4.50	-6.08	-1.58	1.50	0.06	0.07	0.07	0.39	0.82	1.62	H	Both 2-fold
2	4.66	-5.82	-1.16	1.49	0.06	0.07	0.06	0.95	1.31	2.02	V	Both 2-fold
3	4.83	-5.61	-0.78	1.49	0.01	0.01	0.01	0.15	0.10	0.12	H	Both 2-fold
4	4.89	-5.68	-0.79	1.49	0.02	0.02	0.01	0.14	0.12	0.14	H	Both 2-fold
5	5.26	-4.65	0.61	1.50	0.03	0.03	0.04	0.25	0.35	0.89	V	1-fold, 3-fold
6	5.35	-5.24	0.12	1.48	0.02	0.01	0.01	0.18	0.08	0.11	H	Both 2-fold
7	5.47	-5.57	-0.10	1.47	0.02	0.02	0.02	0.15	0.18	0.10	V	1-fold, 2-fold
8	5.68	-5.42	0.25	1.48	0.02	0.02	0.01	0.08	0.19	0.09	V	1-fold, 3-fold
9	5.69	-5.27	0.42	1.49	0.02	0.02	0.02	0.14	0.20	0.10	V	1-fold, 2-fold
10	5.78	-6.02	-0.24	1.50	0.04	0.03	0.03	0.18	0.19	0.15	V	2-fold, 3-fold
11	5.82	-6.06	-0.24	1.49	0.04	0.05	0.03	0.69	1.63	0.26	H	Both 2-fold
12	5.92	-5.55	0.37	1.48	0.07	0.05	0.05	1.00	0.31	0.53	V	1-fold, 3-fold
13	6.00	-5.66	0.34	1.46	0.02	0.03	0.01	0.11	0.21	0.07	V	Both 2-fold
14	6.11	-5.56	0.55	1.50	0.09	0.09	0.10	0.59	0.44	0.60	V	1-fold, 2-fold
15	6.36	-5.93	0.43	1.49	0.05	0.04	0.03	0.80	0.54	0.30	V	2-fold, 3-fold
16	6.95	-6.79	0.16	1.49	0.12	0.12	0.13	0.67	0.60	0.70	V	2-fold, 3-fold

Table 5.4. Oxygen adsorption energies (E_{ads}) for diatomic oxygen on reduced terrace systems, and the difference in energy between vacancy formation and oxygen adsorption (ΔE E_{vf}-E_{ads}). Oxygen-oxygen bond length in the molecular oxygen species, as well as the adsorption mode and coordination of molecular oxygen atoms to surface cations along with lattice oxygen relaxation are also presented. V and H represent vertical or horizontal adsorption modes respectively.

5.4 Reduced Surface Oxidation (Molecular Oxygen Activation)

After exploring the reduction of YSZ steps and terraces, the re-oxidation of these oxygen deficient non-stoichiometric surfaces by molecular oxygen was investigated. Diatomic molecular oxygen was placed above the vacancy region (the location of the gap-state charge density isosurface) of the reduced terrace surfaces. Information surrounding the adsorption of molecular oxygen onto the reduced terrace surfaces is presented in table 5.4.

The adsorption energy for molecular oxygen on the reduced surface is calculated as;

$$E_{ads} = \frac{E_{rs+a} - E_{rs} - E\ O_2}{2} \tag{5.2}$$

where E_{rs} is the energy of the reduced surface and E_{rs+a} is the energy of the reduced surface with molecular oxygen adsorbed.

In each case the diatomic oxygen was very strongly adsorbed to the surface F-centre and resulted in a partially reduced molecular oxygen species on the surface. The oxygen-oxygen bond length increases from 1.23Å in the gas-phase molecule to ~1.49Å in the partially reduced surface adsorbed species in all systems. As with the surface reduction, systems 1, 3, 15 and 16 are discussed in more detail as examples of low and high vacancy formation energy configurations. In systems 1 and 3, both oxygen atoms of the adsorbed molecular oxygen are 2-fold coordinated to surface cations, an example of the 'horizontal' adsorption mode, with one shared cation between them. It is interesting to note that molecular oxygen has the same adsorption mode for both systems 1 and 3, as after initial reduction in system 1, the vacancy relocates into a sub-surface region. However, on molecular oxygen adsorption, an inter-layer oxygen atom (atom 3 in figure 5.4) relaxes into the sub-surface layer and the site of the initially removed oxygen atom becomes occupied by the molecular oxygen species. In systems 15 and 16, both molecular oxygen atoms also share one cation; one atom of the oxygen molecule is located in the surface lattice position of the initially removed oxygen atom and is 3-fold coordinated to surface cations and the other is 2-fold coordinated to surface cations, which is an example of the 'vertical' adsorption mode. The partially reduced adsorbed molecular oxygen species and their highest occupied molecular orbitals (HOMOs) are displayed in figure 5.8. Visualisation of the adsorbed oxygen HOMOs shows that the defect state electron charge density from the reduced surfaces now resides in the oxygen anti-bonding orbital, resulting in a partially reduced oxygen surface species and explaining the observed increase in the oxygen-oxygen bond length. Bader charge analysis demonstrates that the previously reduced surface cations (described in section 5.3.1) return to their original charge states of the stoichiometric surface, and that the molecular oxygen becomes reduced with a final charge of ~ -1.2 e^-,

compared to the neutral gas-phase molecule. Molecular oxygen was also adsorbed onto the lowest energy reduced step surface, with an adsorption energy of - 5.85 eV, which is in line with the findings of a very strong adsorption of molecular oxygen onto a reduced terrace surface resulting in a partially reduced molecular oxygen surface species.

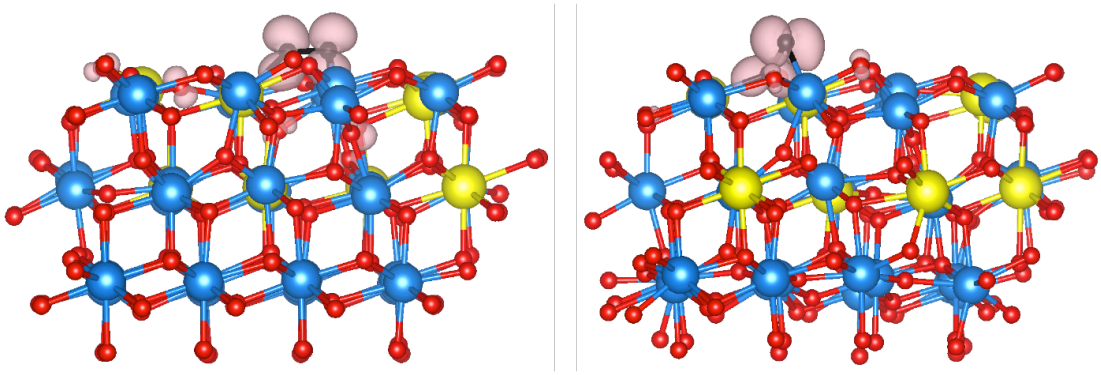

Figure 5.8. Partially reduced molecular oxygen (with partial charge density) adsorbed into the vacancy region of reduced YSZ, system 1 (left) and 16 (right). The black spheres represent atoms of the partially reduced molecular oxygen species.

As with the vacancy formation energies shown earlier and reproduced in table 5.4 (E_{vf}), the adsorption energies for molecular oxygen into the F-centre region of the reduced YSZ surfaces span a wide energy range (-4.65 to -6.79 eV). Our results reveal that the extent of both average lattice oxygen relaxation and the maximum movement of individual oxygen atoms within the lattice was the most important factor in determining the magnitude of the vacancy formation energy. In particular the systems with lower, and therefore more favourable, vacancy formation energies display large relaxations of certain oxygen atoms characterised by maximum oxygen displacements over 1Å and shown pictographically in figure 5.4. However, the explanation for the magnitude of adsorption energy does not appear to be as clear. Whilst there are also large oxygen relaxations present following oxygen adsorption, they do not correlate as well with the absolute adsorption energy. System 2 has the largest maximum relaxation of 2.02Å and has an adsorption energy of -5.82 eV. System 5 has the lowest adsorption energy (-4.65 eV) yet still has a maximum oxygen relaxation of 0.89Å, whereas system 16 has the highest adsorption energy (-6.79 eV), but only has a maximum ionic relaxation of 0.70Å. System 16 does however have the largest average oxygen relaxation. The average oxygen relaxation of lattice oxygen ions upon adsorption of molecular oxygen to the previously reduced surfaces is lower than the corresponding oxygen relaxation observed for the surface reduction process for the majority of systems. For example, the average oxygen relaxation for systems in table 5.4 (following molecular oxygen adsorption) is ~0.05Å or lower, whereas the average oxygen relaxation for systems in table 5.2 (following surface reduction) is ~0.1Å. It is possible that with a larger average ionic relaxation that there is a larger number of atoms with a high maximum

displacement, meaning that a group of atoms, within the local environment as seen previously in figure 5.4, that move a 'large' distance are responsible for accommodating the change that occurs upon reduction or re-oxidation and determining the strength of either process.

One interesting yet unsurprising observation is provided by a comparison of the difference in energy between vacancy formation and oxygen adsorption ($\Delta E\ E_{vf}$-E_{ads}). Only the systems with the lowest vacancy formation energies have large negative energy differences (-0.78 to -1.59 eV). This represents the overall thermodynamics of surface reduction followed by re-oxidation by diatomic molecular oxygen, a negative value represents a favourable process, giving an activated oxygen surface species with a net gain of one oxygen atom to the system.

The net effect of surface reduction followed by molecular oxygen adsorption produces a YSZ surface with one extra oxygen atom, effectively "YSZ+O". A similar concept has been applied before in the work of Shishkin *et al.*[10], amongst others[11]. Their YSZ+O surface is used in response to the experimental finding that CPOM reactions producing oxygen containing products only took place on YSZ samples that had been pre-oxidised[1]. However, the YSZ+O surface used in previous studies[10,11] is constructed by taking a 3-layer (2x2) surface expansion of the cubic-(111) surface of ZrO_2 and replacing two zirconium cations with two yttrium cations. However, instead of removing an oxygen atom for charge compensation, all oxygen atoms remain on their cubic lattice sites. Whilst the overall effect is one of having an extra oxygen in the simulation cell and therefore a YSZ+O surface, this also represents the unphysical case of having a YSZ material in which no charge-compensating stoichiometric oxygen vacancies are present.

5.5 Stoichiometric Surface Oxygen Adsorption

Whilst the above calculations concern themselves with surface reduction followed by molecular oxygen activation on the reduced surface, the interaction of molecular oxygen on the non-reduced YSZ surface containing stoichiometric oxygen vacancies was also investigated. Previous studies for oxygen adsorption on stoichiometric YSZ surfaces have identified three different adsorption modes for molecular oxygen[12,13]; these adsorption modes along with their adsorption energies and characteristics are reproduced in table 5.5.

Study	Adsorption Mode	Adsorption Energy (eV)	O-O Bond Length (Å)	O-O Bader Charge (e^-)
Xia *et al.*[12]	Molecular	-0.35 to -0.02	1.24	-0.02
	Superoxide	-0.47 to +0.61	1.30	-0.56
	Peroxide	+0.94 to +1.04	1.43, 1.53*	-1.64
Cooper *et al.*[13]	Superoxide	-0.47	1.30	-0.57

Table 5.5. Details of molecular oxygen adsorption on stoichiometric YSZ surfaces reproduced from previous computational studies.

*The 'peroxide' O_2 in table 5.5 has two oxygen-oxygen bond lengths reported due to a 'triatomic' form of adsorption whereby one molecular oxygen atom is bonded to a surface lattice oxygen atom.

A variety of molecular oxygen adsorption configurations were investigated over both the multi-region surface slab model and the periodic vacancy model, as described in chapter 4. All three adsorptions modes, previously detected in other computational studies, were also observed in this study. However, whilst the adsorption energies for both the molecular and peroxide adsorption modes are in good agreement with those detailed in table 5.5, no thermodynamically favourable superoxide species was detected. The adsorption energies for molecular oxygen on the stoichiometric YSZ surfaces from this study are given in table 5.6, and the adsorption configurations for the superoxide and peroxide species are shown in figure 5.9.

Multi-Region Slab					Periodic Vacancy Slab				
Sys.	**Adsorption Mode**	**Eads (eV)**	**Bond Length (Å)**	**Bader Charge (e^-)**	**Sys.**	**Adsorption Mode**	**Eads (eV)**	**Bond Length (Å)**	**Bader Charge (e^-)**
1	Molecular	+0.01	1.23	-0.02	**A**	Molecular	-0.06	1.23	-0.02
2	Molecular	-0.42	1.23	-0.04	**B**	Superoxide	+0.96	1.30	-0.38
3	Molecular	+0.01	1.24	-0.02	**C**	Peroxide	+0.85	1.39, 1.58	-1.26
4	Peroxide	+0.75	1.43, 1.49	-1.34	**D**	Peroxide	+0.87	1.39, 1.59	-1.26

Table 5.6. Details of molecular oxygen adsorption on stoichiometric YSZ surfaces.

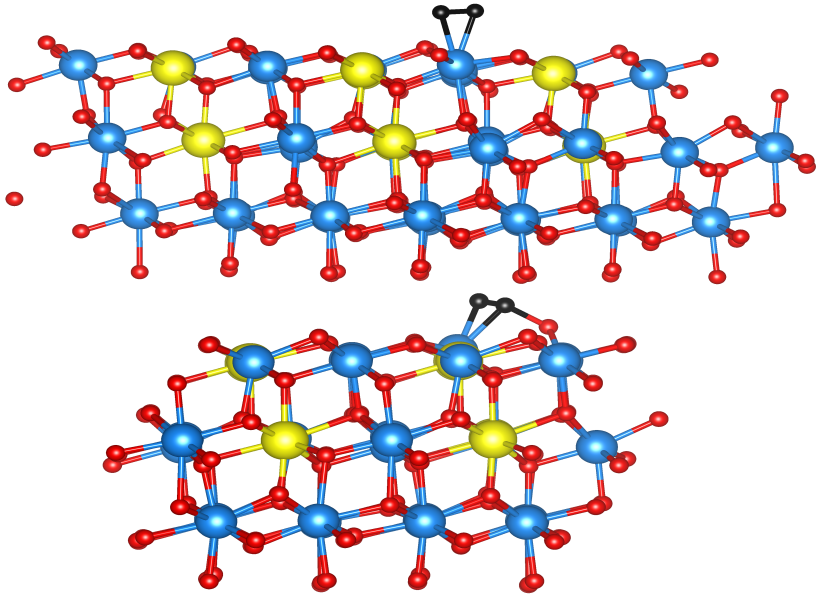

Figure 5.9. Superoxide (top) and Peroxide (bottom) adsorption on the periodic slab model.

From the results obtained both in this work and in previous computational studies molecular oxygen can be seen to adopt three different adsorption modes on stoichiometric YSZ surfaces. However, the nature and strength of these interactions are unclear. The adsorption energy for diatomic oxygen in a molecular configuration in general shows weak physisorbtion of oxygen to the surface, whilst the adsorption of an oxygen molecule as a high-energy 'triatomic' peroxide species is observed both in this study and in previous work. The adsorption of oxygen as a superoxide species is however the most unclear. The work of Xia *et al.*[12] shows that depending on the surface structure, the adsorption energy of the superoxide species can be both thermodynamically favourable or unfavourable with respect to the bare surface and gas-phase oxygen although in this study only unfavourable superoxide adsorption energies were calculated. These contrasting adsorption energy values can possibly be explained by the details of the surface. The thermodynamically favourable superoxide adsorption energy, from the work of Xia *et al.* was obtained on a surface system in which the charge compensating oxygen vacancy remained in the outermost surface layer in the nearest neighbour position to both of the dopant yttrium cations, which has been shown by bulk studies to be the highest energy arrangement for the Y-V-Y defect cluster. On the other hand the thermodynamically unfavourable superoxide adsorption occurred on a surface model in which the charge compensating oxygen vacancy was in the low-energy next nearest neighbour position to both dopant yttrium cations, although still in the outermost surface layer. The periodic vacancy model in this study on which the high-energy superoxide adsorption occurred also has the vacancy NNN to the yttrium cations, although the vacancy is in the sub-surface layer. It was impossible

to stabilise a surface vacancy in the models used here as the vacancy relocated to the sub-surface layer after structural optimisation of the starting surface.

5.6 YSZ Surface Redox Properties Discussion

Our DFT calculations of YSZ surface reduction show that oxygen loss leads to the formation of a doubly occupied defect state that lies within the band-gap of the material, which takes the form of a neutral F-centre vacancy (V^0). The properties of the vacancies calculated in this work for the YSZ surface are similar to those of vacancies calculated in bulk ZrO_2 using periodic[7] and embedded cluster[5] hybrid DFT and the GW approximation[6]. The vacancy formation energy appears to depend on both the nature of the defect state and the oxygen lattice relaxation observed on oxygen loss. The nature of the defect state is dependent on the position of the defect level within the band-gap, which is in turn reliant on the combination of cation orbitals that contribute to the vacancy. Clearly, the oxygen vacancy formation in YSZ is strongly affected by the local environment of the vacancy. Furthermore, the local environment of step surfaces calculated in this study, where large relaxations of surrounding oxygen ions allow vacancies to adopt more stable sites, leads to a significant reduction of the vacancy formation energy (~3.8 eV). The fast diffusion of oxygen and vacancies within YSZ has previously been alluded to as the reason for the increased catalytic activity of YSZ compared to ZrO_2[1]. Additionally, a recent computational study of the properties of un-doped tetragonal zirconia (ZrO_2) nanoparticles found that reduction energies are decreased for nanoparticles when compared to extended surfaces, due in part to the greater structural flexibility gained upon nanostructuring[14].

In agreement with previous studies[12], we find that molecular oxygen will weakly physisorb to stoichiometric YSZ steps and terraces. However, thermodynamically favourable reduced molecular oxygen species present at stoichiometric vacancy sites[12,13] are found only to be meta-stable on larger symmetric slab models. We consider that surface-layer vacancies become artificially stabilised by the constrained system sizes used previously, which becomes apparent on creation of more realistic models[15]. Unlike molecular oxygen adsorption on vacancy sites within stoichiometric YSZ, we find that oxygen will very strongly bind to surface F-centres present in reduced YSZ, resulting in a partially reduced diatomic oxygen surface species.

The first indication of a surface redox mechanism being important in YSZ comes from an experimental study by Zhu et al[1] in which isotopically labelled $^{18}O_2$ is flowed over the YSZ surface as the material is heated. As the temperature increases oxygen exchange is observed, with full conversion occurring at ~900 °C, whereby no $^{18}O_2$ is detected and only $^{16}O_2$ which has to have been liberated from the lattice is found in the product stream. Furthermore an EPR study of nanocrystalline ZrO_2[7] has observed a high concentration of EPR inactive species likely to be associated with diamagnetic states. These are inferred by the observation of a large

strong superoxide signal detected after exposure of the sample to molecular oxygen, despite only a small EPR signal present prior to oxygen treatment. However, assignment of these defects to neutral oxygen vacancies is tentative due to large calculated vacancy formation energies and the lack of coloured samples due to F-centre formation following reductive treatment; nevertheless they do report that their as prepared sample has sub-stoichiometric oxygen content. We have shown that different local geometries present in YSZ increase the likelihood of V^0 formation due to a reduction of the vacancy formation energy. Furthermore, UPS investigation of YSZ[16] shows that the Fermi-level of the material is closer to the conduction band than the valence band suggesting n-type defects are present; the position of the deep gap states are also reproduced in the calculations performed in this study. Additionally, an STM study of YSZ also shows that the Fermi-level lies in the upper-half of the band-gap, whilst demonstrating that high temperature annealing (1000 °C) resulted in oxygen loss and the formation of colour centres verified by the material adopting a “reddish hue”, which disappeared on exposure to oxygen[17]. This demonstration of strong molecular oxygen adsorption to V^0 generated at high temperatures is also in agreement with the temperature dependent isotopic oxygen exchange observed on YSZ[1]. The experimental work described above gives credence to the reduction/oxidation process of the YSZ surface proposed by the computational work in this study, of which a similar phenomenon has been seen previously on thermally reduced TiO_2[18,19,].

5.7 Summary and Conclusions

Bulk ZrO_2 and YSZ surface reduction, achieved by oxygen ion removal, results in the formation of a non-stoichiometric, neutral F-centre vacancy, characterised by the appearance of a doubly-occupied defect state within the band-gap of the material. The charge density of the vacancy remains mostly localised in the region of the vacant ion although some delocalisation of charge onto surrounding cations is observed. The ~5.5 eV vacancy formation energy of bulk ZrO_2 can be lowered to ~4.5 and further to ~3.8 eV for YSZ surfaces and step-edges respectively. The decrease of the vacancy formation energy appears to be associated with the flexibility of the oxygen anion sub-lattice in YSZ and it’s ability to relax in order to best accommodate these non-stoichiometric vacancies. The resultant reduced surfaces can then strongly adsorb and activate diatomic molecular oxygen producing a partially reduced molecular oxygen species and generating an ‘active YSZ+O’ surface.

References:

1. Zhu, J. J.; van Ommen, J. G.; Bouwmeester, H. J. M.; Lefferts, L., Activation of O-2 and CH4 on yttrium-stabilized zircoma for the partial oxidation of methane to synthesis gas. *Journal of Catalysis* **2005,** 233, (2), 434-441.
2. Popov, A. I.; Kotomin, E. A.; Maier, J., Basic properties of the F-type centers in halides, oxides and perovskites. *Nuclear Instruments & Methods in Physics Research Section B-Beam Interactions with Materials and Atoms* **2010,** 268, (19), 3084-3089.
3. Ganduglia-Pirovano, M. V.; Hofmann, A.; Sauer, J., Oxygen vacancies in transition metal and rare earth oxides: Current state of understanding and remaining challenges. *Surface Science Reports* **2007,** 62, (6), 219-270.
4. Pacchioni, G., Modeling doped and defective oxides in catalysis with density functional theory methods: Room for improvements. *Journal of Chemical Physics* **2008,** 128, (18).
5. Ramo, D. M.; Sushko, P. V.; Gavartin, J. L.; Shluger, A. L., Oxygen vacancies in cubic ZrO2 nanocrystals studied by an ab initio embedded cluster method. *Physical Review B* **2008,** 78, (23).
6. Kralik, B.; Chang, E. K.; Louie, S. G., Structural properties and quasiparticle band structure of zirconia. *Physical Review B* **1998,** 57, (12), 7027-7036.
7. Gionco, C.; Paganini, M. C.; Giamello, E.; Burgess, R.; Di Valentin, C.; Pacchioni, G., Paramagnetic Defects in Polycrystalline Zirconia: An EPR and DFT Study. *Chemistry of Materials* **2013,** 25, (11), 2243-2253.
8. Grau-Crespo, R.; Hernandez, N. C.; Sanz, J. F.; de Leeuw, N. H., Redox properties of gold-substituted zirconia surfaces. *Journal of Materials Chemistry* **2009,** 19, (6), 710-717.
9. Ricca, C.; Ringuede, A.; Cassir, M.; Adamo, C.; Labat, F., Revealing the properties of the cubic ZrO2 (111) surface by periodic DFT calculations: reducibility and stabilization through doping with aliovalent Y2O3. *Rsc Advances* **2015,** 5, (18), 13941-13951.
10. Shishkin, M.; Ziegler, T., The Oxidation of H(2) and CH(4) on an Oxygen-Enriched Yttria-Stabilized Zirconia Surface: A Theoretical Study Based on Density Functional Theory. *Journal of Physical Chemistry C* **2008,** 112, (49), 19662-19669.
11. Gorski, A.; Yurkiv, V.; Starukhin, D.; Volpp, H.-R., H2O chemisorption and H-2 oxidation on yttria-stabilized zirconia: Density functional theory and temperature-programmed desorption studies. *Journal of Power Sources* **2011,** 196, (17), 7188-7194.
12. Xia, X.; Oldman, R. J.; Catlow, C. R. A., Oxygen adsorption and dissociation on yttria stabilized zirconia surfaces. *Journal of Materials Chemistry* **2012,** 22, (17), 8594-8612.
13. Cooper, C. S.; Oldman, R. J.; Catlow, C. R. A., Oxidative methane activation over yttrium stabilised zirconia. *Chemical Communications* **2015,** 51, (27), 5856-5859.
14. Puigdollers, A. R.; Illas, F.; Pacchioni, G., Structure and Properties of Zirconia Nanoparticles from Density Functional Theory Calculations. *Journal of Physical Chemistry C* **2016,** 120, (8), 4392-4402.
15. Chaopradith, D. T.; Scanlon, D. O.; Catlow, C. R. A., Adsorption of Water on Yttria-Stabilized Zirconia. *The Journal of Physical Chemistry C* **2015,** 119, (39), 22526-22533.
16. Vohrer, U.; Wiemhofer, H. D.; Gopel, W.; Vanhassel, B. A.; Burggraaf, A. J., Electronic-properties of ion-implanted yttria-stabilized zirconia. *Solid State Ionics* **1993,** 59, (1-2), 141-149.
17. Morrow, S. L.; Luttrell, T.; Carter, A.; Batzill, M., High temperature scanning tunneling microscopy of purely ion conducting yttria stabilized zirconia (YSZ). *Surface Science* **2009,** 603, (13), L78-L81.
18. Carter, E.; Carley, A. F.; Murphy, D. M., Evidence for O-2(-) radical stabilization at surface oxygen vacancies on polycrystalline TiO2. *Journal of Physical Chemistry C* **2007,** 111, (28), 10630-10638.
19. Green, J.; Carter, E.; Murphy, D. M., Interaction of molecular oxygen with oxygen vacancies on reduced TiO2: Site specific blocking by probe molecules. *Chemical Physics Letters* **2009,** 477, (4-6), 340-344.

Chapter 6

Catalytic Partial Oxidation of Methane on YSZ

Chapter 6 utilises the previously created pre-oxidised YSZ surfaces in order to investigate the catalytic partial oxidation of methane on YSZ. The Mars-van Krevelen nature of CPOM on YSZ is demonstrated through the inclusion of lattice oxygen into methane oxidation products. The CPOM reaction pathway is studied in the first instance by investigating the oxidation of methane to the reaction intermediate formaldehyde before this formaldehyde species is further oxidised to the surface formate intermediate or decomposes into syngas.

6.1 Introduction

In this chapter we investigate the catalytic partial oxidation of methane on YSZ using both the active/pre-oxidised YSZ+O surface described in chapter 5, and the original stoichiometric surface first introduced in chapter 4. The use of the active YSZ+O surface for CPOM calculations is inspired by the experimental findings of Zhu *et al.*[1], in which methane pulse experiments are conducted and find that methane oxidation occurs over pre-oxidised YSZ samples and that no oxygen containing oxidation products (CO, CO_2, H_2O) are formed over pre-reduced YSZ samples. These experimental findings are discussed at length in chapter 1. The Mars-van Krevelen nature of CPOM on YSZ is studied by performing geometry optimisation calculations of the different molecular configurations involved in the experimentally proposed CPOM reaction scheme, and various activation barriers are calculated using nudged-elastic band procedures. In particular the oxidation pathways of (i) methane to formaldehyde and (ii) formaldehyde to formate are investigated along with the decomposition of formaldehyde and formate into primary CPOM reaction products.

6.2 Catalytic Partial Oxidation of Methane to Formaldehyde

Following the surface reduction and subsequent re-oxidation process with molecular oxygen, as described in chapter 5, we are left with an activated YSZ surface containing a partially reduced diatomic oxygen species. This redox process generates a catalytically active surface. We first explore the partial oxidation of methane to formaldehyde; adsorption energies of the three intermediate adsorption modes are presented in table 6.1. Four systems have been explored for methane oxidation to formaldehyde; these use the active surface systems 1 and 3 from chapter 5, which have the 1st and 3rd lowest vacancy formation energies. The system number (1 and 3) corresponds to the activated systems produced previously, whilst the designation A, B or C indicates different initial adsorption sites of the carbon CH_3 fragment resulting from hydrogen abstraction from methane. These systems differ in which lattice oxygen atom the CH_3 fragment is adsorbed to. 'E_{ads} active oxygen' denotes that the hydrogen abstracted from the carbon species resides on one of the atoms of the partially reduced molecular oxygen surface species, whereas 'E_{ads} lattice oxygen' means that the abstracted hydrogen is adsorbed onto a lattice oxygen atom, and is only applicable to the first hydrogen abstraction as described in more detail in section 6.2.2

The overall partial oxidation process from methane to formaldehyde can be described as the following; (i) hydrogen abstraction from methane resulting in a *CH_3 fragment absorbed to lattice oxygen and an accompanying surface hydroxyl, (ii) subsequent hydrogen abstraction resulting in an adsorbed *CH_2 fragment and a second surface hydroxyl, and (iii) removal of H_2 from the

system and 'lifting' of oxygen from the surface to leave an adsorbed formaldehyde molecule. The three intermediate configurations in the methane to formaldehyde partial oxidation process for the system 3_A active oxygen pathway are pictured in figure 6.1.

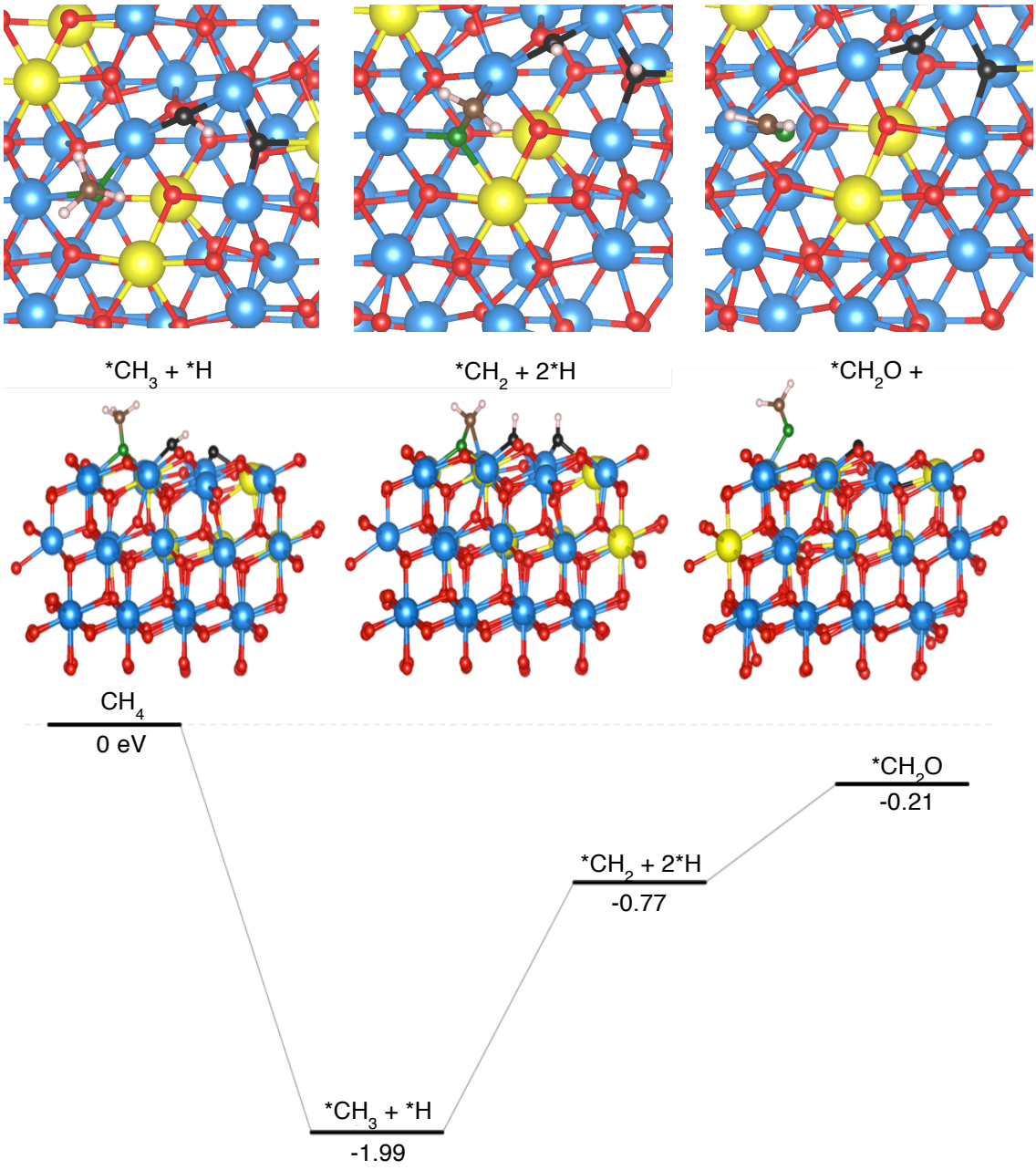

Figure 6.1. The intermediate adsorption modes for the partial oxidation of methane to formaldehyde for the system 3_A active oxygen pathway, with top views given. The green sphere represents the lattice oxygen providing an adsorption site for the $*CH_3$ fragment, with the black spheres the same atoms highlighted in figure 5.8 – chapter 5 as belonging to the activated molecular oxygen species.

	$*CH_3 + *H$		$*CH_2 + 2\,*H$		$*CH_2O + \uparrow H_2$	
System	E_{ads} active oxygen (eV)	E_{ads} lattice oxygen (eV)	E_{ads} active oxygen (eV)	E_{ads} lattice oxygen (eV)	E_{ads} active oxygen (eV)	E_{ads} lattice oxygen (eV)
1_A	- 1.99	- 2.39	- 0.77	- 1.32	- 0.21	- 0.03
3_A	- 1.91	- 2.04	- 0.91	- 1.42	0.27	0.09
3_B	- 1.31	- 1.33	- 0.55	0.29	1.90	- 0.17
3_C	- 1.30	- 1.31	- 0.60	- 0.78	2.53	0.68

Table 6.1. Adsorption energies (E_{ads}) for the intermediate adsorption modes for methane oxidation to formaldehyde, (*) indicates a surface adsorbed species (↑) signifies that the species has been removed from the surface.

Details of the intermediate adsorption modes are discussed in depth in the following sections, although it is instructive to make some general observations about the strengths of the interactions. All configurations of adsorbed $*CH_3$ and a surface hydroxyl group are lower in energy, and therefore more stable, than the bare activated surface and a gas phase methane molecule. The adsorption energies are quite similar for abstracted hydrogen coordinating either directly to the active oxygen or to a surface lattice oxygen ion, with adsorption to the lattice ion more favourable in each case. All but one of the configurations found for the surface adsorbed $*CH_2$ with two surface hydroxyls are thermodynamically favourable with respect to the starting surface and gas phase methane. However, all of the $*CH_2$ and 2-OH systems are higher in energy than their $*CH_3$ and 1-OH predecessor systems. The adsorbed formaldehyde has both favourable and unfavourable adsorption energies compared to gas phase methane, although this complex scenario warrants a more detailed explanation, which will be given below.

6.2.1 Hydrogen Abstraction from Methane

The first step in the partial oxidation of methane to formaldehyde is the initial hydrogen abstraction from methane forming an adsorbed $*CH_3$ fragment, the equivalent of a surface methoxy group, and an adsorbed *H as a surface hydroxyl. Table 6.1 shows that this initial hydrogen abstraction is thermodynamically favourable when compared to the starting activated YSZ surface and gas phase methane. The abstracted hydrogen can reside either directly on an oxygen atom of the partially reduced molecular oxygen species or on a neighbouring lattice oxygen atom with adsorption energies ranging between -1.30 and -2.39 eV. For all $*CH_3$ forming abstraction/adsorption processes the active molecular oxygen species dissociates, with both oxygen atoms becoming lattice oxygen ions (if the abstracted hydrogen adsorbs onto a lattice oxygen) or one oxygen atom becoming a lattice oxygen and the other a surface hydroxyl (if the abstracted hydrogen adsorbs to the active oxygen).

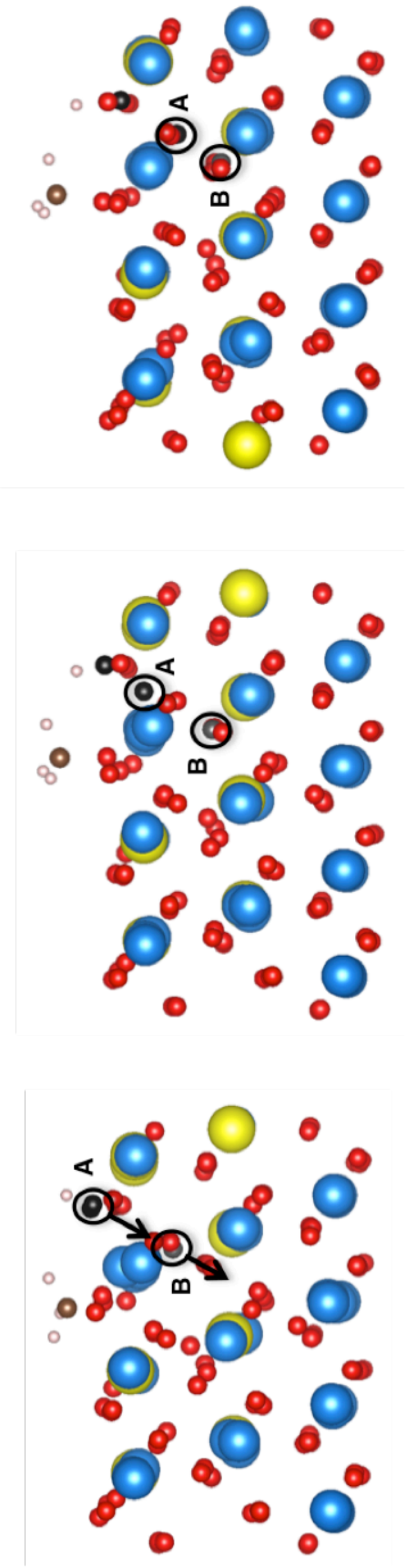

Figure 6.2. Initial (left) and final configurations of atoms after abstraction/adsorption of hydrogen from methane forming surface methoxy and a surface hydroxyl with the abstracted H-atom on active oxygen (center) and on lattice oxygen (right) for system 1_A.

The strongest adsorption energies for the abstraction/adsorption process are encountered on system 1_A, depicted in figure 6.2, being -1.99 eV when the abstracted hydrogen is adsorbed onto the active oxygen and -2.39 eV when this hydrogen adsorbs onto lattice oxygen. In both configurations, there is a concerted movement of oxygen atoms upon structural relaxation that accompanies the abstraction of hydrogen and dissociation of active molecular oxygen. The lattice oxygen atom 'B' moves from the first sub-surface layer into a vacant lattice site in the second sub-surface layer. Atom 'A', originally part of the active oxygen molecule, moves towards the vacant lattice site created by the movement of atom 'B', occupying an inter-layer position in the less favourable active oxygen case and fully filling the newly-created vacant lattice site in the more favourable lattice oxygen case. In a similar situation to that described above, the CH_3 fragment in system 3_A adsorbs onto what is initially an inter-layer lattice oxygen ion, and following structural relaxation this lattice oxygen now occupies a vacant surface lattice site. In contrast to these two systems, very little relaxation of ions within the oxygen sub-lattice occurs upon geometry optimisation for systems 3_B/C.

The activation barrier for hydrogen abstraction from gas phase methane has been estimated to be +1.33 eV by performing a nudged elastic band (NEB) calculation with 5 intermediate images in-between a geometry optimised methane molecule and the $*CH_3$ methoxy and hydroxyl end-point. The NEB relative energy plot is shown in figure 6.3 and the geometries for each image are shown in figure 6.4. The approximate transition-state corresponds to image 3, the highest energy structure, in which the hydrogen has been abstracted from methane and the system goes via a short-lived radical intermediate before coordinating to surface lattice oxygen.

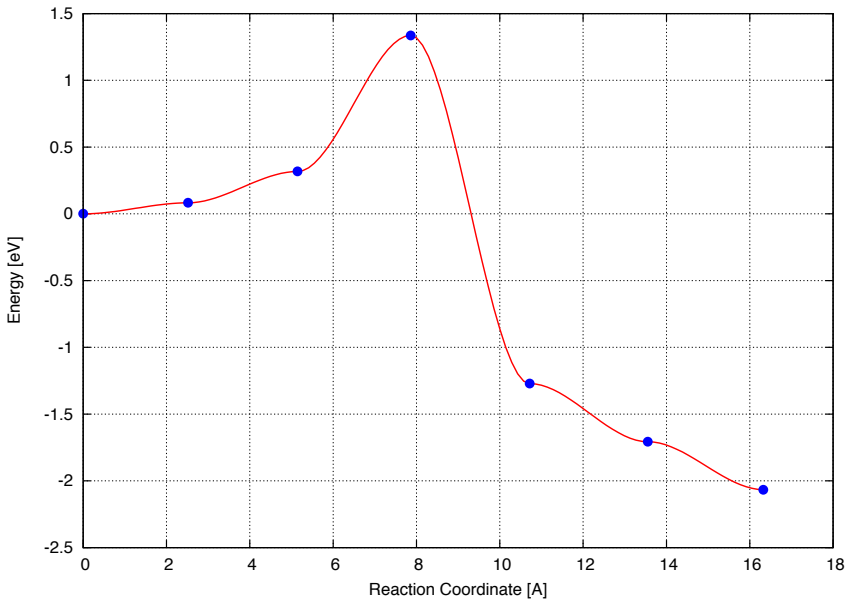

Figure 6.3. Methane to surface methoxy NEB relative energy path w.r.t reaction coordinate for the '1_A active' system.

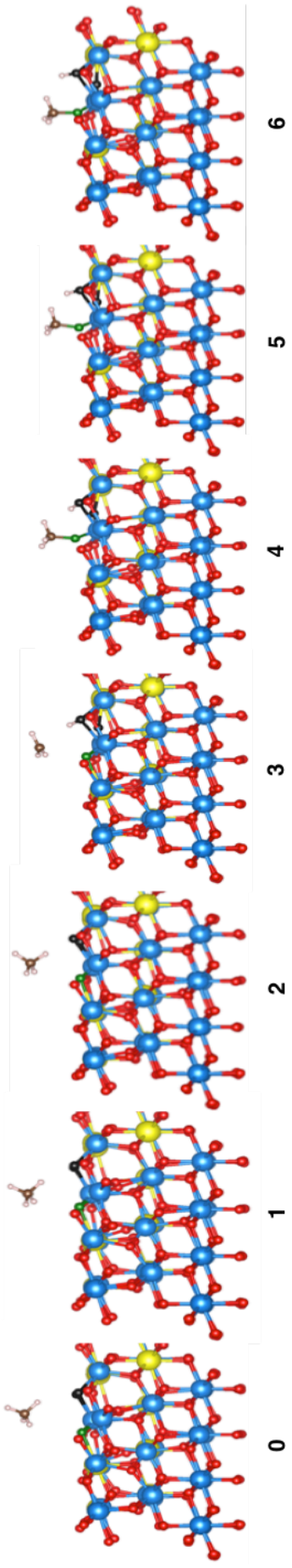

Figure 6.4. Methane to surface methoxy NEB images for the '1_A active' system

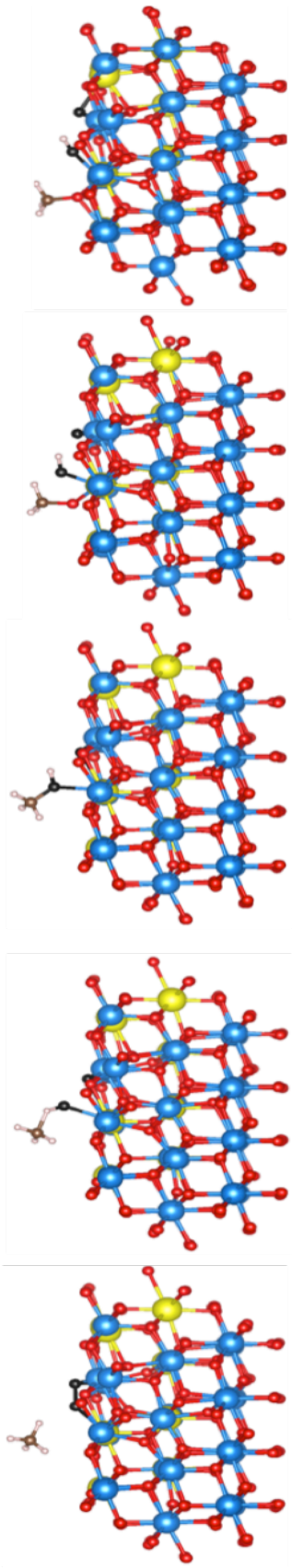

Figure 6.5. Methane to surface methoxy; various images for the '3_A active' system.

In contrast to the hydrogen abstraction pathway observed above for system 1_A in which a methyl radical intermediate is observed, the abstraction pathway calculated for system 3_A proceeds via an adsorbed methanol species. Various images from this pathway are depicted in figure 6.5, and the NEB relative energy plots are given in figure 6.6. Initially, the adsorbed methanol like species was the major pathway intermediate, with the gas phase methane 'snapping' directly to the adsorbed methanol before again 'snapping' to the final adsorbed methoxy configuration. This gave an initial reaction pathway that was entirely downhill in energy. However, intermediates (I1 and I2 figure 6.5) were found by running subsequent NEB calculations with a finer interpolation of 3 images between the methane-methanol and 3 images between the methanol-methoxy structures. Intermediate 1 is 1.4 eV higher in energy than methane in the gas phase, and whilst intermediate 2 is thermodynamically favourable compared to gas-phase methane it corresponds to an approximate activation energy of 1.45 eV for the transformation of adsorbed surface methanol to surface methoxy.

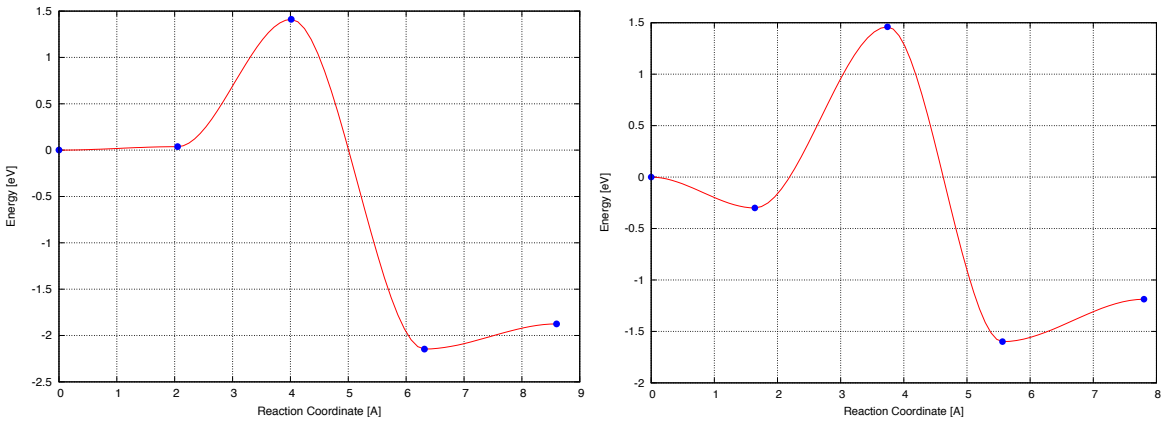

Figure 6.6. Relative NEB energies for the two finer NEB pathways for methane to surface methoxy for the '3_A active' system; methane to surface methanol (left), surface methanol to surface methoxy (right).

For comparison with the mechanism observed on the reduced and re-oxidised surface, adsorption of $*CH_3$ methoxy and a surface hydroxyl on the bare stoichiometric surface is attempted. Only one of the systems optimised to a structure resembling those seen on the active surface and the adsorption energy was +2.12 eV higher in energy than gas phase methane and the stoichiometric starting surface in contrast to the favourable reaction energies calculated for the activated surface.

The NEB pathway for the hydrogen abstraction from methane, forming a surface methoxy species, was also checked with hybrid functional calculations. In order to understand better the activation barrier for this important C-H activation step, single-point calculations for each image of the NEB pathway were conducted at the hybrid-DFT level of theory using the HSE06 exchange-correlation functional. The relative energy difference of the transition state (image 3 in figure 6.4) increases from +1.33 to +1.59 eV. The hybrid functional calculation predicts a higher energy barrier for hydrogen abstraction of ~0.3 eV when compared to the GGA-DFT functional, although even with the increased activation energy this process would still be expected to take place under the catalytic reaction conditions at which methane partial oxidation occurs. Additionally, the final surface state of the methoxy and hydroxyl is ~0.4 eV lower in energy, relatively, for the hybrid calculation when compared to the GGA one. The partial charge density isosurfaces and density of states plots for the methyl radical transition state from both the hybrid- and GGA-DFT calculations are shown in figure 6.7. There is a larger amount of charge density localised on the methyl carbon atom, and less charge density on the surface oxygen atoms, in the hybrid functional calculation when compared to the GGA calculation. Furthermore, examination of the density of states plots explains the increased relative energy of the transition state observed for the hybrid functional. The energy levels of the HOMO of the methyl radical transition state lie at higher energy positions within the band-gap when compared to the GGA calculation, the HOMO energy levels of the GGA calculation remain very close to the valence band.

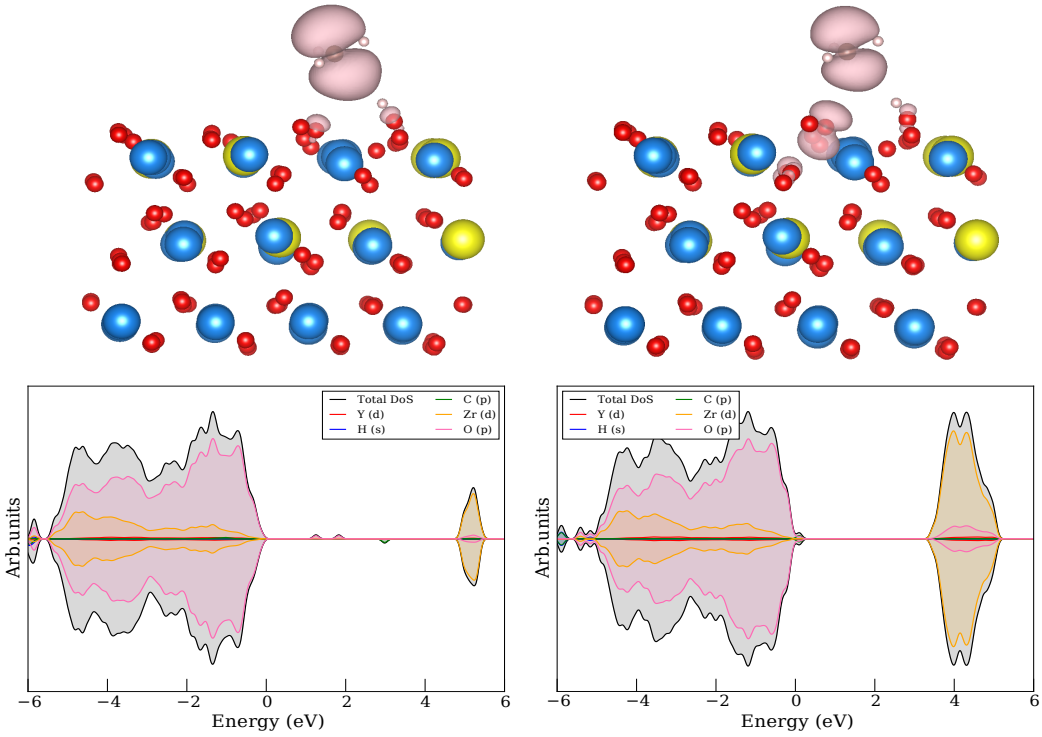

Figure 6.7. Partial charge density (top) and density of states (bottom) for the methyl radical transition state using hybrid (left) or GGA (right) functionals.

6.2.2 Hydrogen Abstraction from *CH_3

Following the first hydrogen abstraction from methane, a second hydrogen abstraction can occur from the adsorbed *CH_3 surface methoxy species. This subsequent oxidation step results in the formation of an adsorbed *CH_2 species and a second surface hydroxyl. The adsorbed *CH_2 species of system 3_A on active oxygen can be seen in the middle image of figure 6.1, and the partial charge density of the 3_A lattice oxygen system HOMO is presented in figure 6.6. As can be seen from both of these images, abstraction of a hydrogen atom from the *CH_3 fragment does not directly result in a molecularly adsorbed formaldehyde species, but instead gives rise to a tetrahedral carbon centre coordinated to the two remaining hydrogen atoms and initial oxygen atom from the surface methoxy group as well as also being coordinated to a surface metal cation. The partial charge density of the 3_A lattice oxygen system HOMO shows a large region of electronic charge between the central carbon atom and the surface metal. In the case of the 3_A lattice oxygen system, pictured in figure 6.8, the 1st abstracted hydrogen is adsorbed onto a lattice oxygen ion and the 2nd abstracted hydrogen is adsorbed onto a lattice oxygen ion that was originally part of the active molecular oxygen species.

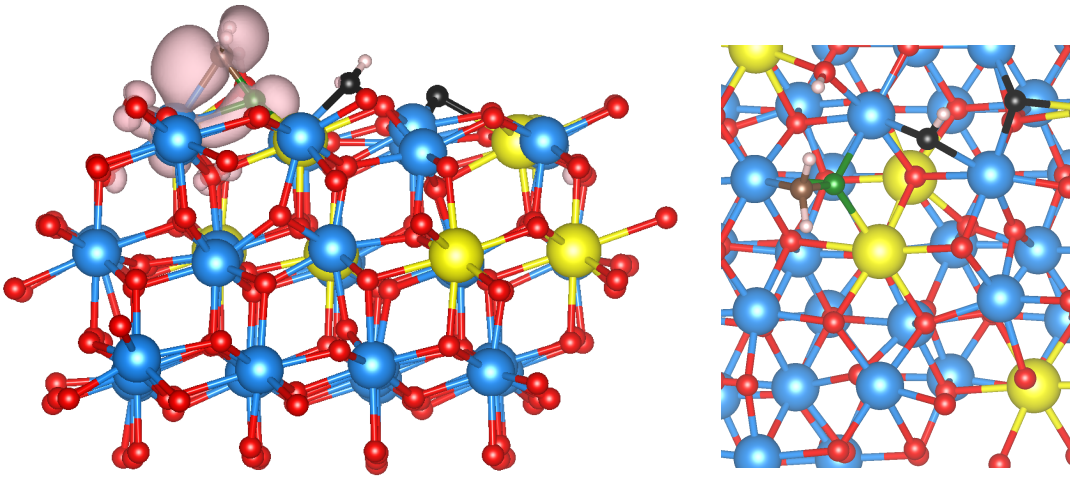

Figure 6.8. Tetrahedral coordinated adsorbed *CH2 species (with two surface hydroxyls) of the 3_A lattice oxygen system, with top view (right).

The adsorption energies for the *CH_2 systems with respect to gas phase methane are displayed again in table 6.2 along with details of the coordination environments present in each system. The systems referred to as ‘active’ or ‘lattice’ follow on from the previous section in which a first hydrogen atom is abstracted from methane, forming *CH_3 and a surface hydroxyl. The active/lattice designation solely depends on whether this initial hydroxyl uses lattice oxygen or one of the atoms from the active oxygen species, all oxygen atoms that could provide the adsorption site of the second abstracted hydrogen in this section are thought of as lattice

oxygen as the active species dissociates upon the first abstraction step. In this section it is instructive to compare between similar systems, for example '3_A lattice' compared with '3_A active'. In general the adsorption/abstraction interactions are stronger on the 'lattice' configuration than the 'active' one, as is the case for the $*CH_3$ surfaces of the previous section. However, there are a number of different factors that could affect the strength of the interaction. We have seen previously in chapter 5, that the extent of oxygen sub-lattice relaxation has a large effect on the strength of reduction or adsorption, which also seems to be the case here: the adsorption/abstraction process is more favourable between systems when there is a larger degree of oxygen lattice relaxation, except for the two system 1_A configuration where the $*CH_2$ on the 'active' surface is coordinated to yttrium instead of zirconium like on the 'lattice' surface. This feature coupled with the least favourable adsorption interactions being on system 3_B suggest that the $*CH_2$ adsorption is more favourable when the carbon atom is coordinated to a zirconium atom instead of yttrium. The $*CH_2$ fragment C-OH and O-OH distances could also influence the adsorption strength. These distances indicate how close the $*CH_2$ is to the surface hydroxyls, with the strongest interaction energies observed for systems in which the $*CH_2$ is closest to the hydroxyls. Furthermore, it appears as if hydrogen bonding between the hydroxyls also stabilises the adsorption interaction. Even though system '3_B active' is coordinated to yttrium, it is possible that the extent of sub-lattice relaxation and hydrogen bonding between hydroxyls stabilises the adsorption making it a stable structure when compared to system '3_B lattice'.

System	E_{ads} (eV)	C-M^+ Coordination	C-OH distances (Å)	O-OH distances (Å)	OH coordination
1_A active	- 0.77	Yttrium	4.24, 4.27	3.08, 3.10	Both 2-fold (b)
1_A lattice	- 1.32	Zirconium	3.05, 3.54	3.36, 4.03	2-fold (b) & 3-fold (m)
3_A active	- 0.91	Zirconium	3.10, 4.90	3.90, 5.51	2-fold (b) & 3-fold (m)
3_A lattice	- 1.42	Zirconium	3.26, 3.67	2.79, 3.00	Both 2-fold (b)
3_B active	- 0.55	Yttrium	3.87, 5.63	2.88, 5.05	1-fold (t) & 2-fold (b) #
3_B lattice	0.29	Yttrium	3.95, 4.33	3.02, 3.25	2-fold (b) & 3-fold (m)
3_C active	- 0.69	Zirconium	3.78, 5.58	3.04, 5.22	1-fold (t) & 2-fold (b) #
3_C lattice	- 0.78	Zirconium	3.03, 3.08	3.08, 3.96	2-fold (b) & 3-fold (m)

Table 6.2. Adsorption energies (E_{ads}) for $*CH_2$ systems and accompanying details of the coordination environments. C-M^+ indicates the type of cation coordinated to carbon, C-OH and O-OH distances give the distance between the $*CH_2$ carbon or $*CH_2$ lattice oxygen and hydroxyl oxygen atoms. The OH coordination gives the degree of coordination to surface cations for each hydroxyl species as well as the type of surface OH; (t) terminal-OH, (b) bridging-OH and (m) multi-coordinated-OH. # indicates that there is hydrogen bonding between the two surface hydroxyls.

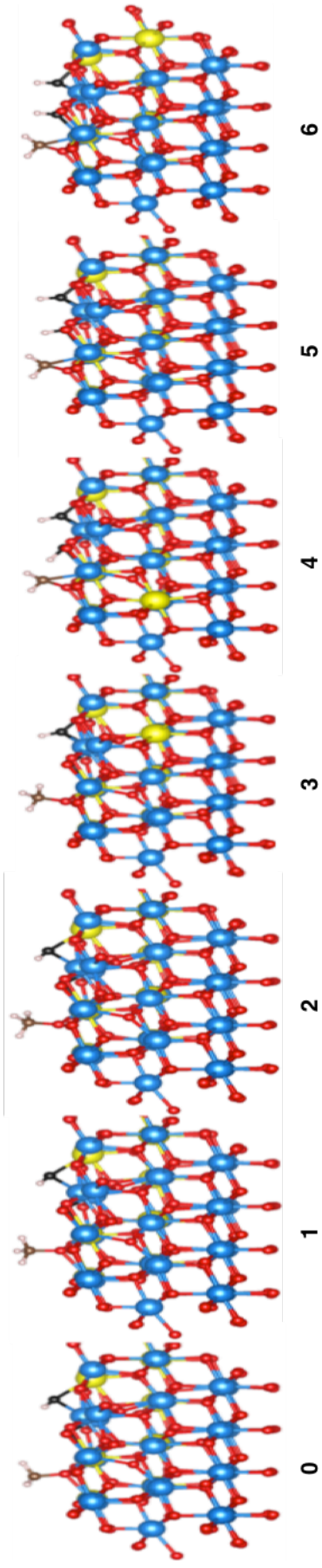

Figure 6.9. Methoxy to adsorbed *CH_2 images for the '3_A active' system.

Whilst the adsorption energies for the adsorbed *CH_2 species are thermodynamically favourable when compared to methane in the gas phase, these intermediate structures are higher in energy than the surface adsorbed methoxy and single surface hydroxyl species. Figure 6.9 displays the intermediate images and figure 6.10 shows the relative energies for the NEB pathway between adsorbed methoxy and adsorbed *CH_2. The final *CH_2 structure is 1.37 eV higher in energy than the starting *CH_3 system, and has an approximate reaction barrier of 1.74 eV.

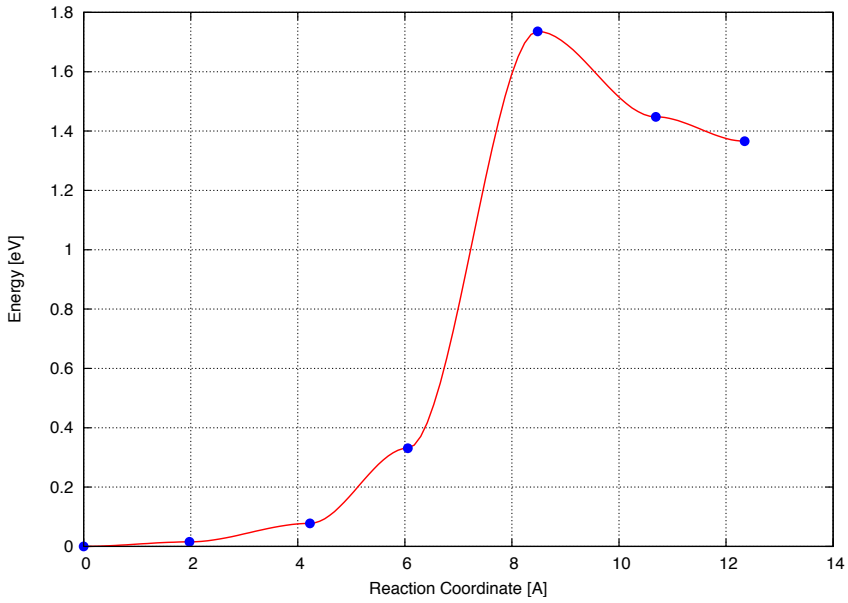

Figure 6.10. Methoxy to adsorbed *CH_2 NEB relative energies for the '3_A active' system.

It is instructive to consider oxygen atom movement in the course of these two hydrogen abstraction steps. The original catalytically active pre-oxidised starting YSZ+O surface is oxygen rich and contains an extra oxygen atom when compared to the stoichiometric YSZ system. This extra oxygen atom is contained within the partially reduced molecular O_2 species. Upon the first hydrogen abstraction step, forming surface methoxy (*CH_3), the molecular O_2 species dissociates, a surface hydroxyl is formed, and the carbon atom coordinates to a surface lattice oxygen atom. The abstracted hydrogen can either form a surface hydroxyl with one of the molecular O_2 atoms or with a lattice oxygen atom; in the case of the former one of the molecular O_2 atoms becomes a surface lattice oxygen and the other is part of the surface adsorbed hydroxyl species, in the latter case both molecular O_2 atoms become lattice oxygen and an original lattice oxygen atom becomes the surface adsorbed hydroxyl. This first surface hydroxyl species now accounts for the 'extra' oxygen atom in the original active surface, with all other oxygen atoms now considered lattice oxygen. A second hydrogen abstraction from the *CH_3 methoxy species, forming the *CH_2 species and a second surface hydroxyl occurs then by the abstracted hydrogen coordinating to a surface lattice oxygen atom. This system with two

surface hydroxyls can be tentatively viewed as having one 'less' lattice oxygen atom than the original YSZ+O surface, although it is possible for one of the hydroxyls to occupy a lattice oxygen position. Finally, as discussed further in the following section, removal of the two hydrogen atoms allows both hydroxyl oxygen atoms to become lattice oxygen species and results in the formation of surface formaldehyde. The 'extra' oxygen atom of the starting YSZ+O system is now contained in the surface adsorbed formaldehyde molecule, with this oxygen atom originating as a surface lattice oxygen species.

6.2.3 Formation of Surface Formaldehyde

As was mentioned in section 6.2.2, surface adsorbed formaldehyde is not immediately formed upon a second hydrogen abstraction, forming a second surface hydroxyl, from the adsorbed $*CH_3$ methoxy group. Even though the adsorbed $*CH_2$ group contains the same stoichiometry as a formaldehyde molecule we find that it is only when the two abstracted hydrogen atoms are removed, effectively leaving as H_2, that the lattice oxygen can be 'lifted' from the surface resulting in a configuration resembling that of adsorbed formaldehyde. Figure 6.11 shows the initial adsorbed $*CH_2$ molecule with surface hydroxyls still present and the corresponding adsorbed formaldehyde molecule after the hydrogen atoms have been removed for system '3_A - active'.

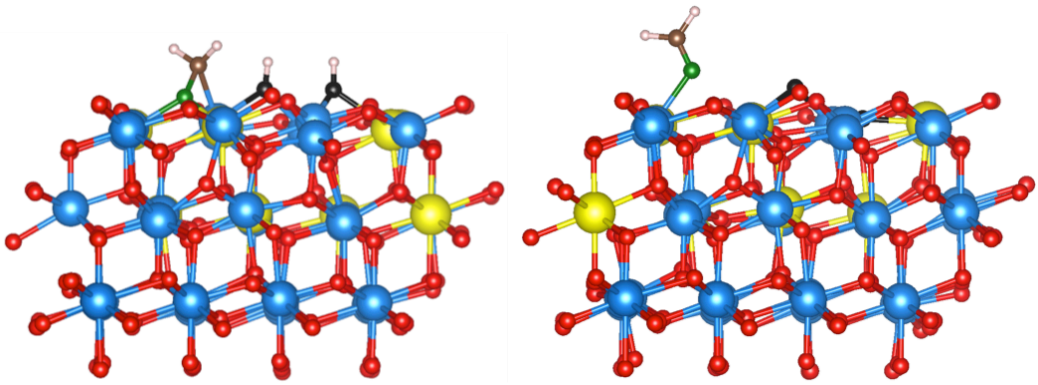

Figure 6.11. Adsorbed $*CH_2$ with surface hydroxyls (left) and adsorbed formaldehyde $*CH_2O$ with hydrogen atoms removed (right), for system 3_A active.

Removal of the hydrogen atoms allows the two oxygen atoms that form the hydroxyls to become surface lattice ions; the leftmost hydroxyl oxygen already occupies a lattice position whilst the rightmost oxygen atom visibly 'sinks' into the lattice; which in turn allows the lattice oxygen coordinated to the $*CH_2$ fragment to be lifted out of the lattice, resulting in a surface adsorbed formaldehyde molecule. This process involving both hydroxyl oxygen atoms being incorporated as lattice oxygen ions after the removal of the hydrogen atoms occurs for all systems except the 3_B and 3_C 'active' systems. The adsorption energies for these surface

adsorbed formaldehyde systems range from -0.21 to +0.68 eV (table 1), when compared to the activated starting surface and gas phase methane. We propose that even the most unfavourable system at +0.68eV may be achievable under the reaction conditions used experimentally (~900 °C). Furthermore, as has been previously proposed[2], there will also be a free energy stabilisation due to the entropy gain upon desorption of H_2 (~1.58 eV at 900°C)[#]. Systems 3_B and 3_C 'active' have significantly higher adsorption energies of +1.90 and +2.53 eV respectively. These systems both contain terminal hydroxyls after the second hydrogen abstraction step. Figure 6.12 shows that when the hydrogen atoms are removed from a system containing a terminal-OH, there is no available lattice site for the hydroxyl oxygen to occupy so it remains in a high-energy position out of the surface.

(# Standard entropy of hydrogen; $S^0_{gas,1bar}$ = 130.68 J/mol*K[3]. At 900°C ≈ 153 kJ/mol ≈ 1.58 eV)

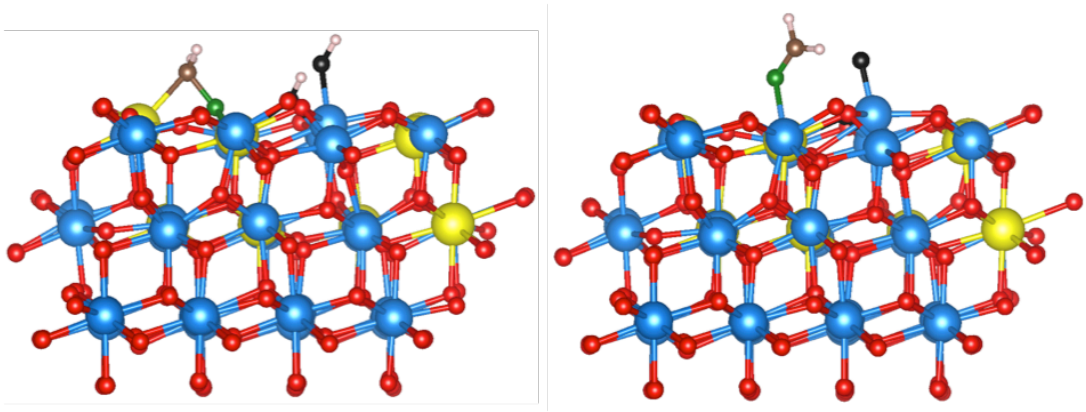

Figure 6.12. Adsorbed *CH_2 with surface hydroxyls (left) and adsorbed formaldehyde *CH_2O with hydrogen atoms removed (right), for system 3_B active.

6.2.4 Surface Formaldehyde Decomposition

The experimentally determined reaction mechanism for CPOM[4], in which formaldehyde is a key intermediate, states that the formaldehyde formed from methane oxidation can either be oxidised further to surface formate or decompose directly into syngas. In the first instance we investigate how this formaldehyde species decomposes on the stoichiometric YSZ surface. Removing one or both of the formaldehyde hydrogen atoms in order to form surface hydroxyl species was investigated. It was found for the 3_A active system that removal of just one hydrogen atom was less thermodynamically unfavourable compared to forming two surface hydroxyls, although both of these scenarios are higher in energy when compared to the stoichiometric YSZ surface and gas-phase formaldehyde. Removing one hydrogen gives an adsorption energy of +0.36 eV whilst removal of both hydrogen atoms results in an adsorption energy of +1.44 eV. The relative energies of these configurations are readily explained upon examination of the electronic structure and band occupancy of the systems. Formaldehyde

adsorption on stoichiometric YSZ induces the presence of an unoccupied state within the band-gap, which becomes occupied upon removal of one or both of the formaldehyde hydrogen atoms in order to form surface hydroxyl species, with the occupied state ~1eV closer to the valence band in the case of one hydroxyl when compared to two hydroxyls. The adsorption configuration and partial charge density of removing one formaldehyde hydrogen atom, forming one surface hydroxyl and an adsorbed *CHO species, is depicted in figure 6.13. The partial charge density takes the form of a C-O anti-bonding orbital with one of the lobes containing the remaining formaldehyde hydrogen and another lobe in between the formaldehyde carbon and surface cation.

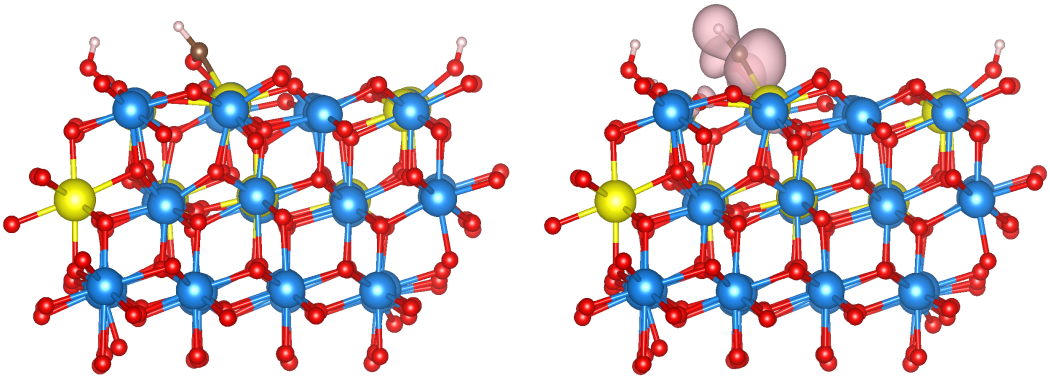

Figure 6.13. Adsorbed *CHO + OH (left) and with partial charge density (right).

This hydrogen abstraction from formaldehyde, forming the adsorbed *CHO + OH, was found to proceed with an activation barrier of 1.46 eV from a nudged-elastic band calculation. The relative energy pathway is given in figure 6.14, and the intermediate geometries are displayed in figure 6.15.

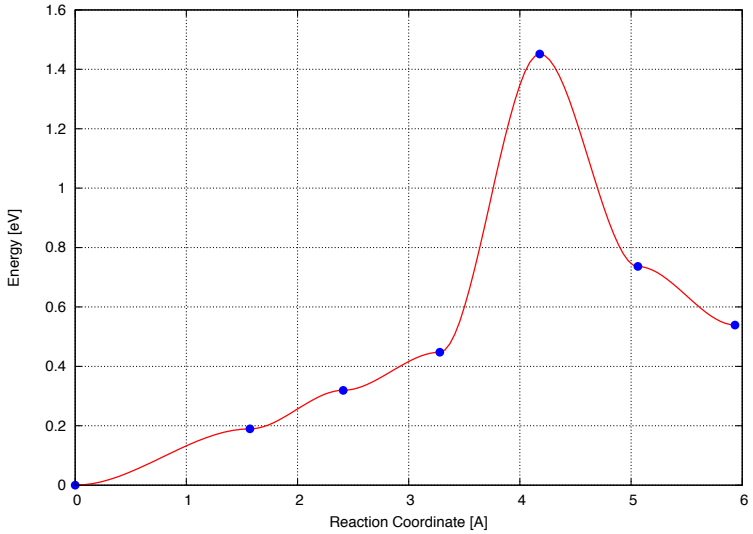

Figure 6.14. Hydrogen abstraction from formaldehyde forming *CHO + OH; NEB relative energies.

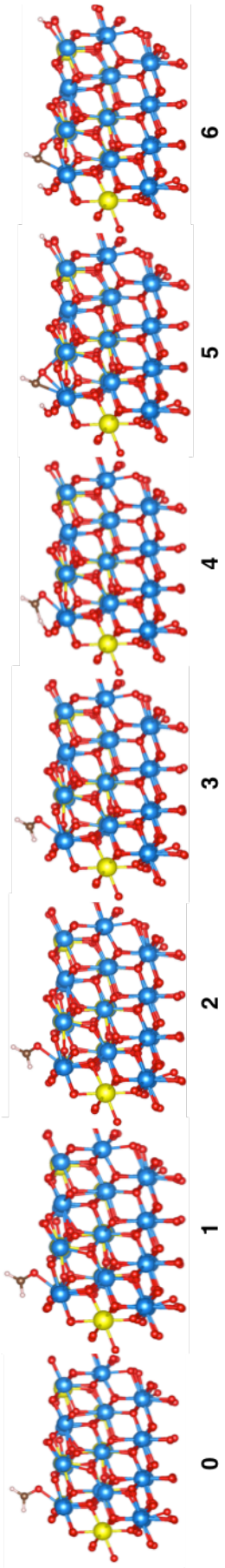

Figure 6.15. Hydrogen abstraction from formaldehyde geometries.

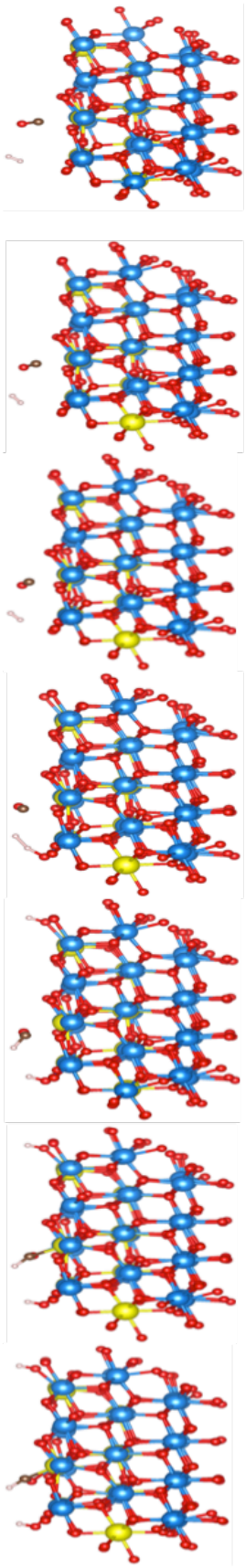

Figure 6.16. Hydrogen desorption geometries from the *CHO + OH configuration.

The desorption of molecular hydrogen from this *CHO + OH configuration was then investigated using a nudged elastic band calculation, and is found to proceed with an activation barrier of 1.53 eV. The resultant structure contains molecular hydrogen and carbon monoxide in the gas phase ~3Å above the YSZ surface, and is of a similar energy to the starting *CHO + OH structure. The intermediate geometries for each structure in the band are depicted in figure 6.16, and the relative energy plot is shown in figure 6.17. The activation barrier is of a similar magnitude to all of the hydrogen abstraction steps, so the decomposition of formaldehyde to syngas is feasible at the catalytic reaction temperatures, and can be expected to occur in the absence of an active oxygen species, which provides the thermodynamic driving force and electron acceptor ability required for the oxidation of formaldehyde to formate, as discussed in section 6.3.

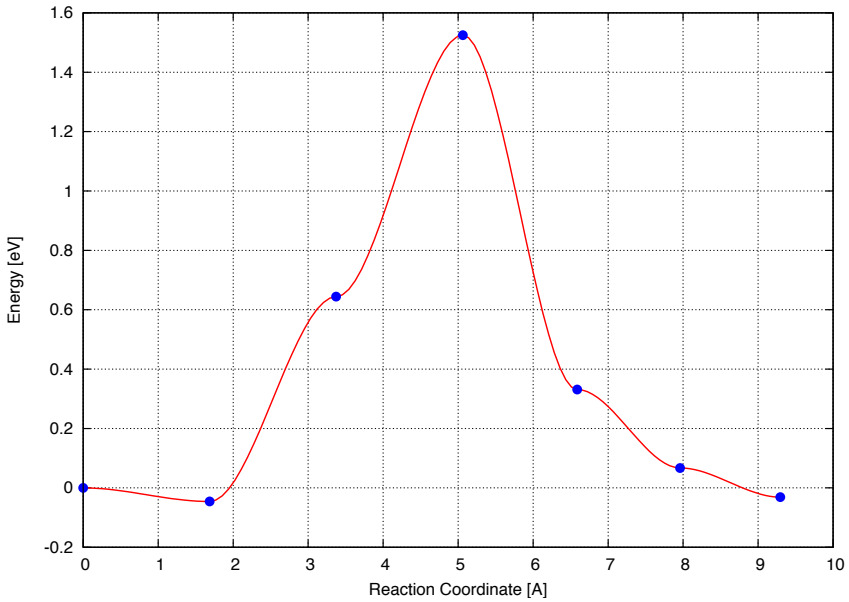

Figure 6.17. Relative energies for hydrogen desorption from the *CHO + OH configuration.

6.3 Oxidative Conversion of Formaldehyde to Formate

The adsorption and oxidative conversion of formaldehyde on YSZ surfaces with partially reduced active oxygen species was investigated on the reduced/re-oxidised terrace surface of system 3 used earlier in section 6.2 and described in chapter 5. Two different formaldehyde adsorption sites have been investigated for oxidation through to surface formate. As with methane, formaldehyde was not found to interact directly with the partially reduced oxygen species but instead would first adsorb to the YSZ surface. Formaldehyde was found to physisorb onto a surface cation via the carbonyl oxygen before undergoing nucleophilic attack from surface lattice oxygen in order to form a dioxymethylene intermediate species, in agreement with the proposed mechanism for the transformation of formaldehyde on zirconia[5].

The active molecular oxygen species could then abstract hydrogen directly from the surface intermediate, giving the final surface adsorbed formate and a surface hydroxyl species or the abstracted hydrogen can form a hydroxyl with a lattice oxygen ion. This hydrogen abstraction and hydroxyl formation process, whether on active or lattice oxygen, causes the molecular oxygen-oxygen bond to break with one oxygen atom incorporated into YSZ as surface lattice oxygen. The adsorption energies for each of the surface species are presented in table 6.3 and are given with reference to the re-oxidised surface system containing partially reduced molecular oxygen and gas-phase formaldehyde.

Surface Species	Adsorption Energy (eV)	
	System 3 – f1	System 3 – f2
Formaldehyde	-0.53	-0.70
Dioxymethylene	-0.63	-0.91
Formate + OH (active)	-3.48	-3.83
Formate + OH (lattice)	-3.44	-4.98

Table 6.3. Adsorption energies for surface formaldehyde and subsequent oxidation species calculated on terrace surface systems.

The adsorption of formaldehyde and conversion to formate on the oxygenated system '3 – f1' is depicted in figure 6.18. Conversion of formaldehyde to dioxymethylene increases the coordination of the central carbon atom and the change from sp^2 to sp^3 hybridisation is reflected in a large reduction of all the bond angles to become closer to the 109.5° expected of an atom in a tetrahedral coordination environment. The hydrogen atoms of the dioxymethylene species in figure 6.13 extend outwards from and behind the plane of the page. As can clearly be seen, surface lattice oxygen is incorporated into the formaldehyde molecule upon formation of the dioxymethylene intermediate. Lastly, on hydrogen abstraction and conversion to surface formate the bond angles return to ~120° in accordance with a trigonal planar geometry.

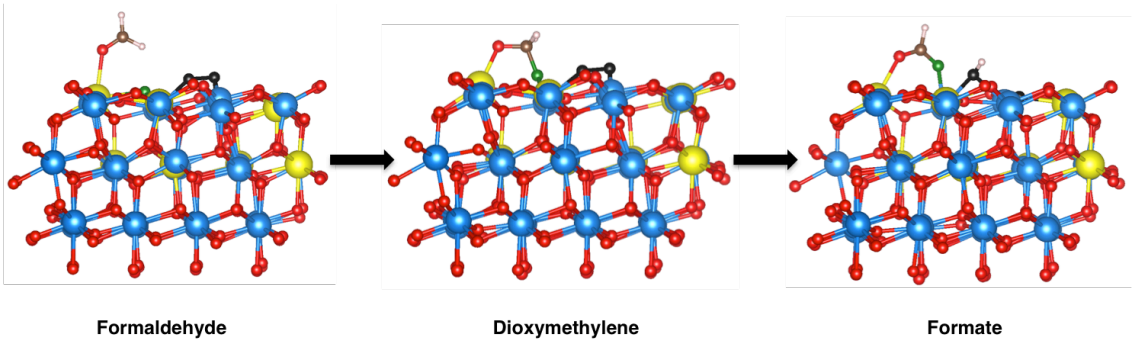

Figure 6.18. Conversion of adsorbed formaldehyde to formate via a dioxymethylene intermediate. The green sphere represents a specific surface lattice oxygen atom.

Activation barriers involved in the oxidative conversion of formaldehyde to formate have been calculated by performing NEB calculations between formaldehyde and dioxymethylene, and dioxymethylene and formate. The conversion of formaldehyde to dioxymethylene consists of the formaldehyde molecule rotating so that it lies in a plane parallel to the surface, before the central carbon coordinates to surface lattice oxygen. This coordination occurs with a relatively low barrier of 0.13 eV. The NEB relative energy plot is shown in figure 6.19 and the corresponding intermediate geometries are shown in figure 6.20.

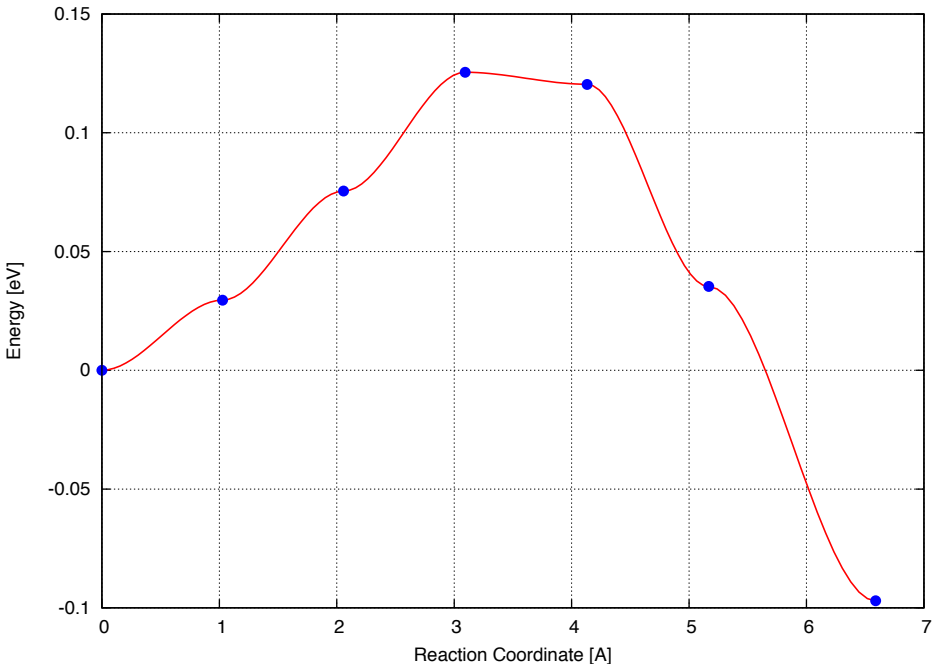

Figure 6.19. Formaldehyde to dioxymethylene relative energies for the '3-f1' system.

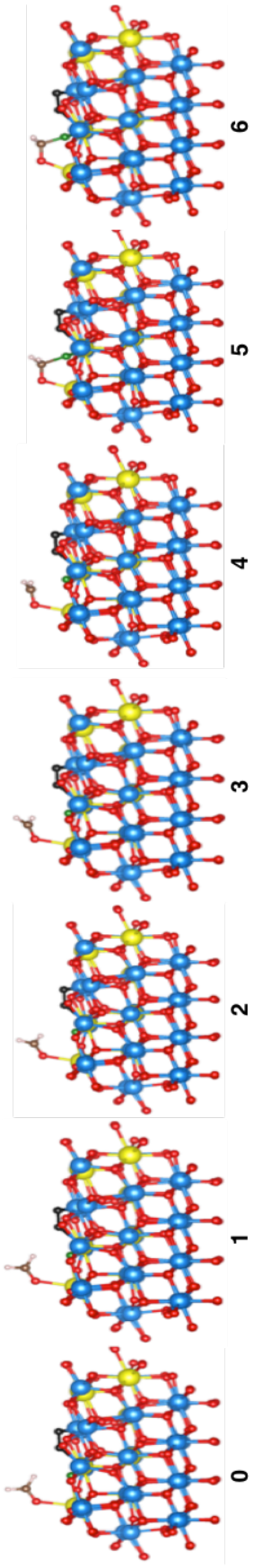

Figure 6.20. Formaldehyde to dioxymethylene images for the '3 – f1' system.

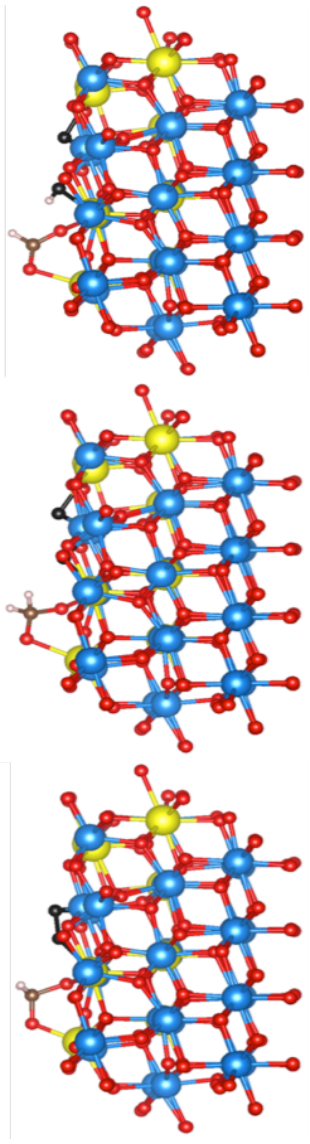

Figure 6.21. Dioxymethylene to formate NEB geometries for the '3-f1' system

The NEB pathway geometries for the hydrogen abstraction from dioxymethylene forming surface formate are displayed in figure 6.21 and the relative energy plot is given in figure 6.22. As with the second methane to methoxy pathway in section 6.2.1, the initial pathway predicted the process to be entirely downhill in energy with the DOM proton 'hopping' directly onto the active oxygen forming surface formate and a hydroxyl with no intermediate structures captured in the first interpolation. However, a second NEB pathway in between the DOM and formate structures with one intermediate geometry was calculated, giving an activation barrier of 1.71 eV. Whilst the hydrogen abstraction scenario is similar to that observed for the first methane to methoxy pathway (figure 6.3) the intermediate structure is very different. The highest energy structure observed in the methane pathway is a methyl radical above the surface with a surface hydroxyl formed on the surface; the dissociation of the active oxygen species occurs in a single concerted step with this hydroxyl formation. However, the highest energy structure observed in the formate formation pathway is a 'twisted' DOM molecule accompanied by the dissociation of the active oxygen species. It is possible that the lower activation barrier observed for hydrogen abstraction from methane when compared to DOM (1.3 vs 1.7 eV) can be attributed to the simultaneous active oxygen dissociation and hydroxyl formation in the former.

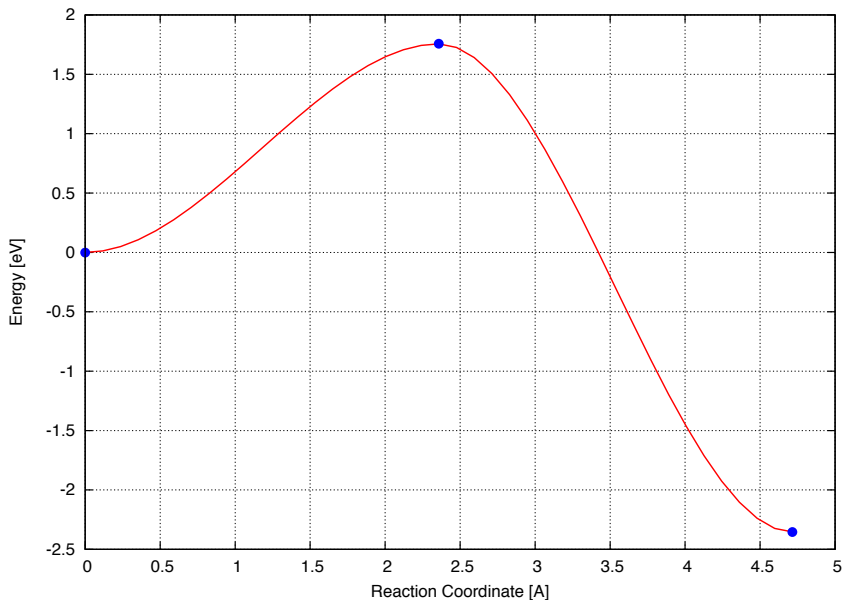

Figure 6.22. Dioxymethylene to formate relative energies for the '3-f1' system.

The formaldehyde to formate pathway has also been explored on the stoichiometric surface in the absence of an activated oxygen species, as was done with the methane to methoxy pathway. It was found that the adsorption of formaldehyde and coordination to surface lattice oxygen to form dioxymethylene proceeded in the same fashion on both the stoichiometric and activated surfaces. However, hydrogen abstraction from the dioxymethylene species on the stoichiometric surface is only slightly thermodynamically favourable when compared to gas

phase formaldehyde (-0.26 eV), and less stable than adsorbed formaldehyde or dioxymethylene. This is in contrast to hydrogen abstraction on the activated surface where there is a very large stabilisation upon oxidation to formate (~ -3.5 eV). Furthermore the formate species observed on the stoichiometric surface is not a planar formate, but 'bent' with the carbon atom coordinated to a surface cation.

6.3.1 Formate Oxidation

The final oxidation of surface formate by lattice oxygen in order to form the primary partial oxidation products; CO, CO_2, H_2, and H_2O was investigated by first abstracting the formate hydrogen, giving an adsorbed CO_2 configuration and two surface hydroxyls. The starting surface formate configuration and subsequent adsorbed CO_2 with two hydroxyls for the '3-f1' system is depicted in figure 6.23. Combinations of the primary partial oxidation products were then removed from the surface, the adsorption energies for the adsorbed CO_2 and two hydroxyls as well as subsequent product removal configurations are given in table 6.4. These adsorption energies are given with respect to the starting activated surface and gas-phase formaldehyde, and where applicable the DFT energies of the molecules removed.

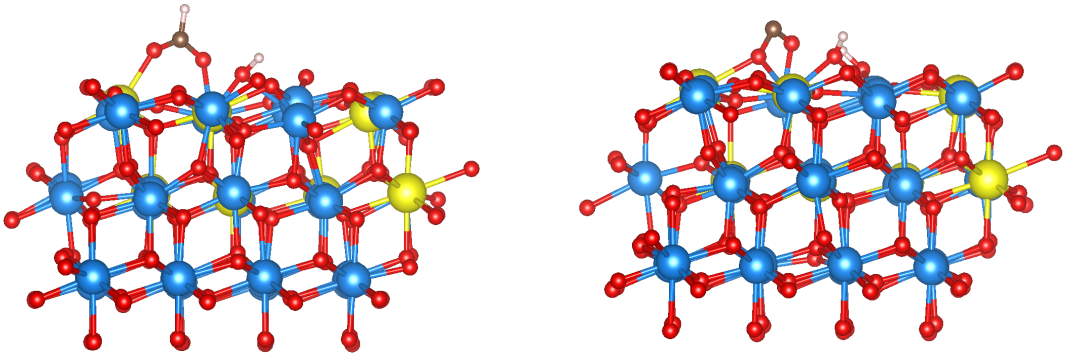

E_{ads} = -3.48 eV E_{ads} = -1.56 eV

Figure 6.23. Starting adsorbed formate + OH (left) and subsequent adsorbed CO_2 + 2OH's (right) for the '3-f1' system, with adsorption energies w.r.t starting active surface and gas-phase formaldehyde.

The nudged-elastic band calculation for hydrogen abstraction from surface formate, in order to form two surface hydroxyls, proceeds with an activation barrier of +2.37 eV. Whilst this is the largest activation energy calculated here for any of the processes involved in CPOM it is also worth noting that the final adsorbed CO_2 + 2OH configuration is 1.92 eV higher in energy than the starting formate + OH configuration, which is also higher than any of the previously seen activation barriers.

Configuration	System Adsorption Energy (eV)	
	3-f1	3-f2
Ads. CO_2 + 2OH	-1.56	-1.95
Remove CO + H_2	+0.51	+0.57
Remove CO + H_2O	-2.36	-2.19
Remove CO_2 + H_2	-2.36	-1.44
Remove CO_2 + H_2O	+1.27	+0.19

Table 6.4. Adsorption energies of adsorbed CO_2 + 2OH configurations and subsequent product removal configurations.

Whilst the configuration of having an adsorbed CO_2 molecule and two surface hydroxyls is lower in energy than the starting active surface and gas-phase formaldehyde, for both the '3-f1' and '3-f2' systems it is higher in energy than the predecessor adsorbed formate and single hydroxyl configuration, again highlighting the stability of formate as an intermediate surface species in CPOM. Furthermore, when considering the removal of combinations of partial oxidation products low adsorption energies are calculated for both CO + H_2O and CO_2 + H_2 desorption, whilst thermodynamically unfavourable adsorption energies are found for CO + H_2 and CO_2 + H_2O desorption. It is interesting to note that the low adsorption energies found here correspond to a reaction in which the combination of products desorbed yields a stoichiometric YSZ surface. The overall process can be summarised as; (i) surface reduction – oxygen atom removal/YSZ-O, (ii) re-oxidation of the surface – O_2 adsorption/YSZ+O generation, (iii) formaldehyde adsorption – YSZ+O + CH_2O. Therefore removal of CO + H_2O or CO_2 + H_2 regenerates the initial stoichiometric YSZ surface prior to surface reduction. This notion is explored further in table 6.5 by considering the thermodynamic reaction energy of product desorption and stoichiometric YSZ regeneration from an adsorbed formate starting surface.

The reaction energies given in table 6.5 are calculated as follows by considering the system energy for the regenerated stoichiometric YSZ surface and the gas-phase energy of the desorbed molecules with respect to the system energy of the starting formate surface;

$$e.g.\ \ Reaction\ Energy = E(YSZ) + E(CO) + E(H_2O) - E(Formate\ surface)$$

Configuration	Reaction Energy (eV)	
	3-f1	3-f2
Formate surface → YSZ + CO + H_2O	+ 1.12	+ 0.79
Formate surface → YSZ + CO_2 + H_2	+ 1.11	+ 1.55
Formate surface → YSZ(reduced) + CO_2 + H_2O	+ 4.75	+ 3.17

Table 6.5. Thermodynamic reaction energies for product desorption from an adsorbed formate starting structure.

The results suggest that when starting with a stable surface formate and hydroxyl configuration, desorption of combinations of partial oxidation products that regenerate a stoichiometric YSZ surface are between ~0.8 to 1.6 eV higher in energy, which is within what can be expected at the catalytic operating temperatures. Additionally when the combination of CO_2 and H_2O desorb, a reduced YSZ surface is produced. This reduced YSZ surface generated from product removal contains the same doubly occupied mid-gap vacancy state obtained when reducing stoichiometric YSZ surfaces, and these reaction energies for the removal of CO_2 and H_2O of +3.17 and + 4.75 eV are much higher than the energies for product removal regenerating stoichiometric YSZ surfaces. However, they are comparable to the vacancy formation energies calculated for stoichiometric surface reduction, which could allow for a mechanism whereby the desorption of total oxidation products propagates the reaction by regenerating the reduced surface sites required for molecular oxygen activation.

6.4 Rate Estimates

The feasibility of the above studied processes and pathways involved in the catalytic partial oxidation of methane on YSZ is briefly discussed by calculating estimated rate constants for reaction temperatures. The rate constants (k) are calculated according to the Arrhenius-ike equation 6.1, in which the pre-exponential term is given by k_BT/h as described in the method of Kozuch and Shaik[6], and are presented in table 6.6.

$$k = \frac{k_BT}{h}\, e^{Ea/RT} \tag{6.1}$$

Process	Ea (eV)	k (s^{-1})	
		673 K	1173 K
Methane → Methoxy	1.33	1566.6	4.72×10^{7}
Methoxy → *CH_2	1.74	1.307	8.16×10^{5}
Formaldehyde → *CHO +OH	1.46	163.3	1.30×10^{7}
***CHO + OH → H_2 + CO**	1.53	48.84	6.52×10^{6}
Formaldehyde → Dioxymethylene	0.13	1.49×10^{12}	6.75×10^{12}
Dioxymethylene → Formate	1.71	2.192	1.10×10^{6}
Formate → *CO + 2OH	2.37	2.50×10^{-5}	1.60×10^{3}

Table 6.6. Rate constant estimates for CPOM processes at temperature of 673 and 1173 K.

The temperatures of 673 and 1173 K roughly correspond to a temperature prior to the onset of CPOM on YSZ and a temperature at which CPOM on YSZ is occurring respectively (according to figure 1.2, chapter 1). As can be seen from the rate constant estimates in table 6.6, the large calculated barriers manifest in very small rate constants for certain processes at the lower temperature, which become accessible at the higher temperature at which the reaction is expected to take place.

6.5 CPOM Reaction Pathway Discussion

Partial oxidation of methane on YSZ has been investigated in two separate oxidation steps (i) the oxidation of methane to the intermediate formaldehyde species and (ii) the oxidation of the formaldehyde produced in the first step to the thermodynamically favourable surface formate species. Finally decomposition of both surface formaldehyde and formate into primary CPOM products is studied. An overall schematic for the two oxidation pathways studied here, as well as the initial generation of the active surface is presented in figure 6.24.

In this schematic the red ‘O’ and blue ‘M’ represent the surface oxygen anions and cations respectively, whilst the green ‘O’ represent the diatomic molecular oxygen which becomes the partially reduced surface species. The distinction aims to highlight the Mars-van Krevelen nature of this catalysis whereby lattice oxygen is incorporated into the primary oxidation products, and the initially adsorbed molecular oxygen replaces this extracted lattice oxygen. The yellow square ‘V’ represents the F-centre vacancy created by surface reduction, and the ‘C’ and ‘H’ carbon and hydrogen originating from either methane of formaldehyde. Note that this schematic is illustrative only; the anion and cation arrangement is not representative of the actual structural ordering of the surface, the molecular oxygen incorporation is similarly also only suggestive of the process.

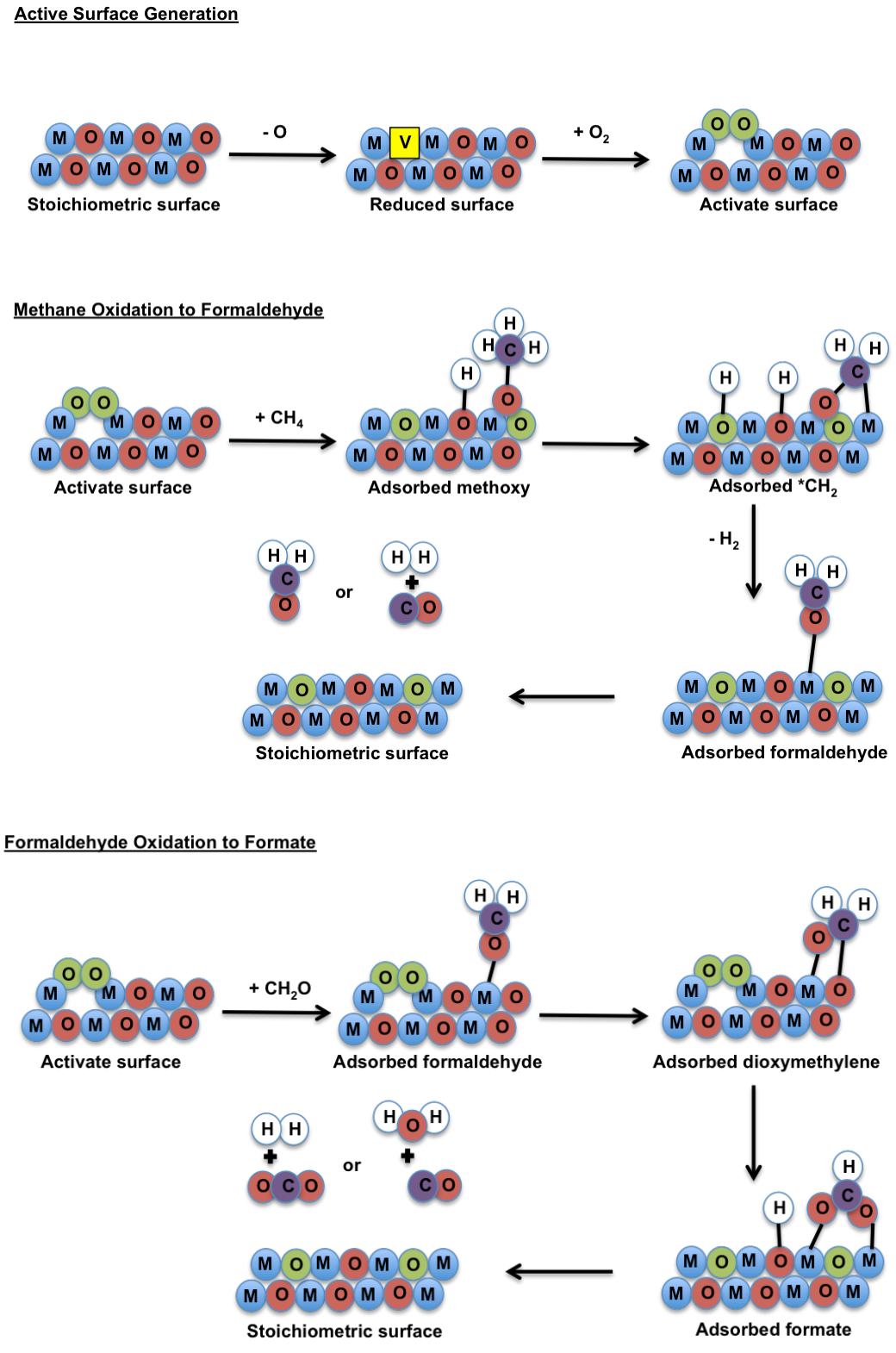

Figure 6.24. Overall schematic of the CPOM mechanistic pathways.

6.5.1 Methane Oxidation to Formaldehyde

Methane oxidation on pre-activated YSZ (reduced and re-oxidised) occurs via two subsequent hydrogen abstraction steps followed by desorption of H_2 gas. Initial hydrogen abstraction from methane results in an adsorbed $*CH_3$ fragment, coordinated to lattice oxygen, taking the form of a surface methoxy group. This coordination to surface oxygen incorporates lattice oxygen into the products in the Mars-van Krevelen type mechanism observed experimentally[4]. The abstracted hydrogen can form a surface hydroxyl with lattice oxygen or an oxygen atom of the partially reduced molecular oxygen surface species. In either case, this abstraction/adsorption process is accompanied by the dissociation of the active molecular oxygen species. As with previous work investigating hydrogen abstraction from methane[7], we find that the role of the active oxygen species is not to provide oxygen but to act as an electron acceptor. The second hydrogen abstraction step removes hydrogen from the surface methoxy species, forming a second surface hydroxyl and an adsorbed $*CH_2$ fragment which has a tetrahedral carbon coordinated to both lattice oxygen and a surface cation. Finally removal of the two hydrogen atoms, effectively as H_2 gas, allows for the oxygen atom of the $*CH_2$ fragment to be lifted out of the surface and rearrange to become a planar adsorbed formaldehyde molecule. A final desorption of the surface formaldehyde species regenerates the stoichiometry of the initial surface prior to reductive treatment. The reaction intermediates and formaldehyde formation mechanism observed in our calculations are in line with previous computational work studying methane oxidation[2].

6.5.2 Formaldehyde Oxidative Conversion

Formaldehyde oxidative conversion to formate is shown to proceed via a mixed nucleophilic/electrophilic mechanism. Formaldehyde first physisorbs to a surface cation before the central carbon is subject to nucleophilic attack by lattice O^{2-}, leading to the formation of a dioxymethylene intermediate. This process occurs on both stoichiometric and reduced YSZ surfaces. However, a second nucleophilic attack in order to abstract hydrogen and form formate does not occur; instead an activated reduced diatomic oxygen species is required to oxidise fully formaldehyde to formate. The strong adsorption energy calculated for this final oxidation step appears to be in agreement with the experimental observation of rapid conversion of formaldehyde to the stable surface formate species on a pre-activated YSZ surface[4,8]. Moreover, the first nucleophilic addition step highlights the incorporation of lattice oxygen into the product and the Mars-van Krevelen nature of catalysis on YSZ, despite the presence of adsorbed molecular oxygen. A similar, but mechanistically very different, result has recently been discovered for methanol oxidation on the reducible oxide ceria, in which hydrogen abstraction by surface lattice oxygen can occur due to the variable oxidation state of cerium[9].

Although formaldehyde conversion to formate is observed experimentally at low temperature[8], the catalyst was pre-activated in oxygen at high temperature and it is likely that active surface oxygen species formed as described in chapter 5 are present. Additionally, the presence of water at the YSZ surface has been observed to stabilise formaldehyde with respect to oxidation to formate[8]. We have previously shown that water will readily dissociate on stoichiometric YSZ with hydroxyl groups filling stoichiometric vacancy sites on the non-reduced surface. This vacancy annihilation by water in combination with the formaldehyde oxidation mechanism proposed here could explain why the presence of water stabilises surface formaldehyde species. It is possible that the presence of hydroxyls filling surface vacancies increases lattice rigidity, reducing the amount of stabilisation that can be achieved by oxygen sub-lattice relaxation and therefore preventing molecular oxygen activation.

6.5.3 Formaldehyde and Formate Decomposition/Oxidation to CPOM Products

In the absence of an active partially reduced molecular oxygen species, formaldehyde can decompose into molecular hydrogen and carbon monoxide on stoichiometric YSZ. The resultant molecular configuration is ~0.5 eV higher in energy than surface adsorbed formaldehyde, although an entropic energy gain can be expected upon this desorption. This decomposition route occurs via hydrogen abstraction from formaldehyde, with an energy barrier of ~1.5 eV, and a subsequent simultaneous second hydrogen atom abstraction and molecular hydrogen desorption step that also proceeds with an energy barrier of ~1.5 eV. Whilst with an active molecular oxygen species, the first hydrogen abstraction step has a slightly higher activation energy of ~1.7 eV there is a very large thermodynamic stabilisation as a result of molecular oxygen dissociation and incorporation into the YSZ lattice. When compared to formaldehyde decomposition, the hydrogen abstraction step from surface formate has a much larger energy barrier of ~2.4 eV, which is in part due to the resultant structure of adsorbed CO_2 and two surface hydroxyls being 1.9 eV higher in energy than the surface formate species. Furthermore inspection of the geometries shows a large distance between the surface formate and a neighbouring surface lattice oxygen species, the large distance covered by the abstracted hydrogen atom results in high-energy structures. However, both the large activation energy for hydrogen abstraction and the strong thermodynamic stabilisation of the surface formate species are in good agreement with the experimental observation that formate is a stable surface intermediate. For example Zhu *et al.*[4] found that at low temperature, on pre-oxidised YSZ, it appeared that the rate-determining step for CPOM is not methane activation but formate decomposition, which is consistent with the activation barriers calculated here.

6.5.4 Overall CPOM

We have investigated the partial oxidation of methane to formate and shown that, in good agreement with experiment[4], this process proceeds via a formaldehyde intermediate. The experimental studies of Zhu et al.[10,4,1,8] find that CPOM produces a mixture of CO, CO_2, H_2 and H_2O. Moreover, they find that temperature programmed desorption of surface formate results in an identical product distribution as CPOM, strongly suggesting that formate is an intermediate in the CPOM process. The addition of formaldehyde into the CPOM reactant stream also increases product yields without influencing the distribution, indicating that formaldehyde is also an intermediate species. They also show that formaldehyde will oxidise to surface formate on pre-activated YSZ, with the formate species stable up to ~475 °C. The results of our calculations presented here have some good agreements with these experimental observations. Additionally, the experimental work notes that when full oxygen conversion has been achieved methane conversion decreases when formaldehyde is added to the reactant feed despite the concentration of methane being an order of magnitude higher than that of formaldehyde. This observation suggests that methane and formaldehyde compete for the same oxidation source and that formaldehyde is more easily oxidised than methane. The competition between methane and formaldehyde for the same oxidant is in agreement with the scenario investigated here whereby methane and formaldehyde oxidation both proceed via the dissociation of an active oxygen species upon hydrogen abstraction, with the larger energetic stabilisation observed for hydrogen abstraction from formaldehyde over the first hydrogen abstraction step for methane. We find in the present work that in both steps, methane oxidation to formaldehyde and formaldehyde oxidation to formate, the central carbon atom coordinates to lattice oxygen incorporating surface oxygen into the products in a Mars-van Krevelen type mechanism. The active oxygen species accepts electronic charge upon hydrogen abstraction and the oxygen atoms are incorporated as lattice O^{2-} ions, which appears to be the thermodynamic driving force for the oxidation process.

Previous attempts to model oxidation reactions at YSZ surfaces have employed the use of a YSZ+O surface[11,2], in which two substitutional yttrium cations replace zirconium ions. However, due to the system size used no charge compensating oxygen vacancies are created, which leads to the unphysical situation of having a YSZ surface with all oxygen lattice sites filled, and as such these systems have overly active oxygen species with the surfaces having negative oxygen vacancy formation energies. The current work benefitted from improvements in computational power allowing larger systems to be modelled, which contain both charge compensating oxygen vacancies inherent in YSZ and active oxygen species on the surface. The method used here of surface reduction by removal of a lattice oxygen atom followed by re-oxidation of the surface by diatomic molecular oxygen in effect also produces a YSZ+O system,

whereby there is one additional oxygen atom in the system when compared to stoichiometric YSZ. However, in the present work the extra oxygen atom takes the form of a partially reduced active diatomic oxygen species, instead of a single oxygen atom on a lattice site, whilst maintaining the charge compensating vacancies inherent to the YSZ system. Therefore, the proposed mechanism for surface reduction and re-oxidation presented here represents a more complete physical and chemical explanation for oxidation reactions at the YSZ surface.

6.6 Summary and Conclusions

Catalytic partial oxidation of methane over pre-oxidised YSZ occurs stepwise with methane first being oxidised to formaldehyde before formaldehyde either decomposes to syngas or is further oxidised to surface formate, which can then liberate primary partial oxidation products. The initial hydrogen abstraction step in both methane oxidation to formaldehyde and formaldehyde oxidation to formate occurs in the presence of a partially reduced molecular oxygen species. The molecular oxygen does not directly interact with the methane or formaldehyde, but instead lattice oxygen coordinates to the central carbon atom, in accordance with the experimentally observed Mars-van Krevelen nature of CPOM on YSZ. Furthermore, the active molecular oxygen species acts as an electron acceptor in the hydrogen abstraction process, and the dissociation of this partially reduced species and subsequent incorporation of the oxygen atoms into the YSZ oxygen anion sub-lattice provides the thermodynamic driving force for these oxidation reactions. Final decomposition of the surface formate species and desorption of the primary CPOM products regenerates the starting stoichiometric YSZ surface.

References:

1. Zhu, J. J.; van Ommen, J. G.; Bouwmeester, H. J. M.; Lefferts, L., Activation of O-2 and CH4 on yttrium-stabilized zircoma for the partial oxidation of methane to synthesis gas. *Journal of Catalysis* **2005,** 233, (2), 434-441.
2. Shishkin, M.; Ziegler, T., The Oxidation of H(2) and CH(4) on an Oxygen-Enriched Yttria-Stabilized Zirconia Surface: A Theoretical Study Based on Density Functional Theory. *Journal of Physical Chemistry C* **2008,** 112, (49), 19662-19669.
3. Chase, M. W., *NIST-JANAF Thermochemical Tables*. In 4th Edition ed.; **J. Phys. Chem. Ref. Data**, 1998; pp 1-1951.
4. Zhu, J. J.; van Ommen, J. G.; Lefferts, L., Reaction scheme of partial oxidation of methane to synthesis gas over yttrium-stabilized zirconia. *Journal of Catalysis* **2004,** 225, (2), 388-397.
5. Busca, G.; Lamotte, J.; Lavalley, J. C.; Lorenzelli, V., FT-IR study of the adsorption and transformation of formaldehyde on oxide surfaces. *Journal of the American Chemical Society* **1987,** 109, (17), 5197-5202.
6. Kozuch, S.; Shaik, S., How to Conceptualize Catalytic Cycles? The Energetic Span Model. *Accounts of Chemical Research* **2011,** 44, (2), 101-110.
7. Cooper, C. S.; Oldman, R. J.; Catlow, C. R. A., Oxidative methane activation over yttrium stabilised zirconia. *Chemical Communications* **2015,** 51, (27), 5856-5859.
8. Zhu, J.; van Ommen, J. G.; Lefferts, L., Effect of surface OH groups on catalytic performance of yittrium-stabilized ZrO2 in partial oxidation of CH4 to syngas. *Catalysis Today* **2006,** 117, (1-3), 163-167.
9. Kropp, T.; Paier, J., Activity versus Selectivity of the Methanol Oxidation at Ceria Surfaces: A Comparative First-Principles Study. *The Journal of Physical Chemistry C* **2015,** 119, (40), 23021-23031.
10. Zhu, J.; Rahuman, M.; van Ommen, J. G.; Lefferts, L., Dual catalyst bed concept for catalytic partial oxidation of methane to synthesis gas. *Applied Catalysis a-General* **2004,** 259, (1), 95-100.
11. Gorski, A.; Yurkiv, V.; Starukhin, D.; Volpp, H.-R., H2O chemisorption and H-2 oxidation on yttria-stabilized zirconia: Density functional theory and temperature-programmed desorption studies. *Journal of Power Sources* **2011,** 196, (17), 7188-7194.

Chapter 7

YSZ Solid Solutions

Solid solutions of yttria doping into zirconia over a range of dopant concentrations are explored in this chapter. Yttrium-vacancy and vacancy-vacancy interactions are investigated in realistic systems at relevant dopant concentrations. A number of macroscopic properties of the YSZ system are calculated using averages of solid solution ensembles in good agreement with experimental values, and the nature of the microscopic local defect structure is revealed.

7.1 Introduction

As discussed in chapter 2, yttria-stabilised zirconia is a solid solution in which Y_2O_3 doping into ZrO_2 stabilises the cubic fluorite phase of zirconia and for each two substitutional yttrium cations doped onto zirconium ion lattice sites a charge compensating oxygen vacancy is introduced. However, the distribution of vacancies and dopant cations within YSZ still remains unclear. The work done thus far investigating vacancy-vacancy interactions provides indications about vacancy pairing and ordering but is largely inconclusive and has been limited to small system sizes and small numbers of hand-picked structures due to the combinatorial complexity of the YSZ system, described in more detail further on. These limitations have meant that previous attempts to identify vacancy-vacancy interactions have not been comprehensive, although investigating higher and more relevant dopant concentrations in larger simulation cells has received a resurgence of late. Parkes *et al.*[1] study 6.7 mol% Y_2O_3 doping by introducing two Y-V-Y defect configuration into a 2x2x2 ZrO_2 supercell; computing the energies of all symmetry independent structures in which no yttrium ions are nearest neighbour to vacancy positions, whilst Dong *et al.*[2] looked at 8 mol% YSZ, eight Y-V-Y defect configuration in a 3x3x3 supercell, by analysing large numbers of structures (~100,000) using random sampling. In this chapter a range of yttria-zirconia solid solutions with varying dopant stoichiometries are investigated using a random sampling method before exploring global optimisation at an industrially relevant concentration. Good agreement is found with experiment for a variety of bulk properties within the sample ensembles, and some of the local structure features present in YSZ are unveiled.

7.2 Parent Oxide Unit Cells

Energy evaluations and geometry optimisations in this study are, largely, calculated using interatomic potential simulations with polarisable shell models in the GULP code[3]. The dominant long-range interactions are Coulombic, whilst the short-range interactions, E_{s-r}, are described by Buckingham potentials (equation 7.1), which were introduced in chapter 3.

$$E_{s-r} = Aexp^{\left(\frac{-r}{\rho}\right)} - \left(\frac{C}{r^6}\right) \tag{7.1}$$

Also as noted in chapter 3, the shell model takes ionic polarisation into account by representing ions as charged massless shells connected to inner atomic cores via a harmonic potential (equation 7.2), where k is the spring constant and d the relative displacement of the core and shell.

$$E_{core-shell} = \frac{1}{2}k_2d^2 \tag{7.2}$$

The Zr-O interaction parameters were derived by Dwivedi and Cormack[4] whilst the Y-O and O-O parameters were determined by Lewis and Catlow[5], and are given in table 7.1. These interatomic potentials have been used previously for studying YSZ systems[6,1].

Short Range Parameters				
Interaction	**A (eV)**	**P (Å)**	**C (eV Å^6)**	**Cut-off (Å)**
Zr-O	985.87	0.3760	0.0	10
O-O	22764.00	0.1490	27.88	12
Y-O	1345.10	0.3491	0.0	10
Shell Model Parameters				
Species	**Y (e)**	**k (eV Å^{-2})**		
O^{2-}	-2.077	27.290		
Zr^{4+}	1.35	169.617		

Table 7.1. Interatomic potential parameters.

7.3 Structure Generation

Although the models used in the previous chapters have included dopant yttrium cations and charge-compensating oxygen vacancies these models are made using an extrapolation of the experimental findings of the defect configurations present in YSZ as well as an extrapolation of calculations of isolated defects demonstrating that it is energetically favourable for oxygen vacancies to occupy 2NN positions to yttrium ions. These models are considered to be good representations of possible YSZ configurations, and are required to be made in this fashion as a full investigation into the microscopic defect arrangement of YSZ is prohibitive for any surface chemistry studies. However, we now turn our attention to this long-standing problem of identifying these defect interactions in realistic systems. The first challenge encountered when attempting to identify the microscopic defect structure of YSZ concerns the combinatorial complexity involved in simulating these solid solutions. Large supercells are required in order to provide realistic system sizes at relevant dopant concentrations. The ZrO_2 unit cell only contains 12 atoms, and already the introduction of one (Y-V_O-Y) defect cluster results in the substitution of half of the cation sites. Recent studies investigate both the 2x2x2 and 3x3x3 supercells, containing 96 and 324 atoms respectively. Using supercells of these sizes allows for relevant dopant concentrations to be simulated and provides more realistic representations of the actual YSZ systems, although the larger the simulation cell the more realistic a system becomes as there is less of an effect of self interactions of the periodic images of the cell interacting with themselves. However, increasingly large simulation cells require larger numbers of dopant yttrium atoms replacing zirconium cations, and oxygen atoms removed forming charge compensating vacancies to achieve the same doping concentration. For just one defect configuration introduced into a 2x2x2 supercell there are 2 substitutional yttrium ions that can be placed on the 32 cation sites, and one oxygen atom removed from the 64 anion sites. In this

work a defect configuration represents introducing two substitutional yttrium ions and one charge compensating oxygen vacancy into the simulation cell in any arrangement. The number of possible combinations is given in equation 7.3, and as the number of defect configurations introduced increases the number of possible combinations scales combinatorially, as exemplified in table 7.2.

$$\frac{32!}{30!\times 2!} \times \frac{64!}{63! \times 1!} = 31{,}744 \tag{7.3}$$

Number of defect clusters	2x2x2 Supercell		3x3x3 Supercell	
	Dopant concentration (mol%)	Number of possible combinations	Dopant concentration (mol%)	Number of possible combinations
1	3.2	31,744	0.01	1,248,048
2	6.7	72,495,360	1.89	1.24×10^{11}
3	10.3	3.78×10^{10}	2.86	3.17×10^{15}

Table 7.2. Combinatorial complexity of introducing (Y-V_O-Y) defect configurations into ZrO_2 supercells.

As can be seen, there are already a large number of possible combinations for 1 defect configuration in the smaller 2x2x2 supercell and although it would be possible to simulate all of these, higher dopant concentrations and larger supercells quickly become unfeasible. However, the search space can be greatly reduced by evaluating the symmetry of the system. For example, whilst there are ~32,000 possible combinations of putting one defect configuration into the 2x2x2 supercell, a large number of these are symmetrically equivalent. In order to generate random structures we define the cation sites of the supercell as one region and the anion sites as another; we then allow random population of the cation sites with the required numbers of yttrium and zirconium atoms, and the same procedure is followed for populating the anion sites with either oxygen atoms or oxygen vacancies. We then use hash-keys in order to determine the cation and anion connectivity, which results in a unique identifier for the corresponding connectivity; symmetrically equivalent structures will contain the same connectivity and will be identified as identical structures. In the case of just one defect configuration, as expected, the number of unique structures generated is far smaller than the possible number of combinations and for the 2x2x2 supercell is ~30, whilst ~300 unique structures are found for the 3x3x3 supercell. This data are presented in table 7.3.

2x2x2 Supercell		3x3x3 Supercell	
Total number of structures generated	**Number of unique structures**	**Total number of structures generated**	**Number of unique structures**
10,000	29	10,000	295
15,000	31	20,000	295
20,000	33	30,000	294
-	-	40,000	288
-	-	50,000	294

Table 7.3. Total number of structures generated and number of unique structures found for doping one defect configuration into different ZrO_2 supercells.

The number of unique structures for one defect configuration in the 2x2x2 supercell is in good agreement with other findings. Parkes *et al.*[7] determine that there are 28 unique structures by generating 32,000 random structures and performing fixed shell energy minimisation calculations in GULP. They argue that structures with the same energy are equivalent, and count 28 plateau regions in their ranked energy distribution. Additionally Cooper *et al.*[8] find 33 symmetrically inequivalent structures using the site occupancy disorder (SOD) program. We also find that the number of unique structures found for 2 defect configurations in the 2x2x2 supercell is greatly reduced by symmetry when compared to the number of possible combinations. Separate structure generation runs, with 5,000 structure increments, were performed from 25,000-155,000 structures; and although the total number of unique structures has not been found the figure appears to be converging between roughly 47,000-50,000 as depicted in figure 7.1. This is a much more manageable number than the ~72.5M possible combinations. However, this approach falls down when considering the much larger search spaces of the larger supercell at relevant dopant concentrations. For example for 9 mol% yttria doping in the 3x3x3 supercell there are 3.32×10^{35} possible combinations. When generating structures in such a large search space it is more instructive to talk of duplicate structures rather than unique ones; at extended structure generation runs of 2M and 10M structures only 652 and 3,266 duplicate structures were found respectively, meaning that almost all of the structures generated were unique. As such it is practically impossible to cover comprehensively all the symmetrically inequivalent structures at relevant dopant concentrations.

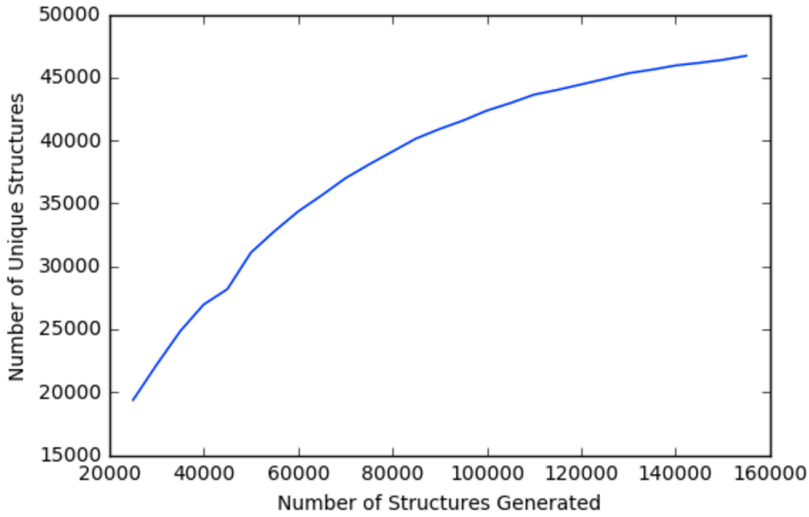

Figure 7.1. Number of unique structures found vs total number of structures generated for 2 defect configurations in a 2x2x2 ZrO_2 supercell.

7.4 Random Sampling

Despite the failure of random structure searching in completely covering the huge search spaces that exist for relevant dopant concentrations in the 3x3x3 supercell, random sampling of the structures can still provide useful information about the yttria-zirconia solid solution. We have performed random structure generation of ~10,000 unique configurations, and a series of subsequent energy optimisations, for 10 different yttria dopant concentrations over the range of 0-50 mol% Y_2O_3 in the 3x3x3 ZrO_2 supercell. Various physical observables of YSZ have been calculated and compared with the experimental literature in order to demonstrate the validity of using ensembles of randomly generated structures to describe the YSZ system, calculated with empirical potentials, over a large range of dopant concentrations. In the first instance we discuss properties of the 9 mol% doping energy distribution as a representative case of sampling different stoichiometries within the range of yttria-zirconia solid solution concentrations before combining the 10 separate sets of results in order to explore the effects of increased yttria concentration. Single-point energy calculations (with all atoms remaining on their lattice sites) of all ~10,000 structures were performed and subsequently both polarizable-shell only minimisations, and full geometry optimisation of the internal atomic coordinates carried out. The resulting energies for these structures, in each of the successive levels of optimisation, follow Gaussian-like distributions. The single-point energy distribution has a remarkably large energy range of 207 eV, which is reduced to 85 eV when the atom shells are allowed to relax. For the full geometry optimisation of the atomic coordinates, the range of the energy distribution shrinks further to just 9.63 eV, and an energetic stabilisation of ~200 eV is calculated when compared to

the single-point energies. The energy rankings of the structures were checked after subsequent optimisations; there is a slight correlation between single-point and shell optimised energies, but there is no correlation between either single-point- or shell- with full geometry-optimisation. The large energy stabilisation that occurs on geometry optimisation is accompanied by a large relaxation of the atomic positions, which is so large that the energy of the starting structure in no way represents the energy of the final structure. We also find that very similar results are found for the energy range, mean, and standard deviation for distributions of 1,000, 10,000 and 50,000 unique random structures subject to full geometry optimisation. This density of states energy distribution for 50,000 unique random structures is displayed in figure 7.2. The energy range, mean (with the lowest energy structure set to zero) and standard deviation are 10.42, 3.695, and 1.176 eV respectively. These results are in good agreement with those found by Dong *et al.*[2] in which they geometry optimise 100,000 random structures with the slightly lower dopant concentration of 8 mol% YSZ (3x3x3 supercell). They also find the energies to follow a Gaussian-like distribution, which spans 15 eV, and has a mean and standard deviation of 5.6 and 1.4 eV respectively. Furthermore the authors note that the properties of the distribution are 'robust' when subdividing the 100,000 configurations into smaller subsets.

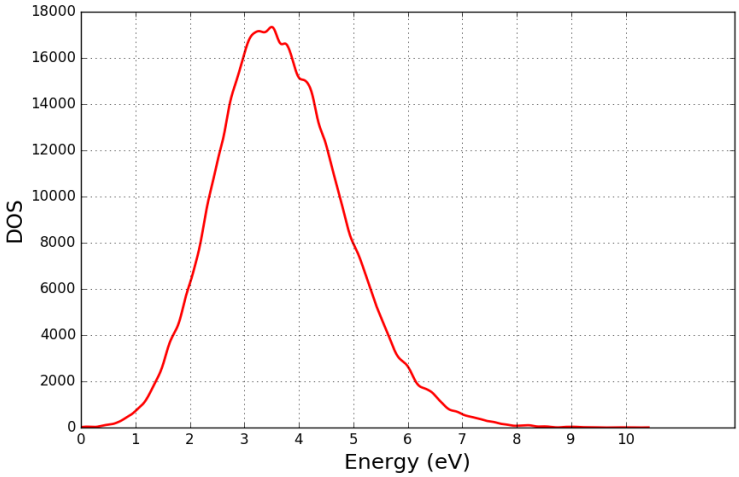

Figure 7.2. Geometry optimised energy distribution of 50,000 unique random configurations of 9 mol% YSZ (3x3x3 ZrO_2 supercell)

7.4.1 Energy of Mixing

The energy of mixing for Y_2O_3 into ZrO_2 is calculated in order to understand the phase behaviour of the solid-solution. As a first approximation to the energy of mixing of yttria into zirconia the energy of the lowest energy structure (E_{low}), found by random sampling, was compared with the ideal energy of that particular concentration. This ideal energy is simply the energy obtained when summing up the energy per formula unit of ZrO_2 or Y_2O_3, taken from unit cell calculations, for the given stoichiometry of these formula units contained within the

supercell. For example a dopant concentration of 9.09 mol% Y_2O_3 in the 3x3x3 unit cell has the following atomic composition; $Y_{18}Zr_{90}O_{215}$, which corresponds to 90 ZrO_2 formula units and 9 Y_2O_3 formula units. The potential energy of mixing (ΔE_{mix}) is then given by equation 7.4, in which E_{fu} is the energy per formula unit.

$$\Delta E_{mix} = E_{low} - \left(\left(90 \times E_{fu} ZrO_2\right) + \left(9 \times E_{fu} Y_2O_3\right) \right) \tag{7.4}$$

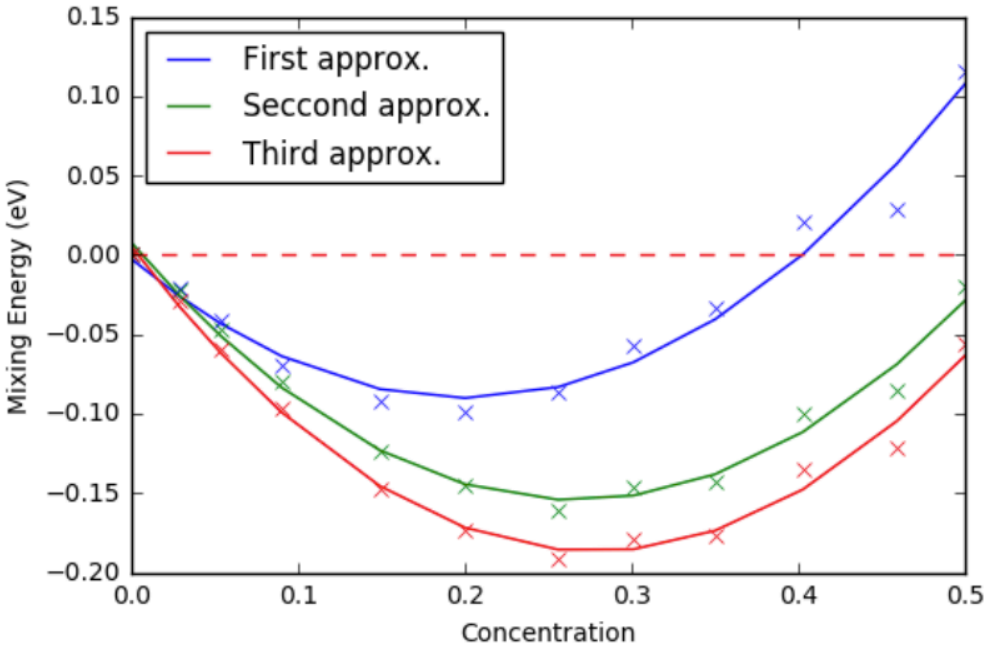

Figure 7.3. Calculated mixing energy over a range of concentrations of Y_2O_3 doping into a 3x3x3 ZrO_2 supercell. Mixing energy values are giver per cation contained in the simulation cell.

The results for the energy of mixing across the entire concentration range calculated are given in figure 7.3. Initially, the mixing energies show that solid-solutions of up to ~35 mol% Y_2O_3 doping are stable with respect to the bulk cubic-zirconia and yttria phases, although doping yttria into zirconia for concentrations above 40 mol% is endothermic. However, at a dopant concentration of 40 mol% YSZ is known to form as the ordered compound $Zr_3Y_4O_{12}$[9,10,11]. This unfavourable energy of mixing could be attributed to a number of factors; for example, it is probable that the true ground state was not found via random sampling. Furthermore, this thermodynamic penalty was also found to be an artefact of performing all of the calculations across the range of concentrations whilst using the pure zirconia lattice parameter. As can be expected when doping the larger yttrium cation onto smaller zirconium cation sites, some lattice expansion will occur. The effect of lattice expansion was investigated by taking geometry optimised structure outputs from the first approximation above, inputting an interpolated lattice

parameter created in a similar fashion to the ideal energy above, and re-optimising the structure allowing both the lattice parameter and internal coordinates to relax. Whilst we allow the lattice to expand in this instance, we enforce the cubicity of the unit supercell, constraining all three supercell lengths to take the same value. Upon allowing for lattice expansion, the average energy for each concentration distribution is lowered. Moreover, we now use a more detailed and accurate method in which the expectation value for the energy is used to determine the energy of mixing instead of the lowest energy structure as in the first approximation. The expectation value of the energy, as calculated in equation 7.5, uses the energy distributions for each concentration; $\langle E \rangle$ is the energy expectation value, E_i is the energy of each structure, E_1 is the lowest energy structure, $k_B T$ is the Boltzmann factor and Z is the partition function which depends on; P the total number of possible cation and anion substitution combinations, and N the number of structures sampled as shown in equation 7.6. Finally, the third approximation of the mixing energy is the Gibbs free energy calculated according to equation 7.7, where Z' is equivalent to Z with the exponent $e^{-E_1/k_B T}$ removed. These second approximation thermally averaged energies of mixing, and third approximation Gibbs free energies of mixing are also plotted in figure 7.3.

$$\langle E \rangle = \frac{1}{Z} \sum_{i=1}^{N} E_i e^{-E_i/k_B T} \tag{7.5}$$

$$Z = \frac{P}{N} \sum_{i=1}^{N} e^{-(E_i - E_1)/k_B T} \cdot e^{-E_1/k_B T} \tag{7.6}$$

$$G = E_1 - k_B T \ln Z' \tag{7.7}$$

7.4.2 Lattice Parameter

As discussed above the energy of mixing is overestimated when performing geometry optimisations over all concentrations using the cubic ZrO_2 lattice parameter, as in the first approximation of figure 7.3, and it was found that allowing for expansion of the cubic lattice lowers the energy of the system. The resulting structures give rise to a distribution of lattice parameter values for each dopant concentration, the expectation values of these lattice parameter distributions are plotted in figure 7.4 and compared to experimentally obtained values[12,13]. The trend of increasing lattice parameter value with increasing dopant concentration for the calculated expectation values matches well with the experimentally determined values. However, the calculated lattice parameter is always lower than the experimental value for a given concentration and it is likely that this difference is due to thermal expansion and we note that vibrational contributions are not captured in the static zero kelvin calculations.

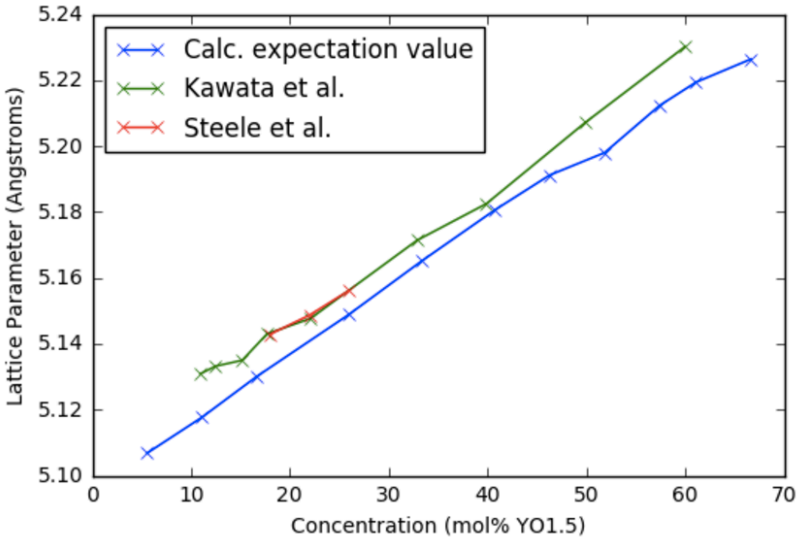

Figure 7.4. Lattice parameter expectation value over a range of dopant concentrations compared with experimental values from Kawata[12] and Steele[13].

7.4.3 Dielectric Constant

The dielectric constant, like the lattice parameter, is another physical observable of the YSZ material that can be measured experimentally and calculated with interatomic potential simulations. Figure 7.5 shows the calculated expectation value, and experimental values, of the static dielectric constant of the material as a function of concentration. The calculated dielectric constant for a particular random structure is reported as having a value for the dielectric constant in the direction of each of the simulation cell axes. In order to calculate the expectation value, the arithmetic mean for each structure is calculated and these mean values are used to generate the expectation value for each ensemble of structures at different dopant concentrations. The results for the calculated dielectric constant expectation values agree well with experiment in general. The trend of declining dielectric constant value above dopant concentrations of 10 mol% doping in the work of Chen *et al.*[14] is replicated in the calculated ensemble averages, although at lower values than in experiment; whereas the calculated values are much closer to those observed in the work of Lanagan *et al.*[15] and also reproduce the peak in the dielectric constant value at low concentration. A much lower value for the pure zirconia dielectric constant is reported in the work of Lanagan *et al.*[15], compared to the calculated value, as the experimental measurement is performed on a sample of monoclinic zirconia whereas the calculated value is that for the cubic unit cell of ZrO_2. The dielectric constant calculated for monoclinic zirconia using the same interatomic potentials is ~21.1, which is closer to the experimental value than the calculated value for the cubic system.

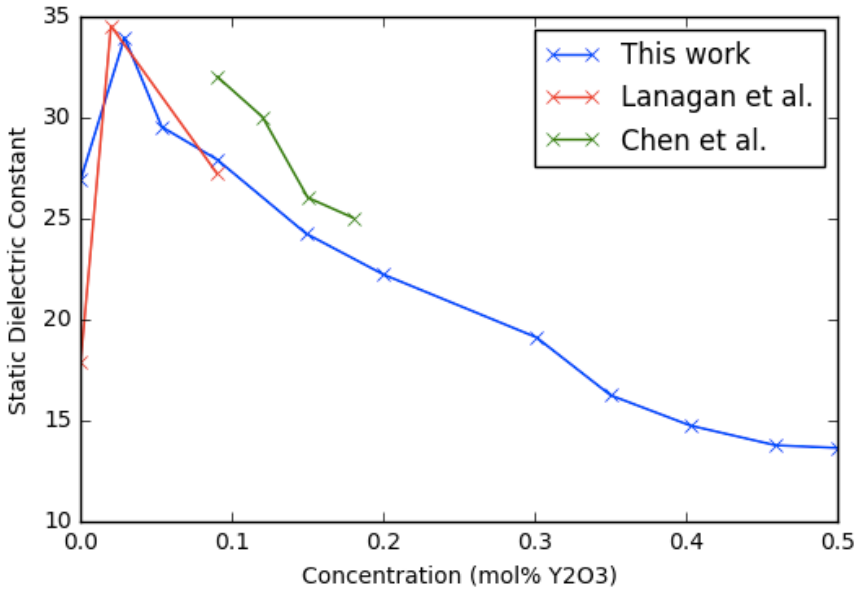

Figure 7.5. Dielectric constant expectation value over a range of dopant concentrations compared with experimental values from Lanagan[15] and Chen[14].

7.4.4 Tetragonality

Although the lattice parameters above were calculated using an enforced cubic supercell, it is well known that YSZ contains some tetragonal distortion of the unit cell, particularly at low dopant concentrations. However, the exact phase-boundary location between the cubic and tetragonal forms with increasing yttrium dopant concentration remains unclear. We have thus carried out further calculations on the four lowest concentration distributions in order to explore the impact of tetragonality. The procedure followed for permitting tetragonality is similar to that of the lattice parameter relaxation under enforced cubicity; the optimised internal coordinate structures using the pure ZrO_2 lattice constant are re-optimised allowing internal coordinates and lattice parameters to relax; each structure is run in triplicate constraining two of the three lattice parameters to have the same length on relaxation in order to enforce tetragonality. The optimised parameters are then averaged in order to obtain a c/a value describing the extent of the tetragonal distortion. Here we consider both the thermally weighted expectation value, calculated using the partition function, and the athermal (arithmetic) average. These c/a values are presented in table 7.4.

Dopant Concentration (mol% $YO_{1.5}$)	c/a Value	
	Athermal Average	Thermally Weighted Average
5.55	1.0141	1.0731
11.11	1.0003	1.0553
16.66	1.0001	0.9997
25.93	1.0000	0.9992

Table 7.4. Amount of tetragonal distortion with increasing concentration, described by c/a value.

In the case of the athermal average, only the very lowest dopant concentration studied displays a significant tetragonal distortion with all higher concentrations remaining essentially cubic. However, for the thermally weighted average only the dopant concentrations of >16 mol% $YO_{1.5}$ remain cubic, whilst significant tetragonal distortion is observed for the 5.55 and 11.11 mol% $YO_{1.5}$ sample distributions. Furthermore, the degree of tetragonality observed for the thermally weighted average values for these lower concentrations is much larger than the tetragonal distortion calculated for the athermal average, by ~6 and 5% respectively for the 5.55 and 11.11 mol% samples. In addition to this difference, we see that the c/a values calculated from the athermal average match closely with experiment, as can be seen in figure 7.6.

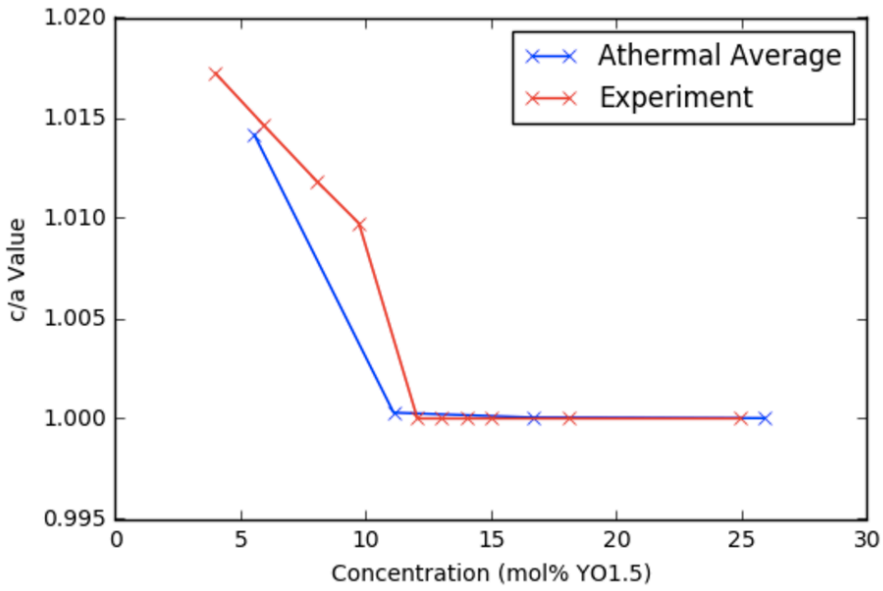

Figure 7.6. Tetragonal lattice parameter c/a value for a range of concentrations; comparing the calculated athermal average and experimental values obtained from H.G.Scott[16] figure 1.

It is interesting to note that the athermal average values are closer to the experimental values than the thermally weighted averages in the low concentration region. From inspecting a number of structures we observe that the lowest energy structures undergo very large tetragonal distortions with the c-lattice parameter of the supercell being ~1Å larger than the a-

lattice parameter. This situation equates to favourable defect alignment causing excessive lattice expansion in one direction, the effect of which may be exacerbated by the periodicity inherent in the calculations. Furthermore, even though these overly elongated structures are of lower energy, one expects that in reality there will be a mean-field pressure effect preventing such excessive expansion. As is discussed in greater detail later, YSZ is a frustrated system in which it is unlikely to ever occupy the true thermodynamic ground-state. This disparity of the thermally weighted average and the effect of excessively expanded structures can be further explained upon examination of the energetic density of states. Structural analysis shows that low energy structures are too expanded, and the DOS for the 5.55 mol% distribution, shown in figure 7.7, shows presence of two separate structural regimes; (i) the low energy over expanded region and (ii) the higher energy small tetragonal distortion region. The low energy overly expanded region will dominate the thermally weighted average, although as discussed above this represents an unphysical situation in real systems.

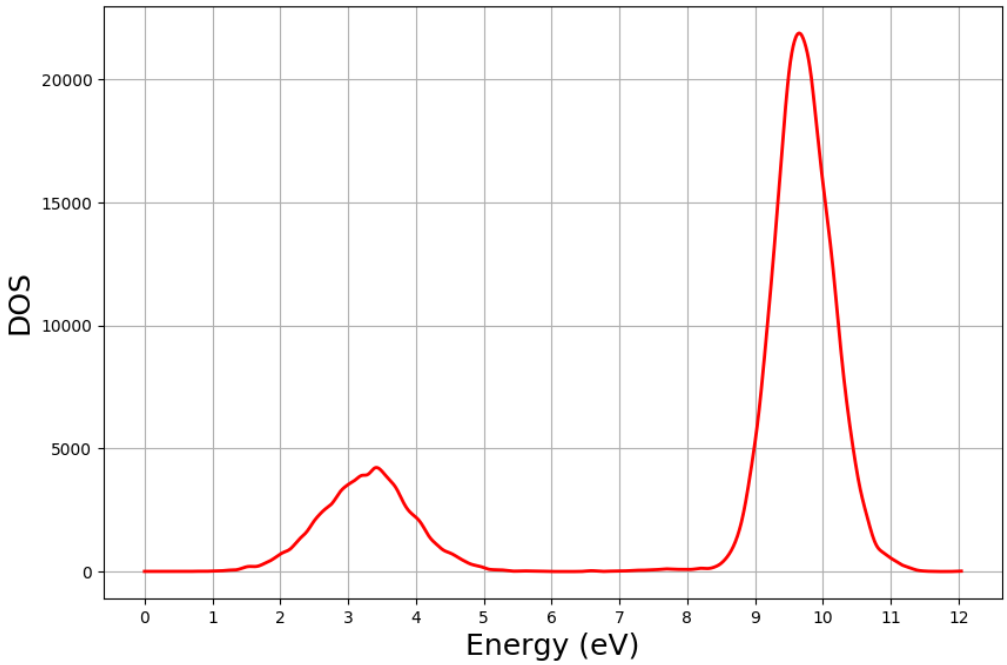

Figure 7.7. Density of states for the 5.55 mol% $YO_{1.5}$ tetragonal structures distribution.

We find that, in good agreement with experiment[16], the cubic phase is stabilised at a dopant concentration of ~ 11 mol% $YO_{1.5}$. Similar findings are also observed in the experimental work of Kawata *et al.*[12], in which the authors find that the lowest dopant concentration they study (10.95 mol% $YO_{1.5}$) only cubic fluorite reflections are detected in the X-ray diffraction pattern and only one cubic lattice parameter is given. However, in a single crystal YSZ neutron diffraction study with 18 mol% $YO_{1.5}$ doping, Faber *et al.*[17] find that the unit cell dimensions of their sample are not cubic, but that it is tetragonally distorted with a c/a value of 1.0141.

7.5 Energy Rankings

As shown above, interatomic potential geometry optimisation of an ensemble of randomly generated YSZ structures over a range of dopant concentrations provides very good agreement with a number of different experimentally obtained physical observables of YSZ. However, in order to determine further the validity of the random sampling approach, applied at the interatomic potential level of theory, we have compared the energy rankings of a number of structures optimised using both inter-atomic potentials and at the DFT level of theory. The rationale of the random sampling approach is to be able to screen a large number of structures cheaply by using interatomic potentials, with selection of candidate structures from the low energy range for further study or application. For this procedure to work, the low energy semi-empirical structures must correlate to low energy DFT structures. To examine whether or not there is a correlation between the energetics of the two sets of calculations, we first geometry optimise the structures using interatomic potentials, and use these geometry optimised structures as inputs for subsequent DFT optimisations. We investigate the case of 6.7 mol% YSZ, in which four substitutional yttrium cations and two oxygen vacancies are introduced into a 96-atom ZrO_2 supercell. Ten structures are selected from each of the low- middle- and high-energy ranges of the ensemble. We examine a number of different exchange-correlation functionals and will also comment on the effects of using unrelaxed structures as DFT inputs as well as optimiser step-size. Although we have seen previously that allowing for lattice expansion results in lower energy structures, in order to maintain consistency across the calculations internal coordinate optimisation is performed using the bulk lattice constant for pure ZrO_2 as optimised for each functional. Furthermore, our energy ranking calculations are for systems towards the low yttrium concentration end of the solid solution range where lattice expansion has the smallest effect.

7.5.1 Effect of Functional

DFT calculations are conducted using the VASP code and three different gradient-corrected DFT functionals were investigated for comparison with the structural energies obtained with interatomic potentials; PBE, PBEsol, and PBEsol-0. Full atomic optimisation was carried out using each functional from a pre-optimised structure obtained using potentials. The energy differences of the structures are compared in figure 7.8, in each case the energy of the lowest energy semi-empirical structure is set to zero on both the semi-empirical and DFT energy scales and energies of the other structures given relative to this.

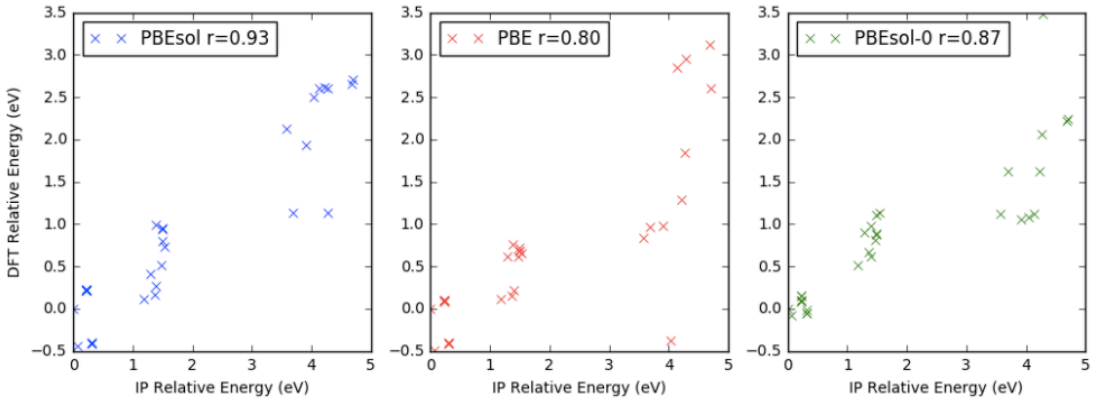

Figure 7.8. Relative energies of interatomic potential (IP) and DFT optimised structures using different exchange-correlation functionals, Pearson correlation 'r' coefficients are given.

There is a good correlation of the relative energies between DFT optimised and potential optimised structures in the case of all three functionals tested, in which the low energy semi-empirical structures correspond to the low energy DFT structures. However, the exact structure ranking changes and the lowest energy DFT structure is not the same structure as the lowest energy structure found by interatomic potentials. Furthermore, one of the highest energy structures according to potential calculations becomes one of the lowest energy structures after DFT optimisation with the PBE functional, although this does not occur for either of the PBEsol functionals. In general the energetic trend is best replicated using the PBEsol functionals and the distinct separation of the low energy structures observed with the hybrid functional PBEsol-0 supports the strategy of selecting low energy structures that have been randomly sampled with interatomic potentials.

7.5.2 Effect of Step Size

In the above comparison between energies of semi-empirical and DFT optimised structures we use the relaxed outputs from empirical calculations as inputs for the DFT calculations and employ a small step size for atomic movement in order to minimise the effect of large atomic movements in the optimisation. However, we have also investigated taking these relaxed empirical structures and further optimising in DFT using the VASP default optimisation parameters. For the large part the energies of the resultant structures remain unchanged, however some structures experience a large reduction in energy. In particular some high-energy structures have energies comparable to the low-energy optimised structures after optimisation with the default step-size. One such example is a high-energy structure initially high in energy after potential optimisation and confirmed to remain a high-energy structure after DFT optimisation using a small step size. However, when relaxing the potential optimised structure

with the larger step size the structure becomes 2.85 eV more stable (in the PBEsol functional case). This gain in energetic stabilisation can be explained upon inspection of the structures. For the smaller step size optimisation there is very little movement of atoms, with an average and maximum oxygen atom movement of 0.12 and 0.51Å respectively, whereas for the larger step size the average and maximum oxygen movement is 0.25 and 2.02Å respectively. Further inspection of the structures show that in the starting structure there is an oxygen vacancy present in a NN position to an yttrium atom, which remains there under optimisation with the small step size. However, optimisation with the large step size leads to one oxygen atom moving over 2Å to fill the vacancy, pushing it to now occupy a NNN position to the yttrium cation. The large initial movement on optimisation, due to the larger step size, allows the structure to optimise to a different minimum on the energy landscape, whilst this minimum is lower in energy the resultant structure is different than the initially potential optimised structure as a result of the large step size causing the optimisation to miss the metastable high-energy structure. Clearly on this complex energy surface, small changes of the minimisation protocols can give significantly different results.

7.5.3 Effect of Input

As well as investigating the effect of step size on the DFT energies, the effect of using the original input coordinates was also studied. Instead of using the pre-relaxed structure from interatomic potential geometry optimisation calculations as the input for DFT optimisation, we used the original unrelaxed atomic coordinates as a starting point for the DFT calculations. In this scenario the input structures for both the potential and DFT optimisations are the same, and the atoms are on the perfect fluorite lattice sites. The relative energies of the semi-empirical and DFT optimised structures, using the PBEsol functional, are displayed in figure 7.9. As can be seen, despite having an r value comparable to those achieved from the pre-relaxed structures, there is a bigger overlap in the energies of the low- and middle-energy range potential structures when geometry optimised with DFT. It is also worth noting that the absolute energies of the structures first optimised with potentials and subsequently optimised with DFT are in general lower than those obtained from direct optimisation of the unrelaxed atomic coordinates in DFT. Additionally the energies of the structures obtained when optimising from the unrelaxed starting point do not change when increasing the step size. In a similar fashion to what is observed with the increased step size effect above, it appears as if optimising from an unrelaxed or relaxed structure with DFT will cause the system to occupy a different minimum on the energy landscape. Furthermore, it should not necessarily be a surprise that despite having the same starting geometry the potential and DFT optimisations relax to different structures as the system will be most sensitive at the high energy starting point where all atoms occupy the perfect fluorite lattice sites.

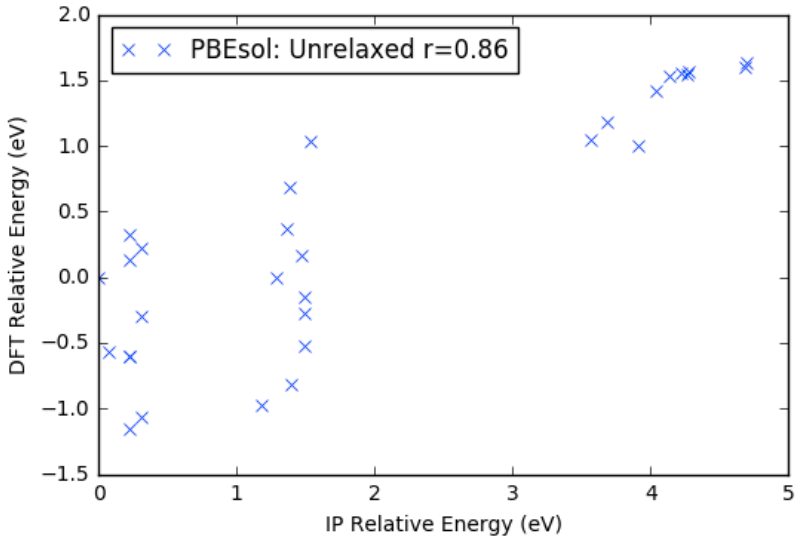

Figure 7.9. Relative energies of IP and DFT optimised structures using unrelaxed atomic coordinates as inputs for both optimisation methods, Pearson correlation 'r' coefficient is given.

One concern when performing IP studies is how well the interatomic potential results reflect those that would be obtained using ab-initio methods. In the recent random sampling study of 8 mol% YSZ by Dong *et al.*[2] the authors first generated a large number of structures before screening them by optimising the internal coordinate geometry with interatomic potentials. Selected structures across the entire energy range were then optimised at the DFT level of theory, using relaxed structures from IP calculations as starting points, utilising the PBE exchange-correlation functional. The authors compare absolute energy differences of the structures and find that increasing interatomic energy of structures correlated well with increasing ab-initio energy, and that whilst the 10 lowest energy structures according to IP results spanned a range of 3 eV for DFT calculated energies these 10 structures all lie in the lower range of DFT energies. The authors therefore conclude that as the correlation between energies is tight, and that trend reversal is not observed, that sampling the low energy range of random structures sufficiently captures the corresponding DFT low energy structures. In an initial investigation by Parkes *et al.*[7] the authors first pre-screen 32,000 randomly generated structures of 3.2 mol% YSZ (one Y-V-Y defect cluster in a 96-atom supercell) by performing fixed-shell single-point calculations using interatomic potentials. They find 28 plateau regions in the energy distribution and determine that structures with the same energy must be symmetry equivalent, leaving 28 unique configurations. The single-point energies of these 28 structures are then calculated with DFT and compared with the semi-empirical single-point energies, the energetic ordering of the structures calculated at both levels of theory remains the same. However, in a subsequent study of the same system the authors geometry optimise the internal coordinates of the 28 inequivalent structures and compare the defect formation energies[18]. They find that whilst the potential model reproduces the general trend of increasing DFT energetics,

and both predict the lowest energy structures to have vacancies in NNN positions to yttrium ions, that the defect formation energies correlate poorly and furthermore DFT and the interatomic potentials predict the minimum energy defect structure to be different, with the potential model also predicting metastable structures to be unstable with respect to local reconstructions. Furthermore, most recently Parkes *et al.* begin to investigate vacancy-vacancy interactions by studying 6.7 mol% YSZ systems consisting of two Y-V-Y dopant clusters in a 96-atom supercell[1]. Again the internal coordinates of all symmetry inequivalent structures (when only NNN or further yttrium-vacancy separations are considered) are relaxed using both DFT and interatomic potentials. In this case the total energies of the systems are compared and again the general trend of increasing energies at both levels of theory is replicated although the correlation between DFT and semi-empirical energies is worse for the higher dopant concentration study, which uses a larger sample size. However, there appears to be good correlation for the high-energy structure range and additionally it is unclear whether or not the internal coordinate relaxation occurs from the initial lattice positions for both DFT and semi-empirical optimisations, or whether the structure is first optimised using potentials and that resultant structure is then re-optimised using DFT as is the case in the study of Dong *et al.*[2] and is found to be more reliable in this study. In the case of the former, when initial lattice positions are used for optimisation at both levels of theory, the resultant optimised structures are extremely sensitive to the optimiser parameters, in particular the step size for atomic movement and too large an initial jump can easily result in the structure optimising from the initial high energy lattice site position into different minima on the energy landscape.

7.6 Local Structure Analysis

The above analysis has shown the good agreement of the calculated properties of YSZ as a function of concentration with various experimentally determined observables; and the structural energy rankings of interatomic potential calculations agreeing with the DFT calculated energies verify and validate the chosen method of random sampling of YSZ solid solutions. Since we can be confident that the low energy structures calculated with interatomic potentials represent the DFT low energy structures (although the detailed rankings may change), it is now instructive to perform local structure analysis of these low energy structures in order to determine the features present in the local environment of YSZ. In particular the vacancy-vacancy and vacancy-cation interactions are studied.

7.6.1 2x2x2 Supercell – 2 Vacancies

The simplest case for identifying vacancy-vacancy interactions is that with two vacancies, and four substitutional yttrium cations, in a 96-atom 2x2x2 supercell of pure cubic ZrO_2, corresponding to a dopant concentration of 6.7 mol% Y_2O_3. The same low- middle- and high-energy structures discussed in section 7.5 are again presented here. The average radial distribution functions (RDFs) for the 10 most stable (lowest energy) structures, both before and after geometry optimisation are shown in figure 7.10. The vacancy-cation and vacancy-vacancy distances are shown. For initial structures, the location of the original oxygen vacancy is trivial as all atoms remain on the perfect fluorite lattice sites, whereas atoms are displaced away from these lattice sites on geometry optimisation. In the case of geometry optimised structures, vacancies are detected by comparing the initial and final structures and identifying regions of space in which an atom would have been found previously.

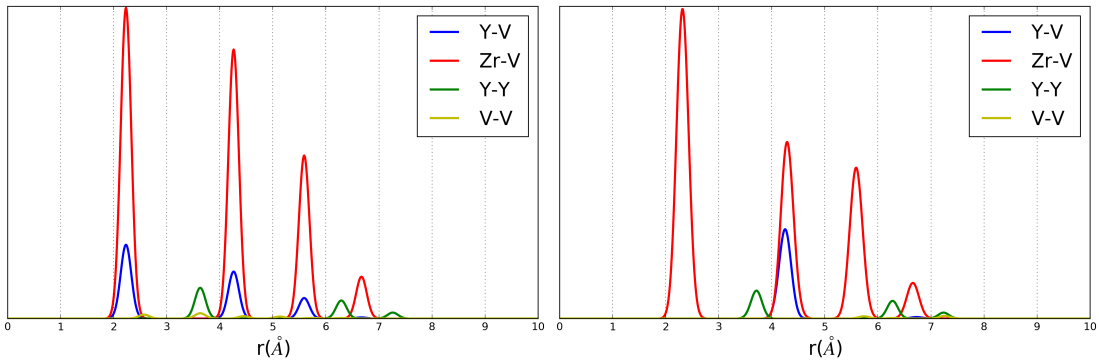

Figure 7.10. Average RDFs for low energy structures of 6.4 mol% Y_2O_3 doping in a 2x2x2 cubic ZrO_2 supercell; before (left) and after (right) geometry optimisation. Yttrium-vacancy (Y-V), zirconium-vacancy (Zr-V), yttrium-yttrium (Y-Y), and vacancy-vacancy (V-V) interactions are shown.

From inspection of the RDF plots before and after geometry optimisation it is immediately noticeable that, although there are vacancies in the first, second, and third coordination sphere of yttrium cations before optimisation, after optimisation vacancies solely reside in next nearest neighbour positions to yttrium. This preference of vacancies to occupy NNN sites to yttrium is in agreement with experiment and further validates the interatomic potentials used in this study. Additionally, vacancies can be seen at distances of ~2.5 and 3.5Å from each other prior to optimisation, although the vacancy-vacancy distance increases to a minimum of ~5.8Å after optimisation suggesting that in low-energy structures vacancies repel each other at low concentration. Furthermore, the stark contrast between the RDF plots before and after optimisation indicates that quite significant changes in atomic positions occur upon structural

relaxation. Figure 7.11 details the atomic movement upon geometry optimisation of a representative low energy structure (structure L1).

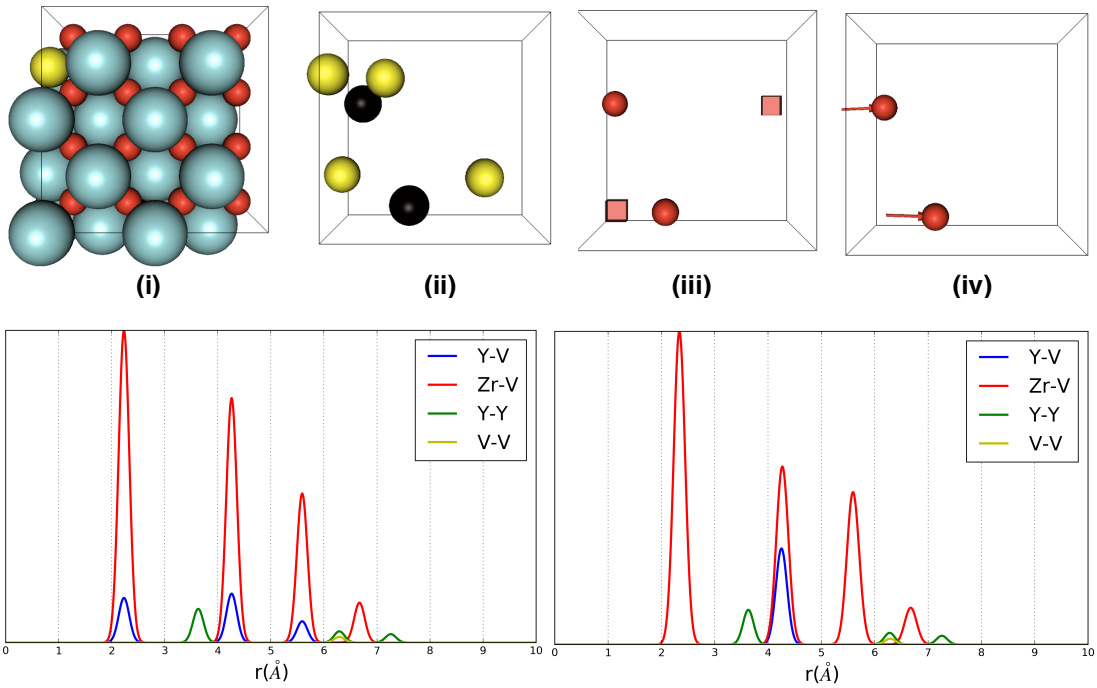

Figure 7.11. Geometry optimisation (top) and RDFs (bottom) for structure L1. The geometry optimisation pictures from left to right show; (i) the initial starting structure, (ii) the initial positions of yttrium (yellow) and vacancies (black), (iii) the new position of vacancies (red cubes) and new oxygen positions (red spheres), and (iv) new oxygen positions with displacement vectors. The RDFs shown are before (left) and after (right) geometry optimisation.

In structure L1 one of the oxygen vacancies is initially NN to an yttrium ion (highest vacancy in figure 7.11 (ii)), and on geometry optimisation this vacancy becomes filled with an oxygen ion with a resultant new vacancy position created from where the oxygen ion has migrated. This oxygen ion has effectively moved from a neighbouring periodic image of the simulation cell, which is why the new vacancy appears on the other side of the cell. Whilst it is to be expected that vacancies NN to yttrium are unfavourable and the filling of this vacancy to leave a NNN vacancy position is in accordance with the experimentally observed structure of YSZ, it is interesting to note that the second vacancy also becomes filled. This second vacancy is not initially NN to yttrium but NNN to one yttrium cation and third nearest neighbour to another. Following geometry optimisation the original vacancy becomes filled with an oxygen ion and the resultant vacancy is NNN to all yttrium cations. Although this second initial vacancy is third nearest neighbour to yttrium it appears that it is more beneficial to maximise NNN interactions to yttrium than to increase the distance to yttrium. The preference for the NNN position of a vacancy to an yttrium ion has previously been described for the isolated vacancy case as balancing the attractive Coulomb force between yttrium and the vacancy and the strain energy

of the larger yttrium cation requiring eightfold coordination, we see here that this also holds for when more than one vacancy is present in the calculation. The phenomenon of maximising yttrium-vacancy NNN interactions has also been seen recently in the work of Dong *et al.*[2] Furthermore as a result of both vacancies 'moving' they remain at the same distance to each other.

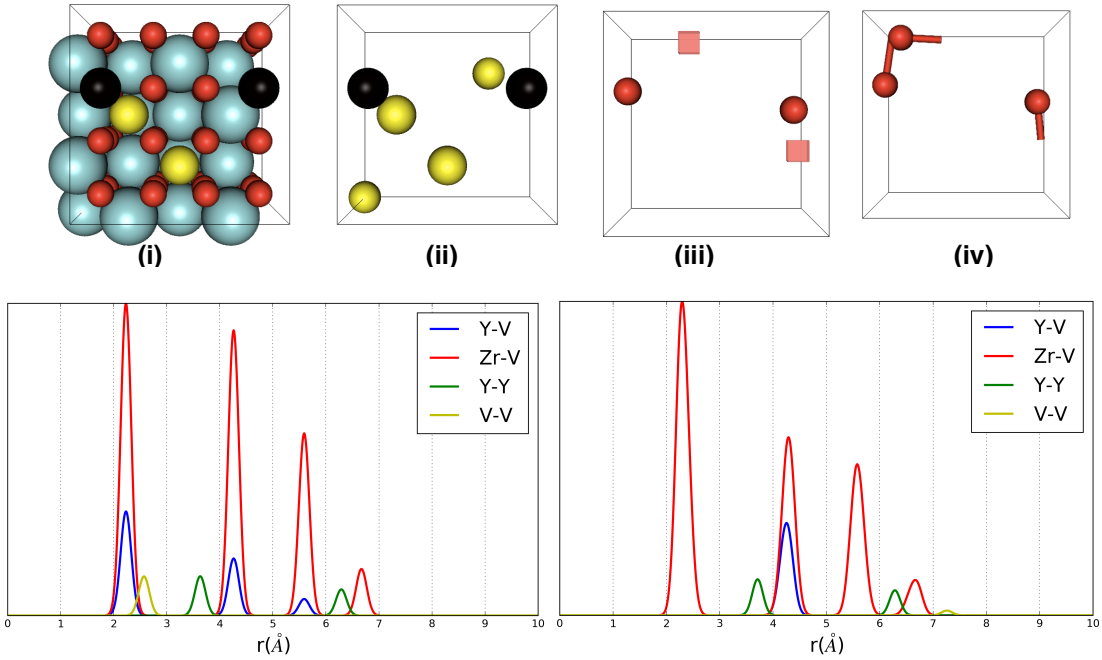

Figure 7.12. Geometry optimisation (top) and RDFs (bottom) for structure L2. The geometry optimisation pictures from left to right show; (i) the initial starting structure, (ii) the initial positions of yttrium (yellow) and vacancies (black), (iii) the new position of vacancies (red cubes) and new oxygen positions (red spheres), and (iv) new oxygen positions with displacement vectors. The RDFs shown are before (left) and after (right) geometry optimisation.

Figure 7.12 depicts the RDFs and the atomic movement on geometry optimisation of another low energy structure (structure L2). As with structure L1, structure L2 also maximises the NNN yttrium-vacancy interactions after structural relaxation. However, in comparison to L1 structure L2 starts with the vacancies occupying nearest neighbour positions to each other at a distance of ~2.6Å, and on geometry optimisation the vacancies repel each other and are now at a distance of over 7Å apart from each other. Furthermore, unlike the case for structure L1 in which only two oxygen atoms are displaced in order to form new vacancy positions, in the case for L2 concerted oxygen movements can be seen.

We can see for structures L1 and L2, and from the average RDF plot for the lowest energy structures that low-energy structures generated from random sampling are favoured as they have oxygen vacancies in NNN positions to dopant yttrium cations, which is consistent with

experimental observations. In addition, examination of the average RDF plots for structures in the middle of the energy range and of the highest energy structures (figure 7.13.) reinforces the notion that having yttrium NNN to vacancies is energetically favourable. The 'middle'-energy and high-energy structures both contain yttrium-vacancy interactions at 1st, 2nd, 3rd, and 4th nearest neighbour distances, with the high energy structures having a higher ratio of nearest neighbour yttrium-vacancy interactions. Furthermore, the middle- and high-energy structures also have vacancies closer to each other than in the low-energy case, with average vacancy-vacancy distances of ~3.6 and 2.8Å respectively.

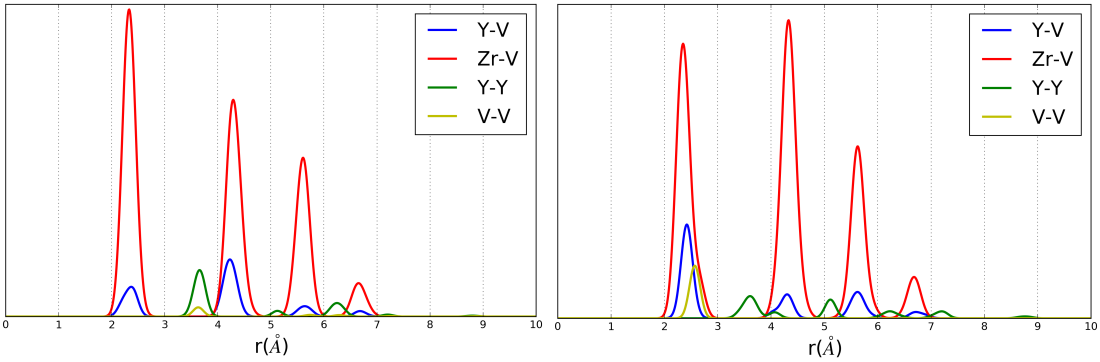

Figure 7.13. Average RDF plots of 10 structures in the middle (left) and high (right) energy ranges, of the randomly generated structure ensemble, following geometry optimisation.

Although it is clear that the yttrium-vacancy NNN interaction affects strongly the system energy, the vacancy-vacancy separation also plays a role in determining the energy of the structure and it is a combination of these two factors that governs the energy of YSZ. For example, one of the high-energy structure RDFs (structure H1) is shown in figure 7.14; as can be seen, there are no NN yttrium-vacancy interactions, the high energy of the system therefore appears to be linked to the NN vacancy-vacancy interaction. Additionally, when comparing the yttrium-yttrium separation for the low, middle, and high energy structures it can be seen that the nearest neighbour peak at ~3.5Å is dominant for the low and middle energy structures whereas the NN and NNN yttrium-yttrium peaks are of similar sizes for the high energy structures. Furthermore only NN and 3NN Y-Y peaks are seen in the low energy systems whilst the 2NN peak is present for the middle structures, although the exact nature of the effect of yttrium-yttrium separation on the energy is unclear. However, it is also worth noting that for the high-energy systems, the majority of the oxygen atoms remain on the perfect cubic fluorite lattice sites after structural optimisation, and that for the low energy structures all of the oxygen atoms are slightly displaced away from the ideal lattice sites, highlighting the local structural disorder of YSZ. Whilst the yttrium-vacancy and vacancy-vacancy interactions are clearly important in determining the structural energy, the extent of oxygen displacement away from lattice sites also contributes to the determination of the system energetics.

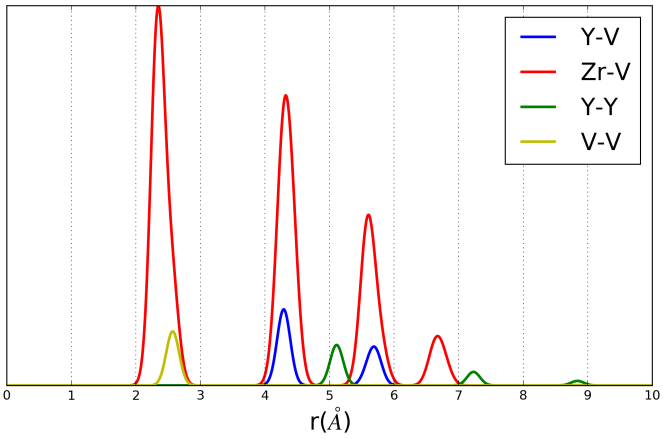

Figure 7.14. High-energy structure H1 RDF plot.

Additionally, RDF plots (figure 7.15) of the DFT output structures further reveal that the PBE_{sol}-0 structures that used pre-relaxed potentials structures as inputs do correspond to the low-energy potentials geometries, and that when optimising the geometry from the same input as the potentials the system relaxes to a different local minimum. The average low-energy structure hybrid functional RDF in figure 7.15 is very similar to the average low-energy IP RDF from figure 7.10, whilst the average DFT optimised RDF from the unrelaxed starting point is very different and has more of the unfavourable yttrium-vacancy NN interactions present.

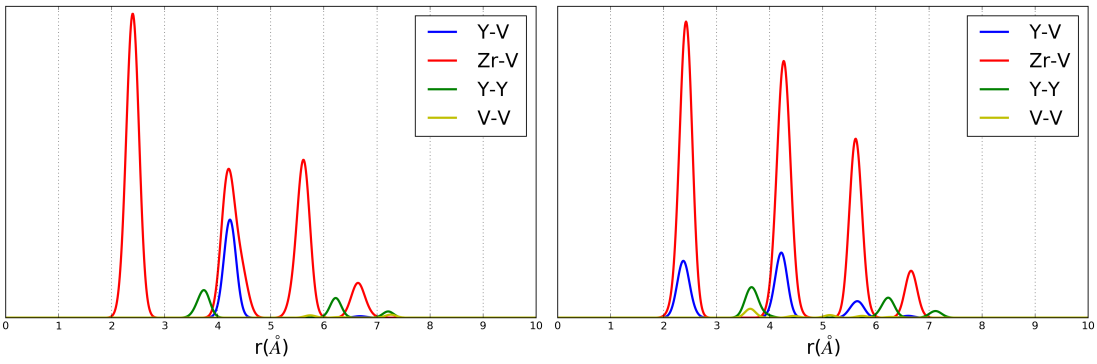

Figure 7.15. Average RDF plots of low-energy structures for DFT optimisation; using PBE_{sol}-0 from pre-optimised inputs (left) and using PBE_{sol} from the unrelaxed potentials input (right).

7.6.2 3x3x3 Supercell – 9 Vacancies

After establishing the optimum yttrium-vacancy and vacancy-vacancy distribution in the simplest case in which multiple vacancies are present in the same simulation cell, these interactions are now examined in the 324-atom 3x3x3 ZrO_2 supercell, containing 9 oxygen vacancies and 18 dopant yttrium cations which equates to the industrially relevant dopant concentration of 9.09

mol% Y_2O_3. The average RDF plots for the lowest and highest energy 10 structures before and after geometry optimisation and lattice parameter relaxation (as described in section 7.4.1) are displayed in figure 7.16. As can be seen, the same features seen previously for the lowest energy structures in 6.7 mol% doping in the 2x2x2 supercell are present for the low energy structures for this higher concentration in the larger simulation cell, namely that on structural optimisation, the NN yttrium-vacancy interaction disappears and the NNN yttrium-vacancy interactions are increased, and that close vacancy-vacancy interactions are un-favourable with a minimum vacancy-vacancy interaction distance of ~4.5Å. Furthermore, the highest energy structures in the larger cell used here also contain features of the highest-energy structures for the smaller cell 2 vacancy case in that NN vacancy-vacancy interactions and NN vacancy-yttrium interactions are present.

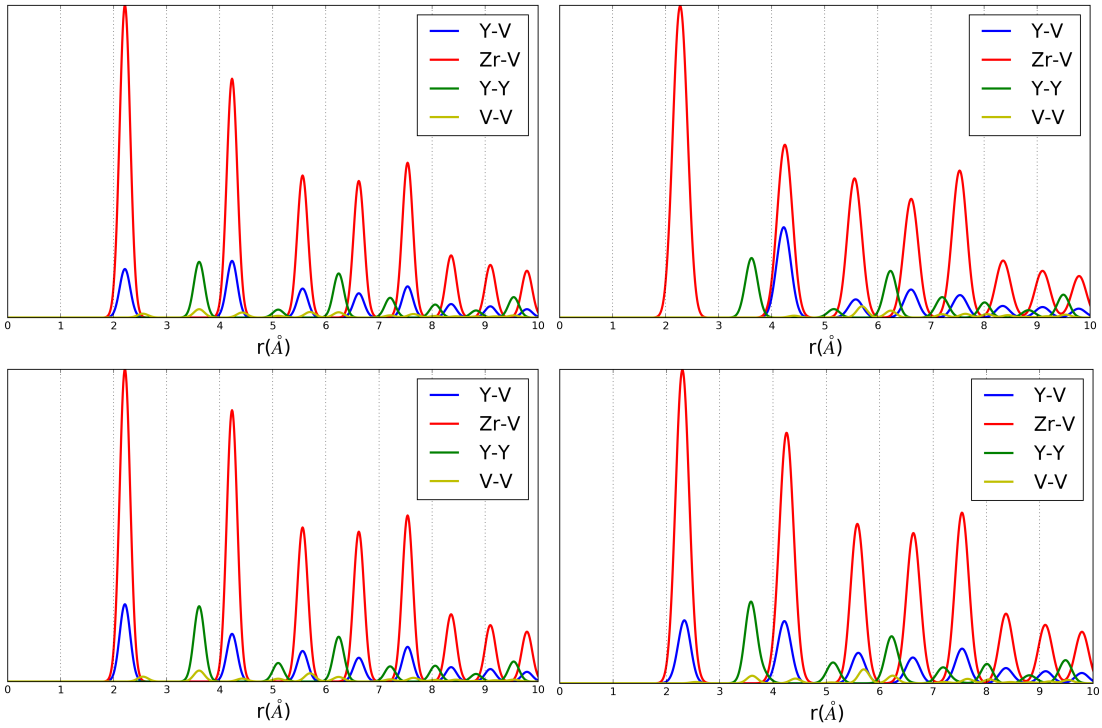

Figure 7.16. Average RDF plots for the 10 best (top) and worst (bottom) structures; before (left) and after (right) geometry optimisation, for 9.09 mol% YSZ.

The yttrium-vacancy and vacancy-vacancy interactions across the YSZ solid-solution range have also been investigated and the average RDF plots after geometry optimisation and lattice parameter relaxation are shown in figure 7.17. Interestingly some NN yttrium-vacancy interactions persist in the low (3 and 6 vacancies) concentration ranges, although the vacancy-vacancy separation remains large. As more vacancies and substitutional yttrium cations are introduced into the simulation cell the NN yttrium-vacancy peak becomes more prominent as it becomes impossible to not have vacancies situated next to yttrium cations, yet there is still a large preference for the NNN site. Furthermore, smaller distances for the vacancy-vacancy

interactions are observed as the vacancy concentration increases, although even at a dopant concentration of 40.26 mol% Y_2O_3 the NN vacancy-vacancy interaction remains relatively unfavoured when compared to larger separations. Throughout the entire concentration range, the NN and 3NN yttrium-yttrium separation over 2NN Y-Y separation, as seen previously for the 2x2x2 supercell, is observed.

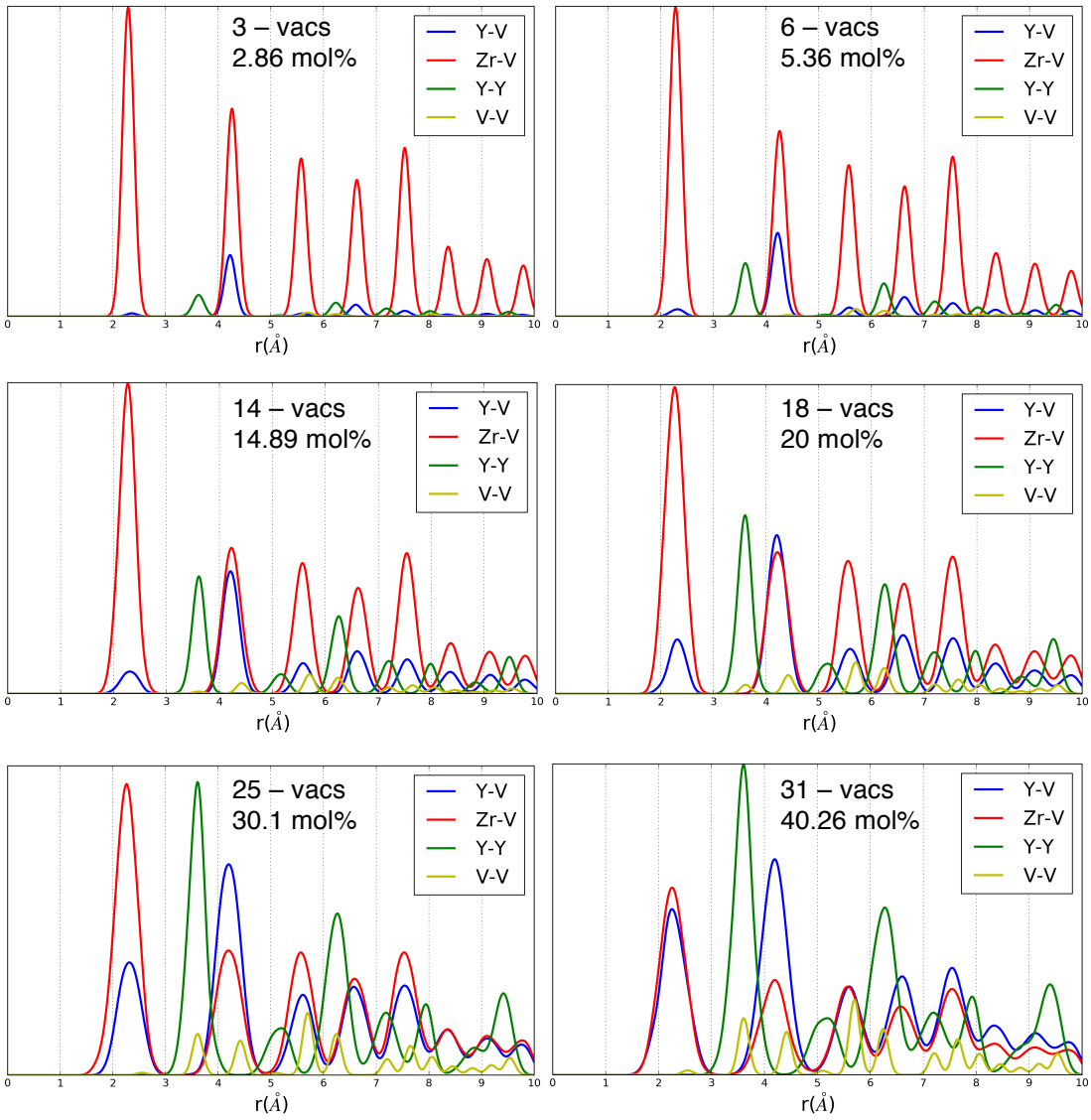

Figure 7.17. Average RDF plots for the 10 lowest energy structures of 3x3x3 ZrO_2 supercells containing; 3, 6, 14, 18, 25, and 31 oxygen vacancies and associated charge compensating substitutional yttrium cations.

7.7 Global Optimisation

The above results for the calculated macroscopic properties of YSZ as well as the analysis of the local structure of configurations generated by a random sampling approach are in good agreement with experimental values and previous computational results. However, as discussed in section 7.4, the search space for realistic system sizes is too large to be comprehensively covered and random sampling is known to be an inefficient method for global optimisation. To that end we have taken the 100 lowest energy configurations from the random sampling search as inputs for a 'basin-hopping' like, solid-solution mixing, approach to finding the global minimum. The input structures, with atoms on ideal cubic lattice sites, of low energy structures following internal coordinate optimisation and lattice parameter relaxation are taken as inputs for this basin-hopping approach. Two 'move-classes' are then allowed; (i) cations can swap with cations in their neighbouring first cation coordination sphere, and (ii) anions and vacancies are allowed to swap with each other within the first anion coordination sphere. On each step in the 'basin-hopping' one cation and one anion swap are permitted. Swaps occur between cubic lattice site positions and system energies are evaluated after structural optimisation. In this series of calculations we use a fixed lattice-parameter length, which is a linear interpolation between the pure ZrO_2 cubic unit cell and the Y_2O_3 unit cell corresponding to the number of formula units of each parent oxide within the system studied, and optimise internal coordinates only. For all 100 input structures, lower energy structures were found as a result of this swapping procedure. Each structure has been run for ~1000 swap steps (minimum 830, maximum 1477) and the starting and final energies, where the final energy is the lowest energy found, for each configuration are displayed in figure 7.18. The energies are given per cation in the supercell; the smallest energetic stabilisation between the starting and final structures is -0.006 eV, whilst the largest stabilisation is -0.058 eV with the average energetic gain being -0.026 eV.

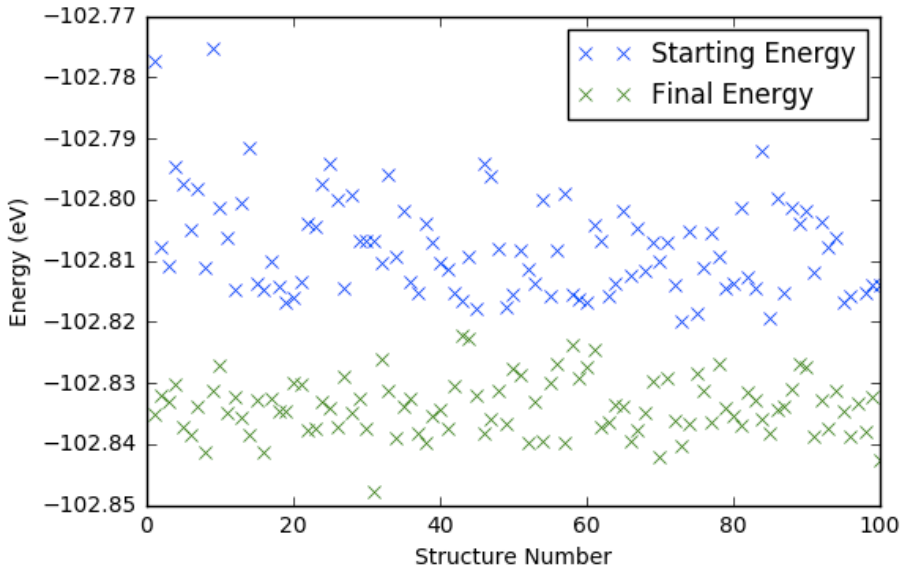

Figure 7.18. Starting and final energies (per cation) for each structure before and after ~1000 swap steps.

The average RDFs for all 100 starting structures and the lowest energy structures found for each 'basin-hopping' run, after internal coordinate optimisation, are given in figure 7.19. Whilst these remain very similar, the lower energy 'final' structures have a larger Y-V NNN peak and a smaller Y-V NN peak when compared to the initial structures.

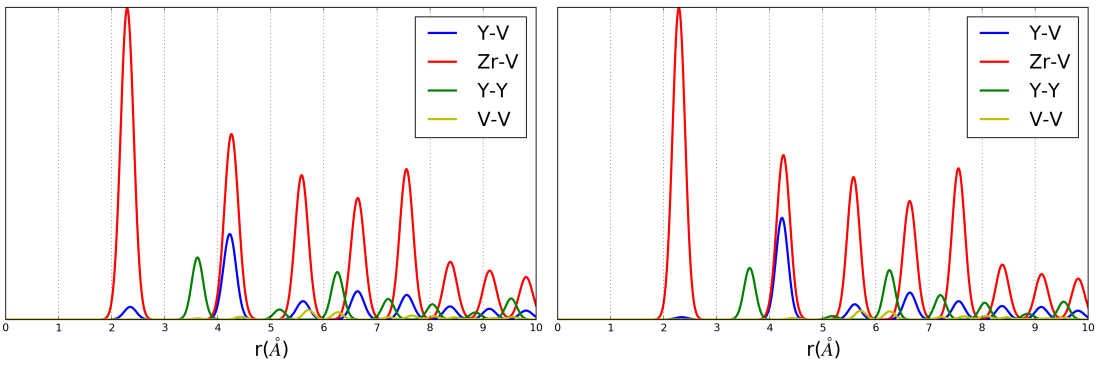

Figure 7.19. Average RDFs for starting (left) and lowest energy 'final' (right) structures from the 100 basin-hopping calculations after ~1000 swaps.

In addition to the average picture in figure 7.19, the same information is also displayed for individual cases. For example the RDFs for the input structures and output structures (after geometry optimisation) for the starting and 'final' basin-hopping configurations of the system that gains the most energetic stabilisation (of -0.058 eV per cation) are shown in figure 7.20.

Compared to the starting configuration the final configuration, which is lower in energy, has a larger Y-V NNN peak and therefore more Y-V NNN interactions. The vacancy-vacancy separation is also larger for the lower energy structure. Interestingly the input RDFs (with atoms on cubic lattice sites) are very similar for both structures, so although the starting configurations may be very similar they optimise to different outputs with a significant energy difference between them. Furthermore, although we perform a global optimisation procedure in order to find lower energy structures, and identify a *de-facto* global minimum in this study, it is worth reiterating that it is unlikely that YSZ will ever be able to achieve the true thermodynamic ground-state configuration, and in reality we expect a large number of different structures to exist that share similar structural features. This global optimisation procedure therefore serves to further identify the low energy structural features of YSZ.

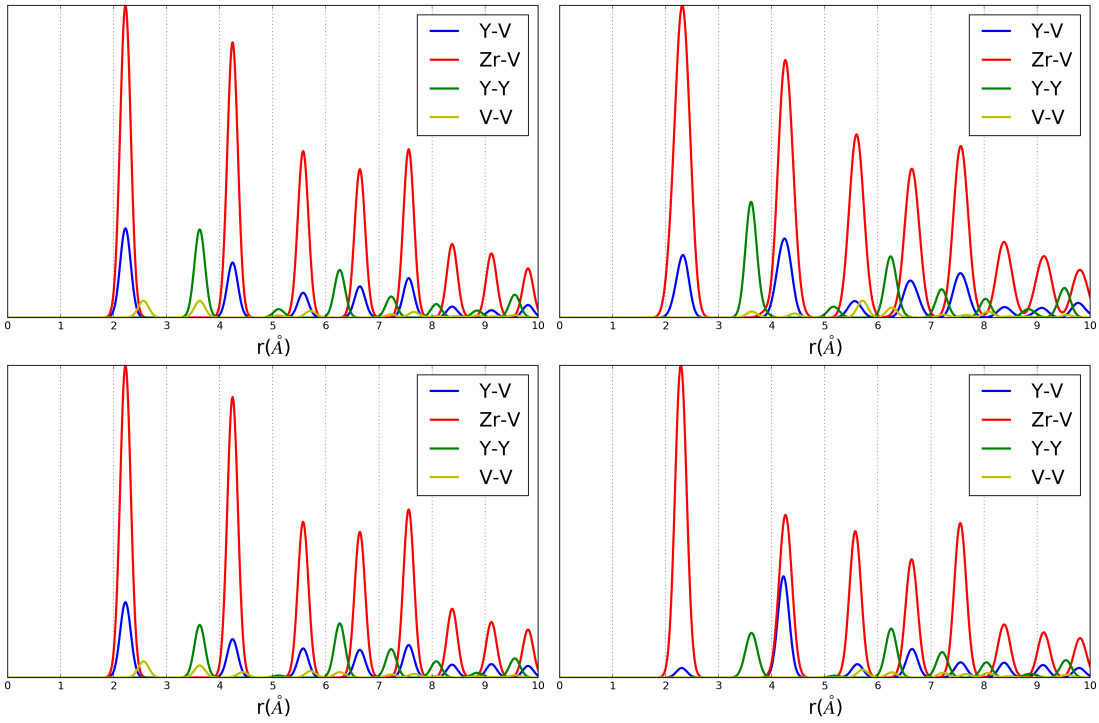

Figure 7.20. RDFs for input structures (left) and output structures (right) of the starting (top) and final (bottom) structures from one 'basin-hopping' atom swapping run (~1000 swaps).

7.7.1 'Global' Minimum

Here the structure and features of the lowest energy structure found during the 'basin-hopping' solid-solution mixing procedure are investigated. This is tentatively labelled the 'global' minimum, as it is the lowest energy system found in this study, although it is not expected to be the true global minimum. In reality we expect a large number of different structures to exist that share similar structural features. This structure (G1) is 0.56 eV lower in energy (0.005 eV per cation) than the second lowest energy system. Figure 7.21 shows the geometry-optimised RDF

of this structure as well as the new and original vacancy positioning and oxygen ion displacement upon structural relaxation. The RDF largely has the same features as low-energy systems seen previously: the Y-V NNN peak is dominant with a large vacancy-vacancy separation (~5.7Å). Additionally the oxygen ion displacement shows that both single and many oxygen/vacancy concerted jumps occur on geometry optimisation in order to leave the vacancies in their most stable locations. Whilst lower energy structures are indeed found via this 'basin-hopping' approach it is not entirely clear why as this large change in vacancy positions upon structural optimisation still occurs. It is therefore assumed that nearest neighbour atomic swaps from favourable configurations of an already low-energy starting structure generated by random sampling also leads to new lower-energy starting structures.

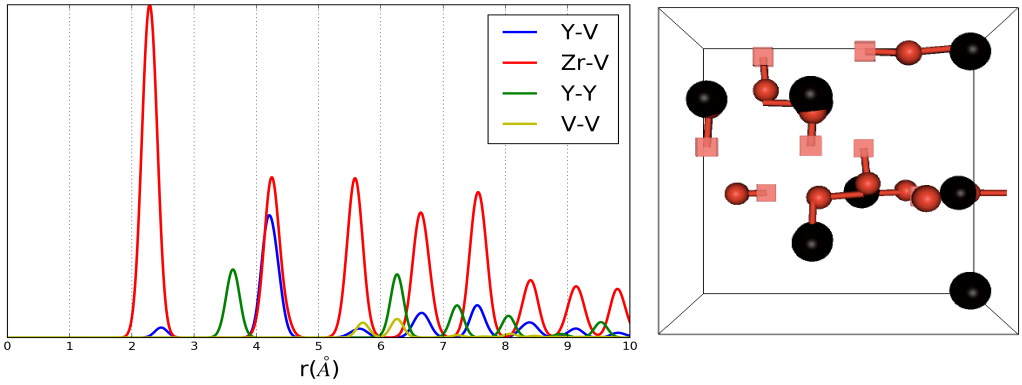

Figure 7.21. RDF (left) and vacancy positions and oxygen ion displacement (right) for the 'global' minimum G1 structure.

Furthermore when inspecting the structure it can be seen that the large Y-V NNN RDF peak is a result of maximising the number of Y-V NNN interactions, with some vacancies being 7-fold coordinated to yttrium cations in the second cation coordination sphere. Figure 7.22 shows the second nearest neighbour yttrium-vacancy coordination connectivity present in this 'global' minimum structure, with oxygen and zirconium atoms not present in the picture. This NNN connectivity forms a 'layer' within the YSZ system, although zirconium and oxygen atoms are interspersed there are four atomic layers (two zirconium, two oxygen) of solely ZrO_2 without yttrium or vacancies present. Within this yttrium-vacancy 'layer' the minimum coordination of one vacancy at a NNN distance to yttrium is 3-fold coordinated, with a further 1 vacancy 4-fold, 4 vacancies 5-fold, 1 vacancy 6-fold, and 2 vacancies 7-fold coordinated to yttrium ions. In contrast to this, a typical high-energy structure from the original random sampling ensemble has roughly 3 yttrium-vacancy NNN interactions, with each vacancy only 1-fold coordinated to yttrium at a 2NN distance.

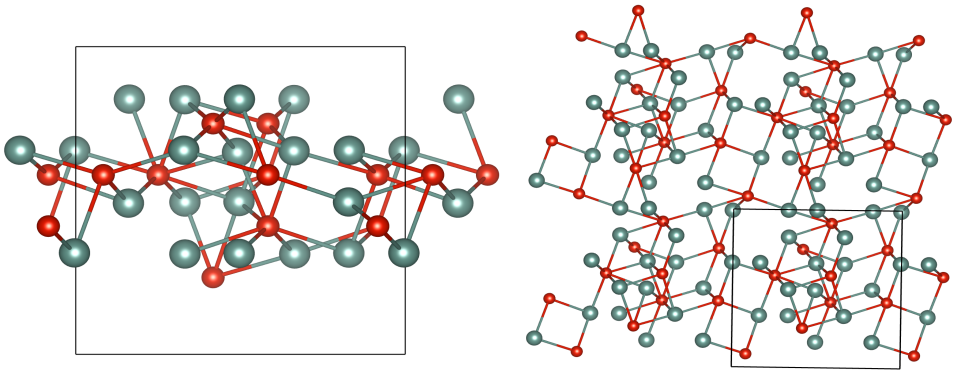

Figure 7.22. Yttrium-vacancy second nearest neighbour connectivity; side view (left) and top view (right). Grey and red spheres represent yttrium atoms and vacancies respectively; the black square denotes the unit cell.

The vacancy-vacancy separation can also be explained in terms of maximising the NNN yttrium-vacancy interactions. Whilst it is expected that vacancies repel at close distance due to being of the same charge, there is not an obvious distance to which they repel. It could be expected that this vacancy-vacancy separation be maximised to negate the Coulomb repulsion between them as much as possible, although some evidence for vacancy 'pairing' has been suggested. In the RDF of the 'global' minimum structure there is a preference for vacancies to be either ~5.7 or 6.3Å apart from each other. When considering the fluorite structure of cubic zirconia and in particular the oxygen anion sub-lattice, the oxygen positions form a primitive cubic lattice with oxygen atoms at each corner of the cube and a cation at the centre of each cube. If considering solely anion-anion coordination the first nearest-neighbour oxygen-oxygen distance is at ~2.5Å, and the distances of ~5.7 and 6.3Å correspond to 5^{th} and 6^{th} nearest-neighbours to the original oxygen atom. If one vacancy is placed in the first anion position, and a second vacancy is placed at either the 5^{th} or 6^{th} nearest neighbour position, both vacancies can be NNN to the same yttrium cation. The vacancy-vacancy separation observed in the RDF of the 'global' minimum structure can therefore also be thought of as the result of maximising the number of yttrium-vacancy 2NN interactions. This situation is depicted below in figure 7.23.

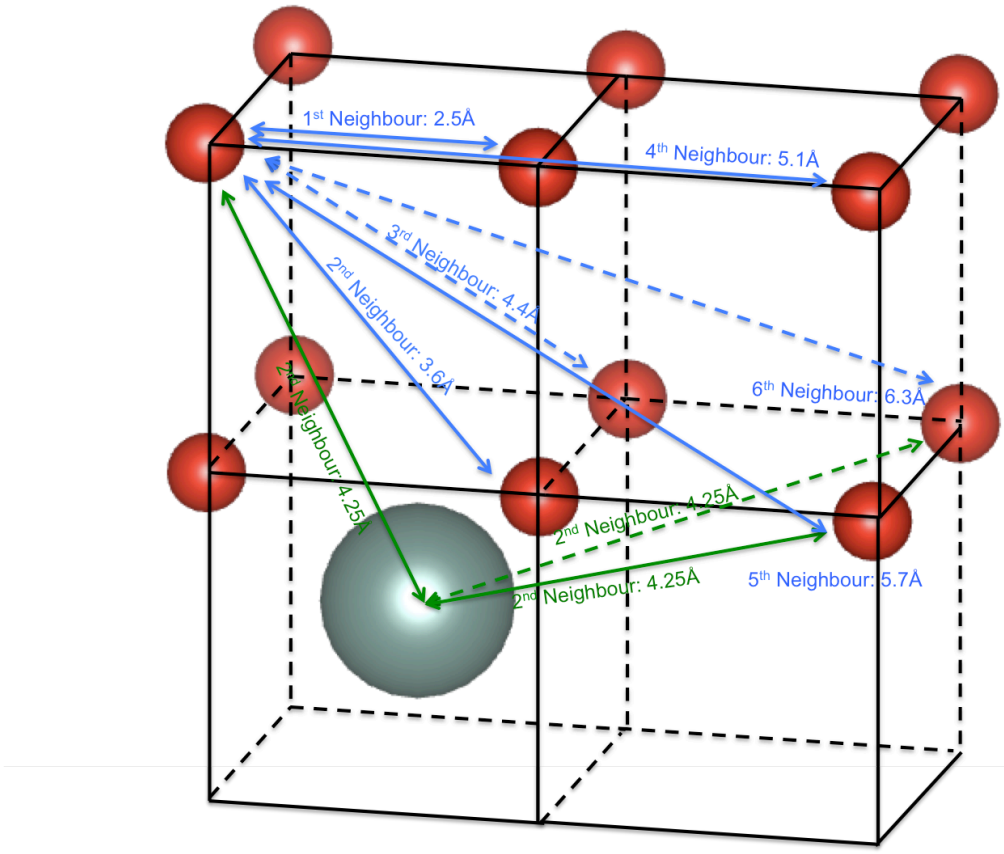

Figure 7.23. Oxygen-oxygen coordination in the cubic fluorite lattice; green lines denote a NNN separation to the same yttrium cation.

7.8 Discussion

Whilst doping ZrO_2 with Y_2O_3 is known to stabilise the cubic phase of zirconia, Raman spectra[19] and Extended X-ray Adsorption Fine Structure (EXAFS)[20] have shown that YSZ displays significant local disorder and that cubic symmetry only appears upon studying the system with longer length diffraction techniques. Some general features of local structure of YSZ are known; EXAFS[20] and ^{89}Y-MAS-NMR[12] studies have shown that on average yttrium cations adopt 8-fold oxygen coordination whilst zirconium cations are 7-fold coordinated by oxygen. This places charge compensating oxygen vacancies in the first coordination sphere of zirconium and the second coordination sphere, or next nearest neighbour (NNN) position, of yttrium. Two simplistic arguments were originally put forward in order to explain this phenomenon; (i) that the larger dopant yttrium cations prefer 8-fold coordination, or (ii) that the zirconium cation prefers to be 7-fold coordinated as it is in the low temperature monoclinic zirconia polymorph. Diffuse neutron

diffraction studies also suggest that oxygen vacancies associate to form pairs along the <111> direction without forming long range ordered phases[9], although the ordered δ-phase ($Zr_3Y_4O_{12}$) has been observed for 40 mol% Y_2O_3 in ZrO_2 and is characterised by chains of oxygen vacancies running along the <111> direction of the original fluorite structure[21].

Our calculations have shown that cubic stabilisation of the lattice parameters occurs at ~10 mol% $YO_{1.5}$ doping and that the structure remains very locally disordered. Additionally in good agreement with experiment there is a preference for yttrium to remain 8-fold coordinated, with oxygen vacancies occupying the NNN lattice positions. We find that it is distinctly favourable energetically to maximise the number of yttrium-vacancy NNN interactions whereby one oxygen vacancy is NNN to many yttrium ions. A similar finding was presented by Dong *et al.*[2], which they explain as YSZ containing two effects: size and charge. From size considerations yttrium has a lower energy when 8-fold coordinated by oxygen atoms but there is a Coulomb attraction between yttrium cations and oxygen vacancies; the NNN Y-V interaction gives a separation distance where both effects reinforce each other. Whilst using NNN vacancy interactions with yttrium ions has been the natural extrapolation, used when creating models for many previous studies, of the dilute limit findings and experimental evidence it has been shown here to hold true for a 9 mol% doping concentration. Furthermore, these results also show that oxygen vacancies repel each other and that it is energetically favourable for vacancies to be further apart. Whilst there is no direct evidence for vacancy alignment in this study one can speculate as to why this may be the case.

From visual inspection of the 'global' minimum structure in figure 7.24 it appears almost as if the yttrium cations are aligned along <111> directions. If this is the case, when coupled with the discovery that oxygen vacancies will maximise NNN interactions with as many yttrium cations as possible this could give rise to the situation where there are separate 'channels' that yttrium cations and oxygen vacancies can occupy. This scenario would then lead to oxygen vacancies residing in 'opposite' <111> directions to the yttrium cations. Finally Pietrucci *et al.*[22] studied vacancy-vacancy interactions and oxygen diffusion in YSZ using *ab-initio* molecular dynamics. They notice that whilst many structures may be locally unstable, even with vacancies large distances apart from one another, multiple-vacancy concerted movement can occur in order to stabilise the system; this phenomenon is observed in this work on geometry optimisation from initial cubic lattice site positions.

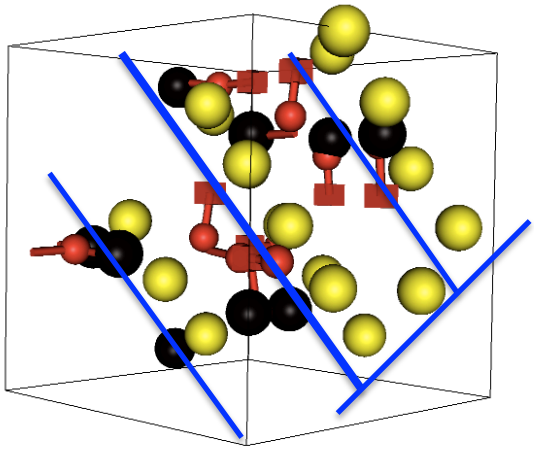

Figure 7.24. 'Global' minimum structure showing vacancies (original and final) oxygen ion displacement, and yttrium ion positions. Blue lines are representative directions.

7.9 Summary and Conclusions

Random sampling of yttria-stabilised zirconia solid solutions over a range of dopant concentrations with empirical potentials provides statistical data about the system in good agreement with a variety of experimentally determined values. Furthermore we identify that low energy structures found with empirical potentials correlate to low energy structures determined by DFT. With regards to the local structure of YSZ upon yttria doping; oxygen vacancies are preferentially located in the 2^{nd} anion coordination sphere of yttrium cations in NNN positions, and maximising the number of yttrium-vacancy NNN interactions results in lowering the energy of the system. Additionally oxygen vacancies repel each other and are preferentially located at 5^{th} or 6^{th} neighbour distances to one another in order to maximise the 2NN yttrium-vacancy interaction.

References:

1. Parkes, M. A.; Tompsett, D. A.; d'Avezac, M.; Offer, G. J.; Brandon, N. P.; Harrison, N. M., The atomistic structure of yttria stabilised zirconia at 6.7 mol%: an ab initio study. *Physical Chemistry Chemical Physics* **2016,** 18, (45), 31277-31285.
2. Dong, Y.; Liang, Q.; Li, J.; Chen, I.-W., A computational study of yttria-stabilized zirconia: I. Using crystal chemistry to search for the ground state on a glassy energy landscape. *Acta Materialia* **2017,** 127, 73-84.
3. Gale, J. D., GULP: A computer program for the symmetry-adapted simulation of solids. *Journal of the Chemical Society-Faraday Transactions* **1997,** 93, (4), 629-637.
4. Dwivedi, A.; Cormack, A. N., A computer-simulation study of the defect structure of calcia-stabilized zirconia. *Philosophical Magazine a-Physics of Condensed Matter Structure Defects and Mechanical Properties* **1990,** 61, (1), 1-22.
5. Lewis, G. V.; Catlow, C. R. A., Potential models for ionic oxides. *Journal of Physics C-Solid State Physics* **1985,** 18, (6), 1149-1161.
6. Xia, X.; Oldman, R.; Catlow, R., Computational Modeling Study of Bulk and Surface of Yttria-Stabilized Cubic Zirconia. *Chemistry of Materials* **2009,** 21, (15), 3576-3585.
7. Parkes, M.; Refson, K.; d'Avezac, M.; Offer, G.; Brandon, N.; Harrison, N., Determining Surface Chemistry and Vibrational Properties of SOFC Anode Materials Through ab initio Calculations. In *Solid Oxide Fuel Cells 13*, Kawada, T.; Singhal, S. C., Eds. 2013; Vol. 57, pp 2419-2427.
8. Cooper, C., Computational Modelling of Yttrium Stabilised Zirconia in Catalysis. In Dept. Chemistry, UCL, 2013; Vol. EngD Thesis.
9. Goff, J. P.; Hayes, W.; Hull, S.; Hutchings, M. T.; Clausen, K. N., Defect structure of yttria-stabilized zirconia and its influence on the ionic conductivity at elevated temperatures. *Physical Review B* **1999,** 59, (22), 14202-14219.
10. Bogicevic, A.; Wolverton, C.; Crosbie, G. M.; Stechel, E. B., Defect ordering in aliovalently doped cubic zirconia from first principles. *Physical Review B* **2001,** 64, (1).
11. Bogicevic, A.; Wolverton, C., Nature and strength of defect interactions in cubic stabilized zirconia. *Physical Review B* **2003,** 67, (2).
12. Kawata, K.; Maekawa, H.; Nemoto, T.; Yamamura, T., Local structure analysis of YSZ by Y-89 MAS-NMR. *Solid State Ionics* **2006,** 177, (19-25), 1687-1690.
13. Steele, D.; Fender, B. E. F., Structure of cubic ZrO2-YO1.5 solid-solutions by neutron-scattering. *Journal of Physics C-Solid State Physics* **1974,** 7, (1), 1-11.
14. Chen, Y.; Sellar, J. R., Systematic study of dielectric and conductivity relaxations in yttria-stabilised zirconia alloys at lower temperatures. *Solid State Ionics* **1996,** 86-8, 207-211.
15. Lanagan, M. T.; Yamamoto, J. K.; Bhalla, A.; Sankar, S. G., The dielectric-properties of yttria-stabilized zirconia. *Materials Letters* **1989,** 7, (12), 437-440.
16. Scott, H. G., Phase relationships in zirconia-yttria system. *Journal of Materials Science* **1975,** 10, (9), 1527-1535.
17. Faber, J.; Mueller, M. H.; Cooper, B. R., Neutron-diffraction study of Zr(Ca,Y)O2-X - evidence of differing mechanisms for internal and external distortions. *Physical Review B* **1978,** 17, (12), 4884-4888.
18. Parkes, M. A.; Refson, K.; d'Ayezac, M.; Offer, G. J.; Brandon, N. P.; Harrison, N. M., Chemical Descriptors of Yttria-Stabilized Zirconia at Low Defect Concentration: An ab Initio Study. *Journal of Physical Chemistry A* **2015,** 119, (24), 6412-6420.
19. Feinberg, A.; Perry, C. H., Structural disorder and phase-transitions in ZrO2-Y2O3 system. *Journal of Physics and Chemistry of Solids* **1981,** 42, (6), 513-518.
20. Catlow, C. R. A.; Chadwick, A. V.; Greaves, G. N.; Moroney, L. M., EXAFS study of yttria-stabilized zirconia. *Journal of the American Ceramic Society* **1986,** 69, (3), 272-277.
21. Ray, S. P.; Stubican, V. S., Fluorite related ordered compounds in ZrO2-CaO and ZrO2-Y2O3 systems. *Materials Research Bulletin* **1977,** 12, (5), 549-556.
22. Pietrucci, F.; Bernasconi, M.; Laio, A.; Parrinello, M., Vacancy-vacancy interaction and oxygen diffusion in stabilized cubic ZrO(2) from first principles. *Physical Review B* **2008,** 78, (9), 7.

Chapter 8

Conclusions & Future Work

The computer simulations performed throughout this thesis have had the aim of understanding better both the fundamental local defect structure present in YSZ and surface catalytic reactions. Some previous notions about the relationship between dopant yttrium ions and charge compensating oxygen vacancies have both been confirmed and advanced, and the understanding of the microscopic defect structure placed on firmer footing. A new redox mechanism has been proposed for generating catalytically active surfaces, and subsequent methane partial oxidation reactions on these surfaces have been investigated.

8.1 Surface Models

The principal difference between the calculations of YSZ surfaces presented throughout this thesis and previous computational YSZ surface studies is with the surface models used to describe the YSZ system. The work presented here uses larger 4x4x1 6 tri-layer surface supercell expansions (~280 atoms) of the cubic ZrO_2 unit cell in order to model the YSZ system, whilst most previous studies use a 2x2x1 3 tri-layer surface supercell (~36 atoms). These much larger surface supercells provide a more realistic representation of the YSZ surface. In particular, extended relaxations of the oxygen anion sub-lattice, allowing for oxygen ion mobility, are made possible which are found to affect adsorption energies. For example the adsorption energy of a molecule on the YSZ surface can be increased by inducing oxygen ion rearrangement in the surface on adsorption, leading to an energetically favourable configuration. Individual cases of this oxygen ion rearrangement have been discussed in the results chapters of this thesis and will be revisited in the conclusions. However, it is important to note that this effect is a common theme for all of the surface calculations performed in this thesis. The result of using these larger surfaces is a more realistic description of the YSZ surface in which the effects of oxygen ion mobility and rearrangement can be modelled. However, the problem arising from using larger surface models is that of requiring larger numbers of substitutional dopant yttrium ions and oxygen vacancies in order to model systems of the same (and of industrially relevant) defect concentrations. The results of chapter 7 give credence to dopant and vacancy positions used in the surface models of this thesis in which the isolated defect cluster findings of having vacancies situated in NNN positions to yttrium cations are extrapolated to multi-vacancy systems, and although a comprehensive search of defect configurations within the surface system has not been performed we consider that the surface models used here are a reasonable representation of the YSZ system under catalytic operation at high temperature.

8.2 Water Adsorption

The adsorption of a single water molecule onto the YSZ surface was conducted by performing geometry optimisation calculations on two separate YSZ symmetric slab models. These models are of stoichiometric YSZ and contain only charge compensating oxygen vacancies. The ‘periodic vacancy’ model, in which dopant yttrium cations and substitutional sub-surface oxygen vacancies occupied identical periodically repeating positions in the surface model, found water to adsorb molecularly with an adsorption energy of -0.5 to -0.8 eV. However, the multi-vacancy model, in which the oxygen vacancies and yttrium cations are more unevenly dispersed in order to represent a more realistic YSZ surface under operating conditions found water to adsorb in both molecular and dissociative configurations. Molecular water adsorption on this multi-

vacancy model calculated stronger water adsorption energies, when compared to the periodic vacancy model, of between -0.7 to -1.2 eV. The stronger water adsorption energies observed on the multi-vacancy model are accompanied by extended relaxation of the oxygen anion sub-lattice, and the configuration of this molecular adsorption mode has the water oxygen atom coordinated to a surface metal cation with some degree of hydrogen bonding between one water hydrogen atom and a surface lattice oxygen atom. Furthermore, multiple-atom concerted movement of oxygen ions allows for a very strong dissociative adsorption mode of water (-2.2 eV) into two hydroxyls, with one hydroxyl occupying the site of a charge compensating surface oxygen vacancy.

8.3 Redox Properties

The redox behaviour of the multi-vacancy YSZ surface was investigated first by considering surface reduction in which an oxygen atom is removed, and secondly the subsequent re-oxidation of the reduced YSZ surface by diatomic molecular oxygen was conducted. Surface reduction in the form of oxygen atom removal led to the formation on doubly occupied F-centre defect states within the band-gap of the material. The partial charge density of these surface F-centres is localised in the oxygen atom vacancy region with some charge delocalisation extending onto neighbouring surface cations. The vacancy formation energy was calculated to be between +4.50 and +6.95 eV. The lower vacancy formation energies typically had zirconium cations surrounding the F-centre, as the charge density was more readily delocalised over zirconium than yttrium. Additionally, the low vacancy formation energies were accompanied by multiple oxygen ion concerted movements within the oxygen anion sub-lattice allowing the F-centre to occupy energetically favourable locations. Furthermore, reduction of YSZ step-surface models was also investigated and as with the low vacancy formation energy terrace systems, oxygen sub-lattice relaxation and mobility on oxygen atom removal allowing F-centre vacancies to occupy energetically favourable locations resulted in reducing the vacancy formation energy to ~ +3.8 eV. Re-oxidation of the surface by the adsorption of diatomic molecular oxygen into the surface F-centre was performed and in each case a very strong adsorption of molecular oxygen onto the reduced surface was observed. Molecular oxygen adsorption energies were calculated to be between -4.6 and -6.8 eV, and resulted in a partially reduced di-atomic molecular oxygen surface species. This overall reduction and re-oxidation process in effect generates a ‘YSZ+O’ surface which contains an additional oxygen atom and is considered to be a pre-oxidised active surface for catalytic reactions.

8.4 Catalytic Partial Oxidation of Methane

The pre-oxidised active 'YSZ+O' surface created by surface reduction and re-oxidation of YSZ was used as the starting surface for investigating the reaction scheme for the catalytic partial oxidation of methane. In essence two oxidation pathways were investigated independently; (i) the oxidation of methane to formaldehyde, and (ii) the oxidation of formaldehyde to formate, which both follow similar reaction mechanisms. In both of these pathways, the carbon atom of the reactant species coordinates to surface lattice oxygen and stepwise hydrogen atom abstractions occur. The partially reduced diatomic surface oxygen species acts as an electron density acceptor and dissociates on the first hydrogen abstraction step; lattice oxygen then forms a surface hydroxyl species and both oxygen atoms of the active oxygen species are incorporated as lattice oxygen. The adsorption/hydrogen abstraction of the initial reactant molecule (methane or formaldehyde) coupled with the dissociation of the active oxygen species and incorporation of its oxygen atoms as lattice oxygen results in very energetically favourable adsorption energies when compared to the gas-phase molecule and the starting YSZ+O surface. Hydrogen abstraction from methane forming adsorbed methoxy $*CH_3$ + OH, and from formaldehyde forming adsorbed formate + OH have adsorption energies of ~ -2.0 and -3.5 eV respectively. A second hydrogen abstraction step by lattice oxygen was then investigated for both oxidation pathways. In the case of methane oxidation to formaldehyde the second hydrogen abstraction leads to an absorbed $*CH_2$ species and two surface hydroxyls, with an adsorbed formaldehyde species (containing lattice oxygen) formed following the desorption of H_2. Following the second hydrogen abstraction from formaldehyde, the surface contains an adsorbed CO_2 species and two surface hydroxyls; desorption of either CO_2 + H_2 or CO + H_2O regenerate a stoichiometric YSZ surface and give oxidation products containing only lattice oxygen. Furthermore, formaldehyde decomposition to syngas in the form of direct hydrogen abstraction from formaldehyde on a stoichiometric YSZ surface (in the absence of an active oxygen species) to adsorbed CO and two hydroxyls was investigated. Nudged elastic band calculations found all but one of the hydrogen abstraction steps to occur with similar energy barriers of ~ +1.3 to +1.7 eV. The highest activation barrier was ~ +2.4 eV for the abstraction of hydrogen from surface formate (second hydrogen abstraction of the formaldehyde oxidation pathway), which could explain the experimentally observed stability of formate on the surface of YSZ. The coordination of carbon to lattice oxygen in these reaction pathways, and the incorporation of active oxygen following hydrogen abstraction and molecular oxygen dissociation highlight the Mars-van Krevelen nature of oxidation reactions on YSZ as seen experimentally.

8.5 Bulk Defect Structure

The local structure of the industrially relevant 9 mol% (Y_2O_3) bulk YSZ has been investigated in realistic system sizes (3x3x3 supercells of cubic ZrO_2 – 324 atoms) using a combination of both random sampling and global optimisation techniques, and a range of different dopant concentration YSZ solid solutions were also studied. Firstly ~ 10,000 unique structures of each dopant concentration were randomly generated and geometry optimised using interatomic potentials. It was found that subsequent geometry optimisation of these already optimised structures using DFT resulted in essentially the same structures with the same local structure features, and that low/high energy IP structures correlate with low/high energy DFT structures respectively. DFT and interatomic potentials are therefore in agreement as to which structural features correspond to low or high energies. Secondly the ensembles of structures are re-optimised allowing the lattice parameter to relax in order to account for lattice expansion. Macroscopic properties of the YSZ solid solution ensembles have been calculated, including the lattice parameter and dielectric constant, and are in good agreement with experimental values, giving confidence that the randomly generated structure ensembles are representative of real YSZ systems and provide sensible structures from which to determine local structure features of YSZ. Radial distribution function analysis of the low energy structures of 9 mol% YSZ show that the next nearest neighbour yttrium-vacancy interaction is indeed a feature of low energy systems and that large vacancy-vacancy separations are also energetically favourable. Furthermore a candidate starting population of the 100 lowest-energy randomly generated structures were taken as inputs for a solid solution swapping 'basin-hopping' global optimisation approach. The overall lowest energy structure, taken to be the de-facto 'global minimum' showed that maximising the number of yttrium-vacancy NNN interactions resulted in reducing the energy of the system, and that vacancy-vacancy separations of 5^{th} and 6^{th} nearest neighbour anion sites are preferred as these correspond to maximising yttrium-vacancy NNN interactions.

8.6 Future Work

The primary objective of the work conducted throughout this thesis was to understand better the nature and mechanism of C-H bond activation/oxidation catalysis on YSZ, in the catalytic partial oxidation of methane in particular. We have presented a new mechanism in which surface reduction and the subsequent re-oxidation by, and activation of, molecular oxygen generates an active surface species. The active molecular oxygen acts as an electron density acceptor upon hydrogen abstraction and the dissociation of the active molecular oxygen species and incorporation into the YSZ oxygen anion sub-lattice provides a large thermodynamic driving force for these hydrogen abstraction/oxidation procedures. We find formaldehyde oxidation to

formate to be strongly exothermic, in good agreement with experimental evidence that formaldehyde readily oxidises to formate on YSZ, and that formate is a stable surface species. Furthermore, the 'spectator' nature of the active oxygen species, the incorporation of active oxygen as lattice oxygen on hydrogen abstraction and molecular oxygen dissociation, and the coordination of reactant carbon to YSZ lattice oxygen account well for the experimentally observed Mars-van Krevelen nature of CPOM. However, despite providing a good account of the steps involved in the reaction pathway of CPOM, the work presented here by no means covers the entire picture of CPOM on YSZ and there are many avenues of study that can be undertaken to build upon these initial results.

In the first instance, whilst we have presented a reduction and re-oxidation mechanism for the YSZ surface, which generates a partially reduced molecular oxygen species, this has so far been modelled as a static procedure using geometry optimisation calculations. However, in reality this is a very dynamic process as evidenced by the isotopic oxygen exchange experiments conducted by Zhu *et al.*[1], which show that with increasing temperature $^{18}O_2$ will be fully exchanged with lattice oxygen in YSZ with only $^{16}O_2$ liberated. The CPOM calculations of this thesis show how active O_2 present following surface reduction and re-oxidation provides a thermodynamic driving force for hydrogen abstraction but the dissociation and incorporation of molecular oxygen, and subsequent liberation of diatomic lattice oxygen molecules in the absence of another surface adsorbed species has not been considered here. One way in which this dynamical process could be studied would be through the use of molecular dynamics simulations carried out at the DFT level of theory.

Following on from the above, the lack of detailed understanding of the state of the surface and the dynamics of these active oxygen species could also impact the catalytic reaction pathways. In the CPOM simulations performed in this study (methane oxidation to formaldehyde, and formaldehyde oxidation to formate), the first hydrogen abstraction step occurs with an active partially reduced molecular oxygen species, whereas the second hydrogen abstraction occurs by lattice oxygen. The rationale followed was that the reduction and re-oxidation generates an active oxygen species at a particular surface location, and that methane or formaldehyde can adsorb in the vicinity of this active oxygen. The first hydrogen abstraction step effectively consumes the active oxygen as both atoms are incorporated as surface lattice oxygen, and the second hydrogen abstraction step in the catalytic pathways investigated here can therefore only occur using lattice oxygen without an active oxygen molecule present. However, it may be possible that the diffusion or mobility of active oxygen species leads to another active oxygen being present and involved in the second hydrogen abstraction steps. Additionally, there may be a high coverage of these active oxygen species already present, which can take part in these subsequent oxidation steps. Greater detail about the true state of the surface can only be

garnered from more detailed experimental studies. However, a number of different computational approaches could be investigated in order to examine the validity of other pathways containing additional active oxygen species. First, an additional active oxygen system could be 'created' simply by the introduction of one oxygen atom, in a configuration similar to the original active oxygen system, in the vicinity of the surface adsorbed reactant species prior to the second hydrogen abstraction step. This approach would be based on active oxygen diffusion/mobility and would need to be coupled to the above suggestion. Secondly a mechanism involving the full redox process could be studied. Following the first hydrogen abstraction step and the 'consumption' of the initial active oxygen, surface reduction calculations, in the form of oxygen atom removal, and re-oxidation calculations prior to the second hydrogen abstraction step could be performed.

Furthermore, perhaps one of the most interesting features of the experimental CPOM work is the finding that the presence of water in the reaction mixture increases selectivity to syngas[2]. The experimental work shows that formaldehyde will readily oxidise to formate on pre-oxidised surfaces so the assumption is that water somehow stabilises surface formaldehyde allowing it to decompose directly to syngas instead of being oxidised to formate. The calculations of this thesis show that hydrogen abstraction from formaldehyde, with active oxygen present, in order to form formate is extremely thermodynamically favourable although how water prevents this oxidation remains unknown. Initially we find that the dissociative adsorption of water can occur on stoichiometric YSZ, with a hydroxyl filling a stoichiometric surface vacancy. We also find that concerted oxygen movement and oxygen mobility upon surface reduction is an important factor in lowering the vacancy formation energy. We have speculated that dissociated water could decrease the reducibility of the surface by occupying these vacancies and inhibiting oxygen mobility, preventing the formation of active oxygen. Surface reduction calculations on this dissociated water surface could be performed in order to test this hypothesis. Alternatively it could be that water coverage prevents the formation of active oxygen or provides a physical barrier between formaldehyde and active surface oxygen species and therefore stabilises formaldehyde with respect to oxidation. These scenarios present yet more avenues for further study.

Finally whilst the focus of the work here has been investigating oxidation catalysis on YSZ, as it has been shown to be an active catalyst in its own right, another common use for YSZ is as a support for metal nanoparticle catalysts. It would therefore be enlightening to study the interactions of metal atoms and particles with the YSZ surface on these larger surface models. Furthermore, a recent study into propane dehydrogenation (PDH) to propene on lanthanum doped zirconia ($LaZrO_x$) found that coordinatively unsaturated zirconium cations, situated next to anion vacancies following reductive treatment, were the active catalytic sites, and that the

role of metal nanoparticles was to promote surface reduction of the $LaZrO_x$[3]. This scenario presents another very interesting direction of study into better understanding the catalytic nature of doped zirconia materials and in particular YSZ.

References:

1. Zhu, J. J.; van Ommen, J. G.; Bouwmeester, H. J. M.; Lefferts, L., Activation of O-2 and CH4 on yttrium-stabilized zircoma for the partial oxidation of methane to synthesis gas. *Journal of Catalysis* **2005,** 233, (2), 434-441.
2. Zhu, J.; van Ommen, J. G.; Lefferts, L., Effect of surface OH groups on catalytic performance of yittrium-stabilized ZrO2 in partial oxidation of CH4 to syngas. *Catalysis Today* **2006,** 117, (1-3), 163-167.
3. Otroshchenko, T.; Sokolov, S.; Stoyanova, M.; Kondratenko, V. A.; Rodemerck, U.; Linke, D.; Kondratenko, E. V., ZrO2-Based Alternatives to Conventional Propane Dehydrogenation Catalysts: Active Sites, Design, and Performance. *Angewandte Chemie-International Edition* **2015,** 54, (52), 15880-15883.

Acknowledgements

First and foremost thanks is owed to my supervisors Professor Richard Catlow and Dr David Scanlon; Richard for providing me with the opportunity to undertake this PhD, his wisdom and guidance over the course of my research have been invaluable and I am deeply thankful and humbled by the kindness and reassurance afforded to me, and David for offering his calculation expertise and challenging me to challenge myself, his good humour has made what can be a stressful and demanding environment instead a relaxed and enjoyable experience. The thoughtful inspiration of both Richard and David has moulded this thesis into the work it has become and for that I will be forever grateful.

Further thanks are owed to many other members of the extended Catlow group network in all its guises. In particular I am indebted to Dr Alexey Sokol for his enthusiasm and patience, which spurred on the solid solution studies of chapter 7, and Dr Tomas Lazauskas for the great deal of assistance he gave me in all facets of setup and analysis for the solid solutions. Furthermore, Dr Scott Woodley provided many insightful inputs into the problems faced along the way and I am extremely appreciative of the help he provided for the use of, and tailoring the KLMC code. Dr Matthew Farrow is also deserving of thanks for his help using KLMC and in running large numbers of calculations, as well as for the initial stages of the solid solution work. Additionally, I am thankful for the help both Dr David Mora-Fonz and Alex Ganose have given me at various stages with running and analysing calculations. Dr Andrew Logsdail was also very helpful in assisting and guiding me through the early stages of my research, as well as being a fantastic source of tickets to sporting events.

My industrial sponsors Johnson Matthey are due thanks for all their involvement, and special thanks go to Martin Fowles, Dr Misbah Sarwar and Dr Crispin Cooper; who always provided new inspiration and stimulation after our project meetings, and who were always eager to offer help.

In addition to the thanks already given, I am grateful to UCL, the EPSRC, and Johnson Matthey for the funding provided, and to UCL and the Materials Chemistry Consortium for access to the Legion, Grace, and ARCHER supercomputing clusters.

I would also like to acknowledge all those who have studied YSZ before me. I truly believe that I have benefited immensely from the vast amount of detailed studies that have been conducted previously, and that any findings made here would not have been possible without them.

Finally thanks is owed to all my friends and family, and to my partner Erin, for the support and being there providing me normality, for all the laughs and being fun, preserving me my sanity.